Synthesis, structural, magnetic and transport properties of layered perovskite-related titanates, niobates and tantalates of the type $A_nB_nO_{3n+2}$, $A'A_{k-1}B_kO_{3k+1}$ and $A_mB_{m-1}O_{3m}$

F. Lichtenberg *, A. Herrnberger, K. Wiedenmann

Experimentalphysik VI, Center for Electronic Correlations and Magnetism (EKM), Institute of Physics, Augsburg University, D - 86135 Augsburg, Germany

PUBLISHED IN PROGRESS IN SOLID STATE CHEMISTRY 36 (2008) 253−387

Abstract. This article represents a continuation of a paper on $A_nB_nO_{3n+2} = ABO_x$ compounds which was published in 2001 in this journal. This work reports also on oxides of the type $A'A_{k-1}B_kO_{3k+1}$ (Dion-Jacobson type phases) and hexagonal $A_mB_{m-1}O_{3m}$. The title materials have in common a layered perovskite-related structure whose layers are formed by corner-shared BO_6 octahedra. The three homologous series differ structurally in their orientation of the BO_6 octahedra with respect to the c-axis. This can be considered as a result from cutting the cubic perovskite ABO_3 structure along different directions followed by an insertion of additional oxygen, namely along the [100], [110] and [111] direction for $A'A_{k-1}B_kO_{3k+1}$, $A_nB_nO_{3n+2}$ and $A_mB_{m-1}O_{3m}$, respectively. The materials, with emphasis on electrical conductors, were prepared by floating zone melting and characterized by thermogravimetric analysis, x-ray powder diffraction and magnetic measurements. On crystals of five different compounds the resistivity was measured along the distinct crystallographic directions. Concerning $A_nB_nO_{3n+2}$ this work is focussed on two topics. The first are materials with paramagnetic rare earth ions at the A site or transition metal ions such as Fe^{3+} at the B site. The second are non-stoichiometric compounds. Furthermore, we discuss issues like occupational order at the B site, the proximity of some materials to the pyrochlore structure, potential magnetic ordering, and a possible coupling between magnetic and dielectric properties. The oxides $A'A_{k-1}B_kO_{3k+1}$ gained attention during a study of the reduced Ba−(Ca,La)−Nb−O system which lead to conducting Dion-Jacobson type phases without alkali metals. Concerning hexagonal $A_mB_{m-1}O_{3m}$ the emphasis of this work are conducting niobates in the system Sr−Nb−O. The title materials have in common a quasi-2D (layered) structure and they are mainly known as insulators. In the case of electrical conductors, however, their transport properties cover a quasi-1D, quasi-2D and anisotropic 3D metallic behavior. Also temperature-driven metal-to-semiconductor transitions occur. A special feature of the quasi-1D metals of the type $A_nB_nO_{3n+2}$ is their compositional, structural and electronic proximity to non-conducting (anti)ferroelectrics. We speculate that these quasi-1D metals may have the potential to create new (high-T_c)superconductors, especially when they are viewed from the perspective of the excitonic type of superconductivity. Referring to literature and results from this work, a comprehensive overview on the title oxides and their properties is presented.

* Present address: ETH Zurich, Department of Materials, CH - 8093 Zurich, Switzerland

Keywords: Titanates; Niobates; Tantalates; Perovskite-related crystal structures; Layered materials; Crystal growth; Floating zone melting; Low-dimensional conductors; Resistivity; Magnetic susceptibility; Magnetic ordering; Ferroelctrics; Antiferroelectrics; Superconductivity; Excitonic Superconductivity

Contents

1 Introduction and overview

1.1 Preliminaries and general survey

This article represents a continuation of a paper on $A_nB_nO_{3n+2} = ABO_x$ compounds which was published in 2001 in this journal [127]. This special group of oxides comprises the highest-T_c ferroelectrics such as $n = 4$ $SrNbO_{3.50}$ [151] and quasi-1D metals such as $n = 5$ $SrNbO_{3.40}$ [110–113,127,136,244] which are in compositional, structural and electronic proximity to non-conducting (anti)ferroelectrics. This suggests the possibility to realize materials with an intrinsic coexistence of metallic conductivity and high dielectric polarizability. Therefore this group of oxides represents an important field of research.

In addition to the $A_nB_nO_{3n+2} = ABO_x$ materials this work reports also on Dion-Jacobson type phases $A'A_{k-1}B_kO_{3k+1}$ and hexagonal $A_mB_{m-1}O_{3m}$. There were several reasons for this extension. First, during a study exploring the substitution of Ca by Ba in $n = 4$ niobates (Ca,La)$NbO_{3.50}$, an additional phase appeared whose type was assigned as $A'A_{k-1}B_kO_{3k+1}$. This lead to the synthesis of $A'A_{k-1}B_kO_{3k+1}$ compounds in the reduced Ba−(Ca,La)−Nb−O system. They represent Dion-Jacobson type phases without any alkali metal. Secondly, associated with structural discussions the hexagonal $A_mB_{m-1}O_{3m}$ oxides are sometimes cited in papers about $A_nB_nO_{3n+2}$ materials, e.g. in the publication by Levin et al. [122]. In addition to that, sometimes an $A_mB_{m-1}O_{3m}$ compound occurred as impurity phase in $A_nB_nO_{3n+2}$ compositions. That way the $A_mB_{m-1}O_{3m}$ phases gained attention and the question for the preparation of electrical conductors of this type did raise. Thirdly, the $A'A_{k-1}B_kO_{3k+1}$, $A_nB_nO_{3n+2}$ and $A_mB_{m-1}O_{3m}$ compounds represent three related structural modifications of the cubic perovskite ABO_3. They emerge from the latter by cutting it along its [100], [110] and [111] direction, respectively, followed by an insertion of additional oxygen. The resulting structures constitute layered, perovskite-related, homologous series whereby the layers along the c-axis are $k = n = m - 1$ BO_6 octahedra thick. The layers are formed by corner-shared BO_6 octahedra along the ab-plane. Their structural difference is mainly given by the kind of orientation of the BO_6 octahedra with respect to the c-axis. This suggests to study and compare the physical properties of related materials of these three series.

Before considering the three title series in detail, we cite two further structure types which are worth mentioning in their context. The first is given by the Ruddlesden-Popper phases $A_{j+1}B_jO_{3j+1}$ which represents a perovskite-related, layered, homologous series. Like the Dion-Jacobson type compounds the Ruddlesden-Popper phases arise from a cut of the cubic perovskite ABO_3 along its [100] direction followed by an insertion of additional oxygen. The oxides of the Ruddlesden-Popper type are usually more familiar because they are known for many different B cations. This is in contrast to the title oxides which are only known for B = Ti, Nb or Ta, or at least the required minimum occupancy of Ti, Nb or Ta at the B site is about 67 %. The second structure worth mentioning is that of La_2RuO_5 which is similar to the $n = 2$ type of $A_nB_nO_{3n+2}$

but its interlayer region is occupied with La and O. To our knowledge La_2RuO_5 is the only compound with this type of structure [1]. The structure of La_2RuO_5 was determined by powder XRD and powder neutron diffraction by Boullay et al. [21] and Ebbinghaus [44], respectively.

The crystal structure of the Ruddlesden-Popper phases $A_{j+1}B_jO_{3j+1}$, Dion-Jacobson type compounds $A'A_{k-1}B_kO_{3k+1}$, $A_nB_nO_{3n+2}$, La_2RuO_5 and hexagonal $A_mB_{m-1}O_{3m}$ is sketched in Fig. 1 − 10. In this work and in the previous article [127] the c-axis is chosen as the longest axis. The group of the $A'A_{k-1}B_kO_{3k+1}$ oxides comprises three different structure types. In this work we call them type I, II and III. They differ in the kind of displacement of adjacent layers, see e.g. Fig. 5 and Table 4 in the paper by Fukuoka et al. [53]. The type I and II is sketched in Fig. 2 and 3, respectively. The displacement realized in the type III structure corresponds to that in $A_{j+1}B_jO_{3j+1}$ which is sketched in Figure 1. Figure 8 serves as an illustration to show how the sketch of the hexagonal $A_mB_{m-1}O_{3m}$ in Fig. 9 and 10 comes about. Table 1 presents a further approach to the structure of hexagonal $A_mB_{m-1}O_{3m}$, namely in terms of cubic closed-packed (ccp) stacking sequences of AO_3 sheets along the c-axis.

To facilitate a comparison between the four series $A_{j+1}B_jO_{3j+1}$, $A'A_{k-1}B_kO_{3k+1}$, $A_nB_nO_{3n+2}$ and $A_mB_{m-1}O_{3m}$, a list with some of their features is presented in Table 2 and 3. Two of them, $A'A_{k-1}B_kO_{3k+1}$ and $A_nB_nO_{3n+2}$, have the same cation ratio of $(A', A)/B = A/B = 1$. Therefore their composition can be represented by the general formula ABO_x. Table 4 presents the oxygen content x in ABO_x and corresponding structure types(s) with compositional examples from literature and this work. In Table 4 two further structure types are mentioned, namely pyrochlore and fergusonite. The latter represents the monoclinically distorted variant of the tetragonal scheelite structure ($CaWO_4$ type). The pyrochlore and the fergusonite structure are neither layered nor related to perovskite.

The Figures 11 − 17 present some structural details of several compounds belonging to $A_{j+1}B_jO_{3j+1}$, $A'A_{k-1}B_kO_{3k+1}$, $A_nB_nO_{3n+2}$ and $A_mB_{m-1}O_{3m}$, especially the distortion of crystallographically inequivalent BO_6 octahedra and the experimentally determined occupancies at the B or A site. In this work and in Ref. [127] the distortion of an octahedron or polyhedron is defined as

$$\text{octahedron or polyhedron distortion} = \frac{(\text{largest} - \text{smallest})\ B - \text{O distance}}{\text{average}\ B - \text{O distance}} \tag{1}$$

The Figures 11 − 17 reveal some features which most of the compounds have in common:

- The distortion of the BO_6 octahedra is largest at the boundary of the layers (because there the deviation from the perovskite structure is greatest).

[1] We notice that La_2RuO_5 displays interesting physical properties. It shows a temperature-driven semiconductor-to-semiconductor transition at about 160 K [100]. This first-order phase transition is discussed in terms of orbital ordering [48,100].

- The distortion of the BO_6 octahedra decreases as moving from the boundary to the inner region of the layers.

- The distortion is very small for those BO_6 octahedra which are located at the center of layers which are 3 or 5 octahedra thick.

- If there are at the A or B site two different cations which differ in their valence, then the site occupancy of those ions with the higher valence is largest at the boundary of the layers and smallest at the center of the layers. The reason for this partial ordering is the following. Compared to the perovskite ABO_3 the amount of oxygen O^{2-} at the boundary of the layers is relatively large. This results in a significant amount of negative charge at the boundary of the layers. To compensate this negative charge the positively charged A or B cations with the higher valence tend to accumulate at the boundary of the layers.

Concerning the latter item, full ordering appears only in few compounds. Full occupational ordering at the B site is reported for the $k = 3$ material $CsLa_2Ti_2NbO_{10}$ (Fig. 11) by Hong et al. [76] and the $n = 5$ types $Ln_5Ti_4FeO_{17} = LnTi_{0.8}Fe_{0.2}O_{3.40}$ with Ln = La, Pr or Nd (Fig. 16) by Titov et al. [227,228]. Full ordering at the A site is reported for $n = 3$ tantalate $Sr_2LaTa_3O_{11} = Sr_{0.67}La_{0.33}TaO_{3.67}$ (Fig. 12) by Titov et al. [224]. We note that for this tantalate the cation arrangement with respect to the valence is opposite to that of the most other materials. The La^{3+} ions, which have a higher valence compared to Sr^{2+}, are exclusively located in the inner region of the layers.

The Tables 5 – 60 present an overview of many compounds of the type $A'A_{k-1}B_kO_{3k+1}$, $A_nB_nO_{3n+2} = ABO_x$ and $A_mB_{m-1}O_{3m}$ reported in literature and this work. Also listed are some of their properties. N denotes the number of 3d, 4d or 5d electrons per Ti, (Ti,V), (Ti,Nb), Zr, Nb, Ta, W or Re at the B site obtained from charge neutrality. a, b, c, β and V represent the lattice parameters and Z stands for the number of formula units per unit cell. In the case of $A_nB_nO_{3n+2} = ABO_x$ there are some special Tables included. The Tables 47 and 48 show the features and the present state of the most intensively studied electrical conductors of the type $A_nB_nO_{3n+2} = ABO_x$ which are niobates with the composition (Sr,La)NbO_x. Furthermore, recent and comprehensive papers which report on several compounds and structure types are listed in the Tables 49 and 50 with title, author(s), year of publication and remarks about the content.

In the following we describe some attributes and the present state of the title oxides.

1.2 $A_nB_nO_{3n+2} = ABO_x$

The features of the $A_nB_nO_{3n+2} = ABO_x$ compounds can be found in Fig. 4 – 6, Table 2 – 4, Fig. 12 – 16 and Table 15 – 50. This special group of oxides comprises several compounds with interesting and unique properties.

The $n = 3$ (II) and the non-integral $n = 4.5$ type such as $LaTi_{0.67}TaO_{0.33}O_{3.67}$ and $LaTiO_{3.44}$, respectively, are examples of materials with an ordered stacking sequence of layers with different thickness, see Figure 4 and 5. Many of the non-integral series members, e.g. the $n = 4.5$ quasi-1D metal $SrNbO_{3.45}$, can be obtained as single phase samples by floating zone melting [127]. This indicates that even the non-integral series members with their long c-axis, e.g. $c \approx 60$ Å for $n = 4.5$, are compounds with a high thermal stability. We note that the term "single phase" refers to the result of a structural analysis by powder XRD.

The existence of significantly non-stoichiometric materials is reported in the previous article, see Table 17 and 18 and Fig. 16 in Ref. [127]. Some examples are the following. The $n = 4$ niobate $Sr_{0.8}LaO_{0.2}NbO_{3.60}$ is over-stoichiometric with respect to the oxygen content. The ideal oxygen content of the $n = 4$ composition is $x = 3.50$. The $n = 5$ niobate $Ca_{0.95}NbO_{3.36}$ is under-stoichiometric with respect to the A site occupancy and the oxygen content. The ideal A site occupancy is 1 and the ideal oxygen content of the $n = 5$ composition is $x = 3.40$. These and some other non-stoichiometric compounds are single phase within the detection limit of powder XRD. We note in this context that the $n = 5$ phases $SrNbO_x$, $CaNbO_x$ and $LaTiO_x$ have a homogeneity range of $3.40 \leq x \leq 3.42$ [127].

Since the publication of the previous article [127] the structures of several compounds were determined by single crystal XRD. For example, the $n = 4$ ferroelectric insulator $SrNbO_{3.50}$ as well as the $n = 5$ quasi-1D metal $LaTiO_{3.41}$ by Daniels et al. [33,34] and the $n = 6$ insulator $Ca(Nb,Ti)O_{3.33}$ as well as the $n = 5$ quasi-1D metal $CaNbO_{3.41}$ by Guevarra et al. [62,63]. For the $n = 4$ ferroelectric insulator $SrNbO_{3.50}$ several structural studies are reported, see Table 19. The structure determination by Daniels et al. [33] indicates that the incommensurate modulation in $SrNbO_{3.50}$ results from the attempt to resolve the strain from very short $Sr - O$ distances at the border of the layers. A structural investigation under high pressure was performed by powder XRD on the $n = 5$ quasi-1D metal $LaTiO_{3.41}$ by Loa et al. [134]. It was found that the $n = 5$ structure remains stable up to a pressure of 18 GPa with a pronounced anisotropy in the axis compressibility of about 1:2:3 for the a-, b- and c-axis. In the range of $18 - 24$ GPa a sluggish but reversible phase transition occurs.

The $A_nB_nO_{3n+2}$ type structures are relatively complex and contain sophisticated features such as incommensurate modulations. There are successful examples to describe the structure of the members of the $A_nB_nO_{3n+2}$ series by an unified four- or five-dimensional superspace approach. To cite some examples we refer to the paper about $Sr_n(Nb,Ti)_nO_{3n+2}$ by Elcoro et al. [46] and $Ca_n(Nb,Ti)_nO_{3n+2}$ ($n = 5$ and 6) by Guevarra et al. [65].

The $n = 4$ materials $CaNbO_{3.50}$, $SrNbO_{3.50}$, $LaTiO_{3.50}$ and $NdTiO_{3.50}$ represent the highest-T_c ferroelectrics with T_c in the range of $1600 - 1850$ K, see Table 19, 21, 22 and 24 [1]. It seems to be a general rule that non-centrosymmetric

[1] To have a comparison with another high-T_c ferroelectric we refer to $LiNbO_3$ which has a T_c of 1480 K [105]. In contrast to the $n = 4$ types whose structure is layered and where the BO_6 octahedra are exclusively corner-shared, the structure of $LiNbO_3$

space groups and ferroelectrics are realized for the even types $n = 2$, $n = 3$ (II), $n = 4$ or $n = 6$, whereas centrosymmetric space groups and antiferroelectrics occur for the uneven types $n = 3$ (I), $n = 5$ or $n = 7$. See Table 4 and 15 − 46.

The niobates and titanates with a reduced composition are anisotropic (semi)conductors. Some of them display along the a-axis a metallic resistivity behavior and undergo at low temperatures a temperature-driven metal-to-semiconductor transition. The temperature dependence of the resistivity along the a-, b- and c-axis of seven different niobates and the $n = 5$ titanate $LaTiO_{3.41}$ can be found in the previous article [127]. They represent a special group of quasi-1D metals. Meanwhile the quasi-1D metallic behavior is established by the resistivity $\rho(T)$ [127] and a comprehensive investigation by Kuntscher et al. [110–113] using angle-resolved photoemission spectroscopy (ARPES) and optical spectroscopy. Presently, the most intensively studied quasi-1D metals are the niobates $SrNbO_{3.41}$ ($n = 5$), $SrNbO_{3.45}$ ($n = 4.5$) and $Sr_{0.8}La_{0.2}NbO_{3.50}$ ($n = 4$) [17,110,111,113,127,242,244]. The features and the present state of these niobates and those of the related ferroelectric insulator $SrNbO_{3.50}$ ($n = 4$) is presented in Table 47 and 48.

The extensive studies by Kuntscher et al. [110,111,113] revealed several interesting properties. For example, in the semiconducting state at low temperatures the $n = 5$ niobate $SrNbO_{3.41}$ displays along the a-axis a very small energy gap at the Fermi level [111,113]. The small value of the gap, about 5 meV, was found by three different experimental techniques, namely by resistivity measurements, optical spectroscopy and high-resolution ARPES. The extreme smallness of the gap is unique among quasi-1D metals. A further interesting feature are the particular differences in $Sr_nNb_nO_{3n+2} = SrNbO_x$ type niobates between the type $n = 4.5$ and 5 and the type $n = 4$ [110,111,113,127], see Table 47 and 48. The $n = 4$ type $Sr_{0.8}La_{0.2}NbO_{3.50}$ displays, compared to related $n = 4.5$ and 5 niobates, a relatively weak metallic character and for $T < T_{MST}$, whereby T_{MST} is the temperature of the metal-to-semiconductor transition in the resistivity, no energy gap along the a-axis was detected by optical spectroscopy. These both findings are probably related to the non-presence of central NbO_6 octahedra in the $n = 4$ niobate where the layers are four NbO_6 octahedra thick. In the case of the types $n = 4.5$ and 5 there are layers which are five NbO_6 octahedra thick. A thickness of five NbO_6 octahedra involves the presence of central NbO_6 octahedra whose distortion is very small, see Figure 15. These central octahedra seem to favor the metallic character as in the $n = 4.5$ and 5 type niobates. This statement is corroborated by LDA band structure calculations on $SrNbO_{3.41}$ ($n = 5$) by Bohnen [111] as well as by Winter et al. [244]. It was found that the largest contribution to the density of states at the Fermi energy comes from those Nb which are located in the central NbO_6 octahedra.

is non-layered and involves corner- and face-shared NbO_6 octahedra. As described in Ref. [144] the structure of $LiNbO_3$ emerges from the cubic perovskite ABO_3 by a rotation of the BO_6 octahedra around its [111] direction. The structure of $LiNbO_3$ represents also a superstructure of corundum, i.e. α-Al_2O_3.

Presently, the nature of the metal-to-semiconductor transition along the a-axis is not completely clarified. For the niobates $SrNbO_{3.41}$ ($n = 5$) and $SrNbO_{3.45}$ ($n = 4.5$) the metal-to-semiconductor transition is discussed in terms of a Peierls type instability by Kuntscher et al., but not all findings can be explained within this picture [110,111,113]. NMR and EPR measurements on $SrNbO_{3.41}$ ($n = 5$) were performed by Weber et al. and their results are discussed in terms of charge density wave formation and Peierls transition [242].

We note that the metal-to-semiconductor transition along the a-axis is also visible in the (real part of the) dielectric constant ε_a at low frequencies. Optical transmission measurements on thin platelets of $SrNbO_{3.41}$ ($n = 5$) and $SrNbO_{3.45}$ ($n = 4.5$) by Kuntscher et al. revealed very high but negative values at $T = 300$ K, as expected for a metal, and very high but positive values at $T = 5$ K [113]. See also Table 48. The high values of ε_a at low frequencies and at low temperatures is related to the smallness of the energy gap along the a-axis [113].

Also the $n = 5$ titanate $LaTiO_{3.41}$ represents a quasi-1D metal. This was revealed by resistivity measurements [127] and optical spectroscopy by Kuntscher et al. [112]. The results from Kuntscher et al. indicate the presence of strong electron-phonon coupling and, along the a-axis, a temperature-driven phase transition at about 100 K and an energy gap of approximately 6 meV which develops below that temperature. The features of $LaTiO_{3.41}$ are discussed within a polaronic picture [112]. Furthermore, the optical response of $LaTiO_{3.41}$ at room temperature was investigated under high pressure by Frank et al. [51]. Their results are discussed in terms of polaronic excitations as well as electronic transitions within a Mott-Hubbard picture in the hole-doped regime. At a pressure of about 15 GPa there are indications for an onset of a dimensional crossover in this highly anisotropic titanate [51]. This is in accordance with the structural study under pressure where in the range of $18 - 24$ GPa a sluggish but reversible phase transition occurs [134].

A special feature of the $A_nB_nO_{3n+2} = ABO_x$ type quasi-1D metals is their compositional, structural and electronic proximity to non-conducting (anti)ferroelectrics. This suggests the possibility to realize compounds with an intrinsic coexistence of metallic conductivity along the a-axis and high dielectric polarizability along a direction perpendicular to that. This statement is supported from the following remarkable experimental results:

- The optical conductivity of the $n = 4$ ferroelectric insulator $SrNbO_{3.50}$ along the b-axis displays a phonon mode at about 54 cm^{-1} which represents the soft mode of the ferroelectric transition [162]. It is reported by Kuntscher et al. that this phonon mode at about 54 cm^{-1} is not only present in the ferroelectric insulator $SrNbO_{3.50}$ ($n = 4$) but also in the weakly pronounced quasi-1D metal $Sr_{0.8}La_{0.2}NbO_{3.50}$ ($n = 4$) and in the quasi-1D metals $SrNbO_{3.45}$ ($n = 4.5$) and $SrNbO_{3.41}$ ($n = 5$) [113].

- The intrinsic high-frequency dielectric constant along the c-axis, $\varepsilon_{c\,\infty}$, of the quasi-1D metal $SrNbO_{3.41}$ ($n = 5$) was obtained from dielectric mea-

surements by Bobnar et al. [17]. At $T = 70$ K, and for lower temperatures, a relatively high value of $\varepsilon_{c\,\infty} \approx 100$ was found. For temperatures above 70 K it was impossible to determine $\varepsilon_{c\,\infty}$ because the conductivity of the sample was too large. Nevertheless, this result is worth mentioning because around 70 K the niobate $SrNbO_{3.41}$ is metallic along the a-axis as indicated by ARPES at 75 K [113] and resistivity measurements [127]. Furthermore, the relatively high value of $\varepsilon_{c\,\infty} \approx 100$ should also be viewed from the perspective of a paper by Lunkenheimer et al. [137] about the origin of apparent colossal dielectric constants. The authors speculate that the highest possible intrinsic dielectric constants in non-ferroelectric materials are of the order 10^2.

Because of their special features the $A_nB_nO_{3n+2}$ compounds represent an interesting field of research.

1.3 Dion-Jacobson type phases $A'A_{k-1}B_kO_{3k+1}$

The $A'A_{k-1}B_kO_{3k+1}$ type compounds are known as Dion-Jacobson phases. They are presented in Fig. 2 and 3, Table 2 − 4, Fig. 11 and Table 5 − 14. Their name is based on publications by Dion et al. about $A'Ca_2Nb_3O_{10}$ ($k = 3$) with monovalent A' = Li, Na, K, Rb, Cs, NH_4 or Tl [36] and by Jacobson et al. about $KCa_2Na_{k-3}Nb_kO_{3k+1}$ with $3 \leq k \leq 7$ [87]. Many of the Dion-Jacobson phases are able to intercalate ions, organic or inorganic molecules such as water in the interlayer region, see e.g. Ref. [59,87]. Some compounds are reported to be ferroelastic, e.g. the $k = 3$ niobate $KCa_2Nb_3O_{10}$ with $T_c = 1000$ °C [38]. For some of the materials listed in Table 5 − 13 the space group is known. Among these only one is non-centrosymmetric, namely the $k = 3$ niobate $KSr_2Nb_3O_{10}$ reported by Fang et al. [49]. Therefore it represents a potential ferroelectric.

Usually the A' are alkali metal ions. A compound without any alkali metal is the $k = 2$ tantalate $BaSrTa_2O_7$ which was recently published by Le Berre et al. [118]. However, we consider also the titanates $BaLn_2Ti_3O_{10}$ with Ln = La, Pr, Nd, Sm or Eu (Table 11) as $k = 3$ types without any alkali metals. In the literature these titanates are not classified as Dion-Jacobson type compounds but their structure seems to be of the type $k = 3$. This statement is also supported by a sketch of the $BaLn_2Ti_3O_{10}$ structure in a paper by German et al. [55].

Most of the published Dion-Jacobson oxides are fully oxidized compounds and therefore insulators. The mixed-valent niobates, however, are (semi)conducting and some of them are metals and even superconductors. Metallic resistivity behavior in the Li-intercalated $k = 2$ type $KLaNb_2O_7$, i.e. $Li_xKLaNb_2O_7$, is reported by Takano et al. [215]. The Li-intercalated $k = 3$ type $KCa_2Nb_3O_{10}$ is a low-T_c superconductor with $T_c \simeq 1$ K, also published by Takano et al. [214,215]. A transition temperature T_c in the range of 3 − 6 K is also reported [52].

1.4 Hexagonal $A_mB_{m-1}O_{3m}$

The properties of the hexagonal $A_mB_{m-1}O_{3m}$ compounds can be found in Fig. 8 − 10, Table 1, Fig. 17 and Table 51 − 60. The tables reveal that these compounds were mainly studied with respect to their structure. As in the case of $A_nB_nO_{3n+2}$ there are materials with an ordered stacking sequence of layers with different thickness, e.g. the $m = 4 + 5$ titanate $La_9Ti_7O_{27}$, see Fig. 9 and 17 and Table 60. Examples of the few reported physical properties are the dielectric constant of some materials and the semiconducting resistivity behavior of polycrystalline $Sr_3Re_2O_9$ ($m = 3$), $Ba_3Re_2O_9$ ($m = 3$) and oxygen-deficient $Ba_5Nb_4O_{15-y}$ ($m = 5$), see Tables 51, 53, 54, 55 and 57.

The arrangement of the BO_6 octahedra in the hexagonal $A_mB_{m-1}O_{3m}$ compounds is very peculiar. Therefore we speculate that they have a potential for attractive physical properties. For example, the mixed-valence $m = 7$ niobate $Sr_7Nb_6O_{21}$ ($Nb^{4.67+}$ / $4d^{0.33}$) reported by Schückel and Müller-Buschbaum [194], see Table 58, is potentially a good electrical conductor. Therefore it is worthwhile to study its resistivity and magnetic susceptibility. Schückel and Müller-Buschbaum synthesized $Sr_7Nb_6O_{21}$ crystals by a laser heating technique and determined the structure by single crystal XRD, but physical properties were not reported.

2 Experimental

2.1 Sample preparation

The starting materials used were MgO, Al_2O_3, $CaCO_3$, TiO_2, TiO, V_2O_5, Mn_2O_3, Fe_2O_3, $SrCO_3$, Nb_2O_5, Nb powder, $BaCO_3$, La_2O_3, CeO_2, Pr_6O_{11}, Nd_2O_3, Sm_2O_3, Eu_2O_3, Gd_2O_3, Yb_2O_3 and Ta_2O_5. Apart from $BaCO_3$ with a purity of 99.8 % the purity of the powders was at least 99.9 %. We note that the purity refers usually to the metal part of the composition. The powders were weighed with an accuracy of 0.5 mg and dryly mixed in an agate mortar. Special care was taken to prepare nearly moisture-free powders. $SrCO_3$ and $BaCO_3$ were heated for several hours at 200 − 250 °C under vacuum and subsequently stored in a dry atmosphere. The oxides, apart from TiO, were heated for at least 1 h in air at an appropriate temperature in the range of 450 − 1100 °C and then also stored in a dry ambience. Very moisture sensitive oxides like Al_2O_3, TiO_2 and La_2O_3 were heated immediately before weighing.

The oxygen content of Nb and TiO was determined thermogravimetrically. Small amounts of the powders were oxidized in static air up to 995 °C. Assuming that the uptake of oxygen leads to 100 % Nb and 100 % Ti, the actual compositions of the powders were found to be $NbO_{0.02}$ and $TiO_{1.03}$. These formulas were utilized for stoichiometric calculations.

To verify the composition of Mn_2O_3 it was first inspected by powder XRD. This revealed the presence of a small amount of MnO_2. Then, a small part of the $Mn_2O_3 = MnO_{1.50}$ batch was heated thermogravimetrically in static air up to 995 °C. The weight versus temperature curve displayed several steps of

mass reduction, but the maximum temperature of 995 °C was not enough to achieve the well-defined final composition $Mn_3O_4 = MnO_{1.33}$ [1]. Nevertheless, a temperature range was identified in which the powder should be heated to remove its moisture content. The actual oxygen content of the Mn_2O_3 batch was estimated as follows. About 2 g powder was heated in a crucible for 4 h at 1250 °C in air by using an ordinary furnace. The weight loss was measured by weighing the crucible with the powder before and after the heating. Based on the assumption that $Mn_2O_3 = MnO_{1.50}$ was completely converted into $Mn_3O_4 = MnO_{1.33}$, it was concluded that the actual composition of Mn_2O_3 resulted in $Mn_2O_{3.02}$.

The most general way to synthesize electrical conducting titanates and niobates A_vBO_x , i.e. reduced mixed-valence compositions, implied the following four steps:

1. A fully oxidized composition $A_vB_{1-w}O_{y-q}$ was prepared. This was done by heating an appropriate mixture of oxides and (if necessary) carbonates with total composition $A_vB_{1-w}O_{y-q+p}(CO_2)_z$ for several hours in air at temperatures in the range of $1200 - 1300$ °C according to

$$A_vB_{1-w}O_{y-q+p}(CO_2)_z \xrightarrow[\text{in air}]{1200\ -\ 1300\ ^\circ\text{C}} A_vB_{1-w}O_{y-q} + \frac{p}{6}O_2 + (CO_2)_z \tag{2}$$

whereby

$$z = CO_2 \text{ content},\ z \geq 0 \tag{3}$$

$$p = \text{Pr content at the } A \text{ site},\ p \geq 0 \tag{4}$$

In the case of the presence of Pr at the A site, i.e. $p > 0$, Equation (2) takes into account the conversion of the brown starting material $Pr_6O_{11} = PrO_{1.83}$ into green $PrO_{1.50} = Pr_2O_3$, i.e.

$$PrO_{1.83} \longrightarrow PrO_{1.50} + \frac{1}{6}O_2 \tag{5}$$

Referring to Eq. (2) the weight loss resulting from the removal of CO_2 and/or O_2 was traced by weighing the powder mixture before and after this process.

[1] It is known that $Mn_2O_3 = MnO_{1.50}$ converts finally into the composition $Mn_3O_4 = MnO_{1.33}$ when heated above 1000 °C in air. However, this reduction from Mn^{3+} (Mn_2O_3) to $Mn^{2.67+}$ (Mn_3O_4) does not necessarily take place if Mn_2O_3 is part of a more complex composition. For example, if the composition 0.5 La_2O_3 + 0.8 TiO_2 + 0.1 $Mn_2O_3 = LaTi_{0.8}Mn_{0.2}O_{3.4}$ is heated for several hours at 1250 °C in air, then the weight of the powder mixture remains practically constant, i.e. Mn remains in the valence state Mn^{3+}.

2. The fully oxidized and carbonate-free composition $A_vB_{1-w}O_{y-q}$ was mixed with a reduced powder B_wO_q ($q \geq 0$) like Nb or TiO, resulting in the composition $A_vB_{1-w}O_y$ according to

$$A_vB_{1-w}O_{y-q} + B_wO_q = A_vBO_y \quad \text{(powder, total mass} \approx 6 \text{ g)} \qquad (6)$$

The oxygen content of the mixture (6) was verified by a thermogravimetric oxidation of a small amount of powder up to 995 °C in static air. The difference between the thermogravimetrically determined oxygen content, y_{exp} , and the theoretical value based on the corresponding stoichiometric calculation, y, was typically found to be $|y_{exp} - y| \leq 0.006$.

3. The powder mixture (6) was pressed into two rectangular rods which were sintered for several hours in a molybdenum furnace (GERO HTK8MO) at a temperature in the range of 1250 − 1400 °C under Ar (purity 5.0) or sometimes also under 98 % Ar + 2 % H_2 . Usually this leads to a small change Δ of the oxygen content y according to

$$A_vBO_y + \frac{\Delta}{2}O_2 \xrightarrow[\text{in Ar}]{\text{1250 - 1400 °C}} A_vBO_{y+\Delta} \quad \text{(sintered rods)} \qquad (7)$$

A photograph of two sintered rods is shown Figure 18. To determine the oxygen content $y + \Delta$, a small piece from the rods was thermogravimetrically oxidized up to 995 °C in static air. In the most cases $\Delta > 0$ was observed, typical values were $\Delta \leq 0.02$. This weak oxidation is probably due to small concentrations of moisture, carbonates and/or hydroxides in the pressed powder (7) and/or related to the degree of purity of the gas atmosphere in the furnace. For some titanate compositions, however, $\Delta < 0$ was found, typically in the range of $\Delta \approx -0.02$. The oxygen partial pressure was not controlled.

4. The sintered rods, see Fig. 18, were subjected to a floating zone melting process under Ar (purity 5.0) whereby the long rod acted as feed material and the small rod as seed part. An optically heated floating zone melting furnace (GERO) was used. The zone speed and the rotation frequency of the seed part was chosen to be 5 − 15 mm/h and 15 rpm, respectively. By the solidification from the melt crystals may arise, especially if the composition melts congruently or nearly so. A control of the oxygen partial pressure was not performed. The as-grown sample was inspected with respect to a change δ of the oxygen content $y + \Delta$ which can be described by

$$A_vBO_{y+\Delta} + \frac{\delta}{2}O_2 \xrightarrow[\text{in Ar}]{\text{solidification from melt}} A_vBO_x \ , \ x = y + \Delta + \delta \quad \text{(as-grown sample)} \qquad (8)$$

To determine the oxygen content $x = y + \Delta + \delta$, small pieces from the as-grown sample were thermogravimetrically oxidized up to 995 °C in static air. The change δ was relatively small in the most cases, typically in the range $0 < \delta \leq 0.01$. For some titanate compositions, however, $\delta < 0$ with typical values of $\delta \approx -0.02$ was observed. The shape of the as-grown sample is nearly cylindrical. Because of the layered structure it is often easy to cleave the sample, see e.g. Figure 24. If the sample contains sufficiently large crystal faces, crystalline platelets of small, medium or large size can be obtained by crushing in an agate mortar, see e.g. Figure 24.

There is another way to prepare electrical conducting titanates and niobates A_vBO_x , i.e. reduced mixed-valence compositions. A powder with a fully oxidized composition A_vBO_y was pressed into two rods which were sintered in air at a temperature in the range of $1250 - 1400$ °C. The sintered, fully oxidized rods were subjected to a floating zone melting process under a reducing atmosphere consisting of 98 % Ar + 2 % H_2 , i.e.

$$A_vBO_y - \frac{\eta}{2}O_2 \xrightarrow[\text{in 98 \% Ar + 2 \% } H_2]{\text{solidification from melt}} A_vBO_x \ , \ x = y - \eta \quad \text{(as-grown sample)} \tag{9}$$

where $\eta \geq 0$. To determine the oxygen content $x = y - \eta$, small pieces from the as-grown sample were thermogravimetrically oxidized up to 995 °C in static air. Compared to the four steps described above this process is much simpler. However, the final oxygen content $x = y - \eta$ cannot be varied systematically. It depends in an unpredictable way on the composition A_vBO_y of the fully oxidized powder. Fully oxidized and therefore insulating materials were synthesized in a similar manner. The only difference was that the atmosphere during floating zone melting consisted of artificial air instead of 98 % Ar + 2 % H_2.

Concerning the preparation, materials which contain Ce often represent a special case. With respect to the oxygen content there are some ranges of composition which are difficult to synthesize because the starting material CeO_2 (Ce^{4+}) is rather inert against reduction into $Ce_2O_3 = CeO_{1.50}$ (Ce^{3+}). This is in contrast to $Pr_6O_{11} = PrO_{1.83}$ ($Pr^{3.67+}$) which converts relatively easily and in a defined way into $PrO_{1.50} = Pr_2O_3$ (Pr^{3+}), which is achieved just by heating it in air at high temperatures of about 1250 °C. Most Ce^{3+} compounds were prepared by floating zone melting in artificial air or in 98 % Ar + 2 % H_2 by using rods with a fully oxidized composition. In contrast to that $CeTiO_{3.51}$ and $CeTiO_{3.40}$ were grown in the following way.

The insulator $CeTiO_{3.51}$ (Ti^{4+}) was synthesized from rods with the fully oxidized composition $CeO_2 + TiO_2 = CeTiO_4$ (Ce^{4+} and Ti^{4+}). The floating zone melting of these rods was performed under Ar which resulted in $CeTiO_{3.51}$.

To prepare the electrical conducting titanate $CeTiO_{3.40}$ ($Ti^{3.8+}$) the mixture $CeO_2 + 0.54\,TiO_2$ (Ce^{4+} and Ti^{4+}) was pre-reacted for 4 hours at 1200 °C in air. Then $0.46\,TiO_{1.03}$ was admixed and the resulting composition $CeTiO_{3.55}$ was

pressed into two rods and sintered for 3 hours under Ar at 1300 °C. The oxygen content before and after sintering was determined thermogravimetrically. After sintering the composition of the rods was $CeTiO_{3.43}$, i.e. a significant reduction of the oxygen content took place. Subsequently the rods were subjected to a floating zone melting process under 98 % Ar + 2 % H_2 . This resulted in an additional but less pronounced reduction of the oxygen content and lead to the composition $CeTiO_{3.40}$ of the as-grown sample.

The oxygen content of the samples was determined by using a thermogravimetric analyzer NETZSCH TG 209 which achieves a maximum temperature of 1000 °C. The accuracy of the thermogravimetrically determined oxygen content was found to be about 0.3 %, i.e. two digits behind comma [127], provided that the cation ratio A_v/B in A_vBO_x remains unchanged. This was true for almost all reactions performed in this work because an evaporation did not take place or was negligible. The oxygen content x was calculated as follows. Assuming that a composition with the general formula RO_x , e.g. $R = A_vB$, can be oxidized (or reduced) to RO_u with a well-defined final maximum (or minimum) oxygen content u, i.e.

$$RO_x + \frac{1}{2}(u-x)\,O_2 \;\rightarrow\; RO_u \tag{10}$$

If m_x is the mass of the sample with composition RO_x , Δm the change of the mass associated with Eq. (10),

$$m_u = m_x + \Delta m \tag{11}$$

the mass of the composition RO_u , M_u the molar mass of RO_u in g/mol and $M_o = 15.9994$ g/mol the molar mass of oxygen O, then the following two ratios are equal:

$$\frac{\Delta m}{m_u} = \frac{M_o}{M_u}\,(u-x) \tag{12}$$

From that and Eq. (11) we obtain

$$x = u - \frac{\Delta m\, M_u}{(m_x + \Delta m)\, M_o} \tag{13}$$

2.2 Powder x-ray diffraction

Bulk structural analysis was performed by powder x-ray diffraction (XRD) with Cu K_α radiation using a PHILIPS (now PANALYTICAL) X'Pert MPD diffractometer. A small part of the as-grown sample was powdered in an agate mortar , mixed with ethanol and then dispersed on a flat sample holder consisting of single crystalline Si. The latter has an orientation that does not cause diffraction peaks in the accessible angle range. The calibration of the system with respect

to the peak position was verified by using a solid, polycrystalline Si reference sample. The position of three Si peaks, $2\Theta = 28.44°$, $56.12°$ and $88.03°$, was measured by means of the Si reference sample before and after every measurement. An accuracy of $\pm\ 0.01°$ with respect to these positions was assured.

Lattice parameter refinement of peaks located in the diffraction angle range $4° \leq 2\Theta \leq 64°$ was done with the PHILIPS (now PANALYTICAL) software X'Pert Plus.

2.3 Magnetic measurements

Magnetic measurements were performed with a SQUID magnetometer (QUANTUM DESIGN MPMS-5S) in the temperature range $2\,\mathrm{K} \leq T \leq 390\,\mathrm{K}$ and in low magnetic fields $100\,\mathrm{G} \leq H \leq 1000\,\mathrm{G}$.

The specimens used were relatively large in size with masses in the range of $100 - 500$ mg. The as-grown samples had a cylindrical or cylinder-like shape. If a cylindrical specimen was broken away from the as-grown sample, then its longitudinal cylinder axis was oriented parallel to the field. Usually the layers grow parallel or $45°$ inclined to the longitudinal cylinder axis. Therefore, for cylindrical specimens the field was oriented parallel or $45°$ inclined to the layers. Sometimes also smaller pieces of non-cylindrical shape with a field parallel to the layers were utilized.

The measurements were performed in such a way that the contribution of the sample holder does not influence the susceptibility measurement. This was achieved as follows. A long straw was fixed at the sample holder. A shorter, transversally deformed straw and the specimen was inserted into the long straw so that the specimen was fixed between both straws just by mechanical pressure. If the straws are sufficiently long and the longitudinal mass density of the straws is homogenous, then there is no contribution from the straws during the periodic motion between the two pick-up coils.

The accuracy of the measured susceptibility was about ± 1 %. This statement refers to the calibration of the SQUID magnetometer which was repeatedly verified by a Pd reference sample.

Usually the unit of the molar susceptibility in the cgs system is written as emu mol^{-1}. To make explicitly clear that this implies the magnetic moment in emu divided by the magnetic field H in G we denote in this work the unit of the molar susceptibility as emu G^{-1} mol^{-1}.

2.4 Resistivity measurements

Dc resistivity measurements between room temperature and $T = 4$ K were done on rectangular plate-like crystals obtained by crushing the melt-grown samples. Often the as-crushed crystals were additionally cleaved and/or cut by means of a razor blade to obtain a rectangular shape with appropriate size. Laue diffraction was used to check the quality and orientation of the crystalline platelets. Typically, the platelets were 0.2 - 0.8 mm thick and 2 - 4 mm long and wide.

The resistivity ρ was measured in a four-point configuration along the *a*-, *b*- and *c*-axis as shown in Fig. 19, 20 and 21. The voltage contacts along the *c*-axis, i.e. perpendicular to the layers, and the current contacts along the *a*-, *b*- and *c*-axis were made by gold wires which were attached to the sample with silver paint. The voltage contacts along the *a*- and *b*-axis, i.e. along the layers, were made on the crystal surface by ultrasonically bonded aluminum wires.

Concerning resistivity measurements on crystals of quasi-1D metals the following should be noted. If the voltage contacts were prepared by silver paint, then no metallic behavior along the *a*-axis was observed [127]. A metallic temperature dependence was detected when the voltage contacts were realized by ultrasonically attached aluminum wires [127]. Also Moini et al. reported that initial measurements on crystals of $La_2Mo_2O_7$ [1] with silver paste contacts lead to erratic results, but the problem was solved by ultrasonically soldered indium contacts [147].

3 Results and discussion: Sample preparation

About 250 different compositions were processed by floating zone melting. Approximately half of them resulted in single phase compounds. Here, the term "single phase" refers to the result of a structural analysis by powder XRD. Concerning the preparation process every composition had its own peculiarities.

The as-grown samples usually consisted of many crystals. The size and the quality of these crystals depend on the composition. Owing to the layered structure, nice crystals can often be obtained by cleaving the as-grown sample. Photographs of several samples and crystals are presented in Fig. 22 − 30. An example of a complete as-grown specimen is shown in Figure 24. Typically, the as-grown samples have a cylindrical shape. In several cases, however, they display an ellipsoid-like form as the specimen presented in Figure 24. Probably this deformation of the shape is related to the layered structure and the different growth velocity along and perpendicular to the layers. In almost all cases the layers grew parallel to the longitudinal cylinder axis, i.e. with the *c*-axis perpendicular to the longitudinal cylinder axis, see Fig. 24, or the layers grow 45° inclined to that axis, see Figure 28. The only example where the *c*-axis grows parallel to the longitudinal cylinder axis was $Sr_{4.6}La_{0.4}Nb_4O_{15.06}$ ($m = 5$ of $A_mB_{m-1}O_{3m}$). During the solidification from the melt this composition showed a strong tendency of disintegration which may be related to this peculiar orientation of the layers. Remarkably, for the similar composition $Sr_5Nb_4O_{15}$ ($m = 5$ of $A_mB_{m-1}O_{3m}$) the *c*-axis grew perpendicular to the longitudinal cylinder axis, see Figure 27.

Three examples of Laue images of plate-like crystals are presented in Fig. 31 − 33. The Laue images were used to check the quality and orientation of crystals for resistivity measurements.

[1] We notice that the crystal structure of $La_2Mo_2O_7$ is neither of the type $n = 4$ of $A_nB_nO_{3n+2}$ nor pyrochlore, it constitutes an own type.

Some examples of the thermogravimetric oxidation behavior of small pieces from as-grown samples with reduced composition are presented in Fig. 34 and 35. When crystalline pieces of $A_mB_{m-1}O_{3m}$ niobates were oxidized, the saturation value of the weight gain was not easily reached. This is shown in Fig. 34 by using the conducting $m = 6$ niobate $Sr_6Nb_5O_{18.07}$ as an example. The saturation was achieved much easier when pulverized crystals were used (Fig. 34). In this case the weight as function of temperature displays a maximum before the saturation regime appears. This maximum may reflect the presence of a catalytic process. Nevertheless, the high temperature saturation value of the weight, which is relevant for the determination of the oxygen content, is the same in both cases.

In the Sr−(Nb,Ti)−O system the following common features were observed for compounds of the type $A_nB_nO_{3n+2} = ABO_x$ and $A_mB_{m-1}O_{3m}$:

- It was impossible to prepare the insulators $Sr_5Nb_4TiO_{17} = SrNb_{0.8}Ti_{0.2}O_{3.40}$ ($n = 5$) and $Sr_6Nb_4TiO_{18}$ ($m = 6$) by floating zone melting. In both cases the solid material from the feed rod had a very strong tendency to grow out of the molten zone and the experiments had therefore to be stopped.

- It was relatively easy to synthesize the both transparent insulators $Sr_4Nb_4O_{14} = SrNbO_{3.50}$ ($n = 4$) and $Sr_5Nb_4O_{15}$ ($m = 5$) by floating zone melting. In both cases nice, plate-like crystals were readily obtained by cleaving the as-grown sample. The preparation of the $n = 4$ ferroelectric insulator $Sr_4Nb_4O_{14}$ by floating zone melting was reported e.g. by Nanamatsu et al. [151] and in the previous article [127]. However, according to the phase diagram of the Sr−Nb−O system, $Sr_4Nb_4O_{14}$ and $Sr_5Nb_4O_{15}$ do not melt congruently [28,119]. Also in a paper by Teneze et al. it is mentioned that $Sr_5Nb_4O_{15}$ decomposes peritectically at 1773 K [213]. Hence crystals of $Sr_5Nb_4O_{15}$ were grown from a non-stoichiometric, Nb-rich mixture which was subjected to a special thermal cycle described in Ref. [213]. Therefore it is worth mentioning that floating zone melting of the stoichiometric compositions of $Sr_4Nb_4O_{14}$ ($n = 4$) and $Sr_5Nb_4O_{15}$ ($m = 5$) lead readily to single phase products and nice crystals.

- In Sr−Nb−O compositions with a Nb valence of about 4.8 or less there is a tendency that a purple-colored phase appears in the as-grown sample. In general this tendency increases with decreasing Nb valence. As reported in the previous paper in the context of $SrNbO_x$, the purple colored phase is probably a Sr-deficient perovskite compound with approximate composition $Sr_{0.8}NbO_3$ [127]. By using a lower zone speed, e.g. 6 mm/h instead of 15 mm/h, the formation of the purple phase can often be suppressed completely or restricted to the first few mm of the as-grown sample. In previous work, this was also observed for $SrNbO_x$ [127].

4 Results and discussion: Dion-Jacobson phases $A'A_{k-1}B_kO_{3k+1}$ without alkali metals

The starting point to work on $A'A_{k-1}B_kO_{3k+1}$ compounds was a study of substituting Ca by Ba in $n = 4$ niobates (Ca,La)$NbO_{3.50}$. With increasing Ba content an additional phase appeared whose type seemed to be $k = 2$ of $A'A_{k-1}B_kO_{3k+1}$. Then a more detailed investigation of the reduced Ba−(Ca,La)−Nb−O system was performed. This lead to $A'A_{k-1}B_kO_{3k+1}$ niobates of the type $k = 2$ and $k = 3$ which represent Dion-Jacobson phases without any alkali metal.

The compounds which were prepared in this work can be found among those listed in the Tables 7 − 12. Examples are the black-blue, conducting niobates $BaCa_{0.6}La_{0.4}Nb_2O_{7.00}$ ($k = 2$) and $BaCa_2Nb_3O_{10.07}$ ($k = 3$) and the transparent insulating $k = 2$ tantalate $BaCaTa_2O_7$ and $k = 3$ titanate $BaLa_2Ti_3O_{10}$. The latter is already reported in the literature, e.g. by German et al. [55]. The $k = 2$ tantalate $BaCaTa_2O_7$ represents the Ca analogue to $BaSrTa_2O_7$ which was recently reported by Le Berre et al. [118]. The powder XRD pattern of several materials are shown in Figure 36. Also compounds with a significant non-stoichiometric composition could be prepared, e.g. the Ba-deficient $k = 3$ niobate $Ba_{0.8}Ca_2Nb_3O_{9.98}$, see Table 12.

One example of an investigated compositional system is $BaCa_{1-y}La_yNb_2O_7$ for $0 \leq y \leq 1$. Only in the range of about $0.3 \leq y \leq 0.5$ it was possible to obtain single phase or nearly single phase samples by floating zone melting. Also the both end compositions $BaCaNb_2O_7$ ($y = 0$) and $BaLaNb_2O_7$ ($y = 1$) lead to multiphase products. The $y = 0$ composition $BaCaNb_2O_7$ is worth mentioning in the context of the corresponding $k = 2$ tantalate $BaCaTa_2O_7$. It represents an example of a niobate composition which leads to a multiphase product whereas the corresponding tantalate mixture results in a (nearly) single phase sample. The same is reported for $BaSrNb_2O_7$ and $BaSrTa_2O_7$ by Le Berre et al. [118]. There are also such examples for $A_nB_nO_{3n+2} = ABO_x$ compounds, e.g. the multiphase niobate sample $Sr_{0.67}La_{0.33}NbO_{3.67}$ [127] and the corresponding single phase $n = 3$ tantalate $Sr_{0.67}La_{0.33}TaO_{3.67}$ listed in Table 17.

The molar magnetic susceptibility $\chi(T)$ of several compounds is shown in Figure 37. Apart from the Curie-like behavior at low temperatures, which is probably due to paramagnetic impurities, the susceptibility of the reduced niobates is practically temperature-independent. This suggests the presence of two different contributions which are known as (nearly) temperature-independent, namely a Pauli-like paramagnetic susceptibility from delocalized electrons and a diamagnetic susceptibility from the closed electron shells of the ionic cores.

On crystals of the $k = 2$ and $k = 3$ niobate $BaCa_{0.6}La_{0.4}Nb_2O_{7.00}$ and $BaCa_2Nb_3O_{10.07}$, respectively, the resistivity $\rho(T)$ was measured along the *a*-, *b*- and *c*-axis. The results are shown in Fig. 38 and 39. Along all three axes the resistivity $\rho(T)$ indicates metallic behavior. Also along the *c*-axis the temperature dependence of $\rho_c(T)$ is metallic, although its order of magnitude, $\rho_c \approx 1\ \Omega$cm, is relatively high. For both compounds the value of ρ_a and ρ_b is significantly different, $\rho_b \approx 10^1 \times \rho_a$ and $\rho_b \approx 10^2 \times \rho_a$ for the $k = 2$ and $k = 3$ niobate, respectively. This difference may be related to the expected structure type, see

Fig. 3, where adjacent layers are displaced against each other only along the b-axis but not along the a-axis. From the resistivity $\rho_a(T)$, $\rho_b(T)$ and $\rho_c(T)$ we conclude that both niobates are anisotropic 3D metals.

It was published by Takano et al. that the Li-intercalated $k = 3$ niobate $KCa_2Nb_3O_{10}$, i.e. $Li_xKCa_2Nb_3O_{10}$, is superconducting with $T_c \simeq 1$ K [214,215]. A transition temperature T_c in the range of $3 - 6$ K is also reported [52]. For temperatures $T \geq 2$ K the as-grown compounds prepared in this work did not show any indications for superconductivity. However, after floating zone melting a certain region of the feed rod displayed a significant diamagnetic signal up to 13 K for some compositions of the system Ba−(Ca,La)−Nb−O and also for a few of $Ca_nNb_nO_{3n+2} = CaNbO_x$. This was observed for that region of the feed rod which contains the crossover between the material solidified from the melt and the unaffected original composition. The diamagnetic signal was also present at small magnetic fields such as 10 G. Therefore it is very unlikely that its origin is related to the diamagnetism from closed electron shells of the ionic cores. Hence it can be considered as a sign for the presence of superconductivity. We do not know which type of phase is here responsible. In this context we mention that superconducting niobates of the type $Ca_2Nb_{1+y}O_x$ are reported by Nakamura [148]. They represent markedly non-stoichiometric perovskite phases and the highest superconducting transition temperature T_c is about 9 K [148] [1].

5 Results and discussion: $A_nB_nO_{3n+2} = ABO_x$

5.1 Structural properties

In the following we discuss three topics, namely the proximity between some $A_nB_nO_{3n+2}$ compounds and the cubic pyrochlore structure with respect to their formation from similar starting compositions, non-stoichiometric materials, and the possibilities of occupational order at the B site in the case of two different B cations.

$A_nB_nO_{3n+2}$ and pyrochlore It is known that the titanates $LnTiO_{3.50} = Ln_2Ti_2O_7$ display an $n = 4$ structure for Ln = La, Ce, Pr or Nd, whereas for Ln = Sm, Eu, Gd, Tb, Dy, Ho, Er, Tm or Yb they crystallize in a cubic pyrochlore structure, see Table 61. However, if $SmTiO_{3.50}$ and $EuTiO_{3.50}$ are prepared under high pressure, they adopt an $n = 4$ structure (Table 61 and 25). This was, for example, published by Titov et al. [219]. Thus, in the rare earth sequence Ln = La, Ce, Pr, Nd, Sm, Eu, Gd, ... Yb, in which the ionic radius of Ln^{3+} decreases from left to right, a compositional-driven structural crossover takes place at Ln = Sm and Eu. The $n = 4$ and the pyrochlore structure differ in the atomic packing density V/Z whereby V is the unit cell volume and Z the number of formula units per unit cell. For the $n = 4$ structure the atomic packing density

[1] We note that for T_c's below about 9 K it is necessary to exclude the possibility of the presence of Nb metal in the sample because Nb is superconducting with a T_c of 9.2 K.

is somewhat smaller (Table 61). An example which illustrates how delicately the structure type depends on the composition is shown in Figure 40. It presents the powder XRD pattern of three compounds of the system $Pr_{1-y}Ca_yTi_{1-y}Nb_yO_{3.50}$ ($0 \leq y \leq 1$). The end members $PrTiO_{3.50}$ ($y = 0$) and $CaNbO_{3.50}$ ($y = 1$) display an $n = 4$ structure. However, a certain range of intermediate compositions are of pyrochlore type, see also Table 62. For $y = 0.5$ a pyrochlore structure is reported by Titov et al. [219], whereas Fig. 40 presents the powder XRD spectrum of the $y = 0.4$ compound $Pr_{0.6}Ca_{0.4}Ti_{0.6}Nb_{0.4}O_{3.50}$. If in the latter the Pr^{3+} ions are replaced by the slightly larger La^{3+} ions, i.e. $La_{0.6}Ca_{0.4}Ti_{0.6}Nb_{0.4}O_{3.50}$, then it crystallizes in an $n = 4$ structure, see Figure 42. Further $A_nB_nO_{3n+2}$ compounds whose atomic packing density V/Z is close to that of the pyrochlore structure are presented in Table 62.

In a compositional system $(ABO_{3.50})_{1-y}(A'B'O_3)_y$ where the $y = 0$ and $y = 1$ end members $ABO_{3.50}$ and $A'B'O_3$ have a pyrochlore and perovskite structure, respectively, there are only a few examples where intermediate compositions adopt an $A_nB_nO_{3n+2}$ structure. Such an example is given by the titanate system $SmTiO_{3.50} - CaTiO_3$. It is reported by German et al. that the $y = 0.33$ composition $Sm_{0.67}Ca_{0.33}TiO_{0.33}$ crystallizes in an $n = 6$ structure [55], see also Table 44 and 62. Therefore it is interesting to consider the related system $SmTiO_{3.50} - SmTiO_3$, i.e. $SmTiO_x$, and look for the existence of reduced $A_nB_nO_{3n+2}$ titanates in the oxygen content range $3 < x < 3.50$. Indeed, some synthesis experiments lead to the $n = 5$ titanate $SmTiO_{3.37}$, see Fig. 41 as well as Table 41 and 61. However, as likewise presented in Fig. 41, there were no indications for the existence of an $n = 4.5$ type phase $SmTiO_{3.44}$. Nevertheless, $SmTiO_x$ represents a further example of a system in which intermediate compositions adopt an $A_nB_nO_{3n+2}$ structure, although the $x = 3$ and $x = 3.5$ end members crystallize in a perovskite and pyrochlore structure, respectively.

A few synthesis experiments were performed to search for the existence of reduced $A_nB_nO_{3n+2}$ titanates in the systems $GdTiO_x$ and $YbTiO_x$ with $x < 3.50$. However, as presented in Table 61, no indications for the presence of $A_nB_nO_{3n+2}$ type phases were observed. The composition $YbTiO_{3.39}$ resulted in a single phase product with an oxygen-deficient pyrochlore structure.

Non-stoichiometric compounds In this section we refer to significantly non-stoichiometric oxides ABO_x , $A_{1-\sigma}BO_x$ and $AB_{1-\sigma}O_x$ with $0 \leq \sigma \leq 0.05$. With respect to the oxygen content x we define a compound as significant non-stoichiometric if $|x - w| > 0.02$ whereby w represents its corresponding ideal, stoichiometric value.

The existence of several non-stoichiometric materials, which appear single phase within the detection limit of powder XRD, were published in the previous article, see Fig. 16 and Table 17 and 18 in Ref. [127]. For non-stoichiometric $n = 2$ oxides see Table 15 in this work. The non-stoichiometric compounds prepared in this work are presented in Table 27, 28, 31, 41 and 42. The non-stoichiometric materials can be classified into four groups:

- ABO_{w+y}: Compounds with an oxygen excess y with respect to the ideal oxygen content w. As an example we cite the $n = 4$ niobate $Sr_{0.8}La_{0.2}NbO_{3.60}$ [127]. The ideal oxygen content of the $n = 4$ type is $w = 3.50$. The excess oxygen is probably accommodated in the interlayer region, see Table 15 and Ref. [127].

- ABO_{w-y}: Materials with an oxygen deficiency y with respect to the ideal oxygen content w. Examples are
  - the $n = 4$ type $La_{0.6}Ca_{0.4}Ti_{0.6}Nb_{0.4}O_{3.40}$, see Table 27
  - the $n = 5$ type $LaTi_{0.8}Al_{0.2}O_{3.31}$, see Table 41.

  The ideal oxygen content of the $n = 4$ and $n = 5$ type is $w = 3.50$ and $w = 3.40$, respectively.

- $AB_{1-\sigma}O_{w-y}$: Compounds with an oxygen deficiency y and a cation deficiency σ at the B site with respect to the ideal oxygen content w and the ideal cation ratio $B/A = 1$. Two of such oxides were prepared, namely
  - the $n = 4$ niobate $Sr_{0.75}La_{0.25}Nb_{0.95}O_{3.43}$, see Table 27
  - the $n = 5$ titanate $LaTi_{0.95}O_{3.31}$, see Table 42.

  The ideal composition of the $n = 4$ and $n = 5$ type is $ABO_{3.50}$ and $ABO_{3.40}$, respectively.

- $A_{1-\sigma}BO_{w-y}$: Materials with an oxygen deficiency y and a cation deficiency σ at the A site with respect to the ideal oxygen content w and the ideal cation ratio $A/B = 1$. So far these compounds are such with a reduced composition. Starting with a given ideal or nearly ideal composition, then an associated non-stoichiometric compound can be obtained by adjusting the deficiency at the O and A site in such a way that the nominal number of electrons per B site remains constant. This implies that the absolute value of the removed positive charge at the A site and the removed negative charge at the O site are equal. Examples are
  - the $n = 4.33$ titanates $CeTiO_{3.47}$ ($3d^{0.06}$) and $Ce_{0.95}TiO_{3.39}$ ($3d^{0.07}$), see Table 28,
  - the $n = 4.5$ niobates $CaNbO_{3.45}$ ($4d^{0.10}$) and $Ca_{0.95}NbO_{3.41}$ ($4d^{0.09}$), see Ref. [127] and Table 31,
  - the $n = 5$ titanates $LaTiO_{3.41}$ ($3d^{0.18}$) and $La_{0.95}TiO_{3.33}$ ($3d^{0.19}$), see Table 35 and 42.

The powder XRD spectra of some non-stoichiometric compounds are presented in Fig. 42 and 43. The composition $La_{0.6}Ca_{0.4}Ti_{0.6}Nb_{0.4}O_x$ (Fig. 42) adopts, as expected, for $x = 3.50$ an $n = 4$ structure. However, for $x = 3.40$ it crystallizes again in an $n = 4$ structure and not, as supposed, in an $n = 5$ type. Usually the structure type alters from $n = 4$ to $n = 5$ as the oxygen content in ABO_x changes from $x = 3.50$ to $x = 3.40$. The reason why this does not occur for $La_{0.6}Ca_{0.4}Ti_{0.6}Nb_{0.4}O_x$ may be related to its complex composition which involves two different cations at the A site and at the B site, respectively.

The materials with the largest degree of non-stoichiometry reported in this work are $n = 5$ titanates of the type $A_{0.95}TiO_{3.21}$, see Table 42. Figure 43 shows the powder XRD spectra of $La_{0.75}Ca_{0.2}TiO_{3.21}$ and related $n = 5$ titanates. It is remarkable that $La_{0.75}Ca_{0.2}TiO_{3.21}$ represents a single phase $n = 5$ titanate, at least within the detection limit of powder XRD. We note that its powder XRD spectrum displays no indications for the presence of peaks from the $n = \infty$ titanate $LaTiO_3$ or $LaTiO_{3.20}$, see Figure 43. The $n = \infty$ $LaTiO_x$ with perovskite structure evinces a relatively large homogeneity range of $3.00 \leq x \leq 3.20$ [126,127] and is compositionally in proximity to the extremely non-stoichiometric $n = 5$ titanates like $La_{0.75}Ca_{0.2}TiO_{3.21}$.

We assume that the vacant A, B and/or O sites are located in the boundary region of the layers. This because it seems likely that the A, B and O ions at the boundary are less strongly bound than those located in the inner region of the layers. In this case the formation of vacancies is easier at the boundary. In this context we mention an interesting paper on the niobate $SrNbO_{3.2} = Sr_5Nb_5O_{16}$ which was published in 1985 by Schückel and Müller-Buschbaum [193]. They prepared small crystals in an H_2/H plasma at high temperatures and determined the structure by single crystal XRD. Physical properties were not reported. The crystal structure of $SrNbO_{3.2} = Sr_5Nb_5O_{16}$ and some of its features is sketched in Fig. 44, see also Table 32. In Ref. [193] the structure was not considered in the context of $A_nB_nO_{3n+2}$. However, Fig. 44 reveals that it can be viewed as an oxygen-deficient $n = 5$ type. The oxygen vacancies are located in one of the both boundary regions of the layers. They are fully ordered in such a way that the corresponding Nb−O chains along the a-axis are interrupted. It is worth mentioning that the space group of $SrNbO_{3.2}$ is reported as non-centrosymmetric, whereas that of $SrNbO_{3.4}$ is centrosymmetric, see also Table 32. The niobates $SrNbO_x$ which are related to the type $n = 5$, i.e. $3.20 \leq x \leq 3.42$ [1], give rise to several interesting questions like

- Is there a continuous structural crossover from $x = 3.40$ to $x = 3.20$ with a smooth transition from disordered (or partially ordered) to fully ordered oxygen vacancies? Or are there well-defined intermediate phases?

- How does the resistivity and magnetic behavior of $SrNbO_{3.20}$ look like, especially when compared to that of the quasi-1D metal $SrNbO_{3.41}$? Is there a dimensional crossover from $x = 3.40$ to $x = 3.20$ or do the quasi-1D features remain? We emphasize that the layers of $SrNbO_{3.41}$ and $SrNbO_{3.20}$ differ in their number of NbO_6 octahedra along the c-axis which results in a different distribution of the octahedra distortions, see Fig. 15 and 44.

Further studies are required to clarify these issues. Because the atomic coordinates of $SrNbO_{3.2} = Sr_5Nb_5O_{16}$ are known [193] it is possible to perform band structure calculations. The outcome could be compared with the results of band structure calculations on $SrNbO_{3.41}$ by Bohnen [110] and Winter et al. [244].

[1] We point out that the homogeneity range of $n = 5$ type $SrNbO_x$ with respect to a preparation by floating zone melting is at least $3.40 \leq x \leq 3.42$ [127].

It was attempted to prepare $SrNbO_{3.20}$ by floating zone melting, however the melting behavior turned out to be very difficult and a multiphase product was obtained. We note that the technique by which Schückel and Müller-Buschbaum synthesized $SrNbO_{3.2}$ crystals [193] suggests that it represents a metastable phase. Some experiments were performed to grow fully oxidized, insulating titanates and niobates of the type $ABO_{3.20}$, but a single phase product could not be obtained. We speculate, however, that the reduced and A site deficient titanates like $La_{0.75}Ca_{0.2}TiO_{3.21}$ are structurally related to $SrNbO_{3.20}$. Of course, this has to be confirmed by structural studies. We notice that the as-grown titanates $La_{0.75}Ca_{0.2}TiO_{3.21}$ and $La_{0.75}Ba_{0.2}TiO_{3.21}$ (Table 42) did not show any pronounced plate-like crystals. Therefore it was not possible to perform resistivity measurements along the three distinct crystallographic directions. Presently, there are two significantly non-stoichiometric compounds on which the resistivity $\rho(T)$ was measured along the a-, b- and c-axis. These are the $n = 5$ materials $Sr_{0.95}NbO_{3.37}$ and $Sr_{0.95}Nb_{0.9}Ta_{0.1}O_{3.37}$, see Figure 46. $Sr_{0.95}NbO_{3.37}$ represents a quasi-1D metal. Its resistivity behavior is similar to that of the $n = 5$ quasi-1D metal $SrNbO_{3.41}$ whose $\rho(T)$ is shown in Figure 77.

As just mentioned, the resistivity of the most non-stoichiometric $n = 5$ materials, $La_{0.75}Ca_{0.2}TiO_{3.21}$ and $La_{0.75}Ba_{0.2}TiO_{3.21}$, was not measured because of the absence of appropriate crystals. Figure 70 presents their molar magnetic susceptibility $\chi(T)$ together with that of another related $n = 5$ titanates, namely three significantly non-stoichiometric compounds and two nearly stoichiometric materials. The $\chi(T)$ curves, however, do not reveal marked differences between the nearly stoichiometric quasi-1D metals $LaTiO_{3.41}$ and $La_{0.9}Ca_{0.1}TiO_{3.38}$ (Table 35 and Fig. 45) and the most non-stoichiometric titanates like $La_{0.75}Ca_{0.2}TiO_{3.21}$. It is very likely that the susceptibility increase at low temperatures reflects the Curie or Curie-Weiss behavior from paramagnetic impurities. Therefore the $\chi(T)$ curves were fitted at low temperatures to the function $D + [C/(T - \theta)]$ and then $C/(T - \theta)$ was subtracted from the as-measured $\chi(T)$. However, also this approach did not reveal a pronounced feature which distinguishes the most non-stoichiometric from the nearly stoichiometric titanates. We note that the increase of the susceptibility at low temperatures starts at higher temperatures for those titanates with Ca or Ba at the A site, compared to those with only La at the A site. Therefore the fit procedure was somewhat arbitrary because it is not clear in which temperature range the contribution from the paramagnetic impurities is much stronger than the intrinsic susceptibility.

Occupational order at the *B* site Assuming that there are two different cations, at the B or A site, which differ in their valence. Then, in the most cases, they are partially ordered in the sense that the concentration of the higher-valent cations increases from the center to the boundary of the layers (Fig. 12, 15 and 16). As mentioned in the introduction, this distribution corresponds to a configuration which compensates the negative charge from the excess oxygen at the boundary of the layers.

There are also a few compounds with a full occupational order at the B site. For the $n = 5$ insulators $Ln\mathrm{Ti_{0.8}Fe_{0.2}O_{3.40}}$ with Ln = La, Pr or Nd it is reported by Titov et al. that the Fe^{3+} ($3d^5$) ions are exclusively located in the central octahedra of the layers [227,228], see Figure 16. Remarkably, in the related materials $Ln\mathrm{Ti_{0.8}Ga_{0.2}O_{3.40}}$ the isovalent, but not isoelectronic, Ga^{3+} ($3d^0$) ions are only partially ordered. According to Titov et al. they are distributed in three inner octahedra sheets of the five $B\mathrm{O_6}$ octahedra thick layers [228,229], see Figure 16.

We note that the $B\mathrm{O_6}$ octahedra distortions in $Ln\mathrm{Ti_{0.8}Fe_{0.2}O_{3.40}}$ and $Ln\mathrm{Ti_{0.8}Ga_{0.2}O_{3.40}}$ show an atypical distribution. For example, in $\mathrm{LaTi_{0.8}Fe_{0.2}O_{3.40}}$ the smallest value is realized at the boundary of the layers and in $\mathrm{PrTi_{0.8}Fe_{0.2}O_{3.40}}$ the change from the boundary to the center of layers is relatively small. In the most compounds with a layer thickness of n = 3, 5 or 6 octahedra the distortions display an opposite behavior, see Fig. 12, 15 and 16.

The possibility of full occupational order at the B site represents an interesting structural phenomenon. Therefore it seems worthwhile to perform further structural studies, especially by single crystal XRD, on several $n = 5$ compounds such as $Ln\mathrm{Ti_{0.8}}B'_{0.2}\mathrm{O}_x$ with $B' = Al^{3+}$, V^{3+}, Cr^{3+}, Mn^{3+} or Fe^{3+}. Examples of such $n = 5$ materials which were prepared in this work are

- $\mathrm{LaTi_{0.8}Al_{0.2}O_{3.40}}$ (Table 36) and $\mathrm{LaTi_{0.8}Al_{0.2}O_{3.31}}$ (Table 41)
- $\mathrm{CeTi_{0.8}Al_{0.2}O_{3.33}}$ (Table 41)
- $\mathrm{PrTi_{0.8}Al_{0.2}O_{3.40}}$ (Table 38) and $\mathrm{NdTi_{0.8}Al_{0.2}O_{3.40}}$ (Table 39)
- $\mathrm{LaTi_{0.8}V_{0.2}O_{3.31}}$ (Table 41) and $\mathrm{SmTi_{0.8}V_{0.2}O_{3.39}}$ (Table 40)
- $\mathrm{LaTi_{0.8}Mn_{0.2}O_{3.4}}$ (Table 37)
- $\mathrm{LaTi_{0.8}Fe_{0.2}O_{3.40}}$ (Table 37) and $\mathrm{NdTi_{0.8}Fe_{0.2}O_{3.40}}$ (Table 39)

Especially for $\mathrm{LaTi_{0.8}Mn_{0.2}O_{3.4}}$ we assume that the Mn^{3+} ions are in the same way fully ordered as the Fe^{3+} ions in $\mathrm{LaTi_{0.8}Fe_{0.2}O_{3.40}}$, because they are isovalent 3d transition metal ions which are adjacent in the periodic table.

At least theoretically, a full occupational order at the B site is also possible in $n = 6$ materials. An example of such $n = 6$ compositions is $Ln\mathrm{Ti_{0.67}}B'_{0.33}\mathrm{O_{3.33}}$. In this case it is hypothetically possible that the B' cations are exclusively located in the both inner octahedra sheets of the six $B\mathrm{O_6}$ octahedra thick layers. It was tried to prepare two such compounds by floating zone melting, namely $\mathrm{LaTi_{0.67}Fe_{0.33}O_{3.33}}$ and $\mathrm{LaTi_{0.67}Mn_{0.33}O_{3.33}}$. The material with $B' = Fe^{3+}$ resulted readily in an $n = 6$ insulator (Table 44), whereas for $B' = Mn^{3+}$ an oxygen-deficient $n = 5$ type was obtained (Table 41). A detailed structural study, especially by single crystal XRD, is necessary to determine the distribution of the Fe^{3+} ions in the $n = 6$ insulator $\mathrm{LaTi_{0.67}Fe_{0.33}O_{3.33}}$.

We suggest that the presence of a full occupational order at B site, compared to a disordered or partially ordered distribution, effects also the physical properties such as the dielectric, optical and magnetic behavior. In a later section we discuss the magnetic features of the $n = 5$ and $n = 6$ insulator $LaTi_{0.8}Fe_{0.2}O_{3.40}$ and $LaTi_{0.67}Fe_{0.33}O_{3.33}$, respectively, in the context of a fully ordered distribution at the B site.

Besides $n = 5$ compounds of the type $AB''_{0.8}B'_{0.2}O_x$ there are further materials for which the distribution of the cations at the B site is of interest. An example is the $n = 5$ titanate $LaTi_{0.9}Mg_{0.1}O_{3.40}$, see Table 36, because of the relatively large charge difference between the Ti^{4+} and Mg^{2+} ions. We speculate that the Mg^{2+} ions are exclusively located at the B sites of the central octahedra, possibly in the ordered sequence Ti−O−Mg−O−Ti−O−Mg−O along the a-axis. Of course, a detailed structural study is required to determine the positions of the Mg^{2+} ions.

5.2 Resistivity

In the previous article the resistivity $\rho(T)$ along the a-, b- and c-axis of eight different compounds were published [127], namely of

- the $n = 4$ niobate $Sr_{0.8}La_{0.2}NbO_{3.50}$
- the $n = 4.5$ niobate $Sr_{0.96}Ba_{0.04}NbO_{3.45}$
- the $n = 5$ niobates $SrNbO_{3.41}$, $Sr_{0.965}La_{0.035}NbO_{3.41}$, $Sr_{0.9}La_{0.1}NbO_{3.41}$, $CaNbO_{3.41}$ and significantly non-stoichiometric $Sr_{0.95}NbO_{3.37}$
- the $n = 5$ titanate $LaTiO_{3.41}$

They all represent quasi-1D metals, although the degree of the metallic character varies among these materials, see Table 47 and Ref. [127]. The metallic resistivity occurs along the a-axis and with decreasing temperature a metal-to-semiconductor transition takes place. The temperature at which the metal-to-semiconductor transition appears depends on composition and varies from about 180 K to 50 K [127]. In the case of the $n = 5$ niobate $Sr_{0.9}La_{0.1}NbO_{3.41}$ the metal-to-semiconductor transition is almost completely suppressed [127].

Within this work the resistivity $\rho(T)$ of two further compounds was measured, namely of the $n = 5$ titanate $PrTiO_{3.41}$ and the significantly non-stoichiometric $n = 5$ type $Sr_{0.95}Nb_{0.9}Ta_{0.1}O_{3.37}$.

Figure 45 displays the resistivity $\rho(T)$ of monoclinic $PrTiO_{3.41}$ along the a- and b-axis as well as perpendicular to the layers. For the sake of comparison the data of the related $n = 5$ titanate $LaTiO_{3.41}$ from Ref. [127] is also shown. According to the results from optical spectroscopy by Kuntscher et al. [112] and the resistivity behavior depicted in Figure 45, $LaTiO_{3.41}$ represents a quasi-1D metal which shows a metal-to-semiconductor transition below 100 K. The pronounced anisotropy of the resistivity and its temperature dependence indicates

the same for $PrTiO_{3.41}$ [1]. Both titanates display qualitatively the same complex temperature dependence of the resistivity $\rho_a(T)$ along the a-axis. For $LaTiO_{3.41}$ this was considered in a small polaron picture by Kuntscher et al. in the following way [112]: Starting from the lowest temperatures, ρ_a decreases strongly because the charge carriers are thermally activated. At about 60 K the charge carriers are free and with a further increase of the temperature ρ_a displays a metallic behavior because the charge carriers are more and more scattered by phonons. Above 200 K ρ_a starts to decrease again which indicates that the transport is dominated by small polaron hopping instead of scattering by phonons.

In contrast to the La^{3+} ions in $LaTiO_{3.41}$ the Pr^{3+} ions in $PrTiO_{3.41}$ carry a localized paramagnetic moment, see Table 64. A comparison between the resistivity $\rho(T)$ of $PrTiO_{3.41}$ with that of $LaTiO_{3.41}$, see Figure 45, do not reveal an obvious feature which can be related to the presence of paramagnetic moments of the Pr^{3+} ions. In a later section, however, we will consider the magnetic susceptibility $\chi(T)$ of the $n = 5$ quasi-1D metals $PrTiO_{3.41}$ and $LaTiO_{3.41}$ and the related $n = 5$ insulator $PrTi_{0.8}Al_{0.2}O_{3.40}$. That will reveal the presence of an interaction between the conduction electrons and the localized paramagnetic moments.

Figure 46 shows the resistivity $\rho(T)$ of the significantly non-stoichiometric $n = 5$ compound $Sr_{0.95}Nb_{0.9}Ta_{0.1}O_{3.37}$ along the a-, b- and c-axis. To facilitate a comparison, the data of the related $n = 5$ quasi-1D metal $Sr_{0.95}NbO_{3.37}$ [127] are also presented. $Sr_{0.95}Nb_{0.9}Ta_{0.1}O_{3.37}$ displays a semiconductor-like behavior along all three crystallographic directions. Probably the Ta^{5+} ions take over 10 % of the Nb^{4+} and Nb^{5+} positions in a random way which leads to a disorder-induced localization along the a-axis.

5.3 Magnetic susceptibility

The molar magnetic susceptibility $\chi(T)$ or $\chi(T)^{-1}$ of several compounds are shown in the Figures 47 - 70. Samples with localized paramagnetic moments from rare earth ions Ln like Ce^{3+}, Pr^{3+}, Nd^{3+}, Eu^{2+}, Gd^{3+} or Yb^{3+} at the A site and/or transition metal ions TM such as Ti^{3+} or Fe^{3+} at the B site often display a Curie-Weiss behavior $\chi(T) = C/(T - \theta)$ for sufficiently high T.

Figure 47, 48 and 49 shows the molar magnetic susceptibility $\chi(T)$ of materials with Ce, Pr and Nd at the A site, respectively. At low temperatures the susceptibility of the Pr titanates displays an attenuated increase with decreasing temperature. This feature is known from Pr_2O_3 and was theoretically described

[1] Although the resistivity $\rho(T)$ along the b-axis is relatively high, approximately 1 Ω cm for temperatures above about 60 K, it displays a metallic temperature dependence in the same temperature range as $\rho(T)$ along the a-axis. Also for the $n = 5$ niobate $SrNbO_{3.41}$ a weakly pronounced metallic temperature dependence of $\rho(T)$ along the b-axis was observed [127], see Figure 77. However, in optical spectroscopy and ARPES a metallic behavior along the b-axis was not detected [113]. This suggests that the metallic behavior along the b-axis is due to an admixture of the metallic a-axis resistivity. That may result from a deviation of the position of the voltage and current contacts and the crystal shape from the ideal case.

by the crystal-field splitting of the magnetic ground state $^3H_4$ (Table 64) of the Pr^{3+} ions [99].

The susceptibility of materials with Sm^{3+} or Eu^{3+} at the A site do not show a Curie-Weiss behavior, see Fig. 51 − 54. In these compounds the Van Vleck type paramagnetism contributes significantly to the susceptibility. Its quantum mechanical origin is based on a non-vanishing non-diagonal matrix element which connects the ground state with a higher state of the multiplet, i.e. the external magnetic field induces an admixture of a higher state to the ground state, see e.g. Ref. [89,104,160] [1]. For low temperatures $T \ll \Delta$ the resulting molar susceptibility χ_V represents the temperature-independent Van Vleck paramagnetism:

$$\chi_V = \frac{2(L+1)S}{3(J+1)\Delta} \frac{\mu_B^2 N_A}{k_B} = \frac{(L+1)S}{4(J+1)\Delta} \quad \mathrm{K^{-1}\ emu\ G^{-1}\ mol^{-1}} \qquad (14)$$

where Δ is the energy difference in K between the first higher level $^{2S+1}L_{J+1}$ and the ground state $^{2S+1}L_J$ of the multiplet [89] [2] [3]. S, L and J are the quantum numbers of the spin, orbital angular momentum and total angular momentum, respectively. Sm^{3+} and Eu^{3+} are those rare earth ions which have the smallest values of Δ and the largest values of χ_V [89], see Table 64. Another way to measure the strength of the Van Vleck paramagnetism is provided by the parameter ξ which is also presented in Table 64. When ξ is multiplied with the temperature T it represents the ratio of the temperature-independent Van Vleck susceptibility χ_V to the Curie susceptibility $\chi_C = C/T$. The highest ξ values are reached for Sm^{3+} and Eu^{3+}. In the ground state the total angular momentum J of Eu^{3+} is $J = 0$, whereas for Sm^{3+} we have $J = 5/2$, see Table 64. This results in a different behavior of $\chi(T)$ for compounds containing Eu^{3+} compared to those with Sm^{3+}.

The behavior of the susceptibility $\chi(T)$ of $EuTiO_{3.50}$ and $EuNbO_4$, see Fig. 54, is similar to that of Eu_2O_3 [160] and typical for Eu^{3+} compounds. At low tem-

[1] We notice that the Van Vleck paramagnetism is due to a mixing of states with different J. The Langevin paramagnetism, from which the Curie behavior is a special case, comes about by the resultant magnetization of states with different m_J . These states differ in their energy in the external magnetic field and therefore their thermally excited population is different. A mixing of states with different m_J occurs when the crystal field splitting is taken into account.

[2] In Ref. [89] χ_V is given as volume susceptibility $\chi_V = (\mu_B^2 N/V) \times 2(L+1)S/[3(J+1)\Delta]$ whereby N/V is the number of ions per volume and $\mu_B = 9.27410 \times 10^{-21}$ erg G^{-1} the Bohr magneton. Equation (14) represents its conversion into the molar susceptibility and was obtained as follows. First, Δ was replaced by $k_B\Delta$ whereby $k_B = 1.38062 \times 10^{-16}$ erg K^{-1} is the Boltzmann constant because we want to measure Δ in K. Secondly, the factor $\mu_B^2 N/(k_B V)$ was replaced by $\mu_B^2 N_A/k_B$ whereby $N_A = 6.02217 \times 10^{23}$ mol^{-1} is the Avogadro number. Thirdly, $\mu_B^2 N_A/k_B$ was calculated by using for μ_B^2 the unit erg G^{-1} emu because 1 erg G^{-1} is equivalent to 1 emu.

[3] The resulting susceptibility becomes temperature-dependent when the thermally excited population of higher multiplet states cannot be neglected [160]. For $T \gg \Delta$ the resulting susceptibility is proportional to T^{-1} [104]. This temperature dependence is equal to that of the Curie or Curie-Weiss susceptibility but its physical origin is not the same.

peratures the susceptibility is relatively high, paramagnetic and temperature-independent, in spite of the fact that $J = 0$, see Table 64. This reflects the exclusive presence of the Van Vleck paramagnetism. The experimental susceptibilities $\chi \approx (6-7) \times 10^{-3}$ emu G^{-1} mol^{-1} of $EuTiO_{3.50}$ and $EuNbO_4$, see Fig. 54, are in good agreement with the theoretical value $\chi_V = 6 \times 10^{-3}$ emu G^{-1} mol^{-1} after Eq. (14), see Table 64. Because of $J = 0$ the Langevin or Curie type magnetism is completely absent. With increasing temperature the susceptibility decreases because higher multiplet states become populated by thermal excitation. A quantum mechanical calculation of $\chi(T)$ is presented e.g. in Ref. [160].

In contrast to the Eu^{3+} compounds, the Sm^{3+} materials show a significant dependence of $\chi(T)$ on the crystal structure type, see Fig. 51 and 54. We are not aware about any specific theoretical calculations of $\chi(T)$ for Sm^{3+} oxides which take into account the crystal field splitting and the Van Vleck paramagnetism including its generalization by considering the thermal population of higher multiplet states. The susceptibility $\chi(T)$ of the simplest Sm^{3+} oxide, Sm_2O_3 , displays the following temperature dependence when starting from the lowest temperature: With increasing temperature $\chi(T)$ decreases, passes through a minimum at $T \approx 350$ K and then it starts to increase again [15]. This behavior was qualitatively explained as follows. Compared to a Curie or Curie-Weiss type behavior the weakened temperature dependence of $\chi(T)$ was ascribed to the Van Vleck susceptibility which is comparable with the Curie susceptibility in the mid and high temperature range, see also Table 64. With further increasing temperature the next higher level of the multiplet, $^6H_{7/2}$, becomes appreciably populated by thermal excitation which leads to an increase of $\chi(T)$. For $SmTiO_{3.37}$ and $Sm_{0.9}La_{0.1}TiO_{3.50}$ the behavior of $\chi(T)$ is qualitatively similar, see Fig. 51 and 52. It is obvious from Fig. 52 that the temperature dependence of $\chi(T)$ at high T is markedly weaker than that of a Curie or Curie-Weiss type. Around 390 K the susceptibility $\chi(T)$ is nearly temperature-independent. An increase of $\chi(T)$ with increasing temperature was not observed, possibly because the temperature was not high enough.

In Figure 52 and 53 $\chi(T)^{-1}$ of $Ce_{0.5}Sm_{0.5}TiO_{3.50}$ is shown. The linear temperature dependence of $\chi(T)^{-1}$ at high temperatures suggests the presence of a Curie-Weiss behavior. However, as displayed in Fig. 53, to a good approximation $\chi(T)^{-1}$ of $Ce_{0.5}Sm_{0.5}TiO_{3.50}$ results from the inverse of the molar weighted sum of $\chi(T)$ of $CeTiO_{3.50}$ and $Sm_{0.9}La_{0.1}TiO_{3.50}$.

Figure 56 presents $\chi(T)$ of several titanates $LnTiO_x$ with $Ln = Ce^{3+}$, Pr^{3+}, Nd^{3+}, Sm^{3+} or Eu^{3+}. The susceptibility of these titanates results predominantly from the localized paramagnetic moments of the Ln^{3+} ions. Therefore Fig. 56 shows a comparison of the magnitude and the temperature dependence of $\chi(T)$ resulting from the different Ln^{3+} ions.

The Figures 60 − 70 present $\chi(T)^{-1}$ or $\chi(T)$ of some compounds whose paramagnetic moments result exclusively from transition metal ions at the B site. In the remaining part of this section we focus the discussion on materials

with B = (Ti,Fe). Compounds with other transition metals besides Ti are mainly discussed in a later section.

The $n = 5$ and $n = 6$ materials $LaTi_{0.8}Fe_{0.2}O_{3.40}$ and $LaTi_{0.67}Fe_{0.33}O_{3.33}$, respectively, are insulators which both contain Ti^{4+} ($3d^0$) and Fe^{3+} ($3d^5$) at the B site. Their molar magnetic susceptibility $\chi(T)$ is presented in Figure 67. For comparison Fig. 67 also shows $\chi(T)$ of the insulators $LaSrFeO_4$ ($j = 1$) and $LaFeO_3$ ($j = n = \infty$) which contain exclusively Fe^{3+} at the B site. The $j = 1$ Ruddlesden-Popper type $LaSrFeO_4$ (Fig. 1) is reported as an antiferromagnet with a Neel temperature of $T_N = 350$ K [95], whereas $LaFeO_3$ is a canted antiferromagnet and thus a weak ferromagnet with $T_N = 740$ K [176]. It is reported by Titov et al. [227,228] that the Fe^{3+} ions in the $n = 5$ compound $LaTi_{0.8}Fe_{0.2}O_{3.40}$ are exclusively located in the central octahedra, see Fig. 16. Thus, the Ti^{4+} and Fe^{3+} ions are fully ordered at the B site in such a way that all B sites of the central BO_6 octahedra are exclusively occupied by Fe^{3+}. These central FeO_6 octahedra form chains along the a-axis without any direct Fe−O−Fe linkage along the b-direction. In this sense the FeO_6 chains do not constitute a quasi-1D but a 1D magnetic system which is surrounded by TiO_6 octahedra and La^{3+} ions. Possibly, the Fe^{3+} ions in the $n = 6$ compound $LaTi_{0.67}Fe_{0.33}O_{3.33}$ are ordered in a similar way, i.e. all B sites of the two central BO_6 octahedra sheets of the 6 octahedra thick layers are exclusively occupied by Fe^{3+}. As discussed below, the behavior of $\chi(T)$ seems to support this assumption. Nevertheless, this has to be confirmed by structural studies. If this turns out to be true, then the chains of the both central FeO_6 octahedra sheets constitute a 2D magnetic system. This because there is, compared to the $n = 5$ compound, an additional direct and zigzag-shaped Fe−O−Fe linkage along the b-direction. See type $n = 6$ in Fig. 5 and imagine that all B sites of the both central BO_6 octahedra sheets are exclusively occupied by Fe^{3+}. We note that in this sense the FeO_6 octahedra in $LaSrFeO_4$ ($j = 1$) and $LaFeO_3$ ($j = n = \infty$) form a 2D and a 3D network, respectively, see Fig. 1. Now, concerning $LaTi_{0.8}Fe_{0.2}O_{3.40}$ ($n = 5$) and $LaTi_{0.67}Fe_{0.33}O_{3.33}$ ($n = 6$), we consider the following two issues because they lead to some interesting speculations. First, the $n = \infty$ compound $LaFeO_3$ displays magnetic ordering, it is a canted antiferromagnet and therefore weakly ferromagnetic. Secondly, it is reported that some of the $n = 6$ ($n = 5$) insulators are (anti)ferroelectric, see Table 32, 44 and 45. This suggests for La(Ti,Fe)O_x and related materials a variety of interesting questions like

- What are the detailed magnetic properties of one (n=5), two (n=6) and possibly three (n=7) FeO_6 octahedra thick layers which form chains along the a-axis and are surrounded by two TiO_6 octahedra thick layers? Are there 1D or 2D features as well as magnetic ordering?

- What are the dielectric features of these compounds? Is there a coupling between dielectric and magnetic properties?

- Are there special (electro- and/or magneto-) optical characteristics?

Although further studies are necessary to clarify these issues, we can draw some conclusions from $\chi(T)^{-1}$ of the $n = 5$ and $n = 6$ materials, see Fig. 68 and 69. The $n = 5$ compound displays a Curie-Weiss-like behavior whereby the $\chi(T)^{-1}$ curve suggests at $T \approx 300$ K a crossover from $\theta = -69$ K < 0 to $\theta = +35$ K > 0, see Figure 69. There are no indications for magnetic ordering. The $\chi(T)^{-1}$ curve of the $n = 6$ compound, see Fig. 68, is markedly different from that of the $n = 5$ type. In both cases there is a change in the slope of $\chi(T)^{-1}$ at $T \approx 300$ K. However, for the $n = 6$ material the slope above 300 K is relatively large. This suggests the presence of a weakly pronounced magnetic ordering below about 280 K or at least, compared to the $n = 5$ type, an enhanced magnetic interaction. The value of 280 K is obtained by extrapolating the slope in the high temperature region down to $\chi^{-1} = 0$. A linear fit of $\chi(T)^{-1}$ to the inverse Curie-Weiss function $(T - \theta)/C$ in the temperature range from 310 − 380 K leads to $\theta = 281$ K and $C = 0.176$ emu G^{-1} K mol^{-1}. The corresponding experimental and theoretical effective moment (see next section) resulting from Fe^{3+} is $p_{exp} = 1.19\ \mu_B$ and $p_{th} = 3.40\ \mu_B$, respectively. The large difference between p_{exp} and p_{th} indicates that the susceptibility is probably not related to a Curie-Weiss behavior.

The significantly different behavior of $\chi(T)$ between the $n = 6$ and $n = 5$ compound supports the suggestion mentioned above, namely that in the $n = 6$ material all Fe^{3+} ions are exclusively located at the B sites of the both central BO_6 octahedra sheets. Compared to the $n = 5$ compound, as described above, this assumption implies an additional Fe−O−Fe linkage along the b-direction which may enhance the magnetic interaction and the tendency for magnetic ordering. The pronounced change of $\chi(T)$ at about 280 K may be considered as an indication for that.

It was also attempted to prepare the $n = 7$ material $LaTi_{0.57}Fe_{0.43}O_{3.29}$ by floating zone melting. However, the as-grown sample consisted mainly of an $n = 6$ phase and no indications for the presence of an $n = 7$ type was found. Maybe it is possible to synthesize the $n = 7$ compound by means of other techniques.

Analogous to La(Ti,Fe)O_x it was attempted to prepare related materials with Mn^{3+} at the B site. The composition $LaTi_{0.8}Mn_{0.2}O_{3.4}$ resulted in a single phase, insulating $n = 5$ type. Its inverse magnetic susceptibility $\chi(T)^{-1}$ displays a Curie-Weiss behavior with a clearly positive Curie-Weiss temperature, see Figure 64 and 66. We speculate that the Mn^{3+} ions in $LaTi_{0.8}Mn_{0.2}O_{3.4}$ are fully ordered in the same way as the Fe^{3+} ions in $LaTi_{0.8}Fe_{0.2}O_{3.4}$. Of course, this has to be confirmed by a structure determination. It was also attempted to synthesize the $n = 6$ compound $LaTi_{0.67}Mn_{0.33}O_{3.33}$. However, this composition lead to an oxygen-deficient $n = 5$ type phase.

In our opinion the current results indicate that compounds of the type $n = 6$ or 7 with transition metal ions such as Mn^{3+} or Fe^{3+} at the B site have the potential for (anti)ferromagnetic order and might show a coupling between magnetic and dielectric properties.

Data evaluation in the case of Curie-Weiss behavior Concerning the fit of the molar magnetic susceptibility $\chi(T)$ to the Curie-Weiss function $C/(T-\theta)$ the following formulas were used for data evaluation.

The experimentally determined effective magnetic moment in units of the Bohr magneton μ_B is

$$p_{exp} = (2.8278\ \mathrm{kg^{1/2}\ m^{-1}\ s^{-1}\ A^{-1}\ K^{-1/2}\ mol^{1/2}}) \times \sqrt{C} \tag{15}$$

To convert C from cgs into SI units, the relation

$$1\ \mathrm{emu\ G^{-1}\ K\ mol^{-1}} = 10^{-1}\ \mathrm{kg^{-1}\ m^2\ s^2\ A^2\ K\ mol^{-1}} \tag{16}$$

was used.

The theoretical effective magnetic moment p_{th} of the compositions $A_{1-y}BO_x$ in units of the Bohr magneton μ_B was obtained in the following way. If there are localized paramagnetic moments from rare earth ions Ln at the A site and/or from transition metal ions TM at the B site, then p_{th} was calculated by the general relation

$$p_{th}^2 = \sum_{i=1}^{N_{Ln}} F_i\,[q_{th}(Ln_i)]^2 + \sum_{j=1}^{N_{TM}} G_j\,[q_{th}(TM_j)]^2 \tag{17}$$

$N_{Ln} = 0, 1, 2, ...$ is the number of different rare earth ions Ln_i with theoretical effective magnetic moment $q_{th}(Ln_i)$ and occupation $0 \le F_i \le 1$ at the A site. $N_{TM} = 0, 1, 2, ...$ is the number of different transition metal ions TM_j with theoretical effective magnetic moment $q_{th}(TM_j)$ and occupation $0 \le G_j \le 1$ at the B site. In terms of the quantum numbers S, L and J the theoretical free-ion value q_{th} in units of the Bohr magneton μ_B is given by

$$q_{th} = g\sqrt{J(J+1)} \tag{18}$$

whereby the free-ion Lande factor g is defined as, see e.g. Ref. [89,104],

$$g = \frac{3}{2} + \frac{S(S+1) - L(L+1)}{2J(J+1)} \tag{19}$$

For theoretical free-ion values q_{th} of some TM and Ln ions see Table 63 and 64.

It seems to be appropriate to recollect the conditions for which Eq. (15) and (18) are valid. They are based on the Curie law which is for the molar susceptibility χ given by

$$\chi(T) = \frac{N_A\,\mu_B^2\,g^2\,J(J+1)}{3k_BT} = \frac{N_A\,q^2}{3k_BT} = \frac{C}{T} \tag{20}$$

where N_A is the Avogadro number, k_B the Boltzmann constant, q the effective magnetic moment in units of μ_B and C the Curie constant. The Curie law is valid for small external magnetic fields H, i.e. $g\mu_B JH \ll k_BT$, see e.g. Ref. [89,104]. Strictly speaking, the derivation of the Curie law, Eq. (20), and Eq. (18) implies also the presence of a strong spin-orbit coupling, i.e. $\hbar^2\Lambda \ll k_BT$, μ_BH where

Λ is the spin-orbit coupling parameter, see e.g. Ref. [161]. This is the case for the 4f electrons of the rare earth ions, see Table 64. If the spin-orbit coupling is relatively weak, as for the 3d transition metal ions, then the effective magnetic moment is not given by Eq. (18) but is calculated to, see e.g. Ref. [161],

$$\tilde{q} = \sqrt{L(L+1) + 4S(S+1)} \tag{21}$$

However, for the 3d transition metal ions the orbital angular momentum L is usually quenched in solids by the electric crystal field from the surrounding ions [1], see e.g. Ref. [104]. That means $L = 0$ and therefore $J = S$, $g = 2$ and $q = \tilde{q}$. Therefore Eq. (18) and (19) can also be applied, at least approximately, for the 3d transition metal ions, see Table 63. Furthermore, the Eqs. (15) − (19) can also be applied if the susceptibility $\chi(T)$ is of the Curie-Weiss type, i.e. $\chi(T) = C/(T - \theta)$. Usually, but not in all cases [234], a Curie-Weiss behavior of $\chi(T)$ indicates the presence of interacting localized paramagnetic moments, see e.g. Ref. [207,234], whereby the absolute value of the Curie-Weiss temperature θ reflects the strength of the interaction.

Unless otherwise stated the temperature-independent diamagnetism from closed electron shells was not taken into account. In most cases the molar susceptibility is at least of the order $(10^{-3} - 10^{-2})$ emu G^{-1} mol^{-1}, see Fig. 47 − 69. The diamagnetic molar susceptibility of ABO_x was estimated to $(-7$ or $-2) \times 10^{-5}$ emu G^{-1} mol^{-1} and is therefore mostly negligible. These two values were obtained as follows. On the one hand, some values from Ref. [115] were used, namely $(-2.4, -0.5$ and $-1.2) \times 10^{-5}$ emu G^{-1} mol^{-1} for Ba^{2+}, Ti^{4+} and O^{2-}, respectively. For a composition $Ln\mathrm{TiO}_{3.40}$ this amounts to -7×10^{-5} emu G^{-1} mol^{-1} whereby for Ln the value of Ba^{2+} was utilized. On the other hand, the absolute value of the experimentally determined susceptibility of diamagnetic insulators is appreciably smaller, e.g. $\approx -2 \times 10^{-5}$ emu G^{-1} mol^{-1} for $\mathrm{LaTiO}_{3.50}$ [127]. We consider the experimental value as more relevant than that obtained by adding up the susceptibilities of the discrete ions. The existence of such a discrepancy is not surprising because the summation of the values of the single ionic constituents does not necessarily result in the true susceptibility of the compound. There is also no unique way for a precise calculation of the diamagnetic susceptibility for all solids. For a discussion of diamagnetism and diamagnetic corrections see Ref. [116] and references therein as well as Ref. [140]. The latter cites MgO as an example with a similar discrepancy between the theoretical and experimental value.

Results and discussion in the case of Curie-Weiss behavior The Tables 65 − 69 and Fig. 60 − 64, 66 and 69 present results from fitting the molar magnetic susceptibility $\chi(T)$ to the Curie-Weiss function $C/(T - \theta)$. In most cases the experimental and theoretical free-ion values of the effective magnetic

[1] The 4f electrons of the rare earth ions are hardly affected by the crystal field because they are located much deeper in the electron shell than the d electrons of the transition metal ions.

moment p are close to each other. For almost all materials $\theta < 0$ was found. This indicates an antiferromagnetic interaction between the localized paramagnetic moments. This is usually due to the indirect superexchange interaction via the surrounding oxygen ions which is typically of an antiferromagnetic type, see e.g. Ref. [158]. There are also a few compounds with $\theta > 0$, especially those with Mn^{3+} at the B site, which indicates the presence of a ferromagnetic interaction.

In the $A_nB_nO_{3n+2}$ structure the kind of the $A - O - A$ linkage is equal along the a- and b-axis but is distinct from that along the c-axis, whereas for $B - O - B$ it is different for all three directions, see Figure 6. Therefore the superexchange between the localized paramagnetic magnetic moments at the A and/or B site is possibly anisotropic. If the occupancy of paramagnetic Ln and/or TM ions at the A and/or B site is less than 1, then the anisotropy and strength of the superexchange may also depend on the degree of (partial) order of the Ln and/or TM ions. A further circumstance which could influence the total exchange interaction between the localized paramagnetic moments is the presence of (quasi-1D) conduction electrons.

In the case of Ln ions at the A site the Curie-Weiss temperatures θ vary from approximately -160 K for $La_{0.76}Ce_{0.12}Yb_{0.12}TiO_{3.4}$ to about 0 K for Eu^{2+} niobates. The largest values of $|\theta|$ are realized for compounds containing Ce^{3+} and/or Yb^{3+} which both have $S = 1/2$ and $L = 3$ but their J is different, see Table 64 and 65 – 69. The question raises why just these two rare earth ions result in the highest values of $|\theta|$. The Eu^{2+} niobates display a Curie-Weiss or Curie behavior down to the lowest temperature of 2 K, see Fig. 55 and Table 68. We do not know the reason why the Curie-Weiss temperatures of Eu^{2+} compounds are practically zero. We notice, however, that for Eu^{2+} there is no crystal field splitting because of $L = 0$ and thus $J = S$, see also Table 64. Because deviations from the Curie-Weiss behavior indicate the presence of interactions beyond the mean-field approximation and/or crystal field splittings, the absence of the latter may lead to an extended validity range of the Curie-Weiss law. However, to our knowledge this does not necessarily imply $\theta \simeq 0$.

Comparing the $n = 4.33$ titanate $CeTiO_{3.47}$ and the $n = 5$ titanate $NdTiO_{3.42}$ with isostructural but significantly non-stoichiometric $Ce_{0.95}TiO_{3.39}$ and $Nd_{0.95}TiO_{3.34}$, respectively, the $|\theta|$ of the latter is approximately twice as high, see Table 65 and 67. We note that the both $n = 5$ titanates $NdTiO_{3.42}$ and $NdTiO_{3.31}$ evince a nearly equal θ, see Table 67. This suggests that the doubling of $|\theta|$ is more related to the deficiency at the A site than to the oxygen deficiency. We do not know the physical origin of this interesting phenomenon. Maybe it is of general relevance in the field of magnetism. One may speculate, for example, if a cation deficiency in (anti)ferromagnetic materials may lead to an enhancement of the magnetic transition temperature. Further studies are necessary to clarify this issue.

In the case of TM ions at the B site the Curie-Weiss temperatures θ vary from approximately -500 K for $La_{0.6}Ca_{0.4}Ti_{0.6}Nb_{0.4}O_{3.40}$ ($(Ti,Nb)^{4.6+}$, $d^{0.2}$) and $LaTi_{0.8}V_{0.2}O_{3.31}$ ($(Ti,V)^{3.6+}$, $3d^{0.6}$) to about $+70$ K for $LaTi_{0.8}Mn_{0.2}O_{3.40}$ (Mn^{3+}, $3d^4$), see Fig. 60 – 69. For $LaTi_{0.8}Al_{0.2}O_{3.31}$ ($Ti^{3.8+}$, $3d^{0.2}$) the tem-

perature dependence of $\chi(T)^{-1}$ in the high temperature range fits less good but approximately to a linear behavior, see Figure 62. A fit to the inverse Curie-Weiss function leads to $\theta \approx -900$ K.

Also the oxygen-deficient $n = 5$ compound $LaTi_{0.67}Mn_{0.33}O_{3.33}$ (Mn^{3+}, $3d^4$), whose $\chi(T)$ is presented in Fig. 65, shows a Curie-Weiss behavior. A linear fit of its $\chi(T)^{-1}$ curve to the inverse Curie-Weiss function $(T-\theta)/C$ in the temperature range 190 K $\leq T \leq$ 380 K leads to $\theta = +69$ K and $C = 1.29$ emu G^{-1} K mol^{-1}. The experimentally determined effective magnetic moment after Eq. (15) and (16) and the corresponding theoretical free-ion value resulting from Mn^{3+} after Eq. (17) and Table 63 is $p_{exp} = 3.21\ \mu_B$ and $p_{th} = 2.81\ \mu_B$, respectively.

Among the materials investigated in this work the only compounds with a clearly positive Curie-Weiss temperature are those with Mn at the B site. This indicates a ferromagnetic interaction between the Mn^{3+} ($3d^4$) ions. Figure 64 shows $\chi(T)^{-1}$ of three samples of the $n = 5$ insulator $LaTi_{0.8}Mn_{0.2}O_{3.4}$ which were prepared by floating zone melting in Ar, air and O_2 , respectively. Also presented in Fig. 64 are the corresponding values of the unit cell volume V (Table 37), the Curie-Weiss temperature θ and the effective magnetic moment p_{exp}. Compared to the specimen synthesized in Ar, the samples grown in air and O_2 display a smaller (higher) value of V and p_{exp} (θ). For the samples grown in air and O_2 this suggests the presence of a small amount of Mn^{4+} because

- the formation of Mn^{4+} is favored by oxidizing preparation conditions and may be realized by a somewhat over-stoichiometric oxygen content $x > 3.40$
- the size of Mn^{4+} is smaller than that of Mn^{3+} which may lead to a diminished unit cell volume V
- the effective magnetic moment of Mn^{4+} is smaller than that of Mn^{3+} (Table 63).

For the two $La(Ti,V)O_x$ compounds, see Fig. 63, the theoretical effective magnetic moment p_{th} was estimated as follows. We assume that the V ions and a part of Ti ions are, at least approximately, in the valence state 3+. Then from Eq. (17) we get

$$p_{th}^2 \;=\; G_1\,[q_{th}(Ti^{3+})]^2 \;+\; G_2\,[q_{th}(V^{3+})]^2 \qquad (22)$$

The occupancy G_2 of V at the B site is given by the V content in the composition formula. Then the occupancy G_1 of Ti^{3+} at the B site can be obtained by

$$G_1 \;=\; N_t \;-\; G_2 N_V \qquad (23)$$

whereby N_t is the total number of 3d electrons per (Ti,V) in the composition $La(Ti,V)O_x$ resulting from charge neutrality and $N_V = 2$ is the number of 3d electrons belonging to the configuration V^{3+} ($3d^2$). Now p_{th} can be calculated by using the values of N_t displayed in Fig. 63 and those of $q_{th}(Ti^{3+})$ and $q_{th}(V^{3+})$ presented in Table 63. In both $La(Ti,V)O_x$ compounds the contribution of Ti^{3+}

and V^{3+} to p_{th} is weighted in a different way:

$LaTi_{0.95}V_{0.05}O_{3.41}$:

$$p_{th}^2 \;=\; G_1\,[q_{th}(Ti^{3+})]^2 \;+\; G_2\,[q_{th}(V^{3+})]^2 \;=\; (0.39 \;+\; 0.40)\;\mu_B^2 \qquad (24)$$

$LaTi_{0.8}V_{0.2}O_{3.31}$:

$$p_{th}^2 \;=\; G_1\,[q_{th}(Ti^{3+})]^2 \;+\; G_2\,[q_{th}(V^{3+})]^2 \;=\; (0.54 \;+\; 1.60)\;\mu_B^2 \qquad (25)$$

Obviously, for $LaTi_{0.95}V_{0.05}O_{3.41}$ the contribution of Ti^{3+} and V^{3+} is nearly equal, whereas for $LaTi_{0.8}V_{0.2}O_{3.31}$ the magnetic moment of V^{3+} predominates.

We note that some materials display a rather high absolute value of the Curie-Weiss temperature θ although only about 20 % percent of the B sites are occupied with localized paramagnetic moments:

- $\theta = -392$ K for the $n = 5$ type $LaTi_{0.95}V_{0.05}O_{3.41}$ ($3d^{0.23}$, $(Ti,V)^{3.77+}$), see Fig. 63
- $\theta = -531$ K for the significantly oxygen-deficient $n = 4$ type $La_{0.6}Ca_{0.4}Ti_{0.6}Nb_{0.4}O_{3.40}$ ($d^{0.20}$, $(Ti,Nb)^{4.60+}$), see Fig. 61
- $\theta \approx -900$ K for the significantly oxygen-deficient $n = 5$ type $LaTi_{0.8}Al_{0.2}O_{3.31}$ ($3d^{0.23}$, $Ti^{3.77+}$), see Fig. 62

This is remarkable because these quite large values indicate the presence of a rather high antiferromagnetic superexchange interaction although the concentration of the localized paramagnetic moments is relatively low. In a 3D crystal structure this would result in a relatively large average distance between the localized paramagnetic moments and thus the superexchange interaction is expected to be relatively small. However, these materials are quasi-2D (layered) and additionally they comprise a quasi-1D character which is constituted by the chains of corner-shared BO_6 octahedra along the a-axis. Furthermore, as described in an earlier section, those cations with the smaller valence like Ti^{3+}, V^{3+} and/or Nb^{4+} tend to concentrate in the inner region of the layers, whereas those with the larger valence as Ti^{4+}, V^{5+} and/or Nb^{5+} tend to accumulate in the boundary region of the layers. Maybe the rather high $|\theta|$ values of some compounds are related to these (low-dimensional) structural features.

The $n = 5$ titanates $LnTiO_{3.4}$ with Ln = La, Ce, Pr, Nd or Sm For some of the electrical conducting titanates $ATiO_{3.4}$ the corresponding insulator $ATi_{0.8}Al_{0.2}O_{3.40}$ was also prepared, namely for A = Pr and Nd [1]. This allows a

[1] It was also attempted to prepare corresponding insulators for A = Ce and Sm, however the preparation by floating zone melting was impossible because of a very difficult melt behavior.

comparison between the susceptibility $\chi(T)$ of the conductor and its corresponding insulator. As apparent from Fig. 48 and 49 the susceptibility of the electrical conducting compound is lower than that of the insulator, especially in the case of A = Pr. The temperature dependence of the difference is plotted in Fig. 57. We want to discuss this feature in more detail by considering the behavior of three related $n = 5$ titanates, namely an insulator and its corresponding electrical conductor, both with a paramagnetic moment at the A site (A = Pr or Nd), and a conducting compound without a paramagnetic moment at the A site (A = La). We choose A = Pr for a discussion because of two reasons. First, the effect is larger for Pr compared to Nd. Secondly, on $PrTiO_{3.41}$ resistivity measurements were performed (see Fig. 45) and the result suggests that $PrTiO_{3.41}$ is a quasi-1D metal like $LaTiO_{3.41}$. To ensure that the difference between the susceptibility of $PrTiO_{3.41}$ and $PrTi_{0.8}Al_{0.2}O_{3.40}$ reflects the intrinsic material behavior, various pairs of samples were measured. Every sample pair consisted of two specimens, $PrTiO_{3.41}$ and $PrTi_{0.8}Al_{0.2}O_{3.40}$, both with approximately equal shape and mass as well as nearly same orientation with respect to the magnetic field. The layers were approximately oriented along the field. Significant variations in the difference curves and individual susceptibilities were not observed.

Figure 58 and 59 presents the molar magnetic susceptibility $\chi(T)$ and $\chi(T)^{-1}$ of the insulator $PrTi_{0.8}Al_{0.2}O_{3.40}$ and the quasi-1D metals $PrTiO_{3.41}$ and $LaTiO_{3.41}$. Table 69 shows the results of fitting the susceptibilities to the function $D + C/(T - \theta)$. The data reveal that the susceptibility $\chi(T)$ and the experimentally determined effective magnetic moment p_{exp} of the quasi-1D metal $PrTiO_{3.41}$ is lower than that of the insulator $PrTi_{0.8}Al_{0.2}O_{3.40}$. Conversely, $|\theta|$ of the quasi-1D metal $PrTiO_{3.41}$ is higher than that of the insulator $PrTi_{0.8}Al_{0.2}O_{3.40}$. This suggests that the localized paramagnetic moments experience an additional and therefore increased antiferromagnetic exchange interaction via the surrounding conduction electrons in $PrTiO_{3.41}$. The enhanced $|\theta|$ as well as the attenuated effective magnetic moment p_{exp} and susceptibility in $PrTiO_{3.41}$ is consistent with such a scenario. We suppose, from a theoretical point of view, that this effect belongs to the Kondo lattice scenario or RKKY interaction, see e.g. Ref. [235] or [159]. However, we are not aware of any specific theoretical model which suits to the quasi-1D metal $PrTiO_{3.41}$.

The difference of the susceptibility between the quasi-1D metal $PrTiO_{3.41}$ and the insulator $PrTi_{0.8}Al_{0.2}O_{3.40}$, $\chi_1 - \chi_2$, has qualitatively the same temperature dependence as that of $LaTiO_{3.41}$ (see Fig. 58). This could represent another hint that the behavior of $\chi_1 - \chi_2$ is related to the conduction electrons, at least for temperatures above $\approx$ 50 K. At low temperatures, however, the origin of the increasing values with decreasing temperature is probably not the same for both curves. For $LaTiO_{3.41}$ it is very likely that this is due to paramagnetic impurities. For $\chi_1 - \chi_2$ we suppose that the approach to zero is due to the metal-to-semiconductor transition in $PrTiO_{3.41}$, i.e. when the conduction electrons disappear its susceptibility merges into that of the insulator $PrTi_{0.8}Al_{0.2}O_{3.40}$.

In the following we present an empirical approach to express the experimentally observed susceptibility $\chi(T)$ of $PrTiO_{3.41}$ by that of $PrTi_{0.8}Al_{0.2}O_{3.40}$ and $LaTiO_{3.41}$, see Fig. 58 and 59 and Table 69. We look first at the susceptibility $\chi(T)$ of the insulator $PrTi_{0.8}Al_{0.2}O_{3.40}$. For temperatures above ≈ 50 K it displays a Curie-Weiss behavior, i.e.

$$\chi_2(T) = \frac{C_2}{T - \theta_2} \qquad (PrTi_{0.8}Al_{0.2}O_{3.40}\ ,\ T > 50\,\mathrm{K}) \tag{26}$$

We use the index 2 to label the insulator $PrTi_{0.8}Al_{0.2}O_{3.40}$. $\theta_2 = -24$ K (see Table 69) indicates the presence of an antiferromagnetic interaction between the localized paramagnetic moments of the Pr^{3+} ions. The similar is valid for the quasi-1D metal $PrTiO_{3.41}$, labelled by the index 1, thus

$$\chi_1(T) = \frac{C_1}{T - \theta_1} \qquad (PrTiO_{3.41}\ ,\ T > 50\,\mathrm{K}) \tag{27}$$

Apart from a Curie contribution C_3/T from paramagnetic impurities for $T \leq 20$ K there is no analogous high T representation for the experimentally determined susceptibility of the quasi-1D metal $LaTiO_{3.41}$, labelled by the index 3, i.e.

$$\chi_3(T) = \text{as-measured curve} \qquad (LaTiO_{3.41}\ ,\ T > 50\,\mathrm{K}) \tag{28}$$

To find an expression for $\chi_1(T)$ of the quasi-1D metal $PrTiO_{3.41}$ we tried to modify $\chi_2(T)$ of the insulator $PrTi_{0.8}Al_{0.2}O_{3.40}$ by using $\chi_3(T)$ of the quasi-1D metal $LaTiO_{3.41}$. This because $\chi_3(T)$ represents the behavior of the conduction electrons, i.e. their degree of polarization by an external field. To a first approximation we assume that $\chi_3(T)$ reflects also the polarization of the conduction electrons by an internal field from localized paramagnetic moments. The latter arise when the diamagnetic La^{3+} ions at the A site are replaced by paramagnetic Pr^{3+}. It seems also reasonable to suppose that $\chi_3(T)$ describes to some extent that part of the exchange interaction between the localized moments which is mediated via the conduction electrons. It turned out that the following ansatz with a parameter f reproduces $\chi_1(T)$ surprisingly well:

$$\chi_4(T) = \frac{C_2}{T - \theta_2 + f\chi_3(T)} \tag{29}$$

The artificially constructed function $\chi_4(T)$ is based on Eq. (26) whereby the negative Curie-Weiss temperature $-\theta_2$ is replaced by a modified "temperature-dependent Curie-Weiss temperature" $-\theta_2 + f\,\chi_3(T)$. The term $f\,\chi_3(T)$ can be considered as an additional interaction with a temperature dependence $\chi_3(T)$. In Figure 58 two versions of $\chi_3(T)$ are shown, namely (a) the as-measured data and (b) a curve obtained by subtracting from (a) the Curie contribution C_3/T from paramagnetic impurities which dominate the low T behavior, see also Table 69. By the requirement that both curves, $\chi_4(T)$ and $\chi_1(T)$, merge at the highest measurement temperature, i.e.

$$\chi_4(T) = \chi_1(T) \text{ for } T = 390\,\mathrm{K}\ , \tag{30}$$

the parameter f was determined to

$$f = [1.384\,(\text{a}) \text{ or } 1.409\,(\text{b})] \times 10^6 \text{ K emu}^{-1}\text{G mol} \tag{31}$$

With this value of f the function $\chi_4(T)$ reproduces $\chi_1(T)$ very well for $T >$ 50 K, see Fig. 58 and 59 and Table 69. That means $\chi_4(T)$ represents again a Curie-Weiss function whereby C_2 and θ_2 in Eq. (26) and (29) are changed into C_1 and θ_1, i.e.

$$\chi_4(T) = \frac{C_2}{T - \theta_2 + f\chi_3(T)} \equiv \frac{C_1}{T - \theta_1} = \chi_1(T) \qquad (\,T > 50\,\text{K}) \tag{32}$$

In this sense the alteration from C_2 and θ_2 into C_1 and θ_1 can be viewed as a renormalization via the conduction electrons which was taken into account by the experimentally determined curve $\chi_3(T)$.

The $n = 5$ titanates $Ln\text{TiO}_{3.4}$ are known for Ln = La, Ce, Pr, Nd and Sm (see Table 35, 38, 40 and 41). In this sequence the ionic radius of Ln decreases from left to right. In perovskites or perovskite-related compounds a decreasing ionic radius at the A site of is often accompanied by a diminishing $B-\text{O}-B$ bond angle which may lead to a reduced band width and therefore to localization. Up to now optical and/or resistivity measurements were performed on $\text{LaTiO}_{3.41}$ and $\text{PrTiO}_{3.41}$ which indicate that they are quasi-1D metals, see Table 35 and Figure 45. Possibly, with a further decreasing ionic radius at the A site, i.e. for Ln = Nd and Sm, a compositional-driven metal-to-semiconductor transition takes place. A comparison between Ln = Pr and Ln = Nd reveals two features which suggests the possible existence of such a transition. First, the absolute value of the susceptibility difference between the electrical conductor and the insulator is higher for Ln = Pr, see Fig. 48, 49 and 57. Assuming that the degree of this difference represents a measure for the number of the existing conduction electrons, in the sense of the discussion above, then for Ln = Nd the 3d electrons are closer to a localization. Secondly, the difference $p_{exp} - p_{th}(Ln^{3+}) > 0$ is larger for Ln = Nd (see Table 67 and 69). Assuming that for Ln = Nd the 3d electrons from Ti^{3+} are localized, then we can take into account the corresponding effective magnetic moment of Ti^{3+} in the calculation of p_{th}. This results in an improved agreement between p_{exp} and p_{th} (see Table 67) and may therefore be viewed as a further hint that for Ln = Nd the 3d electrons are nearer to a localized state. Of course, an unique decision whether $\text{NdTiO}_{3.4}$ and $\text{SmTiO}_{3.4}$ are metals or semiconductors can only be achieved by experiments such as resistivity measurements, optical spectroscopy and/or ARPES.

We now comment the temperature dependence of the susceptibility of $\text{LaTiO}_{3.41}$ (Fig. 58) and related materials such as $\text{SrNbO}_{3.41}$ (Fig. 76). Apart from the low temperature behavior, which is most probably due to paramagnetic impurities, the susceptibility $\chi(T)$ increases with increasing temperature. This behavior seems to be a typical feature of quasi-1D metals for $T < T_{MST}$ as well as for $T > T_{MST}$. Here T_{MST} is the temperature where the metal-to-semiconductor transition takes place. We cite two examples, namely the oxide $\text{Tl}_{0.3}\text{MoO}_3$ with T_{MST} = 180 K [61] and the organic compound TTF-TCNQ with T_{MST} = 53

K [96]. In the case of a Peierls transition and $T < T_{MST}$ the susceptibility decreases with decreasing temperature because of a diminished number of conduction electrons as a result of the opening of an energy gap at the Fermi energy. At present the nature of the metal-to-semiconductor transition of $LaTiO_{3.41}$ and $SrNbO_{3.41}$ is not completely clarified. In the case of $LaTiO_{3.41}$ Kuntscher et al. reports on indications for a phase transition [112]. For $SrNbO_{3.41}$ it is discussed in terms of a Peierls transition by Kuntscher et al., but not all findings can be explained within this picture [111,113]. For both compounds the transition temperature T_{MST} is about 100 K [112,113,127]. At around 100 K and with decreasing temperature the susceptibility of $LaTiO_{3.41}$ (Fig. 58) decreases somewhat faster, whereas that of $SrNbO_{3.41}$ (Fig. 76) has almost reached its constant value. The change of the susceptibility around and below T_{MST} is less sharp and relatively sluggish compared to that of $Tl_{0.3}MoO_3$ and TTF-TCNQ. We note that the intrinsic low temperature susceptibility D of $LaTiO_{3.41}$ and $SrNbO_{3.41}$ is larger than the diamagnetic susceptibility χ_{dia} of the corresponding insulator $LaTiO_{3.50}$ and $SrNbO_{3.50}$, respectively:

- $LaTiO_{3.41}$: $D \simeq +0.3 \times 10^{-5}$ emu G^{-1} mol^{-1} (see Fig. 58 and Table 69)
  $LaTiO_{3.50}$: $\chi_{dia} \simeq -2 \times 10^{-5}$ emu G^{-1} mol^{-1} [127]

- $SrNbO_{3.41}$: $D \simeq -2 \times 10^{-5}$ emu G^{-1} mol^{-1} (see Fig. 76 and Table 70)
  $SrNbO_{3.50}$: $\chi_{dia} \simeq -3 \times 10^{-5}$ emu G^{-1} mol^{-1} [127].

Concerning the temperature dependence of the susceptibility $\chi(T)$ in the range $T > T_{MST}$ we refer to the paper by Weber et al. on $SrNbO_{3.41}$ [242]. They discuss the high temperature behavior of $\chi(T)$ in terms of almost localized spins in a 1D antiferromagnetic Heisenberg chain.

5.4 Speculations about the potential for (high-T_c)superconductivity

We believe that the conducting $A_nB_nO_{3n+2}$ oxides are worth mentioning with respect to hypothetical, novel types of superconductivity. We mention two examples from which perspectives these materials may be viewed, namely bipolaronic and excitonic superconductivity. For the first we refer, for instance, to the Nobel lecture by Bednorz and Müller [14] and the paper by de Jongh [35]. For the second we will present some considerations in the next section.

Furthermore, we refer the reader to the book "Room Temperature Superconductivity" by Mourachkine [141].

We note that, to the best of our knowledge, the present highest superconducting transition temperature (at ambient pressure) is $T_c = 138$ K, realized by the cuprate $Hg_{0.8}Tl_{0.2}Ba_2Ca_2Cu_3O_{8+\delta}$ reported by Sun et al. in 1994 [206].

View from the perspective of excitonic superconductivity The hypothetical excitonic type of superconductivity represents one of several ideas how to realize room temperature superconductors. In the excitonic mechanism of superconductivity the formation of Cooper pairs is based on an electron-electron

mediated interaction. It is assumed that an attractive interaction between conduction electrons may come about via electronic excitations in a spatially adjacent but electronically separated subsystem. The first ideas about excitonic superconductivity, which seems to be favored by low-dimensional systems, were developed by Little as well as by Ginzburg:

- The original idea to realize this in hypothetical quasi-1D organic conductors was proposed by Little [129–132]. He considered conducting chains which are surrounded by electronically polarizable side branches.

- The original proposal to realize this in quasi-2D systems was devised by Ginzburg [58]. He considered a thin metallic sheet which is surrounded by two dielectric layers. Further papers about this approach were published later, e.g. by Allender et al. [5].

Little also considered a system in which the strict electronic separation between conduction electrons and the electronically polarizable subsystem was abandoned, i.e. a certain degree of electron exchange between both subsystems was permitted [130].

Among the literature there are several publications which present some arguments why excitonic superconductivity is not possible. We refer to the latest paper by Little which contains a detailed discussion and refutation of these arguments [132]. A further debate about these objections can be found in the article by Ginzburg [58].

It seems that the $A_nB_nO_{3n+2}$ quasi-1D metals represent interesting materials with respect to the approach by Little as well as by that of Ginzburg. Concerning the approach proposed by Little the most important question is how to accomplish an electronically polarizable subsystem in these oxides. We speculate that such subsystems could be realized by

- an appropriate electronic band structure (for example, this was discussed by Little for some high-T_c superconducting cuprates [132])

- fluctuating valence states related to 4f electrons of rare earth ions at the A site, e.g. Eu^{2+}/Eu^{3+} ($4f^7/4f^6$)

- the different energy levels of the magnetic multiplet of the 4f electrons of rare earth ions at the A site

However, it is beyond the scope of this article to present any theoretical evaluations if and how the conduction electrons may really interact with and via such kinds of subsystems.

With respect to the approach proposed by Ginzburg we may consider the quasi-1D metals of the type $n = 4.5$ as well as $n = 5$ in a way as illustrated in Figure 71:

- The $n = 4.5$ member represents the ordered stacking sequence $n = 4$, 5, 4, 5, ... As shown in Fig. 71 (a) this can be viewed as a heterostructure of dielectric ($n = 4$) and metallic ($n = 5$) layers [1]. The compositional example $SrNbO_{3.44}$ implies nominal 0.11 4d electrons per Nb. The specified allocation in $4d^0$ for the $n = 4$ layers and in an average of $4d^{0.2}$ for the $n = 5$ layers, as shown in Fig. 71 (a), corresponds to the extreme case where all 4d electrons are located in the metallic $n = 5$ layers. This picture or its approximate realization is supported by the experimental finding that the metallic character in conducting (Sr,La)NbO_x is relatively weak for $n = 4$ whereas it is relatively high for $n = 4.5$ and $n = 5$ [113]. This indicates that the metallic character is mainly related to the central octahedra which are present only in $n = 5$ but not in $n = 4$ type layers. We remind that $n = 4$ materials, if they have an insulating d^0 composition, are often known as ferroelectrics such as $SrNbO_{3.50}$.

- As depicted in Fig. 71 (b), even a single $n = 5$ layer or an $n = 5$ material can approximately be considered as a metallic sublayer surrounded by two dielectric sublayers. This picture is supported by results from band structure calculations on $SrNbO_{3.41}$: The major contribution to the electronic density of states (DOS) at the Fermi energy E_F comes from those Nb atoms located in the central octahedra which are almost undistorted [110,244]. The contribution from those Nb atoms located in the other octahedra, which display a relatively high distortion, is relatively small and decreases with increasing distance from the middle of the layers [110,244] [2]. This feature is qualitatively in accordance with the distribution of the Nb valence and 4d electron count which is known for $CaNbO_{3.41}$ (see Fig. 15). The corresponding values are displayed in Fig. 71 (b). They indicate that the Nb valence (4d electron count) is lowest (highest) in the central octahedra and increases (decreases) with increasing distance from the middle of the layers.

The considerations above suggest that the $A_nB_nO_{3n+2}$ quasi-1D metals may have the potential to create new (high-T_c)superconductors. However, the com-

[1] We note that oxides of the type $m = 5 + 6$ of hexagonal $A_mB_{m-1}O_{3m}$ display a stacking sequence of $m - 1$ BO_6 octahedra thick layers which is similar to that of $n = 4.5$ compounds, namely $m - 1 = 4$, 5, 4, 5, ... (see Figure 9). Therefore we may apply the approach illustrated in Fig. 71 (a) also to $m = 5 + 6$ materials by using the $m = 5+6$ niobate $Sr_{11}Nb_9O_{33}$ as example: The $m - 1 = 4$ octahedra thick slabs might represent the dielectric layers because the $m = 5$ niobate $Sr_5Nb_4O_{15}$ is an insulator, whereas the $m - 1 = 5$ octahedra thick slabs might represent the metallic layers because the $m = 6$ niobate $Sr_6Nb_5O_{18}$ is a quasi-2D metal (see section 6 and Fig. 74 and 75).

[2] Possibly, such a relationship between octahedra distortion and contribution to the electronic density of states might also exist in other types of oxides whose layers are 3 or 5 octahedra thick. Therefore, the scenario depicted in Fig. 71 (b) might also be valid for other types of materials, e.g. the $m = 6$ type of hexagonal $A_mB_{m-1}O_{3m}$ (see Fig. 9, 10 and 17) like the $m = 6$ quasi-2D metal $Sr_6Nb_5O_{18}$ (see section 6 and Fig. 74 and 75).

pounds reported in this work and Ref. [127] did not show any indications for the presence of superconductivity above the lowest accessible temperature of 2 K. On the other hand, among these (and other) types of low-dimensional oxides there are still many unexplored chemical compositions. Furthermore, as already realized by Little as well as by Ginzburg, to create excitonic superconductivity several materials parameters have to be concurrently in a right small range. Therefore, in our opinion, it is still worthwhile to continue the search for new (high-T_c)superconductors. In this context we cite the following statement from Mourachkine which is probably of general relevance and independent of the specific underlying mechanism of superconductivity:

"Therefore, synthesizing a room-temperature superconductor, one must pay attention to its structure: the "distance" between failure and success can be as small as 0.01 Å in the lattice constant" [142].

We have already pointed out to a special feature of the $A_nB_n\mathrm{O}_{3n+2} = AB\mathrm{O}_x$ quasi-1D metals, namely their compositional, structural and electronic proximity to non-conducting (anti)ferroelectrics. This suggests the possibility to realize compounds with an intrinsic coexistence of a metallic conductivity along the a-axis and a high dielectric polarizability perpendicular to the a-axis. As presented in section 1.2 and Table 48 this statement is supported by two different experimental results, namely the presence of a ferroelectric soft mode not only in the $n = 4$ ferroelectric insulator $\mathrm{SrNbO}_{3.50}$ but also in related $n = 4$, 4.5 and 5 quasi-1D metals (Sr,La)NbO_x , as well as a high dielectric constant $\varepsilon_{c\,\infty} \approx 100$ in the $n = 5$ type $\mathrm{SrNbO}_{3.41}$ along the c-axis. Possibly, these special features are advantageous for the realization of excitonic or other types of superconductivity in $A_nB_n\mathrm{O}_{3n+2}$ quasi-1D metals. Although it is beyond the scope of this work to present any detailed theoretical considerations of this complex issue, we note that the dielectric constant is related to four different kinds of the polarizability [105]:

Electronic polarizability: This refers to the polarization of the electrons (relative to the nucleus) in a single atom, ion or molecule. As mentioned above, the electronic polarizability and related electronic excitations play an important role in the concept of excitonic superconductivity. At sufficiently high frequencies, like those in the upper optical spectrum, the electronic part is the only relevant contribution to the polarizability. The value of the dielectric constant ε related to the electronic polarizability is usually $\varepsilon_{electronic} < 10$. Theoretically, the possibility of much larger values were considered in the context of the so-called electronic ferroelectricity [9,10,173]. The theoretical considerations with respect to an electronic ferroelectricity are related to the Falicov-Kimball model which describes, in its original version, itinerant d electrons interacting with localized f electrons via an on-site Coulomb interaction.

Ionic (or lattice) polarizability: This polarization refers to the dipole moment which results from a shift of several ions against each other. In the $n = 5$ niobate $\mathrm{SrNbO}_{3.41}$ the large dielectric constant $\varepsilon_{c\,\infty} \approx 100$ along the c-axis reflects very

likely the presence of a high lattice polarizability [17]. Concerning superconductivity, one may consider a high lattice polarizability as advantageous because the corresponding large dielectric constant reduces the Coulomb repulsion between conduction electrons. This may support the formation of Cooper pairs. For example, this was considered for the low-T_c superconductors Na_yWO_3 and $SrTiO_{3-\delta}$ whose non-conducting parent compounds (i.e. $y = \delta = 0$) display a large dielectric constant as well as for high-T_c superconducting cuprates, see e.g. Ref. [16,35,178]. However, in the case of the $A_nB_nO_{3n+2}$ compounds we have to pay attention to the anisotropy. For example, in the $n = 5$ niobate $SrNbO_{3.41}$ the large value $\varepsilon_{c\infty} \approx 100$ refers to the c-axis whereas the conduction electrons display a metallic behavior only along the a-axis.

Dipolar polarizability: This signifies the polarizability of permanent dipole moments, i.e. such which already exist in the absence of an external electric field, e.g. in the case of ferroelectric ordering. In this context we refer also to theoretical models which consider a coexistence of ferroelectricity and superconductivity [16,108].

Interfacial polarizability: This refers to the polarizability of accumulated charges at interfaces in heterogeneous materials. In the case of $A_nB_nO_{3n+2}$ compounds this might represent a significant contribution because at the boundary of the layers there is a relatively large amount of negatively charged oxygen ions (see section 1.1).

We notice that for an experimentally measured value of the dielectric constant the corresponding separate values, which result from the different kinds of the polarizability, are normally not known.

The system Na−W−O In the context of the considerations of the previous section it seems to be interesting to look at the system Na−W−O.

One of the known compounds in this system is $NaWO_3$ (W^{5+}, $5d^1$) which crystallizes in a cubic perovskite structure. The related Na-deficient phases Na_yWO_3 display low-T_c superconductivity with $T_c \leq 3$ K for $0.2 < y < 0.5$, see e.g. Ref. [198]. Na_yWO_3 can be considered as a modification of WO_3 . The crystal structure of WO_3 is of a distorted ReO_3 type, i.e. it can be viewed as an A-free distorted perovskite structure ABO_3 , and displays several temperature-driven phase transitions with six different phases, see e.g. Ref. [74]. WO_3 (W^{6+}, $5d^0$) represents an antiferroelectric insulator with an antiferroelectric transition temperature $T_c \simeq 1000$ K [105]. It shows complex dielectric properties and a large dielectric constant, see e.g. Ref. [74,178].

On the surface of Na-doped WO_3 crystals the presence of superconducting islands with $T_c \simeq 90$ K was reported by Reich et al. [177,178]. Other scientists like Shengelaya et al. confirmed the strong experimental evidence for high-T_c superconductivity without Cu in these Na−W−O samples [200]. Reich et al. suggested that the unknown superconducting phase is possible of a quasi-2D type because it exists on the surface of the Na-doped WO_3 crystals. However, to the best of our knowledge, the research on Na−W−O was finally stopped because, in spite of many efforts, the superconducting phase could not be identified. Neverthe-

less, this indicates the presence of a potential for high-T_c superconductivity in complex oxides which contain an electronically active element from the left side of the transition metal group such as W, Nb or Ti.

The unknown (and possible quasi-2D) superconducting phase reported by Reich et al. might be a compositional, structural and electronical modification of the antiferroelectric insulator WO_3 . Possibly, the unknown superconducting phase could be of the type $A_nB_nO_{3n+2}$, i.e. we speculate about the existence of conducting $A_nB_nO_{3n+2} = ABO_x$ compounds in the reduced Na−W−O system. Indeed, there is a good reason to suggest the existence of such compounds when we consider the systems $SmTiO_x$ (see section 5.1/$A_nB_nO_{3n+2}$ and pyrochlore) and $NaWO_x$ in the following way:

When prepared under high pressure, $SmTiO_{3.50}$ crystallizes in an $n = 4$ structure and represents a ferroelectric insulator (see Table 25). The structure of the other end member in the $SmTiO_x$ system, $SmTiO_3$, is of an orthorhombically distorted $n = \infty$ perovskite type. Normal pressure synthesis experiments of reduced intermediate compositions $SmTiO_x$ with $3 < x < 3.5$ led to an electrically conducting $n = 5$ phase $SmTiO_{3.37}$, whereas indications for the existence of an $n = 4.5$ compound with $x \simeq 3.44$ were not observed (see Table 41 and Figure 41).

Likewise, when prepared under high pressure, also the insulator $NaWO_{3.50}$ crystallizes in an $n = 4$ structure (see Table 18) and represents a potential ferroelectric. The structure of the other end member in the $NaWO_x$ system, $NaWO_3$, is of a cubic $n = \infty$ perovskite type. Therefore, analogous to $SmTiO_x$, we suggest to perform synthesis experiments of reduced intermediate compositions $NaWO_x$ with $3 < x < 3.5$, especially with respect to the search for mixed valence W^{6+}/W^{5+} ($5d^0/5d^1$) electrical conductors of the type $n = 4.5$, 5 or 6.

6 Results and discussion: Hexagonal $A_mB_{m-1}O_{3m}$

The compounds which were prepared in this work can be found among those listed in the Tables 53 − 60.

The starting point for this work on hexagonal $A_mB_{m-1}O_{3m}$ type materials was the mixed-valence $m = 7$ niobate $Sr_7Nb_6O_{21}$ reported by Schückel and Müller-Buschbaum [194], see Table 58. They synthesized $Sr_7Nb_6O_{21}$ crystals by a laser heating technique and determined the structure by single crystal XRD, see Figure 17. Physical properties were not reported. Because $Sr_7Nb_6O_{21}$ ($Nb^{4.67+}$ / $4d^{0.33}$) is potentially a good electrical conductor it seems worthwhile to study its resistivity and magnetic behavior. However, an attempt to prepare $Sr_7Nb_6O_{21}$ by floating zone melting resulted in a multiphase product consisting of $m = 7$, $m = 6$ and $m = 5 + 6$ type phases as well as of purple colored regions. Probably the purple phase is the Sr-deficient perovskite compound $Sr_{0.8}NbO_3$ which was already observed in $A_nB_nO_{3n+2}$ type Sr−Nb−O compositions with a nominal Nb valence of about $Nb^{4.8+}$ and less [127]. With decreasing temperature the magnetic moment of the multiphase $Sr_7Nb_6O_{21}$ composition showed a pronounced transition from paramagnetic to diamagnetic below $T \approx 130$ K.

Then it was attempted to synthesize single phase niobates of the type $m = 6$ and $m = 5 + 6$, i.e. $Sr_6Nb_5O_{18}$ ($Nb^{4.8+}$ / $4d^{0.2}$) and $Sr_{11}Nb_9O_{33}$ ($Nb^{4.89+}$ / $4d^{0.11}$), respectively. In contrast to $Sr_7Nb_6O_{21}$, the $m = 6$ and $m = 5 + 6$ type compositions were obtained as single phase compounds. The resulting niobates were somewhat overstoichiometric with respect to the oxygen content, namely $Sr_6Nb_5O_{18.07}$ and $Sr_{11}Nb_9O_{33.09}$. Possibly, the small amount of excess oxygen is accommodated in the interlayer region. Figure 72 displays the powder XRD spectra of $Sr_6Nb_5O_{18.07}$ ($m = 6$) and $Sr_{11}Nb_9O_{33.09}$ ($m = 5 + 6$) and also those of two structurally related insulators, namely $Sr_5Nb_4O_{15}$ ($m = 5$) and $LaSr_3Nb_3O_{12}$ ($m = 4$).

The molar magnetic susceptibility $\chi(T)$ of the diamagnetic insulator $Sr_5Nb_4O_{15}$ and the two conducting niobates $Sr_{11}Nb_9O_{33.09}$ and $Sr_6Nb_5O_{18.07}$ is presented in Figure 73. At low temperatures $\chi(T)$ increases with decreasing temperature. This is probably due to the Curie behavior of paramagnetic impurities. Table 70 presents the results of fitting $\chi(T)$ of some niobates to the function $D + C/T$ where D represents a diamagnetic, temperature-independent susceptibility and C/T the Curie term. The molar susceptibility without the Curie contribution, i.e. $\chi(\mathrm{T}) - C/T$, is displayed in Figure 74. For the two conducting niobates this representation reveals more clearly the intrinsic temperature dependence of the susceptibility which is relatively strong, especially for $Sr_6Nb_5O_{18.07}$. There is a transition from a paramagnetic into a diamagnetic state which starts at a temperature of $T \approx 150$ K. The transition is relatively slow with respect to its temperature range, but especially for $Sr_6Nb_5O_{18.07}$ it is fairly marked concerning the change of the susceptibility.

Figure 75 shows the resistivity $\rho(T)$ of the $m = 6$ niobate $Sr_6Nb_5O_{18.07}$ along the a- and c-axis. The resistivity anisotropy is relatively high, $\rho_c/\rho_a \approx 10^3$, at least in the high temperature range. Along the a-axis, i.e. along the layers or ab-planes, the high temperature behavior of the resistivity is metallic. With decreasing temperature a metal-to-semiconductor transition occurs at $T \approx 160$ K. This is the same temperature at which the magnetic susceptibility starts to decrease, see Figure 74. The transition from paramagnetic to diamagnetic in the susceptibility $\chi(T)$ is consistent with the metal-to-semiconductor transition in the resistivity $\rho_a(T)$. We assume that the paramagnetism reflects the presence of itinerant electrons. When the latter disappear due to the metal-to-semiconductor transition below $T \approx 160$ K, an exclusively diamagnetic contribution from closed electron shells may remain.

From the behavior of the resistivity $\rho(T)$ and the susceptibility $\chi(T)$ we conclude that the $m = 6$ niobate $Sr_6Nb_5O_{18.07}$ is a quasi-2D metal which displays a temperature-driven metal-to-semiconductor transition below $T \approx 160$ K. The qualitatively similar susceptibility behavior suggests the same conclusion for the $m = 5 + 6$ type $Sr_{11}Nb_9O_{33.09}$, although its resistivity was not measured.

The origin of the metal-to-semiconductor transition in $Sr_6Nb_5O_{18.07}$ is presently not known. One possibility is the existence of a Peierls instability. Although Peierls transitions are mainly associated with quasi-1D systems, there are also some quasi-2D materials in which Peierls instabilities occur. For references see

e.g. the theoretical paper on two-dimensional Peierls instabilities by Yuan [247] and the article by Greenblatt on molybdenum and tungsten bronzes [61]. Examples of quasi-2D metals which display a Peierls type phase transition are AMo_6O_{17} with A = Na, K or Tl and $(PO_2)_4(WO_3)_{2k}$ with $4 \leq k \leq 14$. However, their resistivity behavior is different from that of $Sr_6Nb_5O_{18.07}$. For the molybdates AMo_6O_{17} there is a metal-to-metal transition and a commensurate charge density wave below $T = 120$ K [67,245]. On the monophosphate tungsten bronzes $(PO_2)_4(WO_3)_{2k}$ resistivity measurements were performed for $k =$ 4, 6 and 7 [61]. Below $T = 200$ K and with decreasing temperature they display two metal-to-semiconductor-like transitions in the resistivity $\rho(T)$, but for temperatures below that of the second transition $\rho(T)$ is metallic again. We are not aware of an example of a quasi-2D metal that shows a (Peierls type) metal-to-semiconductor transition and remains semiconducting or insulating down to $T = 4$ K, and whose nominal charge carrier concentration is similar to that of $Sr_6Nb_5O_{18.07}$, i.e. about $d^{0.2}$ per transition metal ion. It should be mentioned that for such a relatively low charge carrier concentration the possibility of a transition into a magnetically ordered state is quite unlikely.

It is worthwhile to compare the properties of the quasi-2D metal $Sr_6Nb_5O_{18.07}$ ($m = 6$ of $A_mB_{m-1}O_{3m}$) with those of the quasi-1D metal $Sr_5Nb_5O_{17.04} = SrNbO_{3.41}$ ($n = 5$ of $A_nB_nO_{3n+2}$, see Table 32, 47 and 48). Both have in common practically the same nominal charge carrier concentration and along the c-axis their layers are $n = m - 1 = 5$ NbO_6 octahedra thick, see Figure 5, 6, 9, 10, 15 and 17. Their difference is given by the kind of orientation of the NbO_6 octahedra with respect to the c-axis. Figure 76 presents their magnetic susceptibility $\chi(T)$ without the Curie contribution C/T from paramagnetic impurities. Their resistivity $\rho(T)$ along the different crystallographic axes is displayed in Figure 77. It is obvious that the temperature dependences of $\chi(T)$and $\rho(T)$ and the metal-to-semiconductor transition is more pronounced for the $m = 6$ niobate $Sr_6Nb_5O_{18.07}$. For the $n = 5$ type $Sr_5Nb_5O_{17.04} = SrNbO_{3.41}$ and also for the $n = 4.5$ type $Sr_9Nb_9O_{31.05} = SrNbO_{3.45}$ the metal-to-semiconductor transition is discussed by Kuntscher et al. in terms of a Peierls type instability, but not all findings can be explained within this picture [111,113]. Analogous to the comparison between the $n = 5$ and $m = 6$ niobates we may also compare the magnetic susceptibility $\chi(T)$ of the ordered $n = 4.5$ and $m = 5 + 6$ intergrowth compounds $Sr_9Nb_9O_{31.05} = SrNbO_{3.45}$ and $Sr_{11}Nb_9O_{33.09}$, respectively. Their $\chi(T)$ without the Curie contribution C/T from paramagnetic impurities is plotted in Figure 78. Their $\chi(T)$ differs qualitatively in the same way as that of the $n = 5$ and $m = 6$ niobates shown in Figure 76.

There is one feature in the structural differences between the $n = 5$ niobate $Sr_5Nb_5O_{17.04}$ and the $m = 6$ niobate $Sr_6Nb_5O_{18.07}$ which is possibly relevant for their different electronic properties. In the $m = 6$ structure the continuous Nb−O intralayer linkage is exclusively realized via adjacent NbO_6 octahedra with a different c-axis height, i.e. there is no direct linkage at the same c-axis level (Fig. 10 and Table 2). Perhaps this corrugated linkage, when compared with the approximately linear Nb−O intralayer linkage in the $n = 5$ structure

(Fig. 6 and Table 2), implies a diminished overlap between the orbitals and may therefore lead to a reduced bandwidth. This could be the reason why the resistivity along the a-axis of the $m = 6$ type is about 10 times smaller than that of the $n = 5$ type, see Figure 77.

We speculate that the electronic properties of the $A_mB_{m-1}O_{3m}$ and $A_nB_nO_{3n+2}$ type niobates are related in a similar way to the layer thickness which is $m-1 = n$ NbO_6 octahedra thick along the c-axis. Compounds of the type $m = 5+6$, $m = 6$, $n = 4.5$ and $n = 5$ comprise layers which are 5 octahedra thick whereby their distortion is very small for those located in the center, see Fig. 15 and 17. For the Sr-based niobates $Sr_nNb_nO_{3n+2} = SrNbO_x$ there are particular differences in the electronic properties between the type $n = 4.5$ and 5 and the type $n = 4$ [110,111,113,127], see Table 47 and 48. For the $n = 4$ type $Sr_{0.8}La_{0.2}NbO_{3.50}$, compared to related $n = 4.5$ and $n = 5$ niobates, the metallic character is relatively weak and at low temperatures, i.e. below that temperature where the metal-to-semiconductor transition in the resistivity occurs, no energy gap was observed in optical spectroscopy. This leads to the question if there are similar differences in the electronic properties between niobates of the type $m = 6$ and $5 + 6$ and the type $m = 5$. Therefore we attempted to prepare $m = 5$ niobates $(Sr,La)_5Nb_4O_{15}$ which are electrical conducting. Two compositions were synthesized, $Sr_{4.6}La_{0.4}Nb_4O_{15.05}$ ($Nb^{4.93+}$ / $4d^{0.07}$) and $Sr_{4.2}La_{0.8}Nb_4O_{15.00}$ ($Nb^{4.8+}$ / $4d^{0.20}$). The first was obtained as a single phase material and its magnetic susceptibility $\chi(T)$ is shown in Figure 73. The second represents the preferred composition because its nominal charge carrier concentration of $4d^{0.20}$ is comparable to that of the $m = 6$ niobate $Sr_6Nb_5O_{18.07}$. It turned out, however, that $Sr_{4.2}La_{0.8}Nb_4O_{15.00}$ was not single phase, although it consisted mainly of the type $m = 5$. Its powder XRD pattern suggested the presence of another phase(s) and/or the existence of a superstructure. A magnetic measurement revealed that its magnetic moment has qualitatively the same temperature dependence as $\chi(T)$ of the single phase sample $Sr_{4.6}La_{0.4}Nb_4O_{15.05}$ which is presented in Figure 73. This temperature dependence is quite different from that of the $m = 5 + 6$ and $m = 6$ niobates, see Figure 73. This may indicate an essential difference in the electronic properties between niobates of the type $m = 6$ and $5+6$ and the type $m = 5$.

To get further insight into the electronic properties of the $A_mB_{m-1}O_{3m}$ niobates we suggest to perform band structure calculations on the $m = 6$ material $Sr_6Nb_4TiO_{18}$ and the $m = 7$ niobate $Sr_7Nb_6O_{21}$. For both compounds the space group and the atomic coordinates were determined by single crystal XRD by Drews et al. [40] and by Schückel and Müller-Buschbaum [194], respectively, see also Fig. 17 and Table 56 and 58. Although the $m = 6$ type $Sr_6Nb_4TiO_{18}$ represents a fully oxidized compound and therefore an insulator, it is most probably isostructural to the quasi-2D metal $Sr_6Nb_5O_{18.07}$. Therefore we assume that for band structure calculations on the $m = 6$ electrical conductor $Sr_6Nb_5O_{18}$ the space group and atomic coordinates from the isostructural insulator $Sr_6Nb_4TiO_{18}$ can be used. In this context we notice that $Sr_6Nb_4TiO_{18}$ is one of only two compounds, among all $A_mB_{m-1}O_{3m}$ materials listed in the

Tables 51 − 60, for which the reported space group is non-centrosymmetric, see Table 56. Therefore it represents a potential ferroelectric. The second of these two compounds is also of the type $m = 6$, namely $La_6Ti_{4.04}Mg_{0.913}O_{18}$, see Table 57. However, only for $Sr_6Nb_4TiO_{18}$ the space group was determined by single crystal XRD.

7 Summary

This work represents the continuation of an article on $A_nB_nO_{3n+2} = ABO_x$ compounds, published in 2001 in this journal [127], and reports also on $A'A_{k-1}B_kO_{3k+1}$ and hexagonal $A_mB_{m-1}O_{3m}$ materials. An overview on the title oxides and their properties has been presented, referring to literature and results from this work.

The three homologous series $A_nB_nO_{3n+2}$, $A'A_{k-1}B_kO_{3k+1}$ and hexagonal $A_mB_{m-1}O_{3m}$ have a layered, perovskite-related structure. Along the c-axis the layers are $n = k = m - 1$ BO_6 octahedra thick and for $n = k = m - 1 = \infty$ the three-dimensional perovskite structure ABO_3 is realized. The three series differ structurally in the orientation of the BO_6 octahedra with respect to the c-axis. For $A_nB_nO_{3n+2}$ and $A_mB_{m-1}O_{3m}$ this results in a relatively complex crystal structure. The $A_nB_nO_{3n+2}$ oxides contain, in addition to their quasi-2D (layered) character, a quasi-1D structural feature which is constituted by chains of corner-shared BO_6 octahedra along the a-axis. Associated with $A_mB_{m-1}O_{3m}$ and $A_nB_nO_{3n+2} = ABO_x$ there are compounds whose unit cells contain an ordered stacking sequence of layers with different thickness, e.g. the $m = 4 + 5$ titanate $La_9Ti_7O_{27}$ and the non-integral $n = 4.5$ series member $SrNbO_{3.44}$, respectively. The majority of the $A_nB_nO_{3n+2}$, $A'A_{k-1}B_kO_{3k+1}$ and $A_mB_{m-1}O_{3m}$ materials have the following in common: The distortion of the BO_6 octahedra is largest at the boundary of the layers and smallest in the center of the layers. Furthermore, if there are at the A or B site two different cations which differ in their valence, then those with the larger (smaller) valence tend to accumulate in the boundary (inner) region of the layers.

Within this work about 250 samples with different composition were prepared by floating zone melting. Approximately half of them resulted in single phase products.

7.1 $A_nB_nO_{3n+2} = ABO_x$

The titanates and niobates of the type $A_nB_nO_{3n+2} = ABO_x$ comprise the highest-T_c ferroelectrics such as the $n = 4$ titanate $LaTiO_{3.50}$ [150] and were mainly known as insulators. In the previous article [127] many $A_nB_nO_{3n+2} = ABO_x$ niobates and titanates with a reduced composition were reported [127]. Some of these electrical conductors, e.g. the $n = 5$ niobate $SrNbO_{3.41}$, are quasi-1D metals [110–113,127,136,244] which are in compositional, structural and electronical proximity to non-conducting (anti)ferroelectrics. This suggests the possibility to realize materials with an intrinsic coexistence of metallic conductivity (along the a-axis) and high dielectric polarizability (perpendicular to

the a-axis). This hypothesis is meanwhile substantiated for some niobates by the results from two different experimental studies. First, the comprehensive optical measurements by Kuntscher et al. [113] revealed the presence of the ferroelectric soft mode not only in the $n = 4$ ferroelectric insulator $SrNbO_{3.50}$ but also in the quasi-1D metals $SrNbO_{3.41}$ ($n = 5$) and $SrNbO_{3.45}$ ($n = 4.5$) and in the weakly pronounced quasi-1D metal $Sr_{0.8}La_{0.2}NbO_{3.50}$ ($n = 4$). Secondly, the dielectric measurements by Bobnar et al. [17] on the $n = 5$ quasi-1D metal $SrNbO_{3.41}$ revealed a rather large value of the intrinsic, high-frequency dielectric constant along the c-axis, namely $\varepsilon_{c\,\infty} \approx 100$.

The results from this work can be summarized as follows:

In the compositional parameter space there are regions where the pyrochlore and $A_nB_nO_{3n+2}$ structure are close together. Several samples with such compositions were prepared. In the $SmTiO_x$ system the $x = 3.5$ and $x = 3$ end members display a pyrochlore and perovskite structure, respectively. Nevertheless, an $n = 5$ titanate with the intermediate composition $SmTiO_{3.37}$ could be prepared. Therefore $SmTiO_x$ represents a further example of only few systems where an intermediate composition adopts an $A_nB_nO_{3n+2}$ structure although both end members are not of that type. Some $GdTiO_x$ and $YbTiO_x$ samples with $x < 3.50$ were also synthesized but indications for the presence of $A_nB_nO_{3n+2}$ phases were not detected.

In the previous article [127] some significantly non-stoichiometric compounds were published. In this work many further significantly non-stoichiometric materials, which appear single phase within the detection limit of powder XRD, were prepared. They are of the type ABO_{w-y} , $A_{1-\sigma}BO_{w-y}$ and $AB_{1-\sigma}O_{w-y}$ whereby $0 < y \leq 0.19$ is the oxygen deficiency with respect to the ideal oxygen content w and $0 < \sigma \leq 0.05$ the cation deficiency with respect to the full occupation of the A or B site. The largest degree of non-stoichiometry was achieved in the $n = 5$ titanates $La_{0.75}Ca_{0.2}TiO_{3.21}$ and $La_{0.75}Ba_{0.2}TiO_{3.21}$. Their formula $A_{0.95}BO_{3.21}$ has to be compared with the ideal $n = 5$ composition $ABO_{3.40}$. Because the synthesis of $La_{0.75}Ca_{0.2}TiO_{3.21}$ and $La_{0.75}Ba_{0.2}TiO_{3.21}$ did not lead to pronounced and appropriate crystals, their resistivity was not measured. Therefore it remains an open question if their physical properties differ markedly from those of the related nearly stoichiometric $n = 5$ quasi-1D metal $LaTiO_{3.41}$. In this context we cited the interesting structure of the niobate $Sr_5Nb_5O_{16} = SrNbO_{3.2}$ reported by Schückel and Müller-Buschbaum [193]. Its structure was not discussed in terms of $A_nB_nO_{3n+2}$, however it can be viewed as an oxygen-deficient $n = 5$ type, i.e. $Sr_5Nb_5O_{17-\Delta} = SrNbO_{3.4-\delta}$ with $\Delta = 1$ and $\delta = 0.2$. The oxygen vacancies in $SrNbO_{3.2}$ are located in one of the both boundary regions of the layers. They are fully ordered in such a way that one boundary consists of NbO_4 polyhedra (instead of NbO_6 octahedra) without Nb−O chains along the a-axis. Physical properties of $SrNbO_{3.2}$ were not reported in Ref. [193] and the attempt in this work to prepare $SrNbO_{3.20}$ by floating zone melting resulted in a multiphase product. Therefore its attributes such as the resistivity $\rho(T)$ and magnetic susceptibility $\chi(T)$ are presently not known. However, they are of particular interest, especially with respect to the related nearly stoichiomet-

ric $n = 5$ quasi-1D metal $SrNbO_{3.41}$. To get further insight into the electronic properties of $Sr_5Nb_5O_{16} = SrNbO_{3.2}$ we suggest to perform band structure calculations by using the space group and atomic coordinates reported by Schückel and Müller-Buschbaum [193].

An interesting structural feature is the possibility of a full occupational order at the B site. Presently only few of such examples are known. It is reported by Titov et al. that the Fe^{3+} ions in the $n = 5$ insulator $LaTi_{0.8}Fe_{0.2}O_{3.40}$ are exclusively located in the central octahedra of layers, whereas in the isostructural $LaTi_{0.8}Ga_{0.2}O_{3.40}$ the Ga^{3+} ions are distributed within the three inner sheets of BO_6 octahedra of the five octahedra thick layers [227,228]. In this work several $n = 5$ compounds of the type $LnTi_{0.8}B'_{0.2}O_x$ with $B' = Al^{3+}$, V^{3+}, Mn^{3+} and Fe^{3+} were prepared. Theoretically, a full occupational order is also possible in $n = 6$ materials such as $LaTi_{0.67}B'_{0.33}O_{3.33}$ where the B' cations are exclusively located in the both inner octahedra sheets of the six BO_6 octahedra thick layers. The attempts to prepare such compounds resulted readily in the $n = 6$ insulator $LaTi_{0.67}Fe_{0.33}O_{3.33}$, whereas for $B' = Mn^{3+}$ an oxygen-deficient $n = 5$ type was obtained. Detailed structural studies are necessary to determine the actual distribution of the B' cations at the B site.

For B' cations such as Fe^{3+} the magnetic properties of corresponding compounds are of special interest. There are two reasons for that. First, they might have the potential to show (anti)ferromagnetic order. As an illustration we cite the sequence $LaTi_{0.8}Fe_{0.2}O_{3.40}$ ($n = 5$), $LaTi_{0.67}Fe_{0.33}O_{3.33}$ ($n = 6$) and $LaFeO_3$ ($n = \infty$) whereby the latter is known as a canted antiferromagnet with weak ferromagnetic properties. Secondly, several $A_nB_nO_{3n+2} = ABO_x$ type insulators are known as (anti)ferroelectrics and thus, if (anti)ferromagnetic order can be realized, a coupling between dielectric and magnetic properties is conceivable. Therefore the magnetic susceptibility $\chi(T)$ of the $n = 5$ and $n = 6$ insulator $LaTi_{0.8}Fe_{0.2}O_{3.40}$ and $LaTi_{0.67}Fe_{0.33}O_{3.33}$ was inspected. For the $n = 5$ compound a Curie-Weiss behavior was observed, where the $\chi(T)$ curve indicates a crossover from $\theta = -69$ K to $\theta = +35$ K at $T \approx 300$ K. The $n = 6$ material, however, shows a complex behavior which suggests a weakly pronounced magnetic order below 280 K or, compared to the $n = 5$ compound, at least an enhanced magnetic interaction between the Fe^{3+} ions. This observation supports the assumption that in both materials the Fe^{3+} ions are exclusively located in the inner BO_6 octahedra of the layers where they form Fe−O chains along the a-axis. For the $n = 5$ compound this implies a direct Fe−O linkage only along the a-axis. In the $n = 6$ material, however, there is an additional zigzag-shaped Fe−O linkage along the b-direction which may lead to an enhanced superexchange interaction. Of course, the actual distribution of the Fe^{3+} ions has to be determined by detailed structural studies. Nevertheless, in our opinion the current results indicate that compounds of the type $n = 6$, and possibly also $n = 7$, with transition metal ions such as Fe^{3+} at the B site have the potential for (anti)ferromagnetic order and might show a coupling between magnetic and dielectric properties.

On all materials synthesized in this work the magnetic susceptibility $\chi(T)$ was measured. Indications for the presence of magnetic order were not detected, apart from one possible exception which is given by the $n = 6$ insulator $LaTi_{0.67}Fe_{0.33}O_{3.33}$. The majority of the compounds display a Curie-Weiss behavior. In the case of rare earth ions at the A site the Curie-Weiss temperatures θ vary from approximately -160 K for the $n = 5$ type $La_{0.76}Ce_{0.12}Yb_{0.12}TiO_{3.4}$ to about 0 K for Eu^{2+} niobates. The largest values of $|\theta|$ were realized for compounds containing Ce^{3+} and/or Yb^{3+} which poses the question why this occurs especially for these rare earth ions. Comparing the $n = 4.33$ titanate $CeTiO_{3.47}$ and the $n = 5$ titanate $NdTiO_{3.42}$ with isostructural but significantly non-stoichiometric $Ce_{0.95}TiO_{3.39}$ and $Nd_{0.95}TiO_{3.34}$, respectively, it was found that the $|\theta|$ of the latter is approximately twice as high. For $n = 5$ titanates $NdTiO_x$ the Curie-Weiss temperatures of the nearly stoichiometric $x = 3.42$ compound and the significantly non-stoichiometric $x = 3.31$ material are nearly equal. This suggests that the doubling of $|\theta|$ is more related to the deficiency at the A site than to the oxygen deficiency. We do not know the physical origin of this interesting phenomenon. Maybe it is of general relevance in the field of magnetism. For example, it gives occasion to speculate if a cation deficiency in (anti)ferromagnetic materials may lead to an enhancement of the magnetic transition temperature. Further studies are necessary to clarify this issue.

In the case of transition metal ions at the B site the Curie-Weiss temperatures θ vary from approximately $+70$ K for the $n = 5$ compound $LaTi_{0.8}Mn_{0.2}O_{3.4}$ (Mn^{3+}, $3d^4$) to about -900 K for the significantly non-stoichiometric $n = 5$ type $LaTi_{0.8}Al_{0.2}O_{3.31}$ ($Ti^{3.8+}$, $3d^{0.2}$). The latter is one example of some materials which display a rather high value of $|\theta|$ although only circa 20 % of the B sites are occupied with localized paramagnetic moments. Further such examples are the $n = 5$ type $LaTi_{0.95}V_{0.05}O_{3.41}$ ($3d^{0.23}$, $(Ti,V)^{3.77+}$) and the significantly non-stoichiometric $n = 4$ type $La_{0.6}Ca_{0.4}Ti_{0.6}Nb_{0.4}O_{3.40}$ ($d^{0.2}$, $(Ti,Nb)^{4.6+}$) with $\theta = -390$ K and -530 K, respectively. Possibly, one of the reasons for these surprisingly high values of $|\theta|$ is the low dimensionality of the crystal structure and/or a partial order of B cations with different valences. Among the compounds investigated in this work, a clearly positive Curie-Weiss temperature, which indicates a ferromagnetic interaction, was found only for those with Mn^{3+} ($3d^4$) at the B site.

The electrical conducting $n = 5$ rare earth titanates $LnTiO_{3.4}$ with Ln = La, Ce, Pr, Nd and Sm and some of the corresponding $n = 5$ insulators $LnTi_{0.8}Al_{0.2}O_{3.40}$ were inspected in detail, especially for Ln = Pr. Resistivity measurements on crystals of the $n = 5$ titanate $PrTiO_{3.41}$ revealed a quasi-1D metallic behavior similar to that of the $n = 5$ quasi-1D metal $LaTiO_{3.41}$. A comparison between the resistivity $\rho(T)$ of $PrTiO_{3.41}$ and $LaTiO_{3.41}$ does not reveal an obvious feature which can be related to the presence of localized paramagnetic moments from the Pr^{3+} ions. However, the existence of an interaction between the localized paramagnetic moments and the conduction electrons becomes visible in the magnetic susceptibility $\chi(T)$. It was found that the Curie-Weiss type susceptibility of the quasi-1D metal $PrTiO_{3.41}$ is lower than that of the corre-

sponding insulator $PrTi_{0.8}Al_{0.2}O_{3.40}$. Using an empirical approach it turned out that the experimentally determined susceptibility

$\chi_1(T) = C_1/(T - \theta_1)$ of the quasi-1D metal $PrTiO_{3.41}$

can be described well by a certain modification of the corresponding susceptibility

$\chi_2(T) = C_2/(T - \theta_2)$ of the insulator $PrTi_{0.8}Al_{0.2}O_{3.40}$.

This was achieved by replacing $T - \theta_2$ by $T - \theta_2 + f\,\chi_3(T)$ where f is a parameter and $\chi_3(T)$ the susceptibility of the quasi-1D metal $LaTiO_{3.41}$ which has no paramagnetic moments at the A site, i.e.

$$\chi_2(T) = C_2/(T - \theta_2) \quad \longrightarrow \quad C_2/(T - \theta_2 + f\,\chi_3(T)\,) \;\equiv\; C_1/(T - \theta_1) = \chi_1(T)$$

In this sense the alteration from C_2 and θ_2 into C_1 and θ_1 can be viewed as a renormalization via the conduction electrons which was taken into account by the experimentally determined function $\chi_3(T)$.

Finally, we have considered the $A_nB_nO_{3n+2}$ quasi-1D metals from the perspective of the hypothetical excitonic type of superconductivity. They appear as interesting materials with respect to two different approaches to realize this type of superconductivity, namely that proposed by Little for quasi-1D conductors [129–132] as well as that devised by Ginzburg for quasi-2D systems [58]. Therefore, in our opinion, the quasi-1D metals represent potential candidates for new (high-T_c)superconductors.

We have also considered the system Na−W−O. As reported by Reich et al. there are strong indications for high-T_c superconducting islands with unknown composition on the surface of Na-doped WO_3 crystals [177,178]. Thus, the reduced Na−W−O system represents an interesting field of research. This raises also the question for the existence of conducting $A_nB_nO_{3n+2}$ phases in this system. Encouraged by the similarities of the structure type versus x relationship in known $SmTiO_x$ and $NaWO_x$ materials, we have suggested to perform synthesis experiments of reduced $NaWO_x$ compositions with $3 < x < 3.5$, especially with respect to the search for electrical conductors of the type $n = 4.5$, 5 or 6.

7.2 Dion-Jacobson type phases $A'A_{k-1}B_kO_{3k+1}$ without alkali metals

The Dion-Jacobson type phases $A'A_{k-1}B_kO_{3k+1}$ are usually known as oxides which contain an alkali metal at the A' site. However, also the rare earth titanates $BaLn_2Ti_3O_{10}$ with Ln = La, Pr, Nd, Sm or Eu display an $k = 3$ structure, although in the literature they are not classified as Dion-Jacobson compounds. Furthermore, an $k = 2$ tantalate without any alkali metal, $BaSrTa_2O_7$, was recently published by Le Berre et al. [118]. The majority of the Dion-Jacobson phases reported in the literature are fully oxidized insulators and many of them

are able to intercalate ions or molecules in the interlayer region. Some $k = 3$ niobates are ferroelastic, e.g. $KCa_2Nb_3O_{10}$ with $T_c = 1000$ °C as reported by Dion et al. [38]. Among the materials with known space group there is only one which is non-centrosymmetric, namely the $k = 3$ niobate $KSr_2Nb_3O_{10}$ reported by Fang et al. [49]. Thus it has possibly ferroelectric properties. Among the published compounds there are also some with a reduced composition. They are (semi)conductors and a few of them are metals and even superconductors. As reported by Takano et al. on polycrystalline samples, the Li-intercalated $k = 2$ and $k = 3$ niobate $Li_xKLaNb_2O_7$ and $Li_yKCa_2Nb_3O_{10}$ shows a metallic resistivity behavior and a superconducting transition at $T \simeq 1$ K, respectively [214,215].

In this work the Ba−(Ca,La)−Nb−O system with reduced compositions was investigated. This lead to Dion-Jacobson type phases $A'A_{k-1}B_kO_{3k+1}$ without alkali metals such as the $k = 2$ niobate $BaCa_{0.6}La_{0.4}Nb_2O_{7.00}$ and the $k = 3$ niobate $BaCa_2Nb_3O_{10.07}$. Their resistivity $\rho(T)$ was measured on crystals along the *a*-, *b*- and *c*-axis which revealed an anisotropic 3D metallic behavior. All as-grown crystalline $A'A_{k-1}B_kO_{3k+1}$ samples were inspected by magnetic measurements down to the lowest accessible temperature of 2 K. Indications for the presence of superconductivity were not found. Furthermore, the $k = 2$ insulator $BaCaTa_2O_7$ was synthesized which represents the Ca analogue to $BaSrTa_2O_7$.

7.3 Hexagonal $A_mB_{m-1}O_{3m}$

Most $A_mB_{m-1}O_{3m}$ compounds reported in the literature are insulators. Among the materials whose space group is known there are only two which are non-centrosymmetric, namely the $m = 6$ types $Sr_6Nb_4TiO_{18}$ and $La_6Ti_{4.04}Mg_{0.913}O_{18}$ reported by Drews et al. [40] and Vanderah et al. [240], respectively. Thus they represent potential ferroelectrics. Among those compounds with a reduced composition only few were investigated by magnetic and resistivity measurements. A semiconducting resistivity behavior on polycrystalline samples is reported for the $m = 3$ compounds $Ba_3Re_2O_9$ and $Sr_3Re_2O_9$ by Chamberland and Hubbard [31] and the oxygen-deficient $m = 5$ niobate $Ba_5Nb_4O_{15-y}$ by Pagola et al. [168].

The starting point to work on $A_mB_{m-1}O_{3m}$ materials was the $m = 7$ niobate $Sr_7Nb_6O_{21}$ published by Schückel and Müller-Buschbaum [194]. They synthesized crystals and determined its structure. Physical properties were not reported. Because $Sr_7Nb_6O_{21}$ represents potentially a good electrical conductor it was attempted to prepare it by floating zone melting. This, however, resulted in a multiphase product. Further synthesis experiments in the reduced Sr−Nb−O system lead to single phase samples $Sr_{11}Nb_9O_{33.09}$ ($m = 5+6$) and $Sr_6Nb_5O_{18.07}$ ($m = 6$). On crystals of the latter resistivity measurements were performed.

The resistivity $\rho(T)$ along the *a*- and *c*-axis and the magnetic susceptibility $\chi(T)$ revealed that the $m = 6$ niobate $Sr_6Nb_5O_{18.07}$ represents a quasi-2D metal which displays a temperature-driven metal-to-semiconductor transition at about 160 K. With decreasing temperature the susceptibility $\chi(T)$ below 160 K shows a sluggish but nevertheless pronounced transition from paramagnetic to diamagnetic. The qualitatively similar behavior of $\chi(T)$ suggests the same conclusion

for the $m = 5 + 6$ niobate $Sr_{11}Nb_9O_{33.09}$, although its resistivity was not measured. The origin of the temperature-driven metal-to-semiconductor transition is presently not known, possibly it represents a 2D Peierls transition.

Compared to the $n = 5$ quasi-1D metal $Sr_5Nb_5O_{17.04} = SrNbO_{3.41}$, the temperature dependence of $\rho(T)$ and $\chi(T)$ of the $m = 6$ quasi-2D metal $Sr_6Nb_5O_{18.07}$ is rather strong in the range of the metal-to-semiconductor transition. This comparison is interesting because these both niobates have a nearly equal nominal number of 4d electrons per Nb, $4d^{0.18}$ and $4d^{0.17}$, and their layers are $n = m - 1 = 5$ NbO_6 octahedra thick. However, they differ structurally in the orientation of the NbO_6 octahedra with respect to the c-axis.

8 Acknowledgement

We acknowledge fruitful collaboration with C. A. Kuntscher, S. Schuppler, P. Daniels, J. Guevarra, A. Schönleber, S. van Smaalen, S. Frank, K. Thirunavukkuarasu, I. Loa, K. Syassen and S. Ebbinghaus. We are grateful to J. Mannhart for his support and for critically reading the manuscript. We thank T. Kopp and P. Lunkenheimer for valuable discussions and G. Hammerl for his help concerning LaTeX. This work was supported by the BMBF (project number 13N6918).

9 Figures and Tables

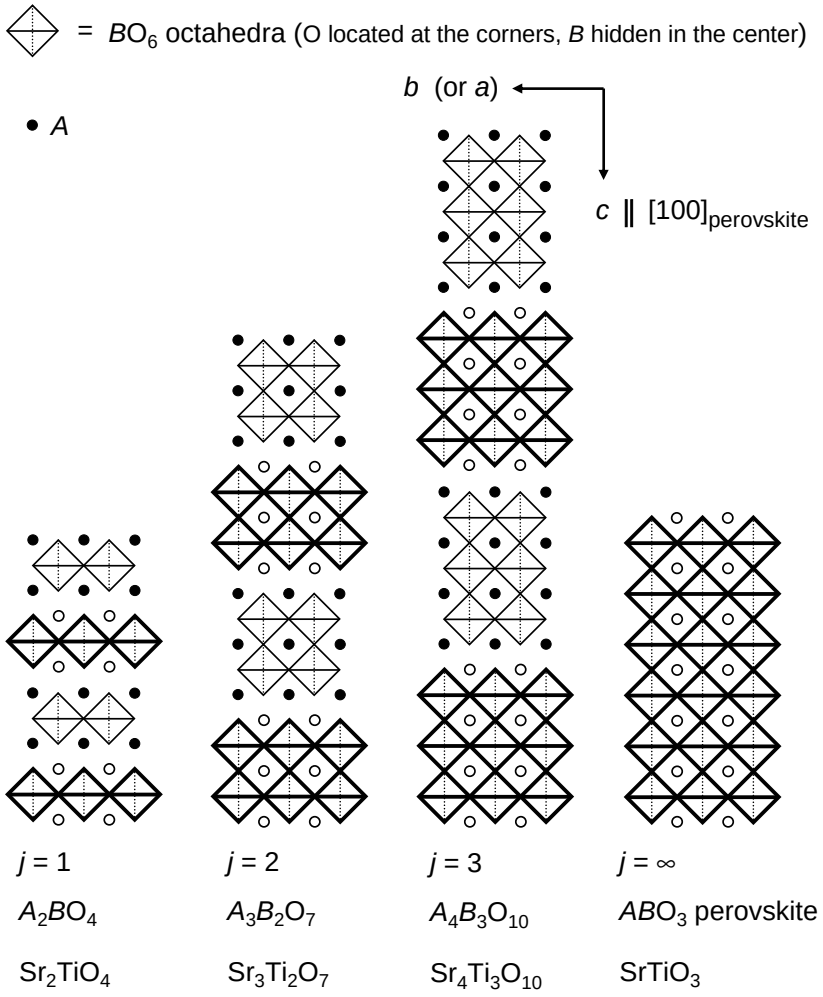

Fig. 1. Sketch of the idealized crystal structure of the $j = 1, 2, 3$ and ∞ members of the perovskite-related layered homologous series $A_{j+1}B_jO_{3j+1}$ (Ruddlesden-Popper phases) projected along the a- (or b-) axis. The layers along the ab-plane are formed by corner-shared BO_6 octahedra. Along the c-axis the layers are j BO_6 octahedra thick. Light and heavy drawing of the BO_6 octahedra as well as filled and open circles indicates a height difference perpendicular to the drawing plane of about 2 Å, the $B-O$ bond length and the half of the octahedron body diagonal. The compositional examples from the Sr−Ti−O system are Ti^{4+} ($3d^0$) insulators.

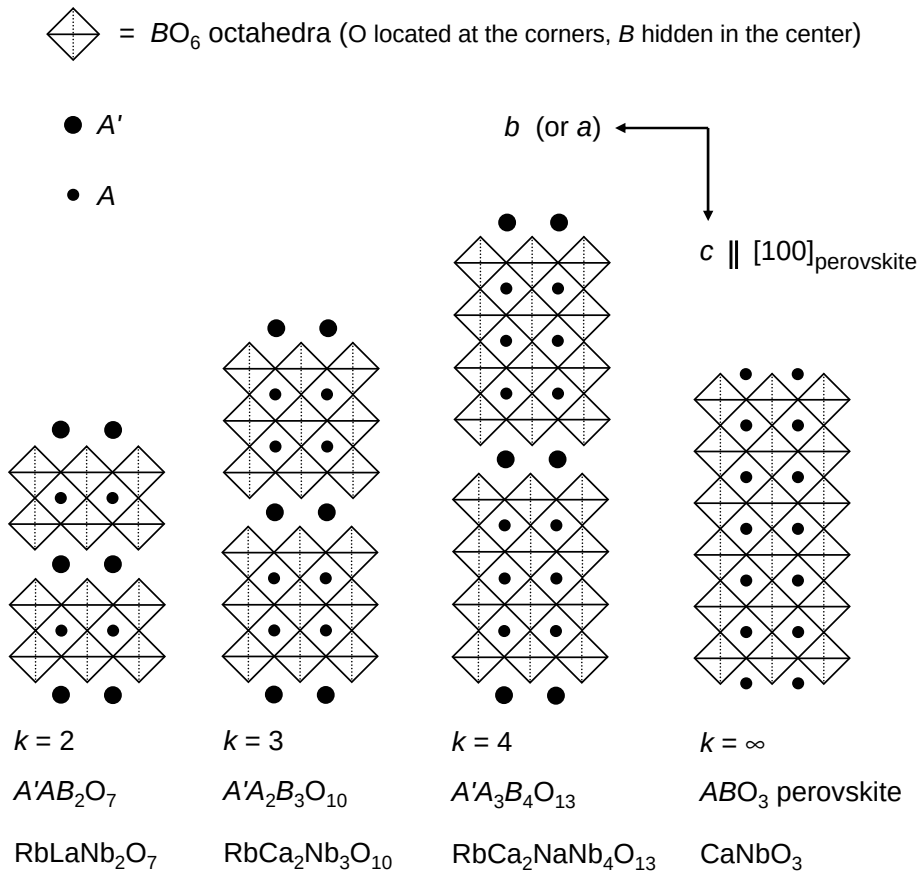

Fig. 2. Sketch of the idealized type I crystal structure of the $k = 2, 3, 4$ and ∞ members of the perovskite-related layered homologous series $A'A_{k-1}B_kO_{3k+1}$ (Dion-Jacobson phases) projected along the a- (or b-) axis. The layers along the ab-plane are formed by corner-shared BO_6 octahedra. Along the c-axis the layers are k BO_6 octahedra thick. Perpendicular to the drawing plane there is a height difference between the BO_6 octahedra and the A cations of about 2 Å, the $B-O$ bond length and the half of the octahedron body diagonal. Compositional examples are taken from the Rb−(Na,Ca,La)−Nb−O system. The type I structure is realized for very large A' cations like Rb^+ or Cs^+.

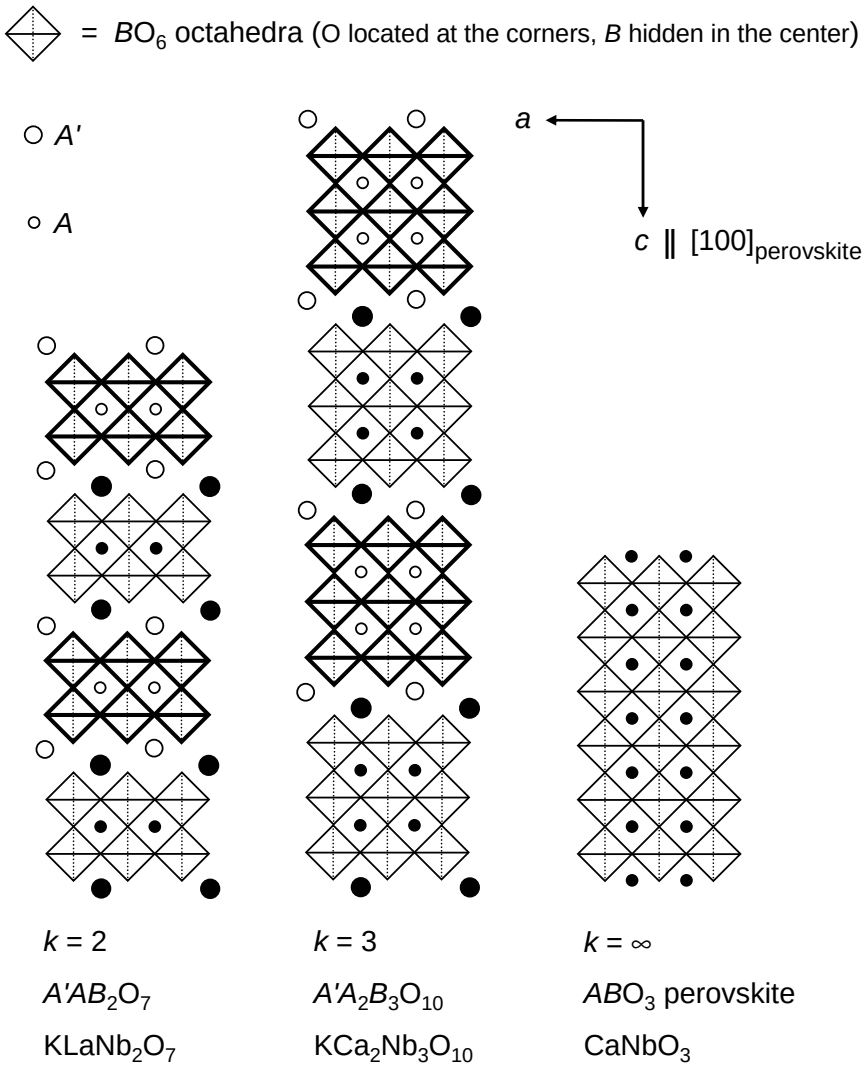

Fig. 3. Sketch of the idealized type II crystal structure of the $k = 2, 3$ and ∞ members of the perovskite-related layered homologous series $A'A_{k-1}B_kO_{3k+1}$ (Dion-Jacobson phases) projected along the b-axis. The layers along the ab-plane are formed by corner-shared BO_6 octahedra. Along the c-axis the layers are k BO_6 octahedra thick. Light and heavy drawing of the BO_6 octahedra as well as filled and open circles indicates a height difference perpendicular to the drawing plane of about 2 Å, the $B-O$ bond length and the half of the octahedron body diagonal. Compositional examples are taken from the K−(Ca,La)−Nb−O system. The type II structure is realized for large A' cations like K^+ or Ba^{2+}.

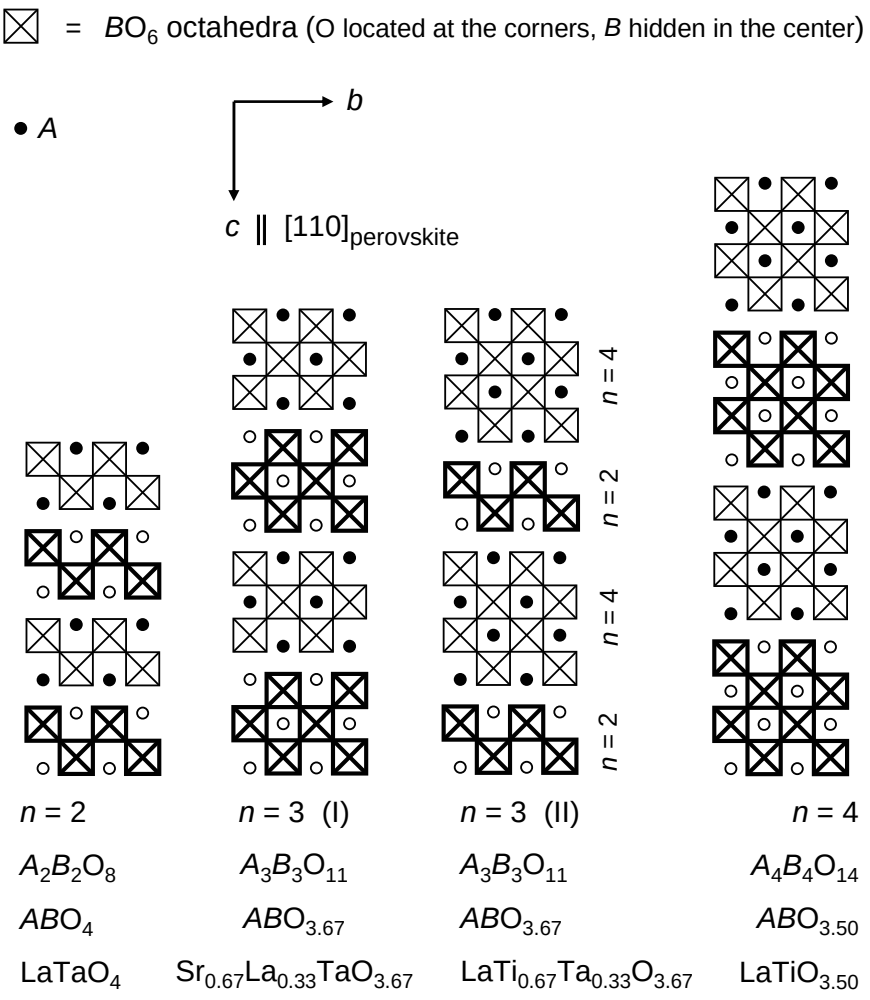

Fig. 4. Sketch of the idealized crystal structure of the $n = 2, 3$ and 4 members of the perovskite-related layered homologous series $A_nB_nO_{3n+2} = ABO_x$ projected along the a-axis. In the formula ABO_x the ideal oxygen content $x = 3 + 2/n$ is specified. Within the layers the corner-shared BO_6 octahedra extend zigzag-like along the b-direction and chain-like along the a-axis, see Figure 6. Along the c-axis the layers are n BO_6 octahedra thick. The $n = 3$ (II) member represents the ordered stacking sequence $n = 2, 4, 2, 4, ...$ Light and heavy drawing of the BO_6 octahedra as well as filled and open circles indicates a height difference perpendicular to the drawing plane of about 2 Å, the $B-O$ bond length and the half of the octahedron body diagonal. The compositional examples from the (La,Sr)−(Ta,Ti)−O system are Ta^{5+} ($5d^0$) / Ti^{4+} ($3d^0$) insulators which are, apart from the $n = 3$ (I) compound, ferroelectric.

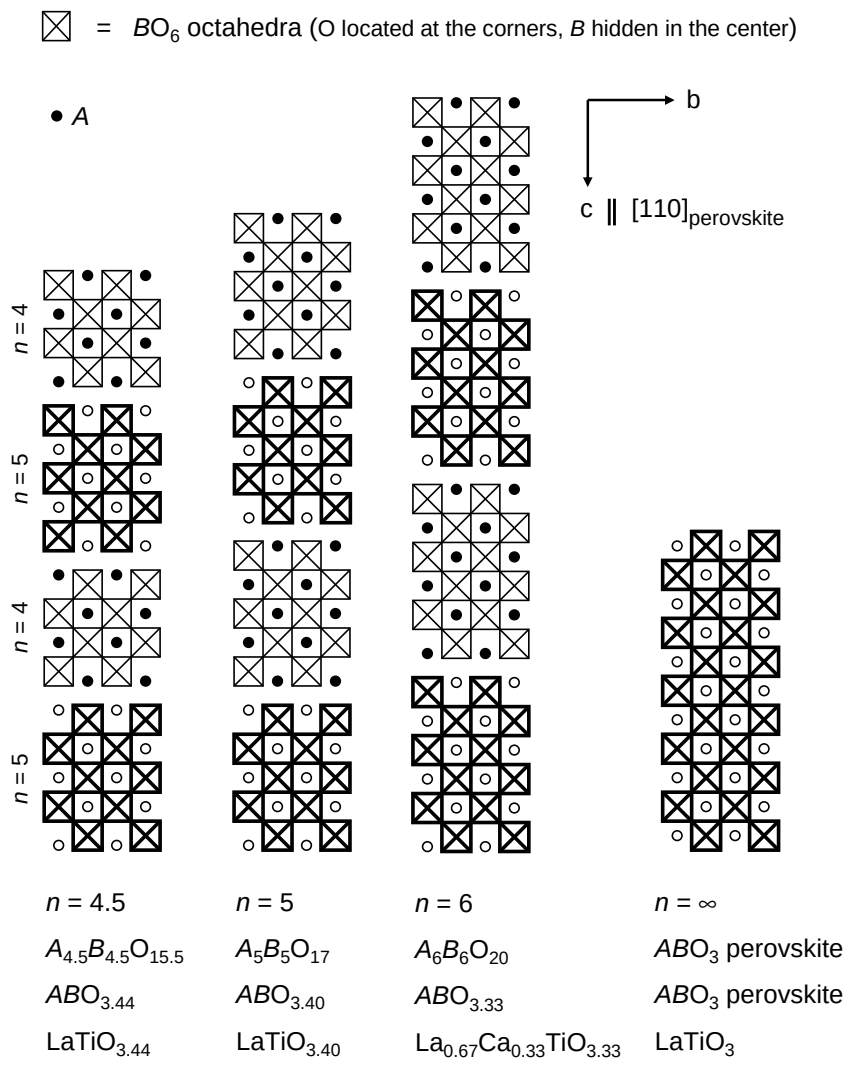

Fig. 5. Sketch of the idealized crystal structure of the $n = 4.5, 5, 6$ and ∞ members of the perovskite-related layered homologous series $A_nB_nO_{3n+2} = ABO_x$ projected along the a-axis. In the formula ABO_x the ideal oxygen content $x = 3 + 2/n$ is specified. Within the layers the corner-shared BO_6 octahedra extend zigzag-like along the b-direction and chain-like along the a-axis, see Figure 6. Along the c-axis the layers are n BO_6 octahedra thick. The $n = 4.5$ member represents the ordered stacking sequence $n = 5, 4, 5, 4, ...$ Light and heavy drawing of the BO_6 octahedra as well as filled and open circles indicates a height difference perpendicular to the drawing plane of about 2 Å, the $B-O$ bond length and the half of the octahedron body diagonal. Compositional examples are taken from the (La,Ca)−Ti−O system.

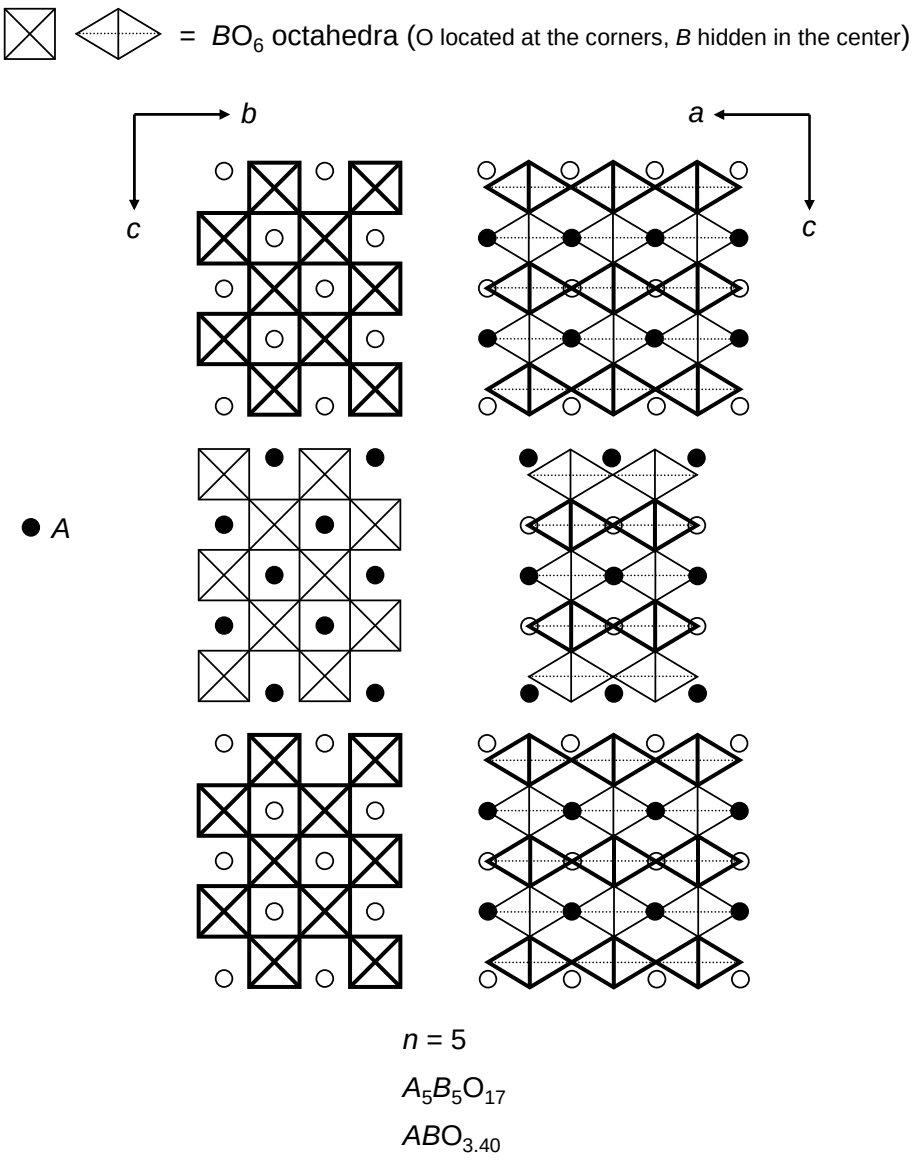

Fig. 6. Sketch of the idealized crystal structure of the perovskite-related layered homologous series $A_nB_nO_{3n+2} = ABO_x$ projected along the a- and b-axis using the $n = 5$ member as a representative example. In contrast to Fig. 4 and 5 the projection along the b-axis clearly shows the chain-like array of the corner-shared BO_6 octahedra along the a-axis. Light and heavy drawing of the BO_6 octahedra as well as filled and open circles indicates a height difference perpendicular to the drawing plane of about 2 Å, the $B - O$ bond length and the half of the octahedron body diagonal.

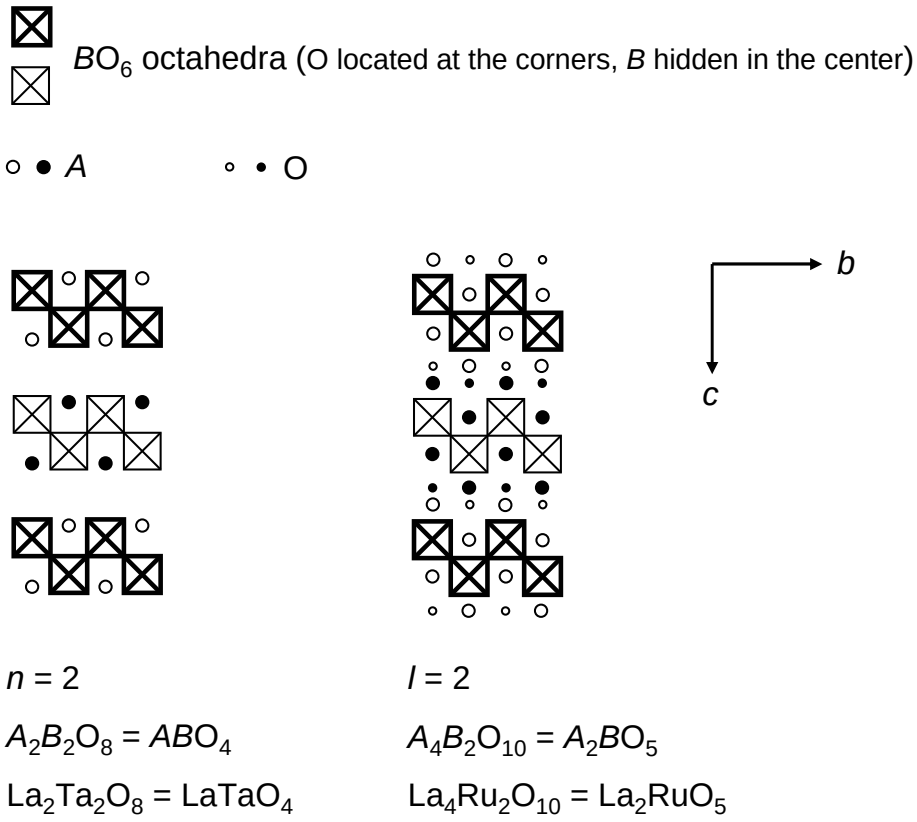

Fig. 7. Sketch of the idealized crystal structure of $LaTaO_4$ and La_2RuO_5 projected along the a-axis. Light and heavy drawing of the BO_6 octahedra as well as filled and open circles indicates a height difference perpendicular to the drawing plane. $LaTaO_4$ is an $n = 2$ member of $A_nB_nO_{3n+2} = ABO_x$, see Figure 4. La_2RuO_5 is structurally similar but its interlayer region is occupied by La^{3+} and O^{2-} ions. To our knowledge La_2RuO_5 is the only compound with this type of structure. Nevertheless, it can be considered as an $l = 2$ member of the hypothetical series $(LaO)_2^{2+}(A'_lB_lO_{3l+2})^{2-} = A_{l+2}B_lO_{3l+4}$. The structure of La_2RuO_5 was determined by Boullay et al. [21] as well as by Ebbinghaus [44].

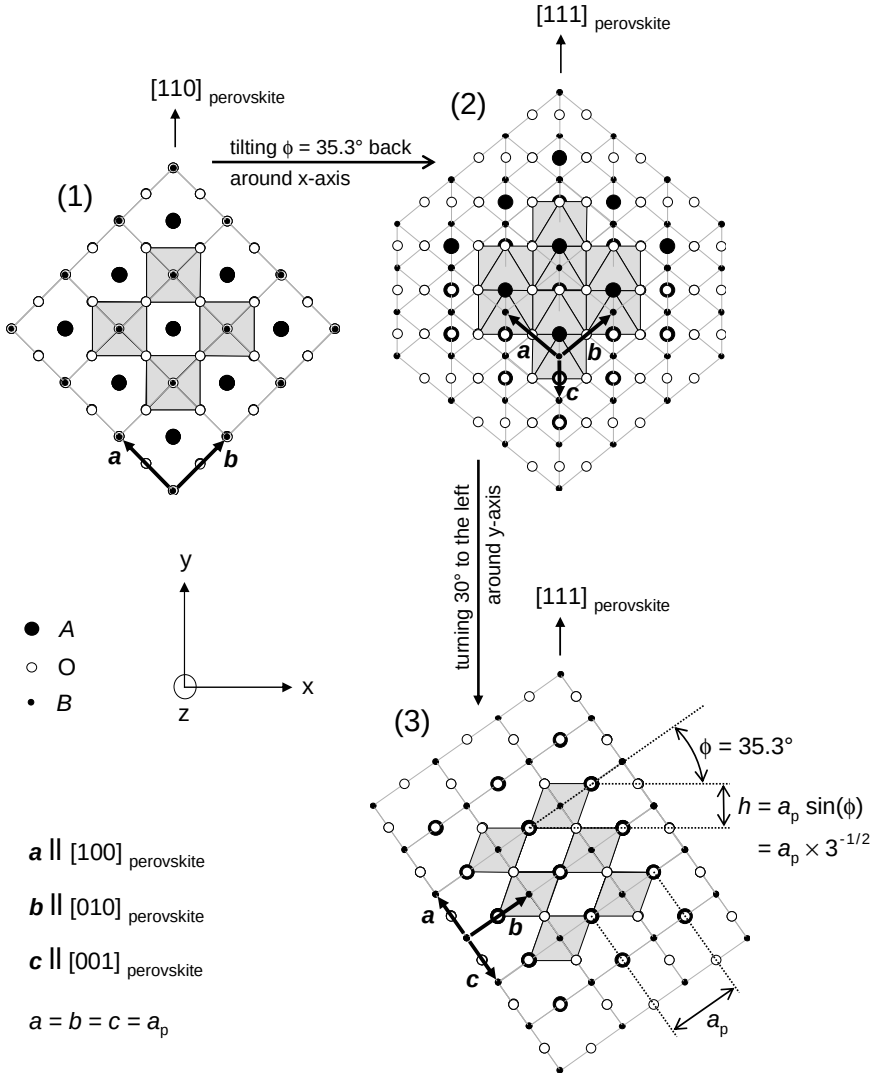

Fig. 8. Special projections of the cubic perovskite structure ABO_3 along the z-axis of a fixed x-y-z reference frame. These projections show how Fig. 9 and 10 come about. $a_p \approx 4$ Å is the lattice parameter of the cubic perovskite. The BO_6 octahedra are accentuated in grey. (1) View of the cubic perovskite structure along its c-axis. (2) The cube stands on one of its corners. This picture results from (1) by tilting it $\phi = 35.3°$ back around the x-axis. $\phi = \arcsin(1/\sqrt{3}) = 35.3°$ is the angle between the space and face diagonal of the cube. (3) This picture results from (2) by turning it 30° to the left around the y-axis. This kind of view is used in Fig. 9 and 10. The height h of the BO_6 octahedra along the [111] perovskite direction is given by $h = a_p \sin(\phi) = a_p/\sqrt{3}$, i.e. $h \approx 2.3$ Å for $a_p = 4$ Å.

m	**ccp** stacking sequence of AO_3 along c-axis	r
4	**ABCA** | **CABC** | **BCAB**	3
4 + 5	**ABCABABCA** | **CABCACABC** | **BCABCBCAB**	3
5	**ABCAB**	1
5 + 6	**ABCABCBCABC** | **BCABCACABCA** | **CABCABABCAB**	3
6	**ABCABC** | **BCABCA** | **CABCAB**	3
7	**ABCABCA** | **CABCABC** | **BCABCAB**	3
∞	**ABC**	1

Table 1. Cubic close-packed (**ccp**) stacking sequences of AO_3 sheets in hexagonal $A_mB_{m-1}O_{3m}$ along the c-axis [45,70,71,143,194,232]. The corresponding repeat number r of basis units determines the minimum length of the unit cell along the c-axis. $m = 4 + 5$ $(5 + 6)$ stands for $A_9B_7O_{27}$ $(A_{11}B_9O_{33})$ and indicates an ordered intergrowth of alternating $m = 4$ and $m = 5$ ($m = 5$ and $m = 6$) type layers along the c-axis. $m = \infty$ indicates the three-dimensional perovskite structure ABO_3. See also Fig. 9 and 10.

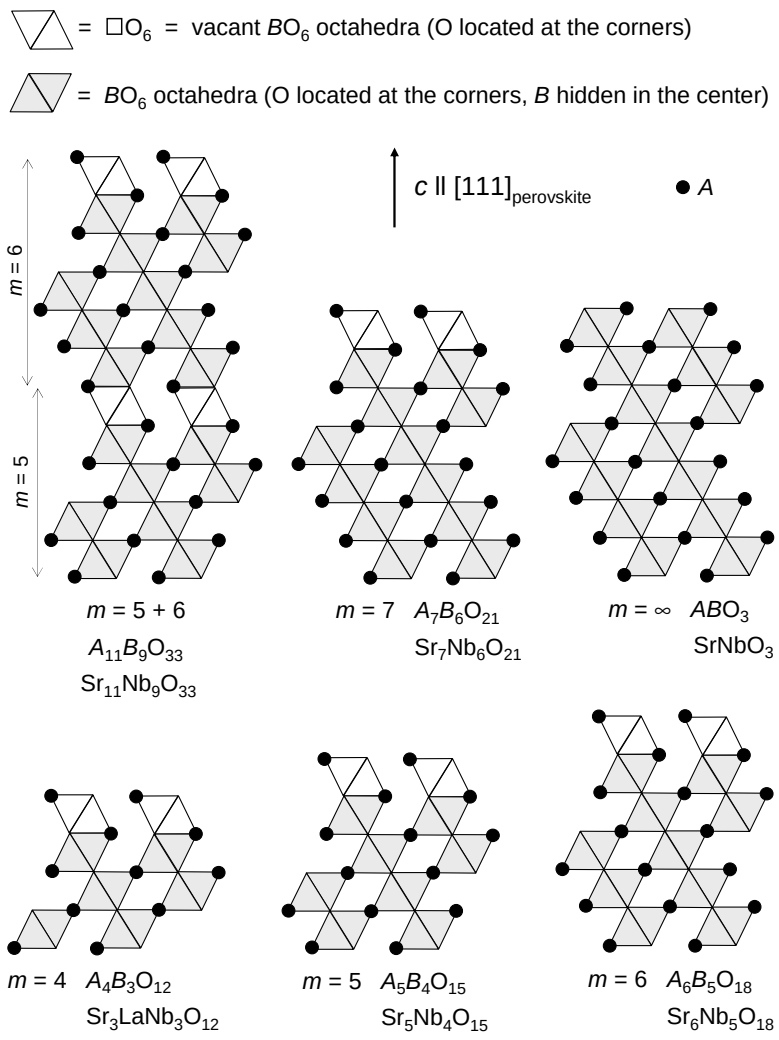

Fig. 9. Sketch of the idealized crystal structure of the $m = 4, 5, 6, 7$ and ∞ members of the hexagonal perovskite-related layered homologous series $A_mB_{m-1}O_{3m}$ projected along the a-axis. How this kind of view comes about is indicated in Figure 8. Shown are the basis units which are $m-1$ BO_6 octahedra thick along the c-axis. If the vacant octahedron is taken into account, then the basis units are m octahedra thick. For $m = \infty$ the three-dimensional perovskite structure ABO_3 is realized. The A cations are located at a height difference perpendicular to the drawing plane. Also shown is an example of an ordered intergrowth of two different types, namely $m = 5 + 6$ which has the formula $A_{11}B_9O_{33}$. Compositional examples are presented from the (Sr,La)−Nb−O system.

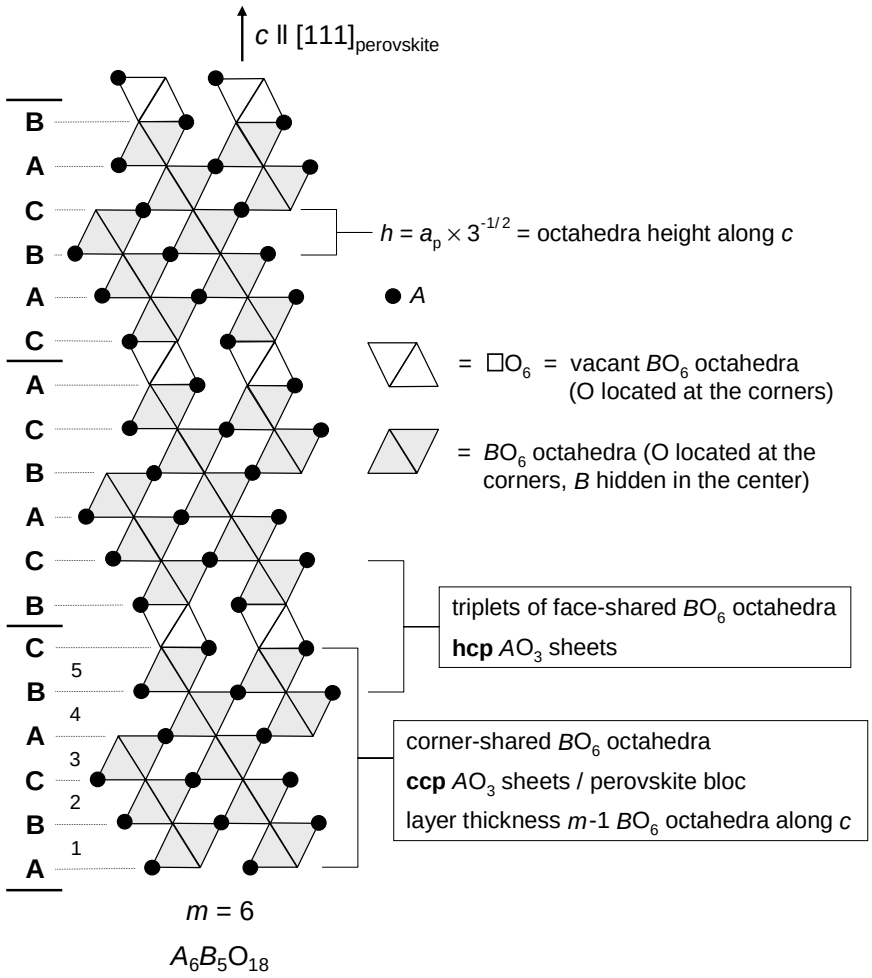

Fig. 10. More detailed sketch of the idealized crystal structure of the hexagonal perovskite-related layered homologous series $A_mB_{m-1}O_{3m}$ projected along the a-axis using the $m = 6$ member as a representative example. How this kind of view comes about is shown in Figure 8. The A cations are located at a height difference perpendicular to the drawing plane. $a_p \approx 4$ Å is the lattice parameter of the cubic perovskite structure. The bold letters **A**, **B** and **C** indicate the stacking sequence of AO_3 sheets along the c-axis and **ccp** (**hcp**) stands for the corresponding cubic (hexagonal) close-packed arrangement. There are $r = 3$ different stacking sequences along the c-axis which are separated by horizontal bars, see also Table 1. Therefore the length of the unit cell along the c-axis is given by $c = 3 \times (6 \times h) = 3 \times (6 \times a_p/\sqrt{3})$. $6 \times h$ is the height of the basis unit consisting of $m = 6$ BO_6 octahedra including the vacant octahedra.

	$A_{j+1}B_jO_{3j+1}$	$A_kB_kO_{3k+1}$	$A_nB_nO_{3n+2}$	$A_mB_{m-1}O_{3m}$
Cation ratio A/B	$(j+1)/j$	1	1	$m/(m-1)$
Symmetry for $j,k,n,m<\infty$	tetragonal or orthorhombic	tetragonal, orthorhombic or monoclinic	orthorhombic or monoclinic	hexagonal
Structure type for $j,k,n,m=\infty$	perovskite ABO_3	perovskite ABO_3	perovskite ABO_3	perovskite ABO_3
Layer thickness along c-axis in numbers of BO_6 octahedra	j	k	n	$m-1$
Orientation of BO_6 octahedra along c-axis referring to cubic perovskite ABO_3	[100]	[100]	[110]	[111]
Displacement between two adjacent layers in terms of vectors $\boldsymbol{a}$ and $\boldsymbol{b}$ of simple a- and b-axis	$(\boldsymbol{a}+\boldsymbol{b})/2$	type III: $(\boldsymbol{a}+\boldsymbol{b})/2$ type II: $\boldsymbol{a}/2$ type I: $\boldsymbol{0}$	$(\boldsymbol{a}+\boldsymbol{b})/2$	
Intralayer structural anisotropy: a- versus b-axis	no or weak	no or weak	strong	no because $a=b$
Type of continuous B–O intralayer linkage	linear along a-axis linear along b-axis	linear along a-axis linear along b-axis	linear along a-axis zigzag along b-axis via adjacent B at different c-axis height	only via adjacent B at different c-axis height (no direct linkage at same c-axis height)

Table 2. Comparison between the layered perovskite-related homologous series $A_{j+1}B_jO_{3j+1}$ (Ruddlesden-Popper phases), $A_kB_kO_{3k+1}$ (Dion-Jacobson phases with $A_k=A'A''_{k-1}$), $A_nB_nO_{3n+2}$ and $A_mB_{m-1}O_{3m}$. Continuation in Table 3.

	$A_{j+1}B_jO_{3j+1}$	$A_kB_kO_{3k+1}$	$A_nB_nO_{3n+2}$	$A_mB_{m-1}O_{3m}$
Integral series members for which bulk compounds are known	$j = 1, 2, 3$	$k =$ 2, 3, 4, 5, 6, 7	$n =$ 2, 3, 4, 5, 6, 7	$m =$ 3, 4, 5, 6, 7, 8
Bulk compounds with ordered intergrowth of layers with different thickness	No	No	Yes [1] e.g. $A_9B_9O_{31}$ ($n = 4.5$)	Yes [2] e.g. $A_{11}B_9O_{33}$ ($m = 5 + 6$)
B cations for which bulk compounds are known	Al Ti V Cr Mn Fe Co Ni Cu Ga Zr Mo Ru Rh Sn Ir Pb U	Ti Nb Ta [3]	Ti Nb Ta [3]	Ti Nb Ta [3] Re [4]
Examples of special properties	Unconventional (i.e. non s-wave) superconductivity: $j = 1$ $(La,Ba)_2CuO_4$: d-wave spin-singlet $T_{c\,max} = 38$ K [12,13,23] $j = 1$ Sr_2RuO_4: p-wave spin-triplet $T_c \simeq 1$ K [128,138,139]	Capability to intercalate ions or molecules in the interlayer region [59] Superconductivity with $T_c \simeq 1$ K by intercalation of Li in $k = 3$ $KCa_2Nb_3O_{10}$ [214,215] Anisotropic 3D metals, e.g. $k = 3$ $BaCa_2Nb_3O_{10}$ [this work]	Among $n = 4$ are the highest-T_c ferroelectrics, e.g. $La_4Ti_4O_{14}$ with $T_c = 1770$ K [85,127,150] Quasi-1D metals, (e.g. $n = 5$ $Sr_5Nb_5O_{17}$) with compositional, structural and electronical proximity to (anti)ferroelectric series members [110–113,127]	Quasi-2D metals, e.g. $m = 6$ $Sr_6Nb_5O_{18}$ [this work]

Table 3. Continuation from Table 2. Comparison between the layered perovskite-related homologous series $A_{j+1}B_jO_{3j+1}$ (Ruddlesden-Popper phases), $A_kB_kO_{3k+1}$ (Dion-Jacobson phases with $A_k = A'A''_{k-1}$), $A_nB_nO_{3n+2}$ and $A_mB_{m-1}O_{3m}$. [1]The formula of these compounds can be described by a non-integral n. [2]The formula of these compounds cannot be described by a non-integral m but by an addition of the both formulas of two corresponding adjacent members, e.g. $m = 5+6$ means $A_5B_4O_{15}$ + $A_6B_5O_{18}$ = $A_{11}B_9O_{33}$. [3]Other elements at the B site are also possible, e.g. Mg, Al, Fe, Ga, Zr or W, however the minimum B site occupancy by Ti, Nb or Ta is about 0.67. [4]Only for $m = 3$.

x in ABO_x	Structure type	A in $ATaO_x$	A in $ANbO_x$	A in $ATiO_x$	AB in ABO_x
4	$n = 2$	La, Ce, Pr, Nd^{hps}			
	fergusonite	Nd, ..., Yb	La, ..., Yb		
3.67	$n = 3$	$La_{0.33}Sr_{0.67}$			$LnTa_{0.33}Ti_{0.67}$ (Ln = La, Pr)
3.50	$k = 2$	$Ba_{0.5}Sr_{0.5}$, $Ba_{0.5}Ca_{0.5}$	$K_{0.5}La_{0.5}$, $Ba_{0.5}La_{0.2}Ca_{0.3}$		
	$n = 4$	Sr	Ca, Sr, $Ca_{0.8}La_{0.2}$	La, Ce, Pr, Nd, Sm^{hps}, Eu^{hps}	NaW^{hps}
	pyrochlore		$Ca_{0.5}La_{0.5}$	Sm, Eu, ..., Yb	
3.46	$n = 4.33$			La, Ce, Nd, $La_{0.92}Ca_{0.08}$	
3.44	$n = 4.5$		Ca, Sr	La, $La_{0.89}Ca_{0.11}$	$CaNb_{0.89}Ti_{0.11}$
3.40	$n = 5$		Ca, Sr	La, Ce, Pr, Nd, Sm	$SrNb_{0.8}Ti_{0.2}$, $SrTa_{0.8}Ti_{0.2}$
3.33	$k = 3$	$Na_{0.33}Ca_{0.67}$	$K_{0.33}Ca_{0.67}$, $Ba_{0.33}Ca_{0.67}$	$Ba_{0.33}Ln_{0.67}$ (Ln = La, Pr, Nd, Sm, Eu)	$Cs_{0.33}Ln_{0.67}Ti_{0.67}Nb_{0.33}$ (Ln = La, Pr, Nd, Sm)
	$n = 6$		$Ca_{0.67}Na_{0.33}$	$Ca_{0.33}Ln_{0.67}$ (Ln = La, Pr, Nd, Sm)	$SrNb_{0.67}Ti_{0.33}$
3.29	$n = 7$				$SrNb_{0.57}Ti_{0.43}$
3.25	$k = 4$		$K_{0.25}Ca_{0.5}Na_{0.25}$		
3.20	$k = 5$		$K_{0.2}Ca_{0.4}Na_{0.4}$		
3	perovskite $n = k = \infty$	K	Ca, Sr, Ba	Ca, Sr, Ln (Ln = La, Ce, ..., Tm)	NaW

Table 4. Oxygen content x in ABO_x and corresponding structure type(s) with compositional examples from literature, databases and this work. k refers to $A_kB_kO_{3k+1}$ with $A_k = A'A''_{k-1}$ and n to $A_nB_nO_{3n+2}$. The superscript *hps* indicates a high pressure synthesis.

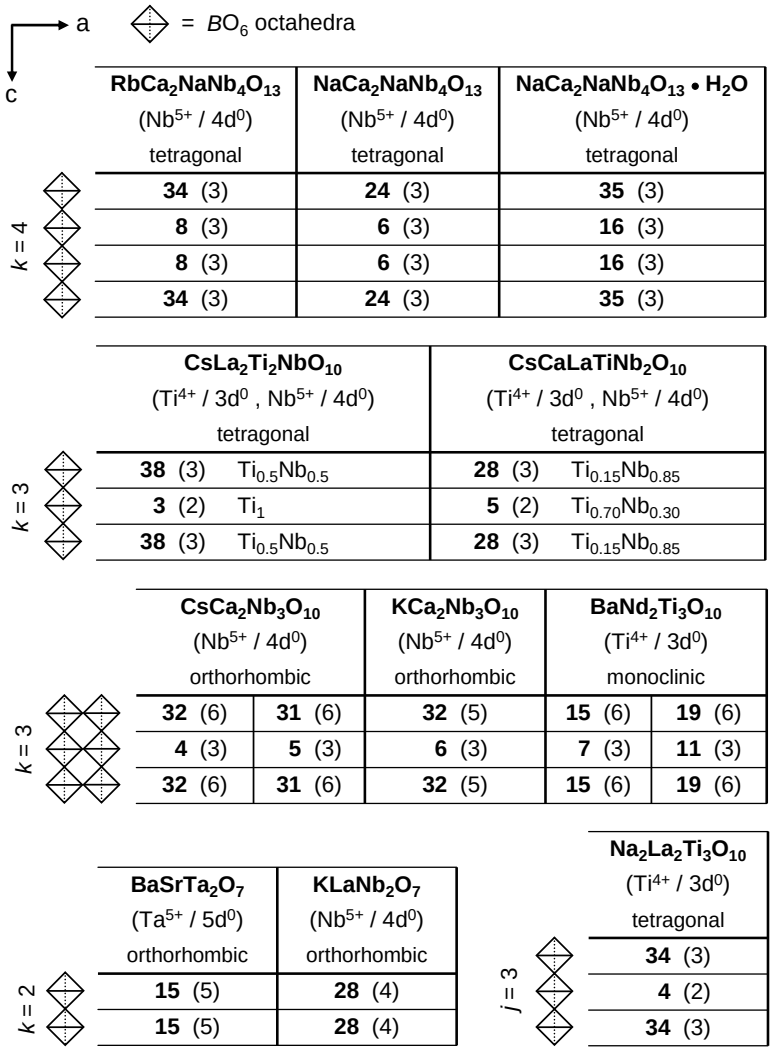

Fig. 11. Features of the BO_6 octahedra of $k = 2$, 3 and 4 members of $A'A_{k-1}B_kO_{3k+1}$ (Dion-Jacobson phases) and an $j = 3$ member of $A_{j+1}B_jO_{3j+1}$ (Ruddlesden-Popper phases). Sketched in the same way as in Fig. 1, 2 and 3 is the idealized structure of the layers which are k or j BO_6 octahedra thick along the c-axis. For the sake of simplicity the A' and A cations are omitted. Shown are the percentage values of the octahedra distortions after Eq. (1) in bold numbers, the number of different $B - O$ bond lengths per octahedron in parenthesis, and the experimentally determined B site occupancies. They were calculated or taken from the crystallographic data presented in Ref. [118,182] ($k = 2$), [230] ($j = 3$), [37,53,109] (lower $k = 3$), [76] (upper $k = 3$), and [185] ($k = 4$). If two adjacent BO_6 octahedra along the a-axis are not equivalent, then two columns are used.

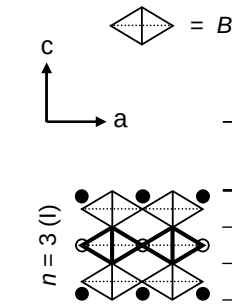

$Sr_{0.67}La_{0.33}TaO_{3.67}$ (Ta^{5+} / $5d^0$) orthorhombic
Sr **12** (3)
La **4** (2)
Sr **12** (3)

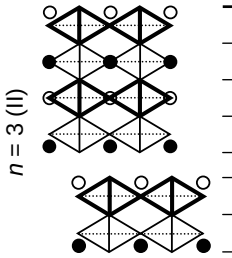

$LaTi_{0.67}Ta_{0.33}O_{3.67}$ (Ti^{4+} / $3d^0$, Ta^{5+} / $5d^0$) orthorhombic	
19 (5)	$Ti_{0.76}Ta_{0.24}$
20 (5)	$Ti_{0.88}Ta_{0.12}$
20 (5)	$Ti_{0.88}Ta_{0.12}$
19 (5)	$Ti_{0.76}Ta_{0.24}$
13 (5)	$Ti_{0.28}Ta_{0.72}$
13 (5)	$Ti_{0.28}Ta_{0.72}$

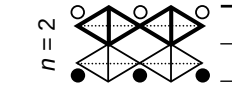

$LaTaO_4$ (Ta^{5+} / $5d^0$)		**$CeTaO_4$** (Ta^{5+} / $5d^0$)	**$NdTaO_4$** (Ta^{5+} / $5d^0$)
monoclinic	*T* = 300 °C orthorhombic	monoclinic	high pressure synthesis monoclinic
8 (6)	**11** (6)	**7** (6)	**11** (6)
8 (6)	**11** (6)	**7** (6)	**11** (6)

Fig. 12. Features of the BO_6 octahedra of $n = 2$ and 3 members of $A_nB_nO_{3n+2} = ABO_x$. Sketched in the same way as in Fig. 6 is the idealized structure of the layers which are n BO_6 octahedra thick along the c-axis. The circles represent the A cations. Shown are the percentage values of the octahedra distortions after Eq. (1) in bold numbers, the number of different $B-$O bond lengths per octahedron in parenthesis, and the experimentally determined A and B site occupancies. They were calculated or taken from the crystallographic data presented in Ref. [30,221] for $n = 2$, [222] for $n = 3$ (II) and [224] for $n = 3$ (I). If the temperature T is not specified, the displayed properties refer to ambient temperature. The two different realizations of $n = 3$, (I) and (II), are also shown in Figure 4.

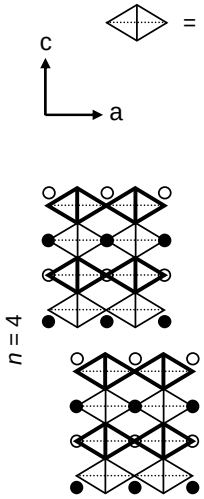

$NdTiO_{3.50}$ (Ti^{4+} / $3d^0$) monoclinic	
17 (6)	**13** (6)
20 (6)	**18** (6)
20 (6)	**18** (6)
17 (6)	**13** (6)
19 (6)	**19** (6)
14 (6)	**14** (6)
14 (6)	**14** (6)
19 (6)	**19** (6)

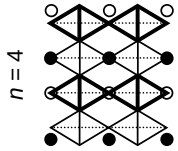

$LaTiO_{3.50}$ (Ti^{4+} / $3d^0$) T_c = 1770 K					**$PrTiO_{3.50}$** (Ti^{4+} / $3d^0$)
orthorhombic		monoclinic		T = 1173 K < T_c orthorhombic	monoclinic
19 (5)	**20** (6)	**21** (6)	**26** (6)	**27** (5)	**18** (6)	**24** (6)
17 (6)	**15** (6)	**20** (6)	**21** (6)	**22** (5)	**18** (6)	**20** (6)
15 (6)	**17** (6)	**20** (6)	**21** (6)	**22** (5)	**18** (6)	**20** (6)
20 (6)	**19** (5)	**21** (6)	**26** (6)	**27** (5)	**18** (6)	**24** (6)

Fig. 13. Features of the TiO_6 octahedra of $n = 4$ titanates of $A_nB_nO_{3n+2} = ABO_x$. Sketched in the same way as in Fig. 6 is the idealized structure of the layers which are n BO_6 octahedra thick along the c-axis. The circles represent the A cations. Shown are the percentage values of the octahedra distortions after Eq. (1) in bold numbers and the number of different $Ti - O$ bond lengths per octahedron in parenthesis. They were calculated or taken from the crystallographic data presented in Ref. [189] (top) and [188,191,82,107] (below). If the temperature T is not specified, the displayed properties refer to ambient temperature. If data of different temperatures are shown, the ferroelectric transition temperature T_c is also provided. If two adjacent TiO_6 octahedra along the a-axis are not equivalent, then two columns are used.

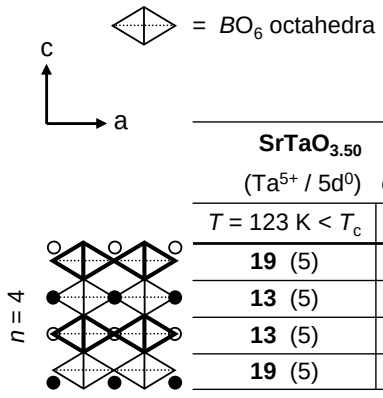

$SrTaO_{3.50}$ T_c = 166 K (Ta^{5+} / $5d^0$) orthorhombic		**$EuTaO_{3.50}$** (Eu^{2+} , Ta^{5+} / $5d^0$) orthorhombic
T = 123 K < T_c	T = 300 K > T_c	
19 (5)	**15** (3)	**13** (3)
13 (5)	**9** (3)	**9** (3)
13 (5)	**9** (3)	**9** (3)
19 (5)	**15** (3)	**13** (3)

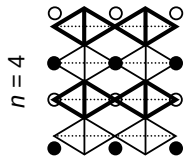

$SrTa_{0.88}Nb_{0.12}O_{3.50}$ T_c = 675 K (Ta^{5+} / $5d^0$, Nb^{5+} / $4d^0$) orthorhombic	
T = 300 K < T_c	T = 773 K > T_c
22 (5)	**13** (3)
17 (5)	**8** (3)
17 (5)	**8** (3)
22 (5)	**13** (3)

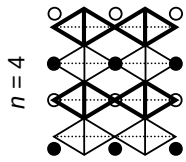

$CaNbO_{3.50}$ (Nb^{5+} / $4d^0$)				**$SrNbO_{3.50}$** (Nb^{5+} / $4d^0$)
monoclinic		orthorhombic		orthorhombic
21 (6)	**25** (6)	**22** (6)	**23** (6)	**23** (5)
18 (6)	**19** (6)	**20** (6)	**19** (6)	**21** (5)
18 (6)	**19** (6)	**19** (6)	**20** (6)	**21** (5)
21 (6)	**25** (6)	**23** (6)	**22** (6)	**23** (5)

Fig. 14. Features of the BO_6 octahedra of $n = 4$ niobates and tantalates of $A_nB_nO_{3n+2} = ABO_x$. Sketched in the same way as in Fig. 6 is the idealized structure of the layers which are n BO_6 octahedra thick along the c-axis. The circles represent the A cations. Shown are the percentage values of the octahedra distortions after Eq. (1) in bold numbers and the number of different $B - O$ bond lengths per octahedron in parenthesis. They were calculated or taken from the crystallographic data presented in Ref. [81,79,86] (top), [81] (middle), and [80,187,78] (below). If the temperature T is not specified, the displayed properties refer to ambient temperature. If data of different temperatures are shown, the ferroelectric transition temperature T_c is also provided. If two adjacent BO_6 octahedra along the a-axis are not equivalent, then two columns are used.

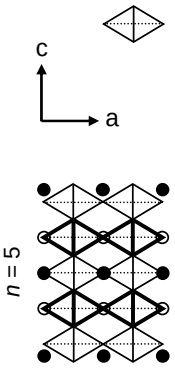

$Ca_{0.8}Na_{0.2}NbO_{3.40}$ (Nb^{5+} / $4d^0$) monoclinic				**$LaTiO_{3.41}$** ($Ti^{3.82+}$ / $3d^{0.18}$) monoclinic	
Ca_1	**19** (6)	Ca_1	**23** (6)	**20** (6)	**24** (6)
$Ca_{0.80}Na_{0.20}$	**15** (6)	$Ca_{0.46}Na_{0.54}$	**16** (6)	**17** (6)	**16** (6)
$Ca_{0.75}Na_{0.25}$	**1** (3)	$Ca_{0.75}Na_{0.25}$	**1** (3)	**3** (3)	**2** (3)
$Ca_{0.80}Na_{0.20}$	**15** (6)	$Ca_{0.46}Na_{0.54}$	**16** (6)	**17** (6)	**16** (6)
Ca_1	**19** (6)	Ca_1	**23** (6)	**20** (6)	**24** (6)

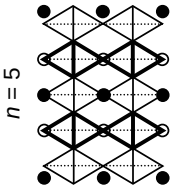

$CaNb_{0.8}Ti_{0.2}O_{3.40}$ monoclinic (Nb^{5+} / $4d^0$, Ti^{4+} / $3d^0$)				**$CaNbO_{3.41}$** ($Nb^{4.82+}$ / $4d^{0.18}$) monoclinic			
$Nb_{0.94}Ti_{0.06}$	**20** (6)	$Nb_{0.96}Ti_{0.04}$	**23** (6)	**21** (5)	$Nb^{4.98+}$	**24** (6)	$Nb^{4.95+}$
$Nb_{0.79}Ti_{0.21}$	**16** (6)	$Nb_{0.81}Ti_{0.19}$	**16** (6)	**16** (6)	$Nb^{4.82+}$	**17** (6)	$Nb^{4.79+}$
$Nb_{0.54}Ti_{0.46}$	**1** (3)	$Nb_{0.58}Ti_{0.42}$	**1** (3)	**2** (3)	$Nb^{4.73+}$	**3** (3)	$Nb^{4.73+}$
$Nb_{0.79}Ti_{0.21}$	**16** (6)	$Nb_{0.81}Ti_{0.19}$	**16** (6)	**16** (6)	$Nb^{4.82+}$	**17** (6)	$Nb^{4.79+}$
$Nb_{0.94}Ti_{0.06}$	**20** (6)	$Nb_{0.96}Ti_{0.04}$	**23** (6)	**21** (5)	$Nb^{4.98+}$	**24** (6)	$Nb^{4.95+}$

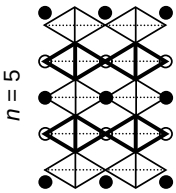

$SrNb_{0.8}Ti_{0.2}O_{3.40}$ (Nb^{5+} / $4d^0$, Ti^{4+} / $3d^0$) orthorhombic		**$SrNbO_{3.41}$** ($Nb^{4.82+}$ / $4d^{0.18}$) orthorhombic
20 (5)	$Nb_{0.90}Ti_{0.10}$	**23** (5)
16 (5)	$Nb_{0.82}Ti_{0.18}$	**17** (5)
2 (3)	$Nb_{0.56}Ti_{0.44}$	**3** (3)
16 (5)	$Nb_{0.82}Ti_{0.18}$	**17** (5)
20 (5)	$Nb_{0.90}Ti_{0.10}$	**23** (5)

Fig. 15. Features of the BO_6 octahedra of $n = 5$ members of $A_nB_nO_{3n+2} = ABO_x$. Sketched in the same way as in Fig. 6 is the idealized structure of the layers which are n BO_6 octahedra thick along the c-axis. The circles represent the A cations. Shown are the percentage values of the octahedra distortions after Eq. (1) in bold numbers, the number of different $B-O$ bond lengths per octahedron in parenthesis, the experimentally determined B and A site occupancies, and for $CaNbO_{3.41}$ the computed Nb valences. They were taken or calculated from the crystallographic data presented in Ref. [252,34] (top), [64,63] (middle), and [39,2] (below). If two adjacent BO_6 octahedra or A sites along the a-axis are not equivalent, then two columns are used.

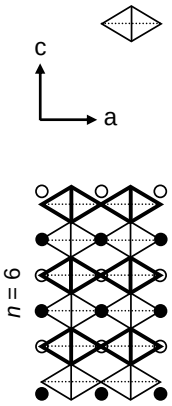

$Nd_{0.67}Ca_{0.33}TiO_{3.33}$ (Ti^{4+} / $3d^0$) orthorhombic		**$CaNb_{0.67}Ti_{0.33}O_{3.33}$** type ($Nb^{5+}$ / $4d^0$, Ti^{4+} / $3d^0$) monoclinic			
$Nd_{0.53}Ca_{0.47}$	**19** (6)	**21** (6)	$Nb_{0.99}Ti_{0.01}$	**23** (6)	$Nb_{0.98}Ti_{0.02}$
$Nd_{0.52}Ca_{0.48}$	**20** (6)	**17** (6)	$Nb_{0.79}Ti_{0.21}$	**20** (6)	$Nb_{0.84}Ti_{0.16}$
$Nd_{0.45}Ca_{0.55}$	**8** (4)	**9** (6)	$Nb_{0.47}Ti_{0.53}$	**12** (5)	$Nb_{0.49}Ti_{0.51}$
$Nd_{0.44}Ca_{0.56}$	**8** (6)	**7** (5)	$Nb_{0.47}Ti_{0.53}$	**5** (4)	$Nb_{0.49}Ti_{0.51}$
$Nd_{0.52}Ca_{0.48}$	**18** (6)	**20** (6)	$Nb_{0.79}Ti_{0.21}$	**19** (6)	$Nb_{0.84}Ti_{0.16}$
$Nd_{0.52}Ca_{0.48}$	**26** (6)	**24** (6)	$Nb_{0.99}Ti_{0.01}$	**25** (6)	$Nb_{0.98}Ti_{0.02}$

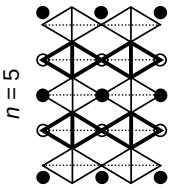

$LaTi_{0.8}Fe_{0.2}O_{3.40}$ orthorhombic (Ti^{4+} / $3d^0$, Fe^{3+} / $3d^5$)	**$PrTi_{0.8}Fe_{0.2}O_{3.40}$** monoclinic ($Ti^{4+}$ / $3d^0$, Fe^{3+} / $3d^5$)	
Ti **3** (5)	Ti **16** (6)	Ti **15** (6)
Ti **16** (5)	Ti **14** (6)	Ti **14** (6)
Fe **15** (3)	Fe **12** (3)	Fe **14** (3)
Ti **16** (5)	Ti **14** (6)	Ti **14** (6)
Ti **3** (5)	Ti **16** (6)	Ti **15** (6)

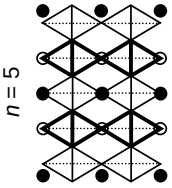

$LaTi_{0.8}Ga_{0.2}O_{3.40}$ orthorhombic (Ti^{4+} / $3d^0$, Ga^{3+} / $3d^0$)	**$PrTi_{0.8}Ga_{0.2}O_{3.40}$** monoclinic ($Ti^{4+}$ / $3d^0$, Ga^{3+} / $3d^0$)	
Ti **6** (5)	Ti **16** (5)	Ti **15** (6)
$Ti_{0.75}Ga_{0.25}$ **11** (5)	Ti **16** (6)	$Ti_{0.5}Ga_{0.5}$ **17** (5)
$Ti_{0.5}Ga_{0.5}$ **6** (5)	Ti **10** (3)	Ga **8** (3)
$Ti_{0.75}Ga_{0.25}$ **11** (5)	Ti **16** (6)	$Ti_{0.5}Ga_{0.5}$ **17** (5)
Ti **6** (5)	Ti **16** (5)	Ti **15** (6)

Fig. 16. Features of the BO_6 octahedra of $n = 5$ and $n = 6$ members of $A_nB_nO_{3n+2} = ABO_x$. Sketched in the same way as in Fig. 6 is the idealized structure of the layers which are n BO_6 octahedra thick along the c-axis. The circles represent the A cations. Shown are the percentage values of the octahedra distortions after Eq. (1) in bold numbers, the number of different $B - O$ bond lengths per octahedron in parenthesis, and the experimentally determined B and A site occupancies. They were calculated or taken from the crystallographic data presented in Ref. [228,229] ($n = 5$ below), [227,228] ($n = 5$ middle) and [153,62] ($n = 6$). If two adjacent BO_6 octahedra along the a-axis are not equivalent, then two columns are used. We note for the $CaNb_{0.67}Ti_{0.33}O_{3.33}$ type that the actual stoichiometry of this studied $n = 6$ crystal deviates from the ideal composition as discussed in Ref. [62].

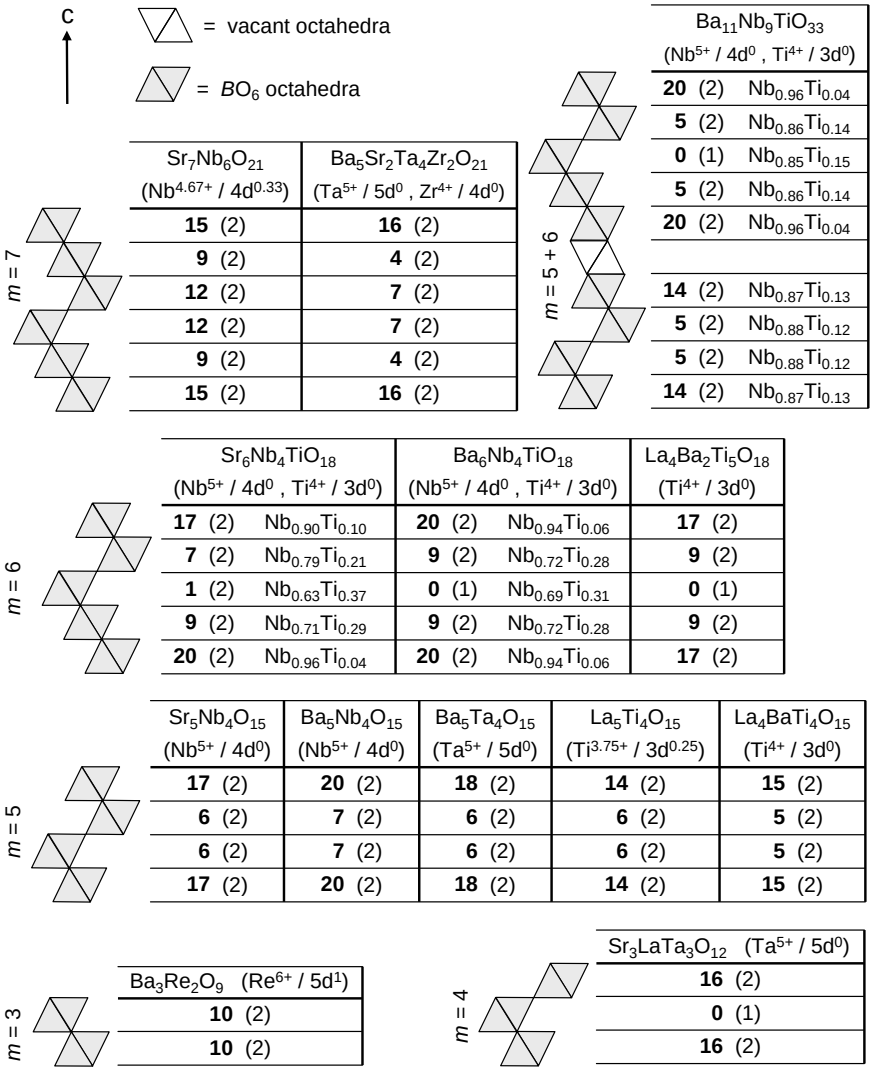

$Sr_7Nb_6O_{21}$ ($Nb^{4.67+}$ / $4d^{0.33}$)	$Ba_5Sr_2Ta_4Zr_2O_{21}$ (Ta^{5+} / $5d^0$, Zr^{4+} / $4d^0$)
15 (2)	**16** (2)
9 (2)	**4** (2)
12 (2)	**7** (2)
12 (2)	**7** (2)
9 (2)	**4** (2)
15 (2)	**16** (2)

$Ba_{11}Nb_9TiO_{33}$ (Nb^{5+} / $4d^0$, Ti^{4+} / $3d^0$)	
20 (2)	$Nb_{0.96}Ti_{0.04}$
5 (2)	$Nb_{0.86}Ti_{0.14}$
0 (1)	$Nb_{0.85}Ti_{0.15}$
5 (2)	$Nb_{0.86}Ti_{0.14}$
20 (2)	$Nb_{0.96}Ti_{0.04}$
14 (2)	$Nb_{0.87}Ti_{0.13}$
5 (2)	$Nb_{0.88}Ti_{0.12}$
5 (2)	$Nb_{0.88}Ti_{0.12}$
14 (2)	$Nb_{0.87}Ti_{0.13}$

$Sr_6Nb_4TiO_{18}$ (Nb^{5+} / $4d^0$, Ti^{4+} / $3d^0$)		$Ba_6Nb_4TiO_{18}$ (Nb^{5+} / $4d^0$, Ti^{4+} / $3d^0$)		$La_4Ba_2Ti_5O_{18}$ (Ti^{4+} / $3d^0$)
17 (2)	$Nb_{0.90}Ti_{0.10}$	**20** (2)	$Nb_{0.94}Ti_{0.06}$	**17** (2)
7 (2)	$Nb_{0.79}Ti_{0.21}$	**9** (2)	$Nb_{0.72}Ti_{0.28}$	**9** (2)
1 (2)	$Nb_{0.63}Ti_{0.37}$	**0** (1)	$Nb_{0.69}Ti_{0.31}$	**0** (1)
9 (2)	$Nb_{0.71}Ti_{0.29}$	**9** (2)	$Nb_{0.72}Ti_{0.28}$	**9** (2)
20 (2)	$Nb_{0.96}Ti_{0.04}$	**20** (2)	$Nb_{0.94}Ti_{0.06}$	**17** (2)

$Sr_5Nb_4O_{15}$ (Nb^{5+} / $4d^0$)	$Ba_5Nb_4O_{15}$ (Nb^{5+} / $4d^0$)	$Ba_5Ta_4O_{15}$ (Ta^{5+} / $5d^0$)	$La_5Ti_4O_{15}$ ($Ti^{3.75+}$ / $3d^{0.25}$)	$La_4BaTi_4O_{15}$ (Ti^{4+} / $3d^0$)
17 (2)	**20** (2)	**18** (2)	**14** (2)	**15** (2)
6 (2)	**7** (2)	**6** (2)	**6** (2)	**5** (2)
6 (2)	**7** (2)	**6** (2)	**6** (2)	**5** (2)
17 (2)	**20** (2)	**18** (2)	**14** (2)	**15** (2)

$Ba_3Re_2O_9$ (Re^{6+} / $5d^1$)
10 (2)
10 (2)

$Sr_3LaTa_3O_{12}$ (Ta^{5+} / $5d^0$)
16 (2)
0 (1)
16 (2)

Fig. 17. Features of the BO_6 octahedra of $m = 3, 4, 5, 6$ and 7 members and an ordered $m = 5 + 6$ intergrowth compound of hexagonal $A_m B_{m-1} O_{3m}$. Sketched in the same way as in Fig. 9 is the idealized structure of the layers which are $m - 1$ BO_6 octahedra thick along the c-axis. For the sake of simplicity the A cations are omitted. Shown are the percentage values of the octahedra distortions after Eq. (1) in bold numbers, the number of different $B - \mathrm{O}$ bond lengths per octahedron in parenthesis, and the experimentally determined B site occupancies. They were calculated or taken from the crystallographic data presented in Ref. [25] ($m = 3$), [7] ($m = 4$), [213,239,199,19,70] ($m = 5$), [40,41,71] ($m = 6$), [194,1] ($m = 7$), and [217] ($m = 5 + 6$).

Composition	***N***	***a***, ***b***, ***c*** (Å), β (°), ***V*** (Å^3), ***Z*** **Remarks / Special Features**	**Ref.**
$CsLaNb_2O_7$	$4d^0$	3.91, 3.91, 11.19, 90, 170.56, 1	[59]
$RbNdNb_2O_7$	$4d^0$	7.70, 7.70, 10.97, 90, 651.0, 4	[38]
$RbLaNb_2O_7$	$4d^0$	3.89, 3.89, 10.99, 90, 165.86, 1	[59]
		In context of superconductivity in Li-intercalated $KCa_2Nb_3O_{10}$ ($k = 3$) LDA band structure calculations performed	[72]
$KNdNb_2O_7$	$4d^0$	7.73, 7.69, 21.55, 90, 1281, 8	[38]
$Li_xKLaNb_2O_7$	$4d^y$	$y = x/2 > 0$ for $x > 0$ Resistivity measurements between 300 K and 0.5 K on polycrystalline Li-intercalated $KLaNb_2O_7$ indicates metallic behavior	[215]
$KLaNb_2O_7$	$4d^0$	7.81, 7.67, 21.54, 90, 1289, 8	[59]
		3.91, 3.89, 21.60, 90, 328.07, 2 Non-centrosym. space group C222 (No. 21)	[182]
β-$NaNdNb_2O_7$	$4d^0$	7.72, 7.72, 20.93, 90, 1247, 8	[38]
α-$NaNdNb_2O_7$	$4d^0$	7.72, 7.72, 20.42, 90, 1217, 8	
$NaLaNb_2O_7 \cdot 2H_2O$	$4d^0$	3.90, 3.90, 25.71, 90, 390.85, 2 Prepared by ion-exchange reaction of $RbLaNb_2O_7$ with molten $NaNO_3$	[59]
$NaLaNb_2O_7 \cdot 1.6H_2O$	$4d^0$	3.90, 3.90, 25.71, 90, 390.72, 2 Prepared by ion-exchange reaction of $KLaNb_2O_7$ with molten $NaNO_3$	[184]
$NaLaNb_2O_7$	$4d^0$	3.90, 3.90, 20.99, 90, 319.91, 2 Prepared by ion-exchange reaction of $RbLaNb_2O_7$ with a molten $NaNO_3$	[59]
		3.90, 3.90, 21.18, 90, 322.55, 2 ($T = 300$°C) Centrosym. space group I4/mmm (No. 139) Prepared by ion-exchange reaction of $KLaNb_2O_7$ with molten $NaNO_3$	[184]

Table 5. $k = 2$ niobates of tetragonal or orthorhombic $A'A_{k-1}B_kO_{3k+1}$ (Dion-Jacobson type phases) with A' = alkali metal and A = La or Nd.

Composition	***N***	***a***, ***b***, ***c*** (Å), β (°), ***V*** (Å^3), ***Z*** **Remarks / Special Features**	**Ref.**
$LiLaNb_2O_7$	$4d^0$	3.88, 3.88, 20.31, 90, 305.28, 2 Prepared by ion-exchange reaction of $RbLaNb_2O_7$ with molten $LiNO_3$	[59]
$HNdNb_2O_7$	$4d^0$	7.69, 7.69, 19.56, 90, 1155, 8 Prepared by proton exchange reaction with aqueous HNO_3	[38]
$HLaNb_2O_7 \cdot xH_2O$	$4d^0$	3.89, 3.89, 12.21, 90, 184.90, 1 Prepared by proton exchange reaction of (K,Rb or Cs)$LaNb_2O_7$ with aqueous HNO_3	[59]
$HLaNb_2O_7$	$4d^0$	3.89, 3.89, 10.46, 90, 158.59, 1 Prepared by proton exchange reaction of (K,Rb or Cs)$LaNb_2O_7$ with aqueous HNO_3	

Table 6. $k = 2$ niobates of tetragonal $A'A_{k-1}B_kO_{3k+1}$ (Dion-Jacobson type phases) with A' = Li or H and A = La or Nd.

Composition	***N***	***a***, ***b***, ***c*** (Å), β (°), ***V*** (Å^3), ***Z*** **Remarks / Special Features**	**Ref.**
$BaSrTa_2O_7$	$5d^0$	3.99, 7.84, 20.16, 90, 631.48, 4 Centrosym. space group Immm (No. 71)	[118]
$BaCaTa_2O_7$	$5d^0$	3.95, 7.72, 19.95, 90, 608.67, 4 Prepared by floating zone melting Presence of small amount of impurity phase(s)	this work
		3.97, 7.75, 20.01, 90, 615.18, 4 Centrosym. space group Immm (No. 71) Structure determined by single crystal XRD	[43]
$BaCa_{0.7}La_{0.3}Nb_2O_{6.97}$	$4d^{0.18}$	3.99, 7.79, 19.92, 90, 619.0, 4 Prepared by floating zone melting	this work
$BaCa_{0.6}La_{0.4}Nb_2O_{7.00}$	$4d^{0.20}$	4.00, 7.80, 19.96, 90, 622.0, 4 Prepared by floating zone melting Resistivity measurements on crystals reveal anisotropic 3D metallic behavior	
$BaCa_{0.5}La_{0.5}Nb_2O_{6.95}$	$4d^{0.30}$	4.00, 7.82, 19.97, 90, 625.5, 4 Prepared by floating zone melting Slightly under-stoichiometric with respect to oxygen content	

Table 7. $k = 2$ niobates and tantalates of orthorhombic $A'A_{k-1}B_kO_{3k+1}$ (Dion-Jacobson type phases) with A' = Ba.

Composition	***N***	***a***, ***b***, ***c*** (Å), β (°), ***V*** (Å^3), ***Z*** **Remarks / Special Features**	**Ref.**
$CsCa_2Nb_2FeO_9$	$4d^0$	3.88, 3.88, 15.14, 90, 227.47, 1 Significantly under-stoichiometric with respect to oxygen content	[237]
$H_{0.95}Cs_{0.05}La_2NbTi_2O_{10} \cdot 1.3H_2O$	$4d^0$ $3d^0$	3.83, 3.83, 16.46, 90, 241.22, 1 Prepared by ion exchange with aqueous HCl	[76]
$CsLn_2NbTi_2O_{10}$	$4d^0$ $3d^0$	3.85, 3.85, 15.39, 228.10, 1 (Ln = La) Lattice parameters for Ln = Pr, Nd or Sm are given in Ref. [76] Structure determined by Rietveld refinement of powder XRD data Ti exclusively located in the central octahedra, i.e. full ordering of Ti^{4+} and Nb^{5+} at the B site, see Figure 11	
$CsCaLaNb_2TiO_{10}$	$4d^0$ $3d^0$	3.87, 3.87, 15.24, 90, 258.06, 1 Structure determined by Rietveld refinement of powder XRD data	
$CsCa_2Nb_3O_{10}$	$4d^0$	7.74, 7.74, 30.18, 90, 1806, 8	[36]
		7.75, 7.74, 30.19, 90, 1810, 8 Centrosym. space group Pnma (No. 62) Ferroelastic with T_c = 560 °C Above T_c symmetry change from orthorhombic to tetragonal	[37]
$Li_xRbCa_2Nb_3O_{10}$	$4d^y$	$y = x/3 > 0$ for $x > 0$ Indications for superconductivity in Li-intercalated $RbCa_2Nb_3O_{10}$ with $T_c \simeq 3$ K from magnetic measurements	[216]
$RbCa_2Nb_3O_{10}$	$4d^0$	7.73, 7.73, 14.91, 90, 889.7, 4 Ferroelastic with T_c = 620 °C	[36] [38]
$TlCa_2Nb_3O_{10}$	$4d^0$	7.71, 7.71, 14.90, 90, 884.8, 4	[36]

Table 8. $k = 3$ members of tetragonal or orthorhombic $A'A_{k-1}B_kO_{3k+1}$ (Dion-Jacobson type phases) with A' = H, Rb, Cs, Tl and A = Ca, La, Pr, Nd, Sm.

Composition	***N***	***a***, ***b***, ***c*** (Å), β (°), ***V*** (Å^3), ***Z*** **Remarks / Special Features**	**Ref.**
$K_{1-x}Ca_{2-x}La_xNb_3O_{10}$	$4d^0$	3.87, 3.86, 29.46, 90, 439, 2 ($x = 0$)	[236]
		3.96, 3.89, 29.79, 90, 458, 2 ($x = 1$)	
		Lattice parameters for other x in Ref. [236]	
$0 \le x \le 1$		Significant deficiency at A' site: $A'_{1-x} = K_{1-x}$	
		$x = 1$ end member $LaCaNb_3O_{10}$ without any interlayer cations A'	
		Also hydrated and anhydrous compounds with H at the A' site reported	
$KCa_{2-x}Ln_xNb_3O_{10}$	$4d^y$	$y = x/3 > 0$ for $x > 0$	[68]
		Ln = La, Ce, Nd, Sm or Gd	[69]
$0 \le x \le x_{max}$		x_{max} = 0.4 (0.1) for Ln = La or Ce (Gd)	
		Lattice parameters are given in Ref. [68,69]	
		Resistivity measurements between 280 K and 4 K on polycrystalline samples shows semiconducting behavior for $x > 0$	
$Li_xKCa_2Nb_3O_{10}$	$4d^y$	$y = x/3 > 0$ for $x > 0$	[214]
		Resistivity and magnetic measurements on polycrystalline Li-intercalated $KCa_2Nb_3O_{10}$ indicate superconductivity with $T_c \le 6$ K	[215] [52]
$KCa_2Nb_3O_{10}$	$4d^0$	7.73, 7.73, 29.47, 90, 1759, 8	[36]
		3.87, 3.85, 29.47, 90, 439.2, 2	[87]
		7.75, 7.72, 29.45, 90, 1762, 8	[38]
		Ferroelastic with T_c = 1000 °C	
		3.88, 7.71, 29.51, 90, 883.2, 4	[53]
		Centrosym. space group Cmcm (No. 63)	
		Structure determined by single crystal XRD	
		Crystals prepared by using excess K_2SO_4 as flux	
$KSr_2Nb_3O_{10}$	$4d^0$	3.92, 3.91, 30.06, 90, 460.34, 2	[75]
		7.82, 7.76, 29.99, 90, 1821, 8	[49]
		Non-centrosym. space group $P2_12_12_1$ (No. 19)	
		Structure determined by single crystal XRD	

Table 9. $k = 3$ niobates of tetragonal or orthorhombic $A'A_{k-1}B_kO_{3k+1}$ (Dion-Jacobson type phases) with A' = K and A = Ca, Sr, La, Ce, Nd, Sm, Gd.

Composition	***N***	***a***, ***b***, ***c*** (Å), β (°), ***V*** (Å^3), ***Z*** **Remarks / Special Features**	**Ref.**
$NaCa_2Ta_3O_{10}$	$5d^0$	3.86, 3.86, 29.22, 90, 435.46, 2 Centrosym. space group I4/mmm (No. 139)	[231]
β-$NaCa_2Nb_3O_{10}$	$4d^0$	7.73, 7.73, 28.98, 90, 1734, 8	[36]
α-$NaCa_2Nb_3O_{10}$	$4d^0$	7.74, 7.74, 28.58, 90, 1712, 8	[38]
$LiCa_2Nb_3O_{10}$	$4d^0$	7.72, 7.72, 28.33, 90, 1688, 8	[36]
$HSr_2Nb_3O_{10} \cdot 0.5H_2O$	$4d^0$	3.90, 3.89, 16.42, 90, 249.23, 1	[49]
$HCa_2Nb_3O_{10} \cdot 1.5H_2O$	$4d^0$	3.85, 3.85, 16.23, 90, 241.07, 1 Prepared by proton exchange reaction of (K, Rb or Cs)$Ca_2Nb_3O_{10}$ in aqueous acid	[88]
		7.71, 7.71, 16.25, 90, 967.2, 4 Prepared by proton exchange reaction of (K, Rb or Cs)$Ca_2Nb_3O_{10}$ with aqueous HNO_3	[38]
$HCa_2Nb_3O_{10}$	$4d^0$	3.85, 3.85, 14.38, 90, 213.26, 1 Prepared by proton exchange reaction of (K, Rb or Cs)$Ca_2Nb_3O_{10}$ in aqueous acid	[88]
		7.71, 7.71, 14.39, 90, 854.3, 4 Prepared by proton exchange reaction of (K, Rb or Cs)$Ca_2Nb_3O_{10}$ with aqueous HNO_3	[38]

Table 10. $k = 3$ niobates and a tantalate of tetragonal or orthorhombic $A'A_{k-1}B_kO_{3k+1}$ (Dion-Jacobson type phases) with A' = H, Li or Na and A = Ca or Sr.

Composition	***N***	***a***, ***b***, ***c*** (Å), β (°), ***V*** (Å^3), ***Z*** **Remarks / Special Features**	**Ref.**
$BaEu_2Ti_3O_{10}$	$3d^0$	7.69, 7.59, 14.20, 97.8, 820.1, 4 Centrosym. space group $P2_1/m$ (No. 11)	[94]
$BaSm_2Ti_3O_{10}$	$3d^0$	7.70, 7.60, 14.21, 97.8, 823.6, 4 Centrosym. space group $P2_1/m$ (No. 11)	[93]
$BaNd_2Ti_3O_{10}$	$3d^0$	3.87, 7.62, 28.16, 90, 829.6, 4 Melts congruently at 1640 °C	[106]
		7.73, 7.67, 14.21, 97.8, 834.3, 4 Centrosym. space group $P2_1/m$ (No. 11) Structural study by HREM	[166]
		7.73, 7.63, 14.23, 97.8, 831.1, 4 Centrosym. space group $P2_1/m$ (No. 11) Structure determined by Rietveld refinement of powder XRD data	[109]
		7.72, 7.62, 14.22, 97.7, 829.5, 4 Centrosym. space group $P2_1/m$ (No. 11)	[92]
$BaPr_2Ti_3O_{10}$	$3d^0$	7.72, 7.62, 14.23, 97.7, 829.9, 4 Centrosym. space group $P2_1/m$ (No. 11)	[91]
$BaLa_2Ti_3O_{10}$	$3d^0$	3.88, 7.67, 28.46, 90, 847.3, 4 Centrosym. space group Cmcm (No. 63)	[55]
		3.88, 7.67, 28.52, 90, 847.4, 4	[66]
		7.76, 7.67, 14.39, 97.8, 849.0, 4 Centrosym. space group $P2_1/m$ (No. 11)	[90]
		3.88, 7.67, 28.54, 90, 849.6, 4 Prepared by floating zone melting	this work

Table 11. $k = 3$ titanates of orthorhombic or monoclinic $A'A_{k-1}B_kO_{3k+1}$ (Dion-Jacobson type phases) with A' = Ba and A = La, Pr, Nd, Sm or Eu. In the literature these titanates are not classified as Dion-Jacobson type compounds, however their structure seems to be of this type.

Composition	***N***	***a***, ***b***, ***c*** (Å), β (°), ***V*** (Å^3), ***Z*** **Remarks / Special Features**	**Ref.**
$BaCa_2Nb_3O_{10.07}$	$4d^{0.29}$	7.77, 7.67, 28.11, 90, 1675, 8 Prepared by floating zone melting Slightly over-stoichiometric with respect to oxygen content Resistivity measurements on crystals reveal anisotropic 3D metallic behavior	this work
$Ba_{0.75}Ca_{2.25}Nb_3O_{9.85}$	$4d^{0.43}$	7.90, 7.80, 27.58, 90, 1699, 8 Prepared by floating zone melting Significantly under-stoichiometric with respect to cation ratio A'/A and oxygen content	
$Ba_{0.8}Ca_2Nb_3O_{9.98}$	$4d^{0.21}$	3.89, 7.74, 28.31, 95.8, 848, 4 Prepared by floating zone melting Significantly under-stoichiometric with respect to A' site occupation	

Table 12. $k = 3$ niobates of orthorhombic or monoclinic $A'A_{k-1}B_kO_{3k+1}$ (Dion-Jacobson type phases) with $A' =$ Ba and $A =$ Ca.

Composition	***N***	***a***, ***b***, ***c*** (Å), β (°), ***V*** (Å^3), ***Z*** **Remarks / Special Features**	**Ref.**
$RbCa_2Na_{1-x}Sr_xNb_4O_{13}$		3.87, 3.87, 19.11, 90, 286.22, 1 ($x = 0.4$) 3.87, 3.87, 19.01, 90, 284.93, 1 ($x = 0.2$) 3.87, 3.87, 18.91, 90, 283.63, 1 ($x = 0$)	[205]
$0 \leq x \leq 0.4$		Centrosym. space group P4/mmm (No. 123) Structure determined by Rietveld refinement of powder XRD data	
$y = x/4$	$4d^y$	Resistivity measurements between 280 K and 80 K on polycrystalline samples shows semiconducting behavior for $x > 0$	
$RbCa_2NaNb_4O_{13}$	$4d^0$	3.87, 3.87, 18.89, 90, 283.00, 1 Centrosym. space group P4/mmm (No. 123) Structure determined by Rietveld refinement of powder XRD data	[185]
		7.74, 7.74, 18.91, 90, 1133, 4	[38]
$KCa_2NaNb_4O_{13}$	$4d^0$	7.73, 7.75, 37.27, 90, 2234, 8	[38]
		3.86, 3.88, 37.23, 90, 557.4, 2	[87]
$NaCa_2Na$ $Nb_4O_{13} \cdot 1.7H_2O$	$4d^0$	3.87, 3.87, 41.61, 90, 624.4, 2 Centrosym. space group I4/mmm (No. 139) Prepared by ion exchange reaction of $RbCa_2NaNb_4O_{13}$ with molten $NaNO_3$ Structure determined by Rietveld refinement of powder XRD data	[185]
$NaCa_2NaNb_4O_{13}$	$4d^0$	3.87, 3.87, 36.94, 90, 553.7, 2 Centrosym. space group I4/mmm (No. 139) Prepared by ion exchange reaction of $RbCa_2NaNb_4O_{13}$ with molten $NaNO_3$ Structure determined by Rietveld refinement of powder XRD data	
β-$NaCa_2NaNb_4O_{13}$	$4d^0$	7.75, 7.75, 36.93, 90, 2215, 8	[38]
α-$NaCa_2NaNb_4O_{13}$	$4d^0$	7.75, 7.75, 36.66, 90, 2201, 8	
HCa_2Na $Nb_4O_{13} \cdot 1.5H_2O$	$4d^0$	7.74, 7.74, 20.17, 90, 1208, 4 Prepared by proton exchange reaction of (K or Rb)$Ca_2NaNb_4O_{13}$ with aqueous HNO_3	
$HCa_2NaNb_4O_{13}$	$4d^0$	7.73, 7.73, 18.37, 90, 1097, 4 Prepared by proton exchange reaction of (K or Rb)$Ca_2NaNb_4O_{13}$ with aqueous HNO_3	

Table 13. $k = 4$ niobates of tetragonal or orthorhombic $A'A_{k-1}B_kO_{3k+1}$ (Dion-Jacobson type phases) with A' = alkali metal or H and A = Ca, Sr, Na.

Composition structure type	***N***	***a***, ***b***, ***c*** (Å), β (°), ***V*** (Å^3), ***Z*** **Remarks / Special Features**	**Ref.**
$KCa_2Na_4Nb_7O_{22}$ $k = 7$	$4d^0$	3.89, 3.87, 60.57, 90, 911.1, 2 Also hydrated phases reported	[87]
$KCa_2Na_3Nb_6O_{19}$ $k = 6$	$4d^0$	3.88, 3.87, 52.80, 90, 793.2, 2 Also hydrated phases reported	
$KCa_2Na_2Nb_5O_{16}$ $k = 5$	$4d^0$	3.88, 3.86, 45.00, 90, 674.8, 2 Also hydrated phases reported	

Table 14. $k \geq 5$ niobates of orthorhombic $A'A_{k-1}B_kO_{3k+1}$ (Dion-Jacobson type phases) with A' = K and A = (Ca,Na).

Composition	***N***	***a***, ***b***, ***c*** (Å), β (°), ***V*** (Å^3), ***Z*** **Remarks / Special Features**	**Ref.**
$CeTaO_{4+y}$	$5d^0$	2×3.88, 5.53, 7.62, 100.9, 2×160.7, 4 ($y = 0$) 1×3.85, 5.49, 7.62, 102.5, 1×157.3, 2 ($y = 0.17$) Centrosym. space group $P2_1/c$ (No. 14) ($y = 0$) Crystals grown in Ar by Czochralski technique ($y = 0$) For $y > 0$ over-stoichiometric with respect to x Oxygen over-stoichiometry by partial oxidation of Ce^{3+} into Ce^{4+} ($0 < y \leq 0.17$) Excess oxygen probably accommodated in the interlayer region whereby $V/Z\,(y = 0.17) < V/Z\,(y = 0)$ because Ce^{4+} markedly smaller than Ce^{3+}	[180]
$LaTa_{0.75}W_{0.25}O_{4.13}$	$5d^0$ $6d^0$	Partial substitution of Ta^{5+} by W^{6+} or La^{3+} by Th^{4+}	[29]
$La_{0.8}Th_{0.2}TaO_{4.10}$	$5d^0$	Over-stoichiometric with respect to x Excess oxygen probably accommodated in the interlayer region	
$LaTa_{1-y}Nb_yO_4$	$5d^0$ $4d^0$	Nb content $y \leq 0.15$	[8]
$LaTaO_4$	$5d^0$	7.82, 5.58, 7.65, 101.5, 328.2, 4 Centrosym. space group $P2_1/c$ (No. 14)	[114] [30]
		3.93, 5.65, 14.70, 90, 326.7, 4 Crystals grown by a MoO_3 flux	[180]
		3.92, 5.61, 14.75, 90, 324.4, 4 Non-centrosym. space group $Cmc2_1$ (No. 36) Prepared by coprecipitation Indications for spontaneous polarization from second harmonic generation	[220]
		3.95, 5.66, 14.64, 90, 327.2, 4 ($T = 300$ °C) Non-centrosym. space group $Cmc2_1$ (No. 36) Structure determined by Rietfield refinement of neutron powder diffraction data	[30]

Table 15. Stoichiometric and significantly non-stoichiometric $n = 2$ members of monoclinic or orthorhombic $A_nB_nO_{3n+2} = ABO_x$ related to $LaTaO_4$ and $CeTaO_4$. The ideal $n = 2$ composition is ABO_4. This table represents a supplement of Table 2 in Ref. [127].

Composition	***N***	***a***, ***b***, ***c*** (Å), β (°), ***V*** (Å^3), ***Z*** **Remarks / Special Features**	**Ref.**
$PrTaO_4$	$5d^0$	7.73, 5.50, 7.61, 100.5, 318.1, 4 Centrosym. space group $P2_1/c$ (No. 14)	[180]
		3.86, 5.49, 15.00, 94.3, 317.5, 4 Prepared by floating zone melting	this work
$NdTaO_4$	$5d^0$	7.70, 5.47, 7.59, 100.0, 314.8, 4 Centrosym. space group $P2_1/c$ (No. 14) Prepared under high pressure	[221]

Table 16. $n = 2$ Pr and Nd tantalates of monoclinic $A_nB_nO_{3n+2} = ABO_x$. This table represents a supplement of Table 2 in Ref. [127].

Composition	***N***	***a***, ***b***, ***c*** (Å), β (°), ***V*** (Å^3), ***Z*** **Remarks / Special Features**	**Ref.**
$LaTi_{0.67}Ta_{0.33}O_{3.67}$	$3d^0$	3.91, 5.59, 20.20, 90, 441.7, 6	[222]
	$5d^0$	Non-centrosym. space group $Pmc2_1$ (No. 26)	[223]
		Prepared by coprecipitation	
		Structure determined by powder XRD	
		Structure type $n = 3$ (II), see Figure 4	
		Indications for spontaneous polarization from second harmonic generation	
$PrTi_{0.67}Ta_{0.33}O_{3.67}$	$3d^0$	3.87, 5.51, 20.30, 90, 432.0, 6	[223]
	$5d^0$	Non-centrosym. space group	
		Prepared by coprecipitation	
		Structure determined by powder XRD	
		Structure type $n = 3$ (II), see Figure 4	
		Indications for spontaneous polarization from second harmonic generation	
$Sr_{0.67}La_{0.33}TaO_{3.67}$	$5d^0$	3.96, 5.62, 20.87, 90, 464.9, 6	[224]
		Centrosym. space group Immm (No. 71)	
		Synthesized by a quenched melt of samples which were prepared by coprecipitation and subsequently calcinated at 1670 K	
		Presence of small amounts of an $n = 4$ and an unidentified phase	
		Structure determined by powder XRD	
		Structure type $n = 3$ (I), see Figure 4	
		La exclusively located at the central positions, i.e. full ordering of La^{3+} and Sr^{2+} at the A site, see Figure 12	
		No indications for spontaneous polarization from second harmonic generation	
		3.96, 5.63, 20.89, 90, 465.6, 6	this
		Prepared by floating zone melting	work

Table 17. $n = 3$ members of orthorhombic $A_nB_nO_{3n+2} = ABO_x$.

Composition	***N***	***a***, ***b***, ***c*** (Å), β (°), ***V*** (Å^3), ***Z*** **Remarks / Special Features**	**Ref.**
$NaWO_{3.50}$	$5d^0$	3.78, 5.43, 26.61, 90, 546, 8 Non-centrosym. space group $Cmc2_1$ (No. 36) Prepared under high pressure Structure determined by single crystal XRD	[174]
$EuTaO_{3.50}$	$5d^0$	3.95, 5.69, 27.14, 90, 611, 8 Centrosym. space group Cmcm (No. 63) Eu in the valence state Eu^{2+} Structure determined by single crystal XRD Crystals originated during attempts to prepare $EuGeO_3$ in a sealed Ta container	[86]
$Sr_{1-y}Eu_yTaO_{3.50}$ $0 \leq y \leq 1$	$5d^0$	Study by XRD, TGA, DTA, magnetic and spectral measurements on polycrystalline samples, Eu in the valence state Eu^{2+} Single phase range $0 \leq y < 0.75$ Lattice parameters in Ref. [183]	[183]

Table 18. $n = 4$ members with B = Ta or W of orthorhombic $A_nB_nO_{3n+2} = ABO_x$. This table represents a supplement of Table 3 in Ref. [127].

Composition	***N***	***a***, ***b***, ***c*** (Å), β (°), ***V*** (Å^3), ***Z*** **Remarks / Special Features**	**Ref.**
$SrNbO_{3.50}$	$4d^0$	3.97, 5.72, 26.86, 90, 610, 8 Non-centrosym. space group $Cmc2_1$ (No. 36) Crystals prepared by floating zone melting Dielectric measurements along *a*- , *b*- and *c*-axis in the temperature range 77 K $\leq T \leq$ 1670 K Ferroelectric with T_c = 1615 K, P_s along *b*-axis	[151]
		3.93, 5.68, 26.73, 90, 597, 8 Non-centrosym. space group $Cmc2_1$ (No. 36) Structure determined by single crystal XRD Crystals prepared by floating zone melting	[78]
		3.95, 5.70, 26.77, 90, 603, 8 Superspace group $Cmc2_1(\alpha 00)0s0$ Incommensurate structure determined by single crystal XRD using synchrotron radiation Crystals prepared by floating zone melting Incommensurate modulation results from the attempt to resolve the strain from very short Sr − O distances of Sr at the border of the layers	[33]
		Phase transitions / different phases studied by structural, dielectric and optical measurements: $T >$ 1615 K: paraelectric, centrosym. space group Cmcm (No. 63) $T <$ 1615 K: ferroelectric, P_s along *b*-axis, non-centrosym. space group $Cmc2_1$ (No. 36) $T <$ 488 K: ferroelectric, P_s along *b*-axis, incommensurate structure $T <$ 117 K: ferroelectric, P_s in *bc*-plane, incommensurate structure For a theory of the phase transitions see Ref. [103]	[151] [3] [162] [246] [24] [249] [17] [103]
		Thin films prepared by sol-gel method and investigated by XRD and dielectric measurements Further references for thin films in Ref. [202]	[202]

Table 19. $n = 4$ $SrNbO_{3.50}$ of orthorhombic $A_nB_nO_{3n+2} = ABO_x$. P_s is the spontaneous polarization. This table represents a supplement of Table 4 in Ref. [127].

Composition	***N***	***a***, ***b***, ***c*** (Å), β (°), ***V*** (Å^3), ***Z*** **Remarks / Special Features**	**Ref.**
$Sr_{0.8}La_{0.2}NbO_{3.50}$	$4d^{0.20}$	3.99, 5.65, 26.56, 90, 598, 8 Prepared by floating zone melting Weakly pronounced quasi-1D metal along a-axis at high T Study of many physical properties: see Table 47 and 48	[127] [113] [17]
$Sr_{1-y}Eu_yNbO_{3.50}$ $0 \leq y \leq 1$	$4d^0$	Study by XRD, TGA, DTA, magnetic and spectral measurements on polycrystalline samples, Eu in the valence state Eu^{2+} Single phase range $0 \leq y \leq 0.5$ Lattice parameters in Ref. [183]	[183]
$Sr_{1-y}Ba_yNbO_{3.50}$	$4d^0$	$0 \leq y \leq 0.32$ Crystals prepared by floating zone melting Study of phase transitions by thermal and dielectric measurements on crystals	[4]
		$0 \leq y < 0.35$ (single phase range) Study on polycrystalline samples by XRD and IR and Raman spectroscopy	[172]
		$0 \leq y \leq 0.6$ Dielectric measurements on polycrystalline samples Ferroelectric T_c decreases with increasing y	[151]
		3.97, 5.73, 26.81, 90, 609.8, 8 ($y = 0.2$) Prepared by floating zone melting	this work
$Sr_{0.8}Ba_{0.1}Ca_{0.1}NbO_{3.50}$	$4d^0$	3.95, 5.70, 26.75, 90, 602.2, 8 Prepared by floating zone melting	this work
$Sr_{0.6}Ba_{0.2}Ca_{0.2}NbO_{3.50}$	$4d^0$	3.95, 5.67, 26.74, 90, 600.2, 8 Prepared by floating zone melting	
$Sr_{0.86}Sm_{0.14}NbO_{3.51}$	$4d^{0.12}$	3.97, 5.65, 26.58, 90, 595.3, 8 Prepared by floating zone melting	

Table 20. $n = 4$ niobates of orthorhombic $A_nB_nO_{3n+2} = ABO_x$ related to $SrNbO_{3.50}$. This table represents a supplement of Table 4 and 5 in Ref. [127].

Composition	***N***	***a***, ***b***, ***c*** (Å), β (°), ***V*** (Å^3), ***Z*** **Remarks / Special Features**	**Ref.**
$CaNbO_{3.50}$	$4d^0$	7.72, 5.51, 13.40, 98.3, 564, 8 Non-centrosym. space group $P2_1$ (No. 4) Crystals prepared by Bridgman technique Ferroelectric with $T_c > 1850$ K = melting point	[149]
		7.70, 5.50, 13.39, 98.3, 561, 8 Non-centrosym. space group $P2_1$ (No. 4) Structure determined by single crystal XRD Crystals prepared by floating zone melting	[80]
		Second harmonic generation suggests a phase transition into an incommensurate phase at $T \approx 750$ K on cooling	[249]
		3.84, 5.49, 26.45, 90, 558, 8 Prepared by floating zone melting	[127]
		7.70, 5.50, 13.39, 98.3, 561, 8 Large crystals grown by Czochralski technique Reported as new non-linear optical crystal: intensity of second harmonic generation ≈ 5 times higher than that of KDP (KH_2PO_4) crystals	[135]
$SrNb_{1-y}Ta_yO_{3.50}$ $0.01 \leq y \leq 0.08$	$4d^0$ $5d^0$	Study of phase transitions in the temperature range 15 K $\leq T \leq$ 500 K by dielectric measurements on crystals Crystals prepared by floating zone melting	[164]
$SrNb_{1-y}V_yO_{3.50}$ $0 \leq y \leq 0.15$	$4d^0$ $3d^0$	Study of structural and dielectric features on polycrystalline samples Dielectric constant increases with increasing y up to $y = 0.10$	[197]
		3.95, 5.70, 26.76, 90, 603, 8 ($y = 0.10$) Prepared by floating zone melting	this work

Table 21. $n = 4$ members of monoclinic or orthorhombic $A_nB_nO_{3n+2} = ABO_x$ related to $CaNbO_{3.50}$ and $SrNbO_{3.50}$. This table represents a supplement of Table 4, 5 and 7 in Ref. [127].

Composition	***N***	***a***, ***b***, ***c*** (Å), β (°), ***V*** (Å^3), ***Z*** **Remarks / Special Features**	**Ref.**
$La_{0.9}Sm_{0.1}TiO_{3.50}$	$3d^0$	7.80, 5.53, 13.00, 98.5, 555, 8 Prepared by floating zone melting	this work
$LaTiO_{3.50}$	$3d^0$	7.81, 5.55, 13.02, 98.7, 558, 8 Non-centrosym. space group $P2_1$ (No. 4) Crystals prepared by floating zone melting Study of ferroelectric, electrooptic and piezoelectric properties Ferroelectric with $T_c = 1770$ K	[150]
		7.81, 5.54, 13.01, 98.7, 557, 8 Non-centrosym. space group $P2_1$ (No. 4) Crystals prepared by floating zone melting Structure determined by single crystal XRD	[191]
		3.95, 5.61, 25.92, 90, 575, 8 ($T = 1173$ K) Non-centrosym. space group $Cmc2_1$ (No. 36) Crystals prepared by floating zone melting Structure determined by single crystal XRD	[82]
		Orthorhombic for $T > 1053$ K Incommensurate phase between $T = 993$ K and 1053 K	[82] [211] [163]
		7.81, 5.55, 13.02, 98.7, 558, 8 Non-centrosym. space group $P2_1$ (No. 4) Crystals prepared by floating zone melting Study of dielectric and optical properties	[248]
		7.81, 5.55, 13.00, 98.6, 575, 8 Prepared by floating zone melting	[127]
		Study of photocatalytic activity (and electronic band structure [77]) for water splitting	[77,101] [238]
		Structural study on thin films grown by MBE	[195,196]
		Preparation and characterization of thin films	[165]
		Thin films grown in capacitor structures show two charge-controlled transport regimes which can be used for switching the devices between two voltages states	[192]

Table 22. $n = 4$ titanates of monoclinic or orthorhombic $A_nB_nO_{3n+2} = ABO_x$ related to $LaTiO_{3.50}$. This table represents a supplement of Table 6 in Ref. [127].

Composition	***N***	***a***, ***b***, ***c*** (Å), β (°), ***V*** (Å^3), ***Z*** **Remarks / Special Features**	**Ref.**
$PrTiO_{3.50}$	$3d^0$	7.70, 5.49, 13.00, 98.5, 543, 8 Non-centrosym. space group $P2_1$ (No. 4) Structure determined by single crystal XRD Crystals prepared by floating zone melting	[107]
		7.71, 5.48, 13.00, 98.8, 543, 8 Non-centrosym. space group $P2_1$ (No. 4) Crystals prepared by floating zone melting Study of dielectric and optical properties	[248]
		7.69, 5.47, 12.99, 98.4, 541, 8 Prepared by floating zone melting	this work
		Study of photocatalytic activity (and electronic band structure [77]) for water splitting	[77] [238]
$Ce_{0.5}Sm_{0.5}TiO_{3.50}$	$3d^0$	7.66, 5.45, 12.99, 98.3, 537, 8 Prepared by floating zone melting	this work
$Ce_{0.5}Pr_{0.5}TiO_{3.50}$	$3d^0$	7.72, 5.49, 12.99, 98.4, 544, 8 Prepared by floating zone melting	
$CeTiO_{3.50}$	$3d^0$	7.75, 5.50, 12.98, 98.6, 548, 8 Polycrystalline sample prepared at 1400° in Ar using the mixture CeO_2 + 0.25 TiN + 0.75 TiO_2	[201]
		7.74, 5.50, 12.99, 98.6, 547, 8 Non-centrosym. space group $P2_1$ (No. 4) Crystals prepared by crystallization from a melt achieved by high frequency heating	[248]
		7.76, 5.51, 12.99, 98.5, 549, 8 Prepared by floating zone melting in Ar using the mixture CeO_2 + TiO_2	this work

Table 23. $n = 4$ titanates of monoclinic $A_nB_nO_{3n+2} = ABO_x$ related to $CeTiO_{3.50}$ and $PrTiO_{3.50}$. This table represents a supplement of Table 6 in Ref. [127].

Composition	***N***	***a***, ***b***, ***c*** (Å), β (°), ***V*** (Å^3), ***Z*** **Remarks / Special Features**	**Ref.**
$La_{0.1}Sm_{0.9}TiO_{3.50}$	$3d^0$	7.63, 5.43, 12.99, 98.5, 532, 8 Prepared by floating zone melting	this work
$Pr_{0.5}Gd_{0.5}TiO_{3.50}$	$3d^0$	7.63, 5.43, 13.00, 98.4, 533, 8 Prepared by floating zone melting	
$La_{0.4}Sm_{0.5}Eu_{0.1}TiO_{3.50}$	$3d^0$	7.68, 5.47, 12.96, 98.3, 538, 8 Prepared by floating zone melting	
$NdTiO_{3.50}$	$3d^0$	7.68, 5.48, 13.02, 98.5, 542, 8 Non-centrosym. space group $P2_1$ (No. 4) Crystals prepared by floating zone melting Study of ferroelectric, electrooptic and piezoelectric properties Ferroelectric with $T_c > 1770$ K	[102]
		7.68, 5.47, 26.01, 98.4, 1080, 16 Non-centrosym. space group $P2_1$ (No. 4) Structure determined by single crystal XRD Crystals prepared by cooling of a melt	[189]
		7.67, 5.48, 13.01, 98.5, 541, 8 Non-centrosym. space group $P2_1$ (No. 4) Crystals prepared by floating zone melting Study of dielectric and optical properties	[248]
		7.67, 5.46, 12.99, 98.5, 538, 8 Prepared by floating zone melting	this work
		Study of photocatalytic activity (and electronic band structure [77]) for water splitting	[77] [238]

Table 24. Miscellaneous $n = 4$ titanates of monoclinic $A_nB_nO_{3n+2} = ABO_x$. This table represents a supplement of Table 6 in Ref. [127].

Composition	***N***	***a***, ***b***, ***c*** (Å), β (°), ***V*** (Å^3), ***Z*** **Remarks / Special Features**	**Ref.**
$EuTiO_{3.50}$	$3d^0$	7.54, 5.38, 12.88, 98.3, 517, 8 Non-centrosym. space group $P2_1$ (No. 4) Prepared under high pressure	[219]
		7.55, 5.39, 12.86, 98.3, 518, 8 Prepared under high pressure Study of ferroelectric properties by second harmonic generation Ferroelectric with $T_c \approx 1500$ K Study of thermal stability	[210]
		Study of the electronic structure of the two modifications, $n = 4$ type (prepared under high pressure) and pyrochlore type, by x-ray emission and photoelectron spectroscopy	[18]
$SmTiO_{3.50}$	$3d^0$	7.56, 5.39, 12.90, 98.5, 520, 8 Non-centrosym. space group $P2_1$ (No. 4) Prepared under high pressure Study of thermal stability Further references in Ref. [219]	[219]
		Prepared under high pressure Study of ferroelectric properties by second harmonic generation Ferroelectric with $T_c = 1350$ K Further references in Ref. [210]	[210]
		Study of the electronic structure of the two modifications, $n = 4$ type (prepared under high pressure) and pyrochlore type, by x-ray emission and photoelectron spectroscopy	[18]
		3.81, 5.42, 25.69, 90, 530, 8 Non-centrosym. space group $Cmc2_1$ (No. 36) Prepared by annealing $SmTiO_3$ powder at 800 °C in air	[250]

Table 25. $n = 4$ titanates of monoclinic or orthorhombic $A_nB_nO_{3n+2} = ABO_x$ with A = Sm or Eu. If these titanates are prepared by common techniques they crystallize in the cubic pyrochlore structure. This table represents a supplement of Table 6 in Ref. [127].

Composition	***N***	***a***, ***b***, ***c*** (Å), β (°), ***V*** (Å^3), ***Z*** **Remarks / Special Features**	**Ref.**
$PrTi_{0.5}Ta_{0.25}Cr_{0.25}O_{3.50}$	$3d^0$ $5d^0$	7.76, 5.49, 25.77, 90, 1098, 16 Prepared by coprecipitation	[209]
$LaTi_{0.5}Ta_{0.25}B'_{0.25}O_{3.50}$	$3d^0$ $5d^0$	B' = Sc, Cr, Fe or Ga Prepared by coprecipitation Lattice parameters in Ref. [209]	
$LnTi_{0.5}Nb_{0.25}Cr_{0.25}O_{3.50}$	$3d^0$ $4d^0$	Ln = La, Pr or Nd Prepared by coprecipitation Lattice parameters in Ref. [209]	
$LnTi_{0.5}Nb_{0.25}B'_{0.25}O_{3.50}$	$3d^0$ $4d^0$	B' = Sc, Fe or Ga for Ln = La B' = Fe for Ln = Pr Prepared by coprecipitation Lattice parameters in Ref. [209]	
$LaTi_{0.75}Nb_{0.125}Fe_{0.125}O_{3.50}$	$3d^0$ $4d^0$	7.83, 5.55, 25.77, 90, 1120, 16 Non-centrosym. space group $Pna2_1$ (No. 33)	[225]
$LaTi_{0.5}Ta_{0.33}Zn_{0.17}O_{3.50}$	$3d^0$ $5d^0$	7.84, 5.58, 26.00, 90, 1137, 16	[208]
$LaTi_{0.5}Ta_{0.33}Mg_{0.17}O_{3.50}$	$3d^0$ $5d^0$	7.84, 5.57, 26.00, 90, 1140, 16	
$LaTi_{0.5}Nb_{0.33}Zn_{0.17}O_{3.50}$	$3d^0$ $4d^0$	7.85, 5.57, 25.95, 90, 1135, 16	
$LaTi_{0.5}Nb_{0.33}Mg_{0.17}O_{3.50}$	$3d^0$ $4d^0$	7.87, 5.56, 25.87, 90, 1132, 16 Melts probably congruently	
		7.84, 5.58, 25.88, 90, 1133, 16 Prepared by floating zone melting	this work
$La_{0.6}Ca_{0.4}Ti_{0.6}Nb_{0.4}O_{3.50}$	$3d^0$ $4d^0$	7.85, 5.53, 26.15, 98.4, 1124, 16 Prepared by floating zone melting	this work
$Pr_{0.5}Ca_{0.5}Ti_{0.5}Nb_{0.5}O_{3.50}$	$3d^0$ $4d^0$	7.71, 5.50, 25.95, 90, 1100, 16 Prepared under high pressure	[219]
$La_{0.5}Ca_{0.5}Ti_{0.5}Ta_{0.5}O_{3.50}$	$3d^0$ $5d^0$	7.83, 5.56, 26.03, 90, 1133, 16 Prepared under high pressure	

Table 26. Miscellaneous $n = 4$ members of orthorhombic or monoclinic $A_nB_nO_{3n+2} = ABO_x$. This table represents a supplement of Table 7 in Ref. [127].

Composition	***N***	***a***, ***b***, ***c*** (Å), β (°), ***V*** (Å^3), ***Z*** **Remarks / Special Features**	**Ref.**
$Sr_{0.75}La_{0.25}Nb_{0.95}O_{3.43}$	$4d^{0.14}$	3.98, 5.65, 26.54, 90, 596.9, 8 Under-stoichiometric with respect to B site occupation and x	this work
$Sr_{0.86}Sm_{0.14}NbO_{3.57}$	$4d^{0}$	3.96, 5.67, 26.67, 90, 598.6, 8 Over-stoichiometric with respect to x	
$Sr_{0.75}La_{0.2}NbO_{3.44}$	$4d^{0.23}$	3.99, 5.66, 26.55, 90, 598.7, 8 Under-stoichiometric with respect to A site occupation and x	
$La_{0.6}Ca_{0.4}Ti_{0.6}Nb_{0.4}O_{3.40}$	$d^{0.20}$	7.82, 5.52, 26.20, 98.3, 1120, 16 Under-stoichiometric with respect to x	
$La_{0.56}Ca_{0.4}Ti_{0.6}Nb_{0.4}O_{3.35}$	$d^{0.17}$	7.83, 5.52, 26.20, 98.3, 1121, 16 Under-stoichiometric with respect to A site occupation and x	

Table 27. Significantly non-stoichiometric $n = 4$ compounds $A_{1-w}BO_x$ with $0 \leq w \leq 0.05$ of orthorhombic or monoclinic $A_nB_nO_{3n+2}$. Also an $n = 4$ niobate with a deficiency at the B site, $AB_{0.95}O_x$, is listed. The ideal $n = 4$ composition is $ABO_{3.50}$. All materials were prepared by floating zone melting. This table represents a supplement of Table 4, 5, 7 and 18 in Ref. [127].

Composition	***N***	***a***, ***b***, ***c*** (Å), β (°), ***V*** (Å^3), ***Z*** **Remarks / Special Features**	**Ref.**
$CeTiO_{3.47}$	$3d^{0.06}$	7.76, 5.50, 82.7, 97.6, 3499, 50 Prepared by floating zone melting	[127]
$Ce_{0.95}TiO_{3.39}$	$3d^{0.07}$	7.74, 5.49, 82.9, 97.6, 3497, 50 Prepared by floating zone melting Under-stoichiometric with respect to A site occupation and x	this work

Table 28. Two $n = 4.33$ titanates of monoclinic $A_nB_nO_{3n+2}$, a compound with the ideal stoichiometric composition $ABO_{3.47}$ and a significantly non-stoichiometric material with the composition $A_{0.95}BO_{3.39}$. This table represents a supplement of Table 8 and 18 in Ref. [127].

Composition	***N***	***a***, ***b***, ***c*** (Å), β (°), ***V*** (Å^3), ***Z*** **Remarks / Special Features**	**Ref.**
$Sr_{0.8}Ba_{0.2}NbO_{3.45}$	$4d^{0.10}$	7.93, 5.72, 59.10, 90, 2682, 36 Prepared by floating zone melting	this work
$Sr_{0.9}Ba_{0.1}NbO_{3.45}$	$4d^{0.10}$	7.92, 5.71, 59.09, 90, 2674, 36 Prepared by floating zone melting	
$SrNb_{0.8}Ta_{0.2}O_{3.45}$	$4d^{0.12}$	7.92, 5.68, 59.23, 90, 2663, 36 Prepared by floating zone melting	
$SrNbO_{3.45}$	$4d^{0.10}$	7.90, 5.68, 59.30, 90, 2661, 36 Prepared by floating zone melting Quasi-1D metal along *a*-axis at high *T* Study of many physical properties: see Table 47 and 48	[127] [113] [110] [136] [17]
$Sr_{0.6}Ba_{0.2}Ca_{0.2}NbO_{3.46}$	$4d^{0.08}$	7.87, 5.67, 59.35, 90, 2647, 36 Prepared by floating zone melting	this work
$Sr_{0.56}Ca_{0.44}NbO_{3.45}$	$4d^{0.10}$	7.82, 5.57, 59.03, 96.8, 2550, 36 Prepared by floating zone melting	
$Sr_{0.44}Ca_{0.56}NbO_{3.45}$	$4d^{0.10}$	7.81, 5.56, 59.09, 96.8, 2547, 36 Prepared by floating zone melting	
$Ca_{0.95}Sm_{0.05}NbO_{3.45}$	$4d^{0.14}$	3.87, 5.50, 58.28, 90, 1238, 18 Prepared by floating zone melting	
$SrNb_{0.89}Ti_{0.11}O_{3.44}$	$4d^0$ $3d^0$	3.95, 5.68, 59.36, 90, 1333, 18 Polycrystalline sample Structural study by TEM and powder XRD Dielectric constant $\varepsilon \approx 56$ (100 kHz, 20 °C)	[120]
		TEM study on polycrystalline samples reveals following symmetry, centrosym. space groups, and (Nb,Ti)O_6 octahedra tilting on cooling: 390 °C $\leq T \leq$ 1000 °C: orthorhombic, Pbam (No. 55), tilted $T <$ 390 °C: monoclinic, $P2_1/c$ (No. 14), tilted	[122]

Table 29. $n = 4.5$ members of orthorhombic or monoclinic $A_nB_nO_{3n+2} = ABO_x$ related to $SrNbO_{3.44}$ and $CaNbO_{3.44}$. This table represents a supplement of Table 10 in Ref. [127].

Composition	***N***	***a***, ***b***, ***c*** (Å), β (°), ***V*** (Å^3), ***Z*** **Remarks / Special Features**	**Ref.**
[1] $Ce_{0.5}Sm_{0.5}TiO_{3.44}$	$3d^{0.12}$	7.90, 5.49, 57.08, 97.5, 2452, 36 Prepared by floating zone melting	this work
$LaTi_{0.89}Al_{0.11}O_{3.44}$	$3d^0$	4.00, 5.53, 57.07, 90, 1262, 18	[55]
$Pr_{0.89}Ca_{0.11}TiO_{3.44}$	$3d^0$	3.86, 5.45, 56.99, 90, 1198, 18	
$La_{0.89}Ca_{0.11}TiO_{3.44}$	$3d^0$	7.81, 5.54, 57.63, 97.8, 2468, 36	[154]
		Structural study by XRD and TEM	[155]
		7.81, 5.54, 57.8, 97.8, 2478, 36 Prepared by floating zone melting	[11]
		7.81, 5.54, 57.3, 97.2, 2457, 36 Prepared by floating zone melting	this work
$LaTi_{0.94}Mg_{0.06}O_{3.44}$	$3d^0$	3.91, 5.54, 57.06, 90, 1237, 18 (from powder XRD)	[240]
		≈ 7.8, ≈ 5.5, ≈ 57, ≈ 98, ≈ 2422, 36 Centrosym. space group $P2_1/c$ (No. 14) (from electron diffraction)	
		Structural study by XRD and TEM and dielectric measurements on polycrystalline samples	
		Dielectric constant ε = 51 (8.4 GHz, 25 °C)	

Table 30. $n = 4.5$ titanates of monoclinic or orthorhombic $A_nB_nO_{3n+2} = ABO_x$. [1]Because a thermogravimetric determination of x was not possible, as discussed in Ref. [127] for $La_{0.5}Ce_{0.5}TiO_{3.4}$, the ideal $n = 4.5$ value $x = 3.44$ was assigned. This table represents a supplement of Table 9 in Ref. [127].

Composition	***N***	***a***, ***b***, ***c*** (Å), β (°), ***V*** (Å^3), ***Z*** **Remarks / Special Features**	**Ref.**
$Sr_{0.75}Eu_{0.2}NbO_{3.41}$	$4d^{0.09}$	7.90, 5.69, 59.15, 90, 2657, 36 Under-stoichiometric with respect to A site occupation and x Eu in the valence state Eu^{2+}	this work
$Ca_{0.85}Sr_{0.1}NbO_{3.40}$	$4d^{0.10}$	7.66, 5.49, 58.85, 96.4, 2460, 36 Under-stoichiometric with respect to A site occupation and x	
$Ca_{0.95}NbO_{3.41}$	$4d^{0.09}$	7.66, 5.49, 58.82, 96.4, 2457, 36 Under-stoichiometric with respect to A site occupation and x	
$La_{0.95}TiO_{3.38}$	$3d^{0.10}$	7.90, 5.52, 56.86, 97.5, 2460, 36 Under-stoichiometric with respect to A site occupation and x	

Table 31. Significantly non-stoichiometric $n = 4.5$ compounds $A_{0.95}BO_x$ of orthorhombic or monoclinic $A_nB_nO_{3n+2}$. The ideal $n = 4.5$ composition is $ABO_{3.44}$. All materials were prepared by floating zone melting. This table represents a supplement of Table 9, 10 and 18 in Ref. [127].

Composition	***N***	***a***, ***b***, ***c*** (Å), β (°), ***V*** (Å^3), ***Z*** **Remarks / Special Features**	**Ref.**
$SrNbO_{3.41}$	$4d^{0.18}$	3.99, 5.67, 32.45, 90, 734, 10 Prepared by floating zone melting	[127]
		Structure determined by single crystal XRD 4.00, 5.67, 32.46, 90, 736, 10 Centrosym. space group Pnnm (No. 58)	[2]
		Quasi-1D metal along a-axis at high T	[127,113]
		Extensive study of many physical properties: see Table 47 and 48	[111,110] [17,242]
$SrNbO_{3.2}$	$4d^{0.6}$	3.99, 5.68, 32.48, 90, 736, 10 Non-centrosym. space group $Pmn2_1$ (No. 31) Structure determined by single crystal XRD Small crystals prepared in an H_2/H plasma Physical properties are not reported In Ref. [193] the structure is not discussed in terms of $A_nB_nO_{3n+2}$, however it can be considered as an oxygen-deficient $n = 5$ type with ordered oxygen vacancies, see Fig. 44	[193]
$SrNb_{0.8}Ti_{0.2}O_{3.40}$	$4d^0$ $3d^0$	3.95, 5.66, 32.52, 90, 728, 10 Centrosym. space group Pnnm (No. 58) Structure determined by single crystal XRD Crystals prepared by flux technique	[39]
		TEM study on polycrystalline samples reveals following symmetry, centrosym. space groups, (Nb,Ti)O_6 octahedra tilting on cooling: $T > 600$ °C: orthorh., Immm (No. 61), untilted $T < 600$ °C: orthorh., Pnnm (No. 58), tilted $T < 250$ °C: incommensurate phase $T < 180$ °C: monocl., P21/c (No. 14), tilted	[122]
		3.95, 5.66, 32.54, 90, 727, 10 Polycrystalline samples Dielectric constant $\varepsilon \approx 80$ (100 kHz, 20 °C)	[120]
		3.95, 5.59, 32.6, 90, 720, 10 Polycrystalline samples Dielectric constant $\varepsilon \approx 60$ (600 kHz, 20 °C) Antiferroelectric with $T_c \geq 590$ °C	[84]
		Structural description by superspace approach	[46]

Table 32. $n = 5$ members of orthorhombic $A_nB_nO_{3n+2} = ABO_x$ related to $SrNbO_{3.40}$. This table represents a supplement of Table 12 and 14 in Ref. [127].

Composition	***N***	***a***, ***b***, ***c*** (Å), β (°), ***V*** (Å^3), ***Z*** **Remarks / Special Features**	**Ref.**
$CaNbO_{3.41}$	$4d^{0.18}$	3.88, 5.49, 32.03, 90, 682, 10 Prepared by floating zone melting According to resistivity measurements on crystals: quasi-1D metal along *a*-axis at high *T* and metal-to-semiconductor transition at low *T*	[127]
		Structure determined by single crystal XRD 7.75, 5.49, 32.24, 96.8, 1363, 20 Centrosym. space group $P2_1/c$ (No. 14)	[63]
$CaNbO_{3.4}$	$4d^{0.2}$	3.86, 5.47, 31.92, 90, 736, 10 Structural study by electron microscopy and diffraction Physical properties are not reported	[73]
		7.74, 5.49, 32.28, 96.9, 1364, 20 Centrosym. space group $P2_1/c$ (No. 14) Polycrystalline sample Physical properties are not reported	[251]
$CaNb_{0.8}Ti_{0.2}O_{3.40}$	$4d^0$	7.69, 5.48, 32.33, 96.8, 1353, 20	[154]
	$3d^0$	7.69, 5.48, 32.25, 96.8, 1349, 20 Centrosym. space group $P2_1/c$ (No. 14) Structure determined by single crystal XRD Crystals prepared by floating zone melting	[64]
		Structural description by superspace formalism	[65]
		3.84, 5.49, 32.05, 90, 676, 10 Non-centrosym. space group P2nn (No. 34) Structure determined by powder XRD	[226]
$SrTa_{0.8}Ti_{0.2}O_{3.40}$	$5d^0$ $3d^0$	7.91, 5.62, 33.03, 97.2, 1458, 20 Prepared by floating zone melting	this work
$Sr_{0.8}Na_{0.2}NbO_{3.40}$	$4d^0$	3.88, 5.66, 32.53, 90, 714, 10	[85]

Table 33. $n = 5$ members of orthorhombic or monoclinic $A_nB_nO_{3n+2} = ABO_x$ related to $CaNbO_{3.40}$ or $SrNbO_{3.40}$. This table represents a supplement of Table 11, 12 and 14 in Ref. [127].

Composition	***N***	***a***, ***b***, ***c*** (Å), β (°), ***V*** (Å^3), ***Z*** **Remarks / Special Features**	**Ref.**
$Ca_{0.8}Eu_{0.2}NbO_{3.40}$	$4d^{0.20}$	3.89, 5.53, 32.06, 90, 690, 10 Prepared by floating zone melting Eu in the valence state Eu^{2+}	this work
$Ca_{0.91}Eu_{0.09}NbO_{3.41}$	$4d^{0.18}$	7.77, 5.51, 32.26, 96.8, 1371, 20 Prepared by floating zone melting Eu in the valence state Eu^{2+}	
$Ca_{0.73}Sr_{0.2}Sm_{0.07}NbO_{3.41}$	$4d^{0.25}$	7.81, 5.53, 32.04, 90, 1385, 20 Prepared by floating zone melting	
$Ca_{0.93}Sm_{0.07}NbO_{3.42}$	$4d^{0.23}$	3.87, 5.47, 32.07, 96.6, 675, 10 Prepared by floating zone melting	
$Ca_{0.8}Na_{0.2}NbO_{3.40}$	$4d^0$	3.85, 5.50, 32.14, 90, 680, 10	[152]
		7.71, 5.48, 32.35, 90, 1358, 20 Centrosym. space group $P2_1/c$ (No. 14) Structure determined by single crystal XRD Crystals prepared by heating the composition $Ca_{0.67}Na_{0.33}NbO_{3.33}$ at 1480 °C in O_2	[252]
		Structural description by superspace approach and prediction of symmetry properties for the whole $4d^0$ series $(Ca,Na)_nNb_nO_{3n+2}$	[47]

Table 34. $n = 5$ niobates of orthorhombic or monoclinic $A_nB_nO_{3n+2} = ABO_x$ related to $CaNbO_{3.40}$. This table represents a supplement of Table 11 in Ref. [127].

Composition	***N***	***a***, ***b***, ***c*** (Å), β (°), ***V*** (Å^3), ***Z*** **Remarks / Special Features**	**Ref.**
$La_{0.8}Ca_{0.2}TiO_{3.40}$	$3d^0$	7.78, 5.52, 31.56, 97.1, 1346, 20	[154]
		7.79, 5.52, 31.50, 97.0, 1345, 20 Prepared by floating zone melting	this work
		Optical (IR) spectroscopy on crystals along *a*- and *b*-axis at $T = 300$ K	[218]
$La_{0.87}Ca_{0.13}TiO_{3.39}$	$3d^{0.09}$	7.83, 5.52, 31.05, 96.1, 1335, 20	this work
		Optical (IR) spectroscopy on crystals at $T = 300$ K: quasi-1D metal along *a*-axis	
$La_{0.9}Ca_{0.1}TiO_{3.38}$	$3d^{0.14}$	7.83, 5.52, 31.07, 96.2, 1336, 20	
		Optical (IR) spectroscopy on crystals at $T = 300$ K: quasi-1D metal along *a*-axis	[218]
$LaTiO_{3.41}$	$3d^{0.18}$	7.86, 5.53, 31.48, 97.1, 1357, 20	[127]
		Prepared by floating zone melting	
		Structure determined by single crystal XRD 7.86, 5.53, 31.45, 97.2, 1356, 20 Centrosym. space group $P2_1/c$ (No. 14)	[34]
		According to optical (IR) and resistivity measurements on crystals: quasi-1D metal along *a*-axis at high T and metal-to-semiconductor transition at low T ($T < 100$ K), indications for strong electron-phonon coupling and at low T for a phase transition and an energy gap of ≈ 6 meV	[127] [112]
		Structural study under pressure by powder XRD: structure stable up to 18 GPa and pronounced anisotropy in the axis compressibilities	[134]
		Optical (mid-IR) micro-spectroscopy on crystals under pressure at room temperature indicates onset of a dimensional crossover at a pressure of about 15 GPa	[51]

Table 35. $n = 5$ titanates of monoclinic $A_nB_nO_{3n+2} = ABO_x$ related to $LaTiO_{3.40}$. This table represents a supplement of Table 13 and 14 in Ref. [127].

Composition	***N***	***a***, ***b***, ***c*** (Å), β (°), ***V*** (Å^3), ***Z*** **Remarks / Special Features**	**Ref.**
$LaTi_{0.8}Cr_{0.2}O_{3.40}$	$3d^0$	3.91, 5.52, 31.22, 90, 674, 10	[55]
$LaTi_{0.95}V_{0.05}O_{3.41}$	$3d^{0.23}$	7.84, 5.52, 31.40, 97.0, 1349, 20 Prepared by floating zone melting	this work
$La_{0.9}Sm_{0.1}Ti_{0.8}Al_{0.2}O_{3.40}$	$3d^0$	7.77, 5.51, 31.24, 96.7, 1328, 20 Prepared by floating zone melting	
$LaTi_{0.8}Al_{0.2}O_{3.40}$	$3d^0$	7.79, 5.51, 31.35, 97.3, 1334, 20 Prepared by floating zone melting	this work
		3.90, 5.51, 31.17, 90, 670, 10	[55]
$LaTi_{0.95}Al_{0.05}O_{3.40}$	$3d^{0.16}$	7.84, 5.51, 31.29, 96.9, 1343, 20 Prepared by floating zone melting	this work
$LaTi_{0.9}Mg_{0.1}O_{3.40}$	$3d^0$	3.92, 5.54, 31.30, 90, 679, 10 (from powder XRD) ≈ 7.8, ≈ 5.5, ≈ 31, ≈ 104, ≈ 1290, 20 Centrosym. space group $P2_1/c$ (No. 14) (from electron diffraction) Structural study by XRD and TEM and dielectric measurements on polycrystalline samples Dielectric constant ε = 34 (5.9 GHz, 25 °C)	[240]
		7.84, 5.53, 31.49, 97.3, 1355, 20 Prepared by floating zone melting	this work
$La_{0.8}Sr_{0.2}TiO_{3.40}$	$3d^0$	7.81, 5.53, 31.51, 97.1, 1350, 20 Structural study by TEM and powder XRD	[22]
		7.82, 5.54, 31.34, 90, 1357, 20 Structural study by TEM and powder XRD	[26] [27]
		7.80, 5.53, 31.55, 97.0, 1352, 20 Prepared by floating zone melting	this work

Table 36. $n = 5$ members of monoclinic or orthorhombic $A_nB_nO_{3n+2} = ABO_x$ related to $LaTiO_{3.40}$. This table represents a supplement of Table 13 and 14 in Ref. [127].

Composition	***N***	***a***, ***b***, ***c*** (Å), β (°), ***V*** (Å^3), ***Z*** **Remarks / Special Features**	**Ref.**
$La_{0.56}Sm_{0.44}TiO_{3.41}$	$3d^{0.18}$	7.83, 5.52, 31.09, 96.5, 1334, 20 Prepared by floating zone melting	this work
$La_{0.9}Sm_{0.1}TiO_{3.41}$	$3d^{0.18}$	7.84, 5.52, 31.40, 97.1, 1350, 20 Prepared by floating zone melting	
[1] $La_{0.76}Ce_{0.12}Yb_{0.12}TiO_{3.4}$	$3d^{0.2}$	7.81, 5.52, 31.23, 96.6, 1338, 20 Prepared by floating zone melting	
$LaTi_{0.8}Ga_{0.2}O_{3.40}$	$3d^0$	3.90, 5.52, 31.61, 90, 681, 10	[85]
		3.91, 5.52, 31.28, 90, 676, 10 Centrosym. space group Pmnn (No. 58) Structure determined by powder XRD Test by second harmonic generation indicates presence of inversion symmetry	[228]
$LaTi_{0.8}Fe_{0.2}O_{3.40}$	$3d^0$	3.91, 5.52, 31.33, 90, 676, 10	[55]
		3.92, 5.53, 31.33, 90, 679, 10 Centrosym. space group Pmnn (No. 58) Structure determined by powder XRD Fe exclusively located in the central octahedra, i.e. full ordering of Ti^{4+} and Fe^{3+} at the *B* site, see Figure 16	[227] [228]
		7.82, 5.54, 31.45, 97.0, 1352, 20 Prepared by floating zone melting	this work
$LaTi_{0.8}Mn_{0.2}O_{3.4}$	$3d^0$	7.86, 5.54, 31.55, 97.4, 1363, 20 (Ar) 7.86, 5.54, 31.54, 97.5, 1360, 20 (air) 7.86, 5.53, 31.55, 97.8, 1358, 20 (O_2) Prepared by floating zone melting in Ar, air and O_2	this work

Table 37. $n = 5$ members of monoclinic or orthorhombic $A_nB_nO_{3n+2} = ABO_x$ related to $LaTiO_{3.40}$. This table represents a supplement of Table 13 and 14 in Ref. [127]. [1]Because a thermogravimetric determination of x was not possible, as discussed in Ref. [127] for $La_{0.5}Ce_{0.5}TiO_{3.4}$, the ideal $n = 5$ value $x = 3.4$ was assigned. This table represents a supplement of Table 13 in Ref. [127].

Composition	***N***	***a***, ***b***, ***c*** (Å), β (°), ***V*** (Å^3), ***Z*** **Remarks / Special Features**	**Ref.**
$PrTi_{0.8}Ga_{0.2}O_{3.40}$	$3d^0$	3.85, 5.47, 31.55, 90, 664, 10	[85]
		7.73, 5.47, 31.46, 97.0, 1328, 20 Centrosym. space group $P2_1/c$ (No. 14) Structure determined by powder XRD	[229]
$PrTi_{0.8}Fe_{0.2}O_{3.40}$	$3d^0$	7.74, 5.49, 31.52, 97.1, 1329, 20 Centrosym. space group $P2_1/c$ (No. 14) Structure determined by powder XRD Fe exclusively located in the central octahedra, i.e. full ordering of Ti^{4+} and Fe^{3+} at the *B* site, see Figure 16	[227]
		3.85, 5.46, 31.40, 90, 660, 10	
$PrTi_{0.8}Cr_{0.2}O_{3.40}$	$3d^0$	3.86, 5.47, 31.21, 90, 660, 10	[55]
$PrTi_{0.8}Al_{0.2}O_{3.40}$	$3d^0$	7.82, 5.50, 30.96, 96.5, 1323, 20 Prepared by floating zone melting	this work
$Pr_{0.8}Sr_{0.2}TiO_{3.40}$	$3d^0$	3.87, 5.49, 31.32, 90, 666, 10	[55]
$Pr_{0.8}Ca_{0.2}TiO_{3.40}$	$3d^0$	3.84, 5.45, 31.16, 90, 652, 10	[85]
$PrTiO_{3.41}$	$3d^{0.18}$	7.85, 5.52, 31.03, 96.5, 1337, 20 Prepared by floating zone melting Quasi-1D metal along *a*-axis at high *T* and metal-to-semiconductor transition at low *T* according to resistivity measurements on crystals	this work
[1] $Ce_{0.62}Sm_{0.38}TiO_{3.4}$	$3d^{0.2}$	7.83, 5.52, 31.01, 96.6, 1330, 20 Prepared by floating zone melting	
[1] $Ce_{0.5}Pr_{0.5}TiO_{3.4}$	$3d^{0.2}$	7.86, 5.51, 31.13, 96.6, 1339, 20 Prepared by floating zone melting	
$CeTiO_{3.40}$	$3d^{0.20}$	7.85, 5.52, 31.24, 97.0, 1344, 20 Prepared by floating zone melting	

Table 38. $n = 5$ members of monoclinic or orthorhombic $A_nB_nO_{3n+2} = ABO_x$ related to $CeTiO_{3.40}$ and $PrTiO_{3.40}$. [1]Because a thermogravimetric determination of x was not possible, as discussed in Ref. [127] for $La_{0.5}Ce_{0.5}TiO_{3.4}$, the ideal $n = 5$ value $x = 3.4$ was assigned. This table represents a supplement of Table 13 in Ref. [127].

Composition	***N***	***a***, ***b***, ***c*** (Å), β (°), ***V*** (Å^3), ***Z*** **Remarks / Special Features**	**Ref.**
$NdTi_{0.8}Ga_{0.2}O_{3.40}$	$3d^0$	3.82, 5.42, 31.23, 90, 647, 10	[85]
		7.69, 5.46, 31.44, 97.0, 1309, 20 Centrosym. space group $P2_1/c$ (No. 14) Structure determined by powder XRD	[229]
$NdTi_{0.8}Fe_{0.2}O_{3.40}$	$3d^0$	3.85, 5.46, 31.27, 90, 658, 10	[55]
		7.67, 5.44, 31.42, 97.0, 1302, 20 Centrosym. space group $P2_1/c$ (No. 14) Structure determined by powder XRD Fe exclusively located in the central octahedra, i.e. full ordering of Ti^{4+} and Fe^{3+} at the *B* site	[227]
		7.80, 5.47, 30.72, 95.9, 1303, 20 Prepared by floating zone melting	this work
$NdTi_{0.8}Cr_{0.2}O_{3.40}$	$3d^0$	3.84, 5.45, 31.18, 90, 653, 10	[55]
$NdTi_{0.8}Al_{0.2}O_{3.40}$	$3d^0$	7.80, 5.49, 30.92, 96.5, 1315, 20 Prepared by floating zone melting	this work
$Nd_{0.8}Cd_{0.2}TiO_{3.40}$	$3d^0$	3.84, 5.45, 31.58, 90, 661, 10	[55]
$Nd_{0.8}Sr_{0.2}TiO_{3.40}$	$3d^0$	3.86, 5.48, 31.32, 90, 662, 10	[55]
		Structural study by TEM and XRD Prepared by arc-melting	[204]
$NdTi_{0.9}Mg_{0.1}O_{3.40}$	$3d^0$	3.85, 5.46, 31.27, 90, 658, 10	[55]

Table 39. $n = 5$ members of monoclinic or orthorhombic $A_nB_nO_{3n+2} = ABO_x$ related to $NdTiO_{3.40}$. This table represents a supplement of Table 13 in Ref. [127].

Composition	***N***	***a***, ***b***, ***c*** (Å), β (°), ***V*** (Å^3), ***Z*** **Remarks / Special Features**	**Ref.**
$SmTi_{0.8}V_{0.2}O_{3.39}$	$3d^{0.42}$	7.79, 5.50, 30.90, 95.9, 1317, 20 Prepared by floating zone melting	this work
$NdTiO_{3.4}$	$3d^{0.2}$	7.8, 5.5, 15.8, 96.5, 95.9, 673, 10 Lattice parameters estimated from electron diffraction Prepared by arc-melting	[32]
		7.8, 5.5, 31.6, 97.7, 1392, 20 Lattice parameters from electron diffraction Centrosym. space group $P2_1/c$ (No. 14) Structural study by TEM Prepared by arc-melting	[186]
$NdTiO_{3.42}$	$3d^{0.16}$	7.83, 5.52, 30.96, 95.9, 1330, 20 Prepared by floating zone melting	this work

Table 40. $n = 5$ titanates of monoclinic $A_nB_nO_{3n+2} = ABO_x$ related to $NdTiO_{3.40}$ and $SmTiO_{3.40}$. This table represents a supplement of Table 13 in Ref. [127].

Composition	***N***	***a***, ***b***, ***c*** (Å), β (°), ***V*** (Å^3), ***Z*** **Remarks / Special Features**	**Ref.**
$SmTiO_{3.37}$	$3d^{0.26}$	7.80, 5.52, 30.93, 96.1, 1323, 20	this
$NdTiO_{3.31}$	$3d^{0.38}$	7.82, 5.50, 30.86, 96.5, 1318, 20	work
$PrTiO_{3.33}$	$3d^{0.34}$	7.80, 5.50, 31.26, 96.6, 1332, 20	
$SmTi_{0.78}Al_{0.22}O_{3.33}$	$3d^{0.15}$	7.77, 5.49, 30.83, 95.9, 1308, 20	
$CeTi_{0.8}Al_{0.2}O_{3.33}$	$3d^{0.18}$	7.83, 5.51, 31.08, 97.0, 1332, 20	
$La_{0.9}Sm_{0.1}Ti_{0.8}Al_{0.2}O_{3.30}$	$3d^{0.24}$	7.78, 5.51, 31.24, 96.7, 1330, 20	
$LaTi_{0.8}Fe_{0.2}O_{3.34}$	[2] $3d^{0.15}$	7.82, 5.54, 31.40, 96.6, 1351, 20	
$LaTi_{0.8}Mn_{0.2}O_{3.34}$	[1] $3d^{0.15}$	7.86, 5.54, 31.80, 97.4, 1373, 20	
$LaTi_{0.67}Mn_{0.33}O_{3.33}$	$3d^{0}$	7.86, 5.54, 31.53, 97.4, 1361, 20	
$LaTi_{0.8}V_{0.2}O_{3.31}$	$3d^{0.58}$	7.84, 5.52, 31.39, 97.0, 1349, 20	
$LaTi_{0.8}Al_{0.2}O_{3.31}$	$3d^{0.23}$	7.78, 5.52, 31.26, 96.7, 1333, 20	
$La_{0.89}Ca_{0.11}TiO_{3.36}$	$3d^{0.17}$	7.84, 5.52, 31.09, 96.1, 1357, 20 Optical (IR) spectroscopy on crystals at $T = 300$ K: quasi-1D metal along a-axis	[127] [218]

Table 41. Significantly non-stoichiometric $n = 5$ compounds ABO_x with $3.31 \leq x \leq 3.37$ of monoclinic $A_nB_nO_{3n+2}$. The ideal $n = 5$ composition is $ABO_{3.40}$. All materials were prepared by floating zone melting. [1]The value $N = 3d^{0.15}$ per Ti refers to an assumed valence distribution of $Ti^{3.85+}$ and Mn^{3+} ($3d^4$), the opposite extreme case would be Ti^{4+} ($3d^0$) and $Mn^{2.4+}$ ($3d^{4.6}$). [2]The value $N = 3d^{0.15}$ per Ti refers to an assumed valence distribution of $Ti^{3.85+}$ and Fe^{3+} ($3d^5$), the opposite extreme case would be Ti^{4+} ($3d^0$) and $Fe^{2.4+}$ ($3d^{5.6}$). This table represents a supplement of Table 13 and 14 in Ref. [127].

Composition	***N***	***a***, ***b***, ***c*** (Å), β (°), ***V*** (Å^3), ***Z*** **Remarks / Special Features**	**Ref.**
$Sr_{0.95}Nb_{0.9}Ta_{0.1}O_{3.37}$	$4d^{0.18}$	3.98, 5.67, 32.46, 90, 733, 10	this
$Sr_{0.95}Nb_{0.95}Ti_{0.05}O_{3.35}$	$d^{0.15}$	3.98, 5.67, 32.38, 90, 729, 10	work
$Sr_{0.97}NbO_{3.39}$	$4d^{0.16}$	3.99, 5.67, 32.46, 90, 733, 10	
$Sr_{0.85}Ca_{0.1}NbO_{3.37}$	$4d^{0.16}$	3.97, 5.65, 32.39, 90, 727, 10	
$Ca_{0.85}Sm_{0.1}NbO_{3.38}$	$4d^{0.24}$	3.87, 5.48, 31.96, 90, 677, 10	
$Ca_{0.95}NbO_{3.33}$	$4d^{0.24}$	3.85, 5.49, 32.22, 96.6, 677, 10	
$La_{0.47}Sm_{0.5}$ $Ti_{0.95}Al_{0.05}O_{3.36}$	$3d^{0.15}$	7.80, 5.48, 30.96, 96.2, 1317, 20	
$Nd_{0.95}TiO_{3.34}$	$3d^{0.17}$	7.78, 5.47, 31.50, 96.0, 1332, 20	
$La_{0.75}Ba_{0.2}TiO_{3.21}$	$3d^{0.23}$	7.86, 5.54, 31.48, 96.7, 1362, 20	
$La_{0.75}Ca_{0.2}TiO_{3.21}$	$3d^{0.23}$	7.83, 5.52, 31.36, 97.0, 1346, 20	
$La_{0.85}Ca_{0.1}TiO_{3.26}$	$3d^{0.23}$	7.84, 5.52, 31.41, 97.0, 1351, 20	
$LaTi_{0.95}O_{3.31}$	$3d^{0.19}$	7.87, 5.53, 31.44, 97.1, 1357, 20	
$La_{0.95}TiO_{3.33}$	$3d^{0.19}$	7.84, 5.53, 31.43, 97.0, 1353, 20	
$La_{0.965}TiO_{3.35}$	$3d^{0.20}$	7.86, 5.53, 31.47, 97.1, 1357, 20 Optical (IR) spectroscopy on crystals at $T = 300$ K: quasi-1D metal along a-axis	this work [218]
$La_{0.975}TiO_{3.37}$	$3d^{0.19}$	7.86, 5.53, 31.47, 97.1, 1358, 20	this work

Table 42. Significantly non-stoichiometric $n = 5$ compounds $A_{1-w}BO_x$ with $0 < w \leq 0.05$ and $3.21 \leq x \leq 3.37$ of monoclinic or orthorhombic $A_nB_nO_{3n+2}$. Also an $n = 5$ titanate with a deficiency at the B site, $AB_{0.95}O_x$, is listed. The ideal $n = 5$ composition is $ABO_{3.40}$. All materials were prepared by floating zone melting. This table represents a supplement of Table 13, 14 and 18 in Ref. [127].

Composition	***N***	***a***, ***b***, ***c*** (Å), β (°), ***V*** (Å^3), ***Z*** **Remarks / Special Features**	**Ref.**
$NdTiO_{3.36}$	$3d^{0.28}$	Composition prepared by arc-melting Crystal of $n = 5.5$ type detected by TEM, i.e. ordered stacking sequence $n = 5, 6, 5, 6, ...$	[32]

Table 43. An $n = 5.5$ type of $A_nB_nO_{3n+2} = ABO_x$.

Composition	***N***	***a***, ***b***, ***c*** (Å), β (°), ***V*** (Å^3), ***Z*** **Remarks / Special Features**	**Ref.**
$Sm_{0.67}Ca_{0.33}TiO_{3.33}$	$3d^0$	3.81, 5.42, 36.73, 90, 759, 12	[55]
		7.63, 5.41, 36.88, 96.0, 1514, 24 Prepared by floating zone melting	this work
$Nd_{0.67}Cd_{0.33}TiO_{3.33}$	$3d^0$	3.84, 5.45, 36.37, 90, 761, 12	[55]
$Nd_{0.67}Ca_{0.33}TiO_{3.33}$	$3d^0$	7.66, 5.44, 36.64, 90, 1526, 24 Non-centrosym. space group $Pna2_1$ (No. 33) Structure determined by single crystal XRD Crystals prepared by floating zone melting	[153]
		7.66, 5.44, 18.42, 95.7, 764, 12 Non-centrosym. space group $P2_1$ (No. 4) Crystals grown by flux technique using different fluxes, especially PbO Second harmonic generation experiment suggests presence of ferroelectricity	[167]
		Preparation of an incommensurate modification and structural study using a four-dimensional space	[157] [60]
		7.66, 5.45, 36.73, 90, 1533, 24	[55]
$NdTiO_{3.33}$	$3d^{0.33}$	Composition prepared by arc-melting	[32]
$Pr_{0.67}Ca_{0.33}TiO_{3.33}$	$3d^0$	3.85, 5.46, 36.76, 90, 773, 12	[55]
$La_{0.67}Sr_{0.33}TiO_{3.33}$	$3d^0$	7.79, 5.54, 36.84, 90, 1588, 24 Prepared by floating zone melting	[127]
		7.83, 5.44, 18.57, 96.0, 788, 12 7.82, 5.54, 18.55, 96.1, 799, 12 Structural study by TEM and powder XRD	[27] [26]
$LaTi_{0.67}Fe_{0.33}O_{3.33}$	$3d^0$	7.80, 5.55, 36.88, 90, 1596, 24 Prepared by floating zone melting	this work

Table 44. $n = 6$ titanates of orthorhombic or monoclinic $A_nB_nO_{3n+2} = ABO_x$. This table represents a supplement of Table 15 in Ref. [127].

Composition	***N***	***a***, ***b***, ***c*** (Å), β (°), ***V*** (Å^3), ***Z*** **Remarks / Special Features**	**Ref.**
$SrNb_{0.67}Ti_{0.33}O_{3.33}$	$4d^0$ $3d^0$	3.94, 5.63, 38.4, 90, 854, 12 Non-centrosym. space group $Cmc2_1$ (No. 36) Polycrystalline samples Ferroelectric with $T_c = 630$ °C	[83] [84]
		3.93, 5.63, 38.05, 90, 844, 12 Polycrystalline samples Dielectric constant $\varepsilon \approx 77$ (100 kHz, 20 °C)	[120]
		TEM study on polycrystalline samples Above $T \approx 200$ °C commensurate phase Below $T \approx 200$ °C incommensurate phase Down to $T = -170$ °C no lock-in transition	[122]
$CaNb_{0.67}Ti_{0.33}O_{3.33}$	$4d^0$ $3d^0$	7.67, 5.46, 18.91, 95.8, 789, 12 Non-centrosym. space group $P2_1$ (No. 4)	[156] [154]
		7.68, 5.47, 37.75, 95.9, 1576, 24 Non-centrosym. space group $P2_1$ (No. 4) Structure determined by single crystal XRD Actual stoichiometry of the studied crystal deviates from ideal composition	[62]
		Structural description by superspace formalism	[65]

Table 45. Miscellaneous $n = 6$ members of monoclinic or orthorhombic $A_nB_nO_{3n+2} = ABO_x$. This table represents a supplement of Table 15 in Ref. [127].

Composition	***N***	***a***, ***b***, ***c*** (Å), β (°), ***V*** (Å^3), ***Z*** **Remarks / Special Features**	**Ref.**
$SrNb_{0.57}Ti_{0.43}O_{3.29}$	$4d^0$ $3d^0$	3.93, 5.61, 43.61, 90, 963, 14 Polycrystalline samples Dielectric constant $\varepsilon \approx 61$ (100 kHz, 20 °C)	[120]
		TEM study on polycrystalline samples reveals following symmetry, centrosym. space groups, (Nb,Ti)O_6 octahedra tilting on cooling: $T > 470$ °C: orthorh., Immm (No. 61), untilted $T < 470$ °C: orthorh., Pnnm (No. 58), tilted $T < 100$ °C: incommensurate phase Down to $T = -170$ °C no lock-in transition	[122]
$Ca_{0.57}Na_{0.43}NbO_{3.29}$	$4d^0$	3.86, 5.5, 43.8, 90, 930, 14	[152]

Table 46. $n = 7$ members of orthorhombic $A_nB_nO_{3n+2} = ABO_x$.

	$SrNbO_{3.50}$	$Sr_{0.8}La_{0.2}NbO_{3.50}$	$SrNbO_{3.45}$	$SrNbO_{3.41}$
N	$4d^0$	$4d^{0.20}$	$4d^{0.10}$	$4d^{0.18}$
Structure type	$n = 4$ [33] [78,151]	$n = 4$ [127,243]	$n = 4.5$ [127,125,243]	$n = 5$ [2,127] [125,133]
Structure determined by single crystal XRD	Yes [33,78]	No	No	Yes [2]
LDA band structure calculations performed	No	No	No	Yes [110,244]
dc (low f optical) resistivity ρ in 10^{-3} Ωcm along a-, b-, c-axis at $T \simeq 300$ K	very high	$\rho_a \approx 6$ (6) $\rho_b \approx 40$ (30) $\rho_c \approx 1500$ [127,113]	$\rho_a \approx 5$ [1] (1) $\rho_b \approx 150$ [1] (30) $\rho_c \approx 20000$ [1] [127,113]	$\rho_a \approx 0.4$ (0.2) $\rho_b \approx 30$ (30) $\rho_c \approx 1000$ [127,113]
Quasi-1D metal along a-axis at high T (from $\rho(T)$, ARPES, optical spectroscopy)	No	Yes, but metallic character relatively weak [127,113]	Yes [127,110] [113,136]	Yes [127,113,111]
Metal-to-semiconductor transition along a-axis in $\rho_a(T)$ at low T	No	Yes at $T \approx 90$ K [127]	Yes at $T \approx 110$ K [127]	Yes at $T \approx 60$ K [127]
Opening of an energy gap Δ at Fermi energy along a-axis at low T		No from optical spectroscopy [113]	Yes $\Delta \approx 7$ meV from optical spectroscopy [113]	Yes $\Delta \approx 5$ meV from optical spectroscopy, high-resolution ARPES, $\rho_a(T)$ [111]

Table 47. Features and present state of the most intensively studied electrical conductors of the type $A_nB_nO_{3n+2} = ABO_x$. Also scheduled is the related high-T_c ferroelectric insulator $SrNbO_{3.50}$ ($T_c = 1615$ K). [1]The dc resistivity was measured on crystals with a different but very similar composition $Sr_{0.96}Ba_{0.04}NbO_{3.45}$ [127]. Continuation in Table 48.

	$SrNbO_{3.50}$	$Sr_{0.8}La_{0.2}NbO_{3.50}$	$SrNbO_{3.45}$	$SrNbO_{3.41}$
N	$4d^0$	$4d^{0.20}$	$4d^{0.10}$	$4d^{0.18}$
Structure type	$n = 4$ [33] [78,151]	$n = 4$ [127,243]	$n = 4.5$ [127,125,243]	$n = 5$ [2] [127,125,133]
Phonon mode in optical conductivity at ≈ 54 cm^{-1} along b-axis related to ferroelectric transition in $SrNbO_{3.50}$ (ferroelectric soft mode)	Yes [113]	Yes [113]	Yes [113]	Yes [113]
Dielectric constant ε along a-, b- and c-axis:				
ε_a at $T = 300$ K	75 [2] [151]		≈ -6000 [3] [113]	≈ -7000 [3] [113]
at $T = 5$ K			≈ 3000 [3] [113]	≈ 12000 [3] [113]
ε_b at $T = 300$ K	43 [2] [151]		≈ 40 [3] [113]	≈ 50 [3] [113]
at $T = 5$ K			≈ 50 [3] [113]	≈ 60 [3] [113]
ε_c at $T = 300$ K	46 [2] [151] 28 [2] [17]		≈ 50 [2] [17]	
for $T \leq 70$ K				≈ 100 [2,4] [17]
Magnetic behavior for $T \leq 390$ K	dia-magnetic [127]	para- or dia-magnetic [127] depending on T	diamagnetic [127]	diamagnetic [127,242]

Table 48. Continuation from Table 47. Features and present state of the most intensively studied electrical conductors of the type $A_nB_nO_{3n+2} = ABO_x$. Also scheduled is the related high-T_c ferroelectric insulator $SrNbO_{3.50}$ ($T_c = 1615$ K). [2]High frequency value from capacitor measurements. [3]Low frequency value from optical spectroscopy. [4]For T > 70 K the determination of ε_c was prevented by a too low resistivity of the sample.

Title, *author(s)*, year, Ref.	Remarks about the content
Crystal chemical aspects of the layered perovskite-like oxide ferroelectrics of the $A_nM_nO_{3n+2}$ type, *Isupov* 1999 [85]	Overview on many insulating d^0 compounds, discussion of ferroelectric and structural properties
Symmetry classification of the layered perovskite-derived $A_nB_nX_{3n+2}$ structures, *Levin and Bendersky* 1999 [121]	Overview on several insulating d^0 compounds, discussion of structural features
A structural study of the layered perovskite-derived $Sr_n(Nb,Ti)_nO_{3n+2}$ compounds by transmission electron microscopy, *Levin et al.* 2000 [122]	Structural study on polycrystalline and insulating d^0 compositions with $n = 4$, 4.5, 4.78, 5, 5.5, 6 and 7, also at different temperatures
Electronic structure of layered perovskite-related $Sr_{1-y}La_yNbO_{3.5-x}$ *Kuntscher et al.* 2000 [110]	ARPES and NEXAFS on $SrNbO_{3.45}$ ($n = 4.5$) and $Sr_{0.9}La_{0.1}NbO_{3.39}$ ($n = 5$) crystals and LDA band structure calculation on $SrNbO_{3.41}$ ($n = 5$)
Intergrowth polytypoids as modulated structures: a superspace description of the $Sr_n(Nb,Ti)_nO_{3n+2}$ compound series *Elcoro et al.* 2001 [46]	Unified four- and five-dimensional superspace approach to describe the complex structural features such as incommensurate modulations in this insulating d^0 compound series
Synthesis of perovskite-related layered $A_nB_nO_{3n+2} = ABO_x$ type niobates and titanates and study of their structural, electric and magnetic properties, *Lichtenberg et al.* 2001 [127]	Overview on many compounds and their properties, presentation of results from own work with focus on electrical conductors
Dielectric properties and charge transport in the $(Sr,La)NbO_{3.5-x}$ system, *Bobnar et al.* 2002 [17]	Studies on crystals of insulating $SrNbO_{3.50}$ ($n = 4$) and electrical conducting $Sr_{0.8}La_{0.2}NbO_{3.50}$ ($n = 4$), $SrNbO_{3.45}$ ($n = 4.5$) and $SrNbO_{3.41}$ ($n = 5$)
Electronic and vibrational properties of the low-dimensional perovskites $Sr_{1-y}La_yNbO_{3.5-x}$, *Kuntscher et al.* 2004 [113]	

Table 49. Recent comprehensive papers about $A_nB_nO_{3n+2} = ABO_x$ which report on several compounds and structure types. Continuation in Table 50.

Title, *author(s)*, year, Ref.	Remarks about the content
Studies on the reorganization of extended defects with increasing n in the perovskite-based $La_4Sr_{n-4}Ti_nO_{3n+2}$ series *Canales-Vazquez et al.* 2005 [27]	Structural studies by TEM, XRD, neutron diffraction on polycrystalline samples. Layered structure lost for $n = 12$ whereby excess oxygen accommodated within perovskite framework in randomly distributed short-range linear defects. Magnetic and thermogravimetric measurements on a reduced and therefore conducting $n = 12$ sample.
Synthesis, structural, magnetic and transport properties of layered perovskite-related titanates, niobates and tantalates of the type $A_nB_nO_{3n+2}$, $A'A_{k-1}B_kO_{3k+1}$ and $A_mB_{m-1}O_{3m}$, *Lichtenberg et al.* [this work]	Concerning $A_nB_nO_{3n+2}$: overview on many compounds and their properties, presentation of results from own work with focus on electrical conductors, materials with localized paramagnetic moments and non-stoichiometric compounds

Table 50. Continuation from Table 49. Recent comprehensive papers about $A_nB_nO_{3n+2} = ABO_x$ which report on several compounds and structure types.

Composition	***N***	***a***, ***c*** (Å), ***V*** (Å^3), ***Z*** **Remarks / Special Features**	**Ref.**
$Ba_3Re_2O_9$	$5d^1$	5.77, 20.80, 599.7, 3 Centrosym. space group $R\bar{3}m$ (No. 166) Structure determined by single crystal XRD	[25]
		5.75, 20.61, 590.1, 3 Polycrystalline samples Two-probe resistivity measurements between 77 K and 523 K shows semiconducting behavior Magnetic measurements between 80 K and 300 K suggests Curie-Weiss behavior	[31]
$Sr_3Re_2O_9$	$5d^1$	5.55, 20.12, 535.7, 3 Polycrystalline samples Two-probe resistivity measurements between 77 K and 523 K shows semiconducting behavior Magnetic measurements between 80 K and 300 K suggests temperature-independent paramagnetism	[31]

Table 51. $m = 3$ members of hexagonal $A_mB_{m-1}O_{3m}$.

Composition	***N***	***a***, ***c*** (Å), ***V*** (Å^3), ***Z*** **Remarks / Special Features**	**Ref.**
$LaSr_3Ta_3O_{12}$	$5d^0$	5.65, 27.25, 754.3, 3 Centrosym. space group $R\overline{3}m$ (No. 166) Structure determined by single crystal XRD	[7]
		5.66, 27.25, 754.9, 3	[203]
$PrSr_3Ta_3O_{12}$	$5d^0$	5.65, 27.16, 750.3, 3	[203]
$LaBa_3Ta_3O_{12}$	$5d^0$	5.75, 28.20, 806.3, 3 Centrosym. space group $R\overline{3}m$ (No. 166)	[97]
$NdBa_3Ta_3O_{12}$	$5d^0$	5.73, 28.18, 802.1, 3	

Table 52. $m = 4$ tantalates of hexagonal $A_mB_{m-1}O_{3m}$.

Composition	***N***	***a***, ***c*** (Å), ***V*** (Å^3), ***Z*** **Remarks / Special Features**	**Ref.**
$LaSr_3Nb_3O_{12}$	$4d^0$	5.66, 27.19, 753.3, 3	[203]
		5.65, 27.16, 751.4, 3 Prepared by floating zone melting	this work
$PrSr_3Nb_3O_{12}$	$4d^0$	5.65, 27.13, 749.2, 3	[203]
$NdSr_3Nb_3O_{12}$	$4d^0$	5.64, 27.12, 747.4, 3	
$LaBa_3Nb_3O_{12}$	$4d^0$	5.75, 28.16, 806.9, 3 Crystals grown by zone melting Measurement of optical properties and dielectric constant ε $\varepsilon \simeq 22 - 24$ for 300 K $\leq T \leq$ 850 K	[6]
		5.75, 28.11, 805.2, 3 Centrosym. space group $R\bar{3}m$ (No. 166)	[97] [181]
		5.75, 28.07, 804.6, 3 Prepared by floating zone melting	this work
$PrBa_3Nb_3O_{12}$	$4d^0$	5.74, 28.15, 804.3, 3	[6]
		5.74, 28.09, 801.8, 3	[97]
$NdBa_3Nb_3O_{12}$	$4d^0$	5.74, 28.13, 802.9, 3	[6]
		5.74, 28.08, 800.7, 3	[97]
$Ba_4Nb_2WO_{12}$	$4d^0$ $6d^0$	5.78, 28.06, 810.6, 3 Centrosym. space group $R\bar{3}m$ (No. 166)	[181]
$La_4Ti_3O_{12}$	$3d^0$	5.56, 26.23, 702.0, 3	[50]
		5.55, 26.18, 699.4, 3	[54]
		5.56, 26.23, 702.2, 3 Centrosym. space group $R\bar{3}m$ (No. 166)	[19]
		Structural study by TEM	[212]

Table 53. $m = 4$ members of hexagonal $A_mB_{m-1}O_{3m}$.

Composition	***N***	***a***, ***c*** (Å), ***V*** (Å^3), ***Z*** **Remarks / Special Features**	**Ref.**
$Ba_5Ta_4O_{15}$	$5d^0$	5.78, 11.82, 341.5, 1 Centrosym. space group $P\overline{3}m1$ (No. 164) Structure determined by single crystal XRD	[199]
$Sr_5Nb_4O_{15}$	$4d^0$	5.67, 22.97, 638.6, 2 Centrosym. space group $P\overline{3}c1$ (No. 165) Structure determined by single crystal XRD Crystals grown by slow cooling of a Nb-rich melt consisting of Nb_2O_5 and $SrCO_3$	[213]
		5.66, 11.45, 317.1, 1 (5.65, 22.90, 633.9, 2) Prepared by floating zone melting	this work
$Sr_{4.6}La_{0.4}Nb_4O_{15.06}$	$4d^{0.07}$	5.66, 22.85, 634.1, 2 Prepared by floating zone melting	this work
$Sr_{5-y}Ba_yNb_4O_{15}$ $0 \le y \le 5$	$4d^0$	Polycrystalline samples Measurement of Raman and IR spectra and dielectric constant ε	[175]
$Sr_5Nb_4O_{15}$		5.63, 11.40, 312.9, 1, $\varepsilon = 40$	
$Sr_2Ba_3Nb_4O_{15}$		5.76, 11.81, 339.3, 1, $\varepsilon = 50$	
$Ba_5Nb_4O_{15}$		5.79, 11.75, 341.1, 1, $\varepsilon = 38$	
$Ba_5Nb_4O_{15}$	$4d^0$	5.80, 11.79, 343.5, 1 ($y = 0$) Centrosym. space group $P\overline{3}m1$ (No. 164) Structure determined by Rietfield refinement of neutron powder diffraction data	[169]
		5.80, 11.79, 342.9, 1 Centrosym. space group $P\overline{3}m1$ (No. 164) Structure determined by single crystal XRD Crystals grown by slow cooling of a melt	[239]
$Ba_5Nb_4O_{15-y}$ $0 \le y \le 0.56$	$4d^0$ – $4d^{0.28}$	Polycrystalline samples Resistivity measurements between 80 K and 300 K for $y = 0.08$, 0.13 and 0.56 shows semiconducting behavior	[168]

Table 54. $m = 5$ members of hexagonal $A_mB_{m-1}O_{3m}$.

Composition	***N***	***a***, ***c*** (Å), ***V*** (Å^3), ***Z*** **Remarks / Special Features**	**Ref.**
$CaLa_4Ti_4O_{15}$	$3d^0$	5.53, 11.02, 292.0, 1	[54]
$SrLa_4Ti_4O_{15}$	$3d^0$	5.55, 11.07, 295.2, 1	
$BaLa_4Ti_4O_{15}$	$3d^0$	5.57, 11.23, 301.5, 1	
		5.57, 22.50, 605.0, 2 Centrosym. space group $P\bar{3}c1$ (No. 165) Structure determined by single crystal XRD	[70]
$La_5Ti_4O_{15}$	$3d^{0.25}$	5.57, 21.99, 592.0, 2 Centrosym. space group $P\bar{3}c1$ (No. 165) Structure of polycrystalline samples determined by XRD end TEM Physical properties are not reported	[19] [171]
		Structural study by TEM	[212]
$La_5Ti_{3.5}Mg_{0.5}O_{15}$	$3d^0$	5.56, 10.99, 294.7, 1	[54]
		5.56, 10.99, 294.7, 1 Centrosym. space group $P\bar{3}m1$ (No. 164) Structural study by XRD and TEM and dielectric measurements on polycrystalline samples Dielectric constant $\varepsilon = 38$ (6 GHz, 25 °C)	[240]
$La_5Ti_3FeO_{15}$	$3d^0$	5.57, 11.00, 294.6, 1 Centrosym. space group $P\bar{3}m1$ (No. 164)	[56]

Table 55. $m = 5$ titanates of hexagonal $A_mB_{m-1}O_{3m}$.

Composition	***N***	***a***, ***c*** (Å), ***V*** (Å^3), ***Z*** **Remarks / Special Features**	**Ref.**
$Sr_6Nb_5O_{18.07}$	$4d^{0.17}$	5.66, 41.33, 1148, 3 Prepared by floating zone melting Quasi-2D metal at high T and metal-to-semiconductor transition at $T \approx 160$ K according to resistivity measurements on crystals and magnetic susceptibility	this work
$Sr_6Nb_4TiO_{18}$	$4d^0$ $3d^0$	5.64, 41.35, 1141, 3 Non-centrosym. space group R3m (No. 160) Structure determined by single crystal XRD Crystals grown by flux technique	[40]
		5.65, 13.75, 380, 1 Structural study by TEM and powder XRD on polycrystalline samples	[170]
		Preparation by floating zone melting impossible because material grows very strongly out of the molten zone	this work
$Ba_6Nb_4TiO_{18}$	$4d^0$ $3d^0$	5.79, 42.49, 1232, 3 Centrosym. space group $R\overline{3}m$ (No. 166) Structure determined by Rietfield refinement of neutron powder diffraction data	[41]
		5.77, 42.43, 1224, 3 Prepared by floating zone melting Presence of small amount(s) of other phase(s)	this work
$Ba_6Nb_4ZrO_{18}$	$4d^0$	5.82, 42.63, 1251, 3 Centrosym. space group $R\overline{3}m$ (No. 166)	[190]
$Ba_6Nb_{4.5}B'_{0.5}O_{18}$ B' = Sc, In, Yb, Tm, Lu	$4d^0$	Lattice parameters available in Ref. [145]	[145]
$Ba_5SrTa_4ZrO_{18}$	$5d^0$ $4d^0$	5.80, 42.54, 1240, 3 Centrosym. space group $R\overline{3}$m (No. 166) Structure of polycrystalline samples determined by XRD and TEM	[1]

Table 56. $m = 6$ members of hexagonal $A_mB_{m-1}O_{3m}$.

Composition	***N***	***a***, ***c*** (Å), ***V*** (Å^3), ***Z*** **Remarks / Special Features**	**Ref.**
$Ba_2La_4Ti_5O_{18}$	$3d^0$	5.58, 41.18, 1112, 3 Centrosym. space group $R\overline{3}$ (No. 148) Structure determined by single crystal XRD Crystals grown by flux technique	[71]
		5.58, 41.09, 1108, 3 Prepared by floating zone melting	this work
		5.58, 41.14, 1111, 3 Polycrystalline sample Dielectric constant $\varepsilon = 46$ (≈ 5 GHz, 25 °C)	[241]
$Ca_2La_4Ti_5O_{18}$	$3d^0$	5.52, 39.79, 1048, 3	[54]
$La_6Ti_5O_{18}$	$3d^{0.4}$	5.57, 39.56, 1062, 3 Structure of polycrystalline samples determined by XRD end TEM Physical properties are not reported	[19]
		Structural study by TEM	[212]
$La_6Ti_4MgO_{18}$	$3d^0$	5.57, 39.73, 1066, 3 Non-centrosym. space group R3m (No. 160) Structural study by XRD and TEM and dielectric measurements on polycrystalline samples Dielectric constant $\varepsilon = 34$ (6.1 GHz, 25 °C)	[240]
		5.57, 39.69, 1065, 3	[54]
$La_6Ti_3Fe_2O_{18}$	$3d^0$	5.57, 39.74, 1066, 3 Centrosym. space group $R\overline{3}m$ (No. 166)	[57]

Table 57. $m = 6$ titanates of hexagonal $A_mB_{m-1}O_{3m}$.

Composition	***N***	***a***, ***c*** (Å), ***V*** (Å^3), ***Z*** **Remarks / Special Features**	**Ref.**
$Sr_7Nb_6O_{21}$	$4d^{0.33}$	5.67, 48.36, 1347, 3 Centrosym. space group $R\overline{3}$ (No. 148) Structure determined by single crystal XRD Crystals isolated from a sample prepared by a laser heating technique Physical properties are not reported	[194]
		Preparation by floating zone melting resulted in a multiphase sample consisting of phases of the type $m = 7$, $m = 6$, $m = 5 + 6$ and $Sr_{0.8}NbO_3$	this work
$Ba_7Nb_4Ti_2O_{21}$	$4d^0$ $3d^0$	5.77, 49.49, 1425, 3 Centrosym. space group $R\overline{3}m$ (No. 166)	[146]
		Appears also in a modified crystal structure called twinned perovskite	[233]
$Ba_7Nb_{4.5}B'_{0.5}TiO_{21}$ B' = Sc, In, Yb, Tm, Lu	$4d^0$ $3d^0$	Lattice parameters available in Ref. [146]	[146]
$Ba_6LaNb_3Ti_3O_{21}$	$4d^0$ $3d^0$	5.71, 49.12, 1388, 3	
$Ba_5Sr_2Ta_4Zr_2O_{21}$	$5d^0$ $4d^0$	5.80, 49.60, 1445, 3 Centrosym. space group $R\overline{3}m$ (No. 166) Structure of polycrystalline samples determined by XRD end TEM	[1]

Table 58. $m = 7$ members of hexagonal $A_mB_{m-1}O_{3m}$.

Composition	***N***	***a***, ***c*** (Å), ***V*** (Å^3), ***Z*** **Remarks / Special Features**	**Ref.**
$Ba_8Nb_{4.5}Lu_{0.5}Ti_2O_{24}$	$4d^0$ $3d^0$	Structure of polycrystalline samples determined by XRD end TEM	[233]

Table 59. An $m = 8$ member of hexagonal $A_mB_{m-1}O_{3m}$. According to Trolliard et al. [233] the most other $m = 8$ compounds have a crystal structure which is somewhat different from that sketched in Fig. 9 and 10. The interlayer region of this so-called twinned perovskite structure consists of two partially occupied octahedra instead of one fully vacant octahedra [233].

Structure type **Formula** **Composition**	***N***	***a***, ***c*** (Å), ***V*** (Å^3), ***Z*** **Remarks / Special Features**	**Ref.**
$m = 5 + 6$ $A_{11}B_9O_{33}$ $Sr_{11}Nb_9O_{33.09}$	$4d^{0.09}$	5.66, 75.67, 2102, 3 Prepared by floating zone melting	this work
$m = 5 + 6$ $A_{11}B_9O_{33}$ $Ba_3Sr_8Nb_9O_{33.15}$	$4d^{0.08}$	5.69, 76.53, 2145, 3 Prepared by floating zone melting	this work
$m = 5 + 6$ $A_{11}B_9O_{33}$ $Ba_{11}Nb_8TiO_{33}$	$4d^0$ $3d^0$	5.78, 77.80, 2256, 3 Centrosym. space group $R\overline{3}m$ (No. 166) Structure determined by Rietfield refinement of XRD and neutron powder diffraction data Structural study by a four-dimensional superspace approach	[217] [20]
		Structural study by TEM	[232]
$m = 4 + 5$ $A_9B_7O_{27}$ $Ba_9Nb_6WO_{27}$	$4d^0$ $6d^0$	5.79, 63.41, 1843, 3 Centrosym. space group $R\overline{3}m$ (No. 166)	[98]
$m = 4 + 5$ $A_9B_7O_{27}$ $La_9Ti_7O_{27}$	$3d^{0.14}$	5.57, 118.4, 3175, 6 Centrosym. space group $R\overline{3}c$ (No. 167) Structure of polycrystalline samples determined by XRD end TEM Physical properties are not reported	[19]

Table 60. Compounds with an ordered intergrowth of alternating layers of the type $m = m' + (m' + 1)$ of hexagonal $A_mB_{m-1}O_{3m}$.

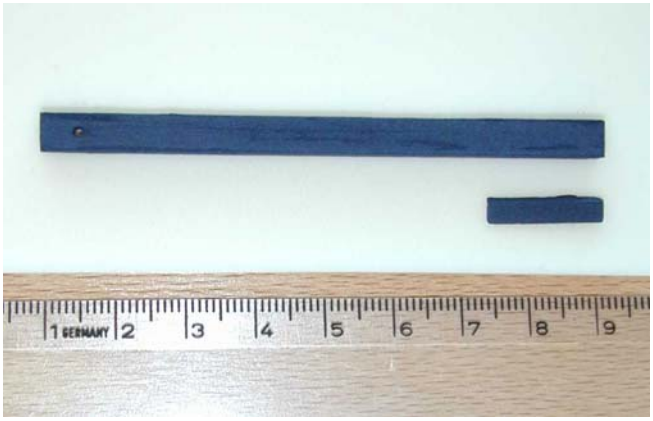

Fig. 18. Photograph of two sintered polycrystalline rods. The length of the long rod is 8 cm.

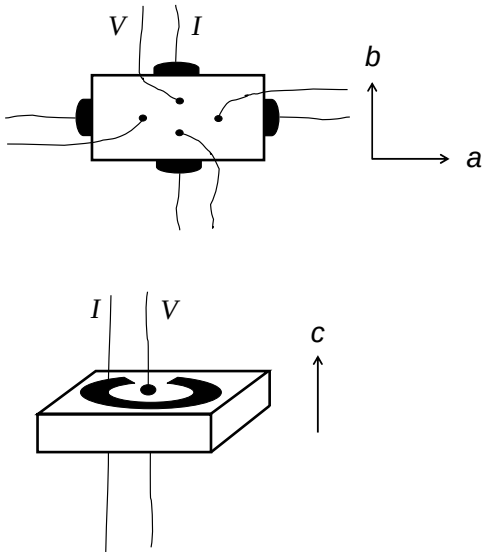

Fig. 19. Sketch of the arrangement of electrical contacts for resistivity measurements in a four-point configuration at a plate-like crystal along the *a*-, *b*- and *c*-axis. V and I denote the voltage and current contacts, respectively. In the case of a hexagonal $A_mB_{m-1}O_{3m}$ crystal the in-plane V and I contacts were prepared only along one direction, e.g. along the *a*-axis. Photographs of a crystal with electrical contacts are shown in Fig. 20 and 21.

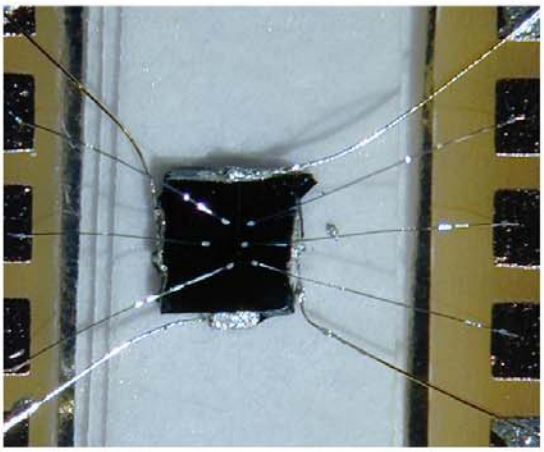

Fig. 20. Photograph of a crystal prepared for a resistivity measurement along two different directions within the ab-plane, usually along the a- and b-axis. The size of this crystal is $(1.7 \times 1.7 \times 0.3)$ mm^3. At the four sides the current leads, 50 µm diameter Au wire, are attached with silver paint. In the case of a hexagonal $A_m B_{m-1} O_{3m}$ crystal only two current leads along one direction are necessary, e.g. along the a-axis. On the top there are six voltage contacts, 25 µm diameter Al wire, which were mechanically fixed by ultrasonical bonding. Although one current direction requires only two voltage contacts, the presence of more contacts can be very useful, e.g. if one of them fails.

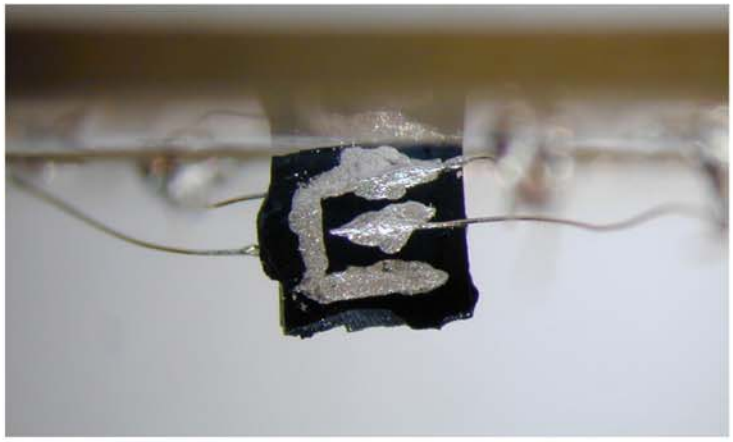

Fig. 21. Photograph of the same crystal as that presented in Fig. 20, but now with contacts for a resistivity measurement perpendicular to the layers. Shown is one of the both sides with two contacts which were prepared by silver paint and 50 µm diameter Au wire. The U-like shape is used as current contact and the other in the middle as voltage contact. There are two corresponding contacts on the other side of the crystal.

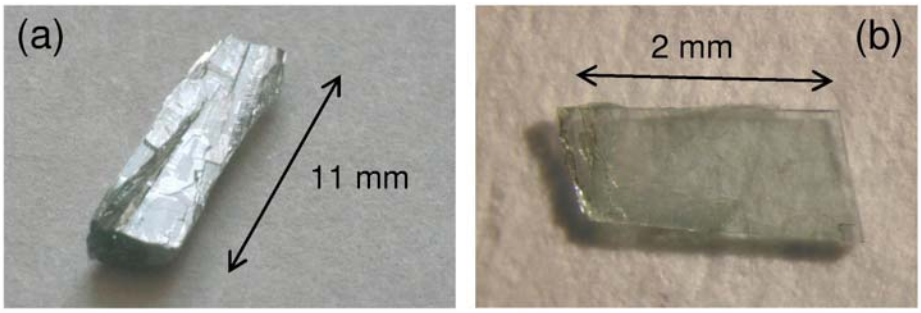

Fig. 22. Photographs of the light green transparent insulator $BaLa_2Ti_3O_{10}$ ($k = 3$ of $A'A_{k-1}B_kO_{3k+1}$) grown with a zone speed of 15 mm/h. The layers grow parallel to the longitudinal cylinder axis. Medium size and flat platelets can be found by cleaving the as-grown sample.
(a) Part of the as-grown sample.
(b) Plate-like crystal obtained by cleaving the as-grown sample.

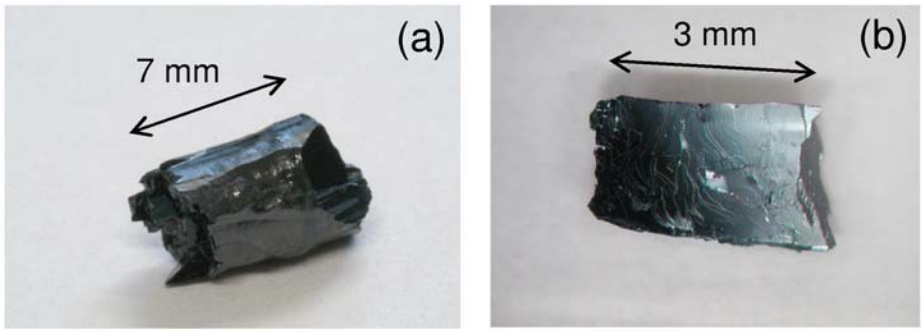

Fig. 23. Photographs of the black-blue anisotropic 3D metal $BaCa_{0.6}La_{0.4}Nb_2O_{7.00}$ ($k = 2$ of $A'A_{k-1}B_kO_{3k+1}$) grown with a zone speed of 15 mm/h. The layers grow parallel to the longitudinal cylinder axis. Medium size and flat platelets can be found by cleaving the as-grown sample.
(a) Part of the as-grown sample.
(b) Plate-like crystal obtained by cleaving the as-grown sample.

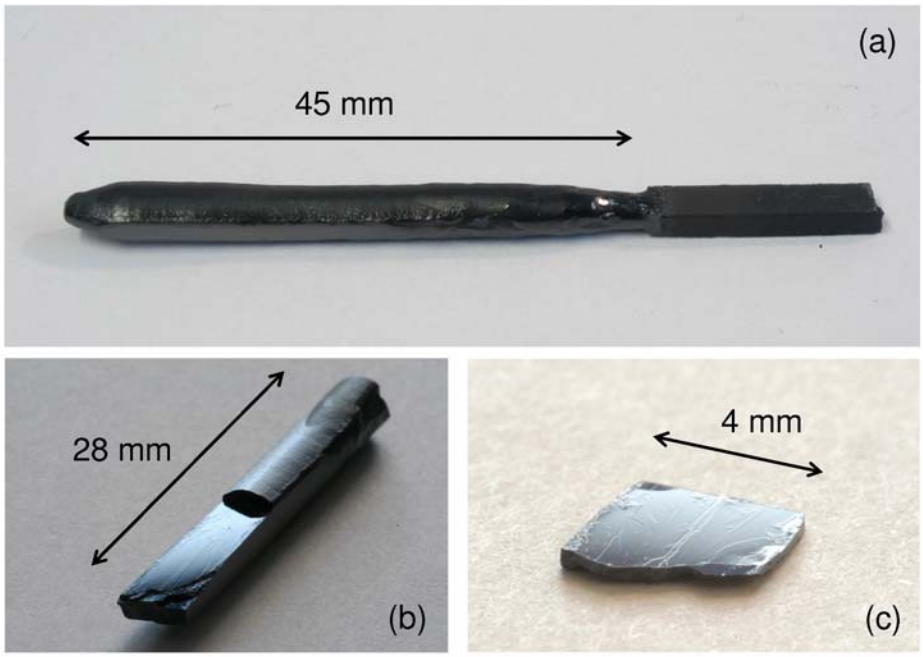

Fig. 24. Photographs of black-blue $Ca_4EuNb_5O_{17} = Ca_{0.8}Eu_{0.2}NbO_{3.40}$ ($n = 5$ of $A_nB_nO_{3n+2} = ABO_x$) grown with a zone speed of 15 mm/h. The layers grow parallel to the longitudinal cylinder axis. Large size and flat platelets can be found by cleaving the as-grown sample.
(a) The whole as-grown sample including the polycrystalline seed rod.
(b) Part of the as-grown sample.
(c) Plate-like crystal obtained by cleaving the as-grown sample.

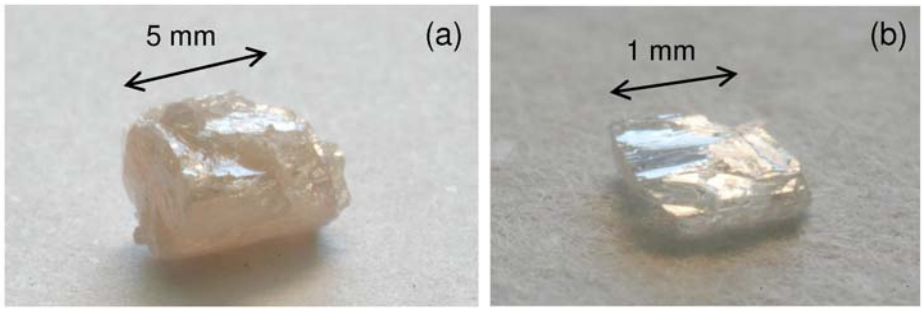

Fig. 25. Photographs of the faintly pink transparent insulator $Sr_2LaTa_3O_{11} = Sr_{0.67}La_{0.33}TaO_{3.67}$ ($n = 3$ of $A_nB_nO_{3n+2} = ABO_x$) grown with a zone speed of 15 mm/h. This is an example of a composition which does not lead to large or medium size crystals. Only small and irregular shaped crystals were found by cleaving the as-grown sample.
(a) Part of the as-grown sample.
(b) A small piece obtained by cleaving the as-grown sample.

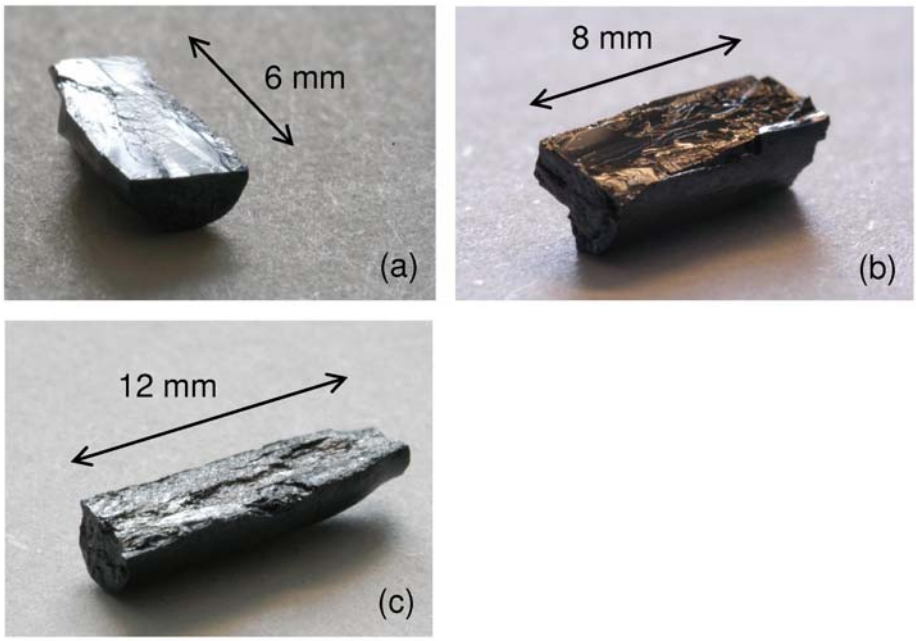

Fig. 26. Photographs of a part of the as-grown sample of three black, electrical conductive compounds which were grown with a zone speed of 15 mm/h.
(a) $CeTiO_{3.40}$, $n = 5$ of $A_nB_nO_{3n+2} = ABO_x$. This is an example of materials which are difficult to synthesize with respect to the oxygen content. In this case the difficulty is related to the peculiarities associated with one of the starting materials, namely CeO_2.
(b) $SmTiO_{3.37}$, $n = 5$ of $A_nB_nO_{3n+2} = ABO_x$. This is one of the few examples of an $A_nB_nO_{3n+2}$ compound in a system where the end members are not of the type $A_nB_nO_{3n+2}$. In this case the system is $SmTiO_x$ whose end members are $SmTiO_3$ with perovskite structure and $SmTiO_{3.50}$ with pyrochlore structure.
(c) $La_{0.6}Ca_{0.4}Ti_{0.6}Nb_{0.4}O_{3.40}$, significantly non-stoichiometric $n = 4$ of $A_nB_nO_{3n+2} = ABO_x$. This is an example of a composition which does not lead to crystals of appreciable size. It has a polycrystalline appearance.

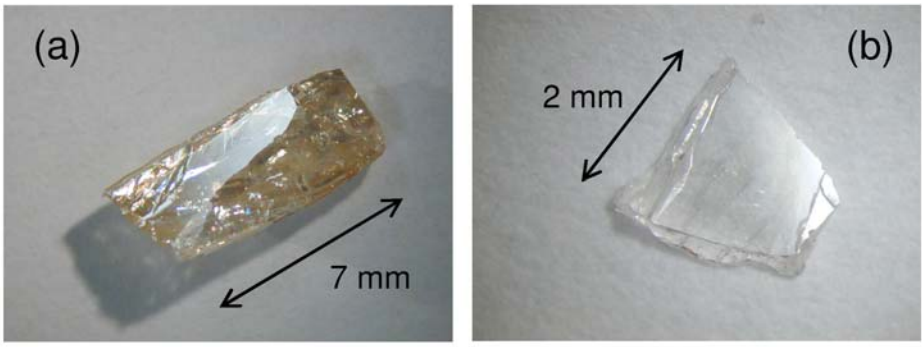

Fig. 27. Photographs of the light yellow transparent insulator $Sr_5Nb_4O_{15}$ ($m = 5$ of $A_mB_{m-1}O_{3m}$) grown with a zone speed of 15 mm/h. The layers grow approximately parallel to the longitudinal cylinder axis. Medium size and flat platelets can be found by cleaving the as-grown sample.
(a) Part of the as-grown sample.
(b) Plate-like crystal obtained by cleaving the as-grown sample.

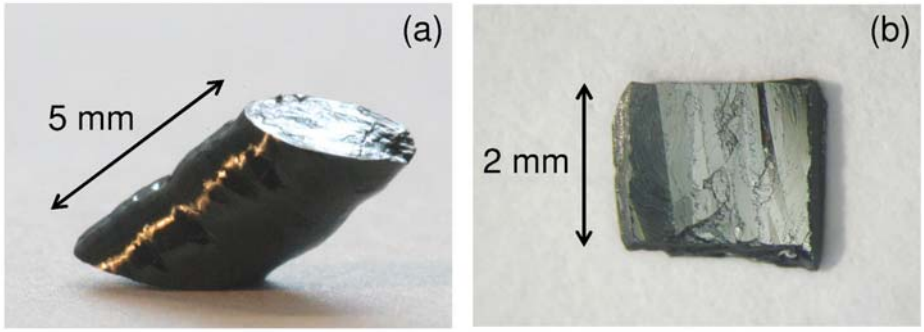

Fig. 28. Photographs of the black-blue quasi-2D metal $Sr_6Nb_5O_{18.07}$ ($m = 6$ of $A_mB_{m-1}O_{3m}$) grown with a zone speed of 8 mm/h. The layers grow 45° inclined to the longitudinal cylinder axis. Medium size platelets can be found by cleaving the as-grown sample.
(a) Part of the as-grown sample.
(b) Plate-like crystal obtained by cleaving the as-grown sample.

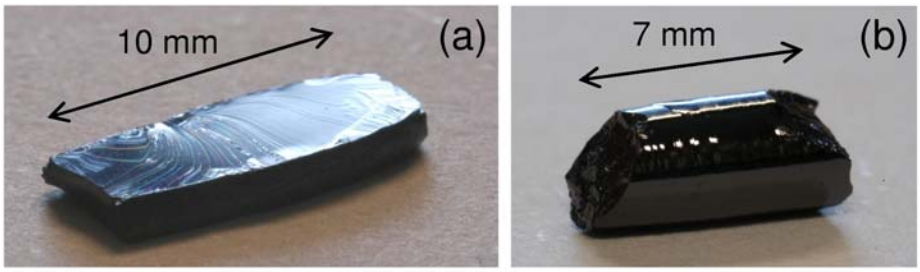

Fig. 29. Photographs of two brown-black insulators which were grown with a zone speed of 15 mm/h and whose structure is not of the type $A'A_{k-1}B_kO_{3k+1}$, $A_nB_nO_{3n+2}$ or $A_mB_{m-1}O_{3m}$. They were prepared for magnetic measurements, see Figure 67.
(a) Plate-like crystal of $LaSrFeO_4$ which was obtained by cleaving the as-grown sample. It is an $j = 1$ Ruddlesden-Popper phase $A_{j+1}B_jO_{3j+1}$.
(b) Part of the as-grown sample of $LaFeO_3$ with orthorhombically distorted perovskite structure.

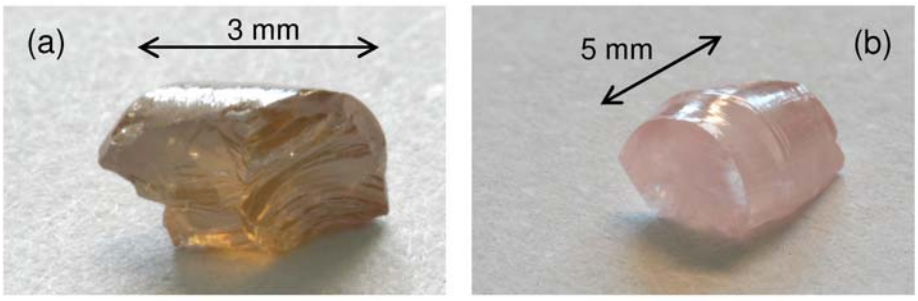

Fig. 30. Photographs of a part of the as-grown sample of two transparent insulators whose structure is not of the type $A'A_{k-1}B_kO_{3k+1}$, $A_nB_nO_{3n+2}$ or $A_mB_{m-1}O_{3m}$. (a) Yellow $SmTiO_{3.50}$ with pyrochlore structure, grown with a zone speed of 15 mm/h. (b) Pink $EuNbO_4$ with fergusonite structure, grown with a zone speed of 10 mm/h. They were prepared for magnetic measurements, see Fig. 51 and 54, and $SmTiO_{3.50}$ also for structural studies, see Table 61.

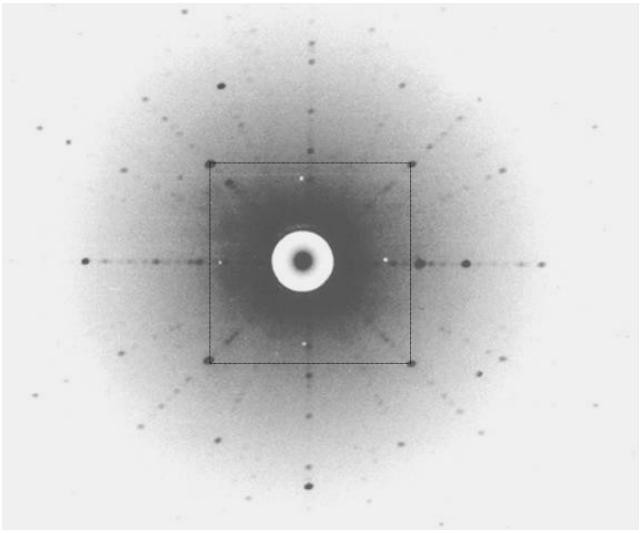

Fig. 31. Dark/bright-inverted Laue image perpendicular to the *ab*-plane of a plate-like crystal of orthorhombic $BaCa_{0.6}La_{0.4}Nb_2O_{7.00}$ ($k = 2$ of $A'A_{k-1}B_kO_{3k+1}$). Because the lattice parameters $a = 3.99\,\text{Å}$ and $b/2 = (7.80/2)\,\text{Å} = 3.90\,\text{Å}$ are close to each other, the outlined rectangle with the aspect ratio $a^{-1}/(b/2)^{-1} = 1.02$ appears practically as a square. Therefore it was impossible to distinguish between the *a*- and *b*-direction. In the case of a doubled axis the observed diffraction spots are probably related to the simple axis because those spots related to the superstructure are usually much weaker and therefore not visible.

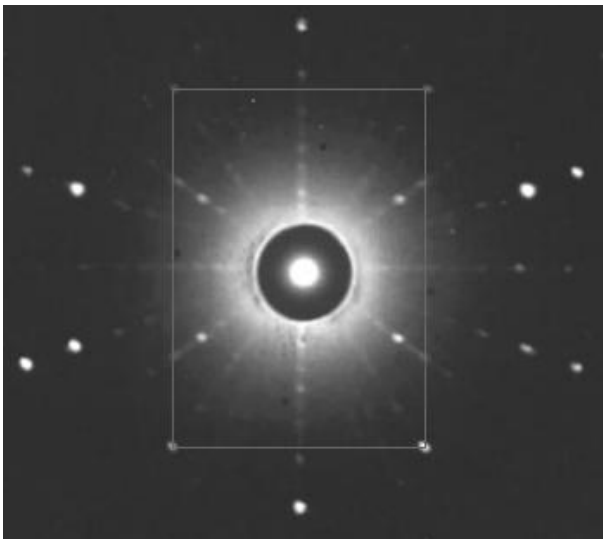

Fig. 32. Laue image perpendicular to the *ab*-plane of a plate-like crystal of monoclinic $PrTiO_{3.41}$ ($n = 5$ of $A_nB_nO_{3n+2} = ABO_x$). The aspect ratio of the outlined rectangle corresponds to the lattice parameter ratio $(a/2)^{-1}/b^{-1} = [(7.85/2)\ \text{Å}]^{-1}/[5.52\ \text{Å}]^{-1} = 1.41 \simeq \sqrt{2}$ but also $b^{-1}/a^{-1} = (5.52\ \text{Å})^{-1}/(7.85\ \text{Å})^{-1} = 1.41 \simeq \sqrt{2}$ leads to the same result. The determination of the *a*- and *b*-direction by the first relation is in accordance with measurements of the resistivity ρ because then $\rho_a < \rho_b$ was observed. Probably the observed diffraction spots are related to the simple *a*-axis because those spots related to the superstructure of the doubled *a*-axis are usually much weaker and therefore not visible.

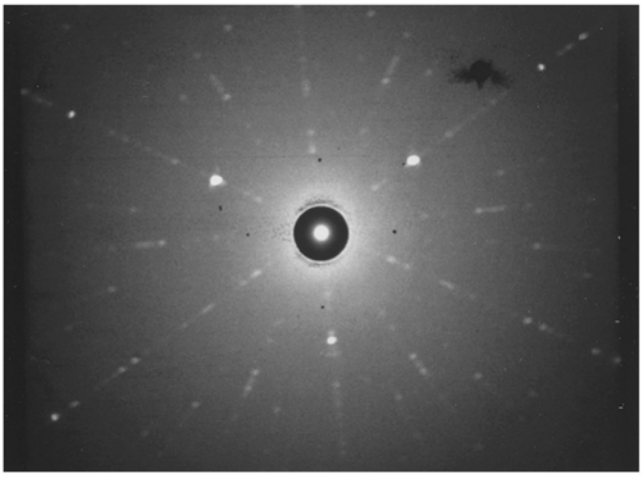

Fig. 33. Laue image perpendicular to the *ab*-plane of a plate-like crystal of hexagonal $Sr_{11}Nb_9O_{33.09}$ ($m = 5 + 6$ of $A_mB_{m-1}O_{3m}$).

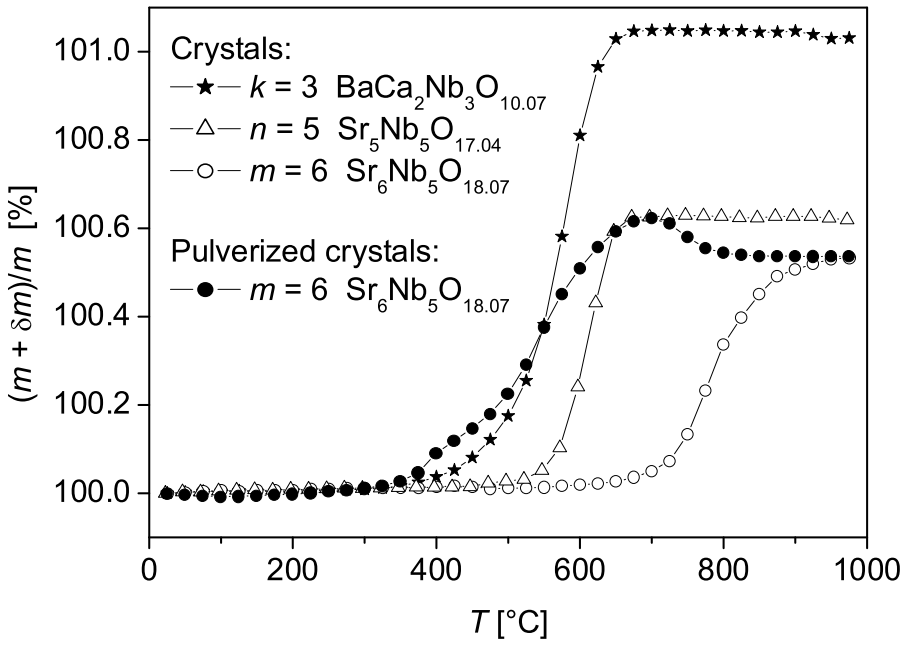

Fig. 34. Thermogravimetric behavior of the oxidation of some reduced niobates. Shown is the relative specimen mass, $(m + \delta m)/m$, as function of temperature T. The specimen were heated in static air from room temperature to 995°C with a rate of 10°C/min for $BaCa_2Nb_3O_{10.07}$ ($k = 3$ of $A'A_{k-1}B_kO_{3k+1}$) and $Sr_5Nb_5O_{17.04}$ ($n = 5$ of $A_nB_nO_{3n+2}$) and 9°C/min for $Sr_6Nb_5O_{18.07}$ ($m = 6$ of $A_mB_{m-1}O_{3m}$).

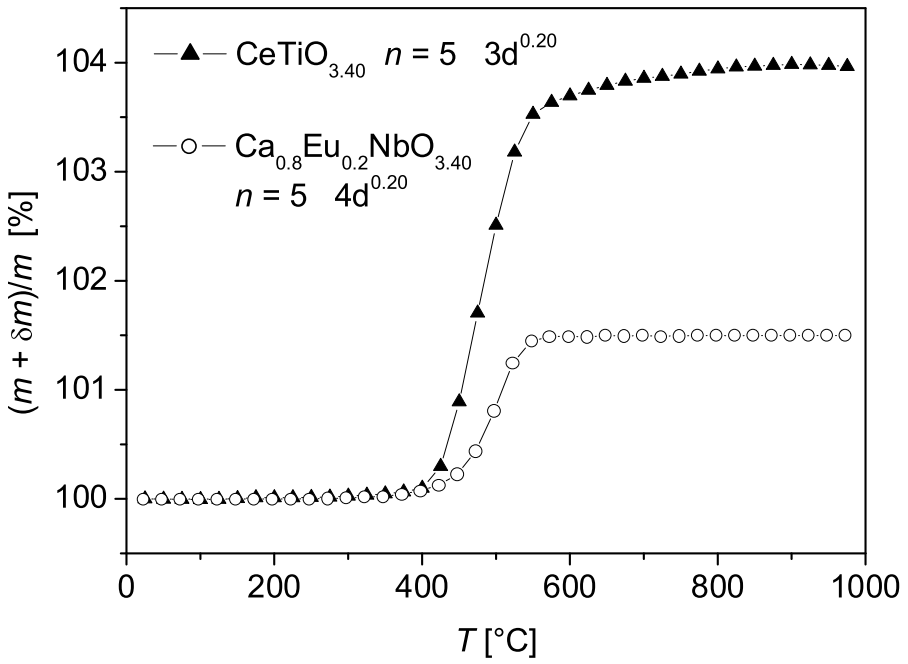

Fig. 35. Two examples of the thermogravimetric oxidation of compounds with Ce^{3+} or Eu^{2+} at the A site of $A_nB_nO_{3n+2} = ABO_x$, namely the $n = 5$ titanate $CeTiO_{3.40}$ and the $n = 5$ niobate $Ca_{0.8}Eu_{0.2}NbO_{3.40}$. Shown is the relative specimen mass, $(m + \delta m)/m$, as function of temperature T. The specimen were heated in static air from room temperature to 995°C with a rate of 9°C/min. The oxidation not only implies $Ti^{3.8+} \rightarrow Ti^{4+}$ and $Nb^{4.8+} \rightarrow Nb^{5+}$ but also $Ce^{3+} \rightarrow Ce^{4+}$ and $Eu^{2+} \rightarrow Eu^{3+}$, respectively.

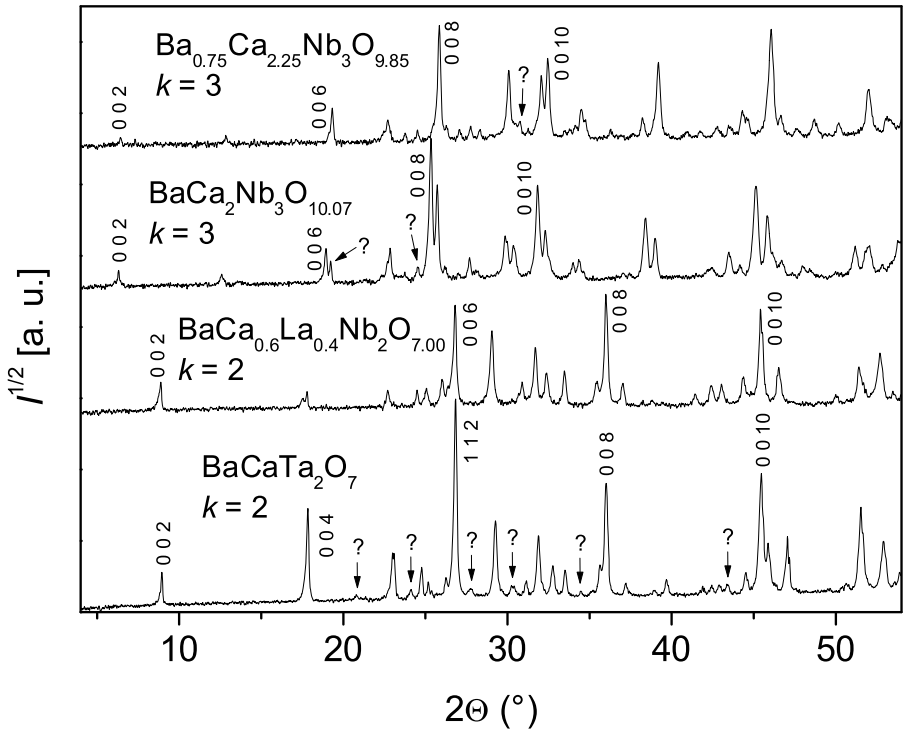

Fig. 36. Powder XRD pattern of orthorhombic $k = 2$ and $k = 3$ niobates and an $k = 2$ tantalate. Most of the observed peaks fit to an orthorhombic $A'A_{k-1}B_kO_{3k+1}$ structure. For clarity only a few peaks are indexed. The small peaks labelled by an arrow and a question mark do not fit to the $A'A_{k-1}B_kO_{3k+1}$ structure and may therefore indicate the presence of a small amount of impurity phase(s). The peak labelling of the $k = 2$ tantalate $BaCaTa_2O_7$ refers to a lattice parameter refinement with a simple a-axis and a body centered cell as obtained from single crystal XRD by Ebbinghaus [43].

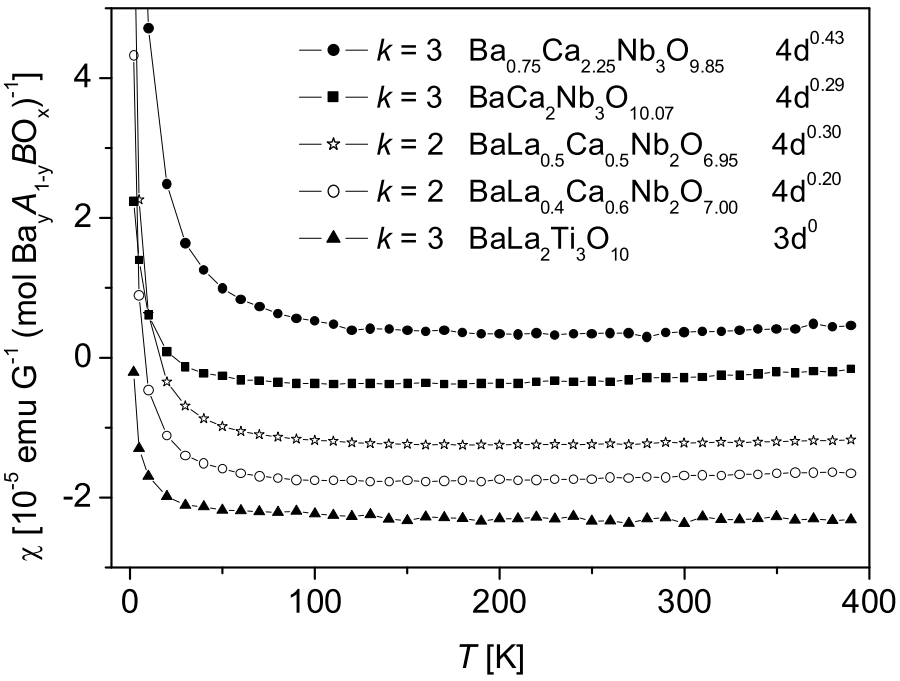

Fig. 37. Molar magnetic susceptibility χ as function of temperature T in low fields $H \leq$ 1000 G of some $A'A_{k-1}B_kO_{3k+1}$ compounds with $A' =$ Ba. To facilitate a comparison, the molar susceptibility is normalized to 1 mol B, i.e. to the formula $Ba_yA_{1-y}BO_x$ with $B =$ Nb or Ti.

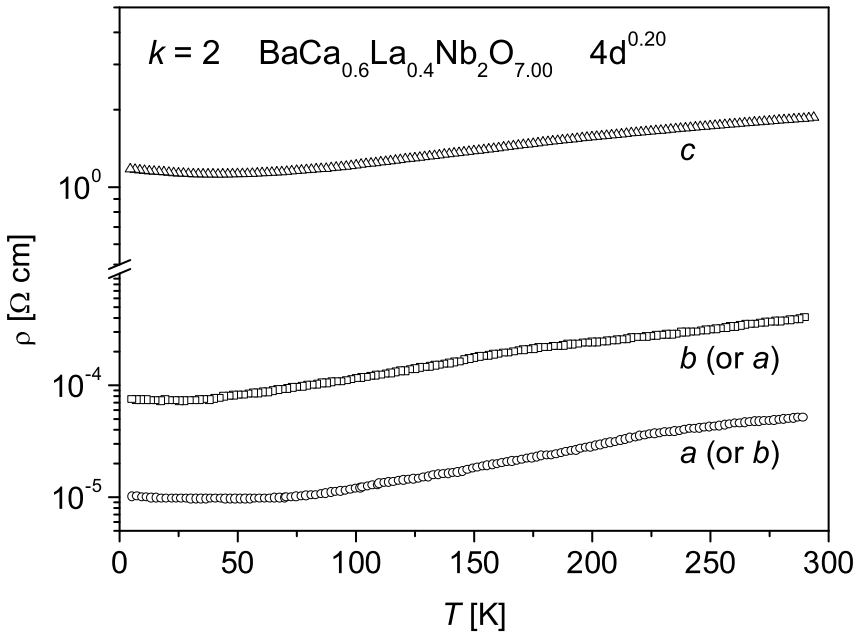

Fig. 38. Log-linear plot of the resistivity ρ versus temperature T of the $k = 2$ niobate $BaCa_{0.6}La_{0.4}Nb_2O_{7.00}$ along the a-, b- and c-axis. Because the lattice parameters $a = 3.99\,\text{Å}$ and $b/2 = (7.80/2)\,\text{Å} = 3.90\,\text{Å}$ are close to each other, a distinction between the a- and b-axis by Laue images was not possible, see Fig. 31.

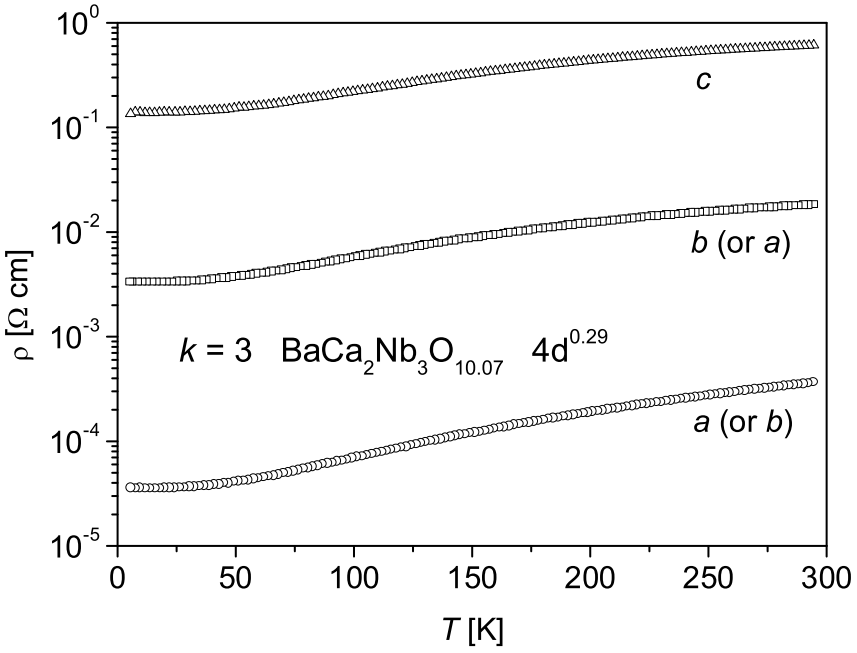

Fig. 39. Log-linear plot of the resistivity $\rho(T)$ of the $k = 3$ niobate $BaCa_2Nb_3O_{10.07}$ along the a-, b- and c-axis. Because the lattice parameters $a = 7.67$ Å and $b = 7.77$ Å are close to each other, a distinction between the a- and b-axis by Laue images was not possible.

LnTiO$_x$	Structure type	a, b, c [Å], β [°]	V [Å^3]	Z	V/Z [Å^3]	$\Delta(V/Z)$ [Å^3]	Ref.
YbTiO$_{3.39}$	Pyrochlore, no indications for $A_nB_nO_{3n+2}$	10.03, 90	1008	16	63.0		this work
YbTiO$_{3.50}$	Pyrochlore	10.03, 90	1009	16	63.1		[179]
GdTiO$_{3.39}$ GdTiO$_{3.34}$	Multiphase: pyrochlore, perovskite and ? but no indications for $A_nB_nO_{3n+2}$						this work
GdTiO$_{3.50}$	Pyrochlore	10.23, 90	1070	16	66.9		[179]
EuTiO$_{3.50}$	Pyrochlore	10.21, 90	1063	16	66.4		this work
	Pyrochlore	10.18, 90	1055	16	65.9	1.2	[210]
	$n = 4$ (**hps**)	7.55, 5.39, 12.86, 98.3	517.8	8	64.7		
SmTiO$_{3.50}$	Pyrochlore	10.20, 90	1061	16	66.3	1.3	[219]
	$n = 4$ (**hps**)	7.56, 5.39, 12.90, 98.5	519.9	8	65.0		
SmTiO$_{3.50}$ SmTiO$_{3.37}$	Pyrochlore $n = 5$	10.24, 90 7.80, 5.52, 30.93, 96.1	1072 1323	16 20	67.0 66.2	0.8	this work
Sm$_{0.9}$La$_{0.1}$ TiO$_{3.50}$	$n = 4$	7.63, 5.43, 12.99, 98.5	532.1	8	66.5		
Gd$_{0.5}$Pr$_{0.5}$ TiO$_{3.50}$	$n = 4$	7.63, 5.43, 13.00, 98.4	532.8	8	66.6		
NdTiO$_{3.50}$	$n = 4$	7.67, 5.46, 12.99, 98.5	538.2	8	67.3		
NdTiO$_x$ $3.31 \leq x$ $x \leq 3.50$	$A_nB_nO_{3n+2}$						[32,102] [186,188] this work

Table 61. Structure type and atomic packing density V/Z of some titanates LnTiO$_x$. Presented are the lattice parameters a, b, c, β, V and the number of formula units Z per unit cell. **hps** stands for high pressure synthesis. The pyrochlore structure is cubic and n refers to a monoclinic $A_nB_nO_{3n+2}$ structure. $\Delta(V/Z)$ is the difference of the atomic packing density between the pyrochlore and the $A_nB_nO_{3n+2}$ structure. See also Table 62.

ABO_x	Structure type	a, b, c [Å], β [°]	V [Å^3]	Z	V/Z [Å^3]	Ref.
$Sm_{0.67}Ca_{0.33}TiO_{3.33}$	$n = 6$	7.63, 5.41, 36.88, 96.0	1514	24	63.1	this work
		3.81, 5.42, 36.73, 90	759.0	12	63.3	[55]
$Nd_{0.67}Ca_{0.33}TiO_{3.33}$	$n = 6$	7.66, 5.44, 36.64, 90	1526	24	63.6	[153]
$SmTi_{0.8}V_{0.2}O_{3.39}$	$n = 5$	7.79, 5.50, 30.90, 95.9	1317	20	65.9	this work
$NdTi_{0.8}Fe_{0.2}O_{3.40}$	$n = 5$	7.80, 5.47, 30.72, 95.9	1303	20	65.2	this work
		7.67, 5.44, 31.42, 97.0	1302	20	65.1	[227]
$NdTi_{0.8}Al_{0.2}O_{3.40}$	$n = 5$	7.80, 5.49, 30.92, 96.5	1315	20	65.8	this work
$NdTiO_{3.31}$	$n = 5$	7.82, 5.50, 30.86, 96.5	1318	20	65.9	work
$Nd_{0.95}TiO_{3.34}$	$n = 5$	7.78, 5.47, 31.50, 96.0	1332	20	66.6	
$Ca_{0.5}La_{0.5}NbO_{3.5}$	pyrochlore	10.50, 90	1158	16	72.4	[42]
$Ca_{0.8}La_{0.2}NbO_{3.51}$	$n = 4$	3.90, 5.50, 26.25, 90	562.9	8	70.3	[127]
$CaNbO_{3.50}$ [1]	pyrochlore	10.44, 90	1138	16	71.1	[123]
$CaNbO_{3.50}$	$n = 4$	7.69, 5.50, 13.37, 98.3	558.9	8	69.9	this
$Pr_{0.6}Ca_{0.4}Ti_{0.6}Nb_{0.4}O_{3.50}$	pyrochlore	10.36, 90	1111	16	69.4	work
$PrTiO_{3.50}$	$n = 4$	7.69, 5.47, 12.99, 98.4	540.7	8	67.6	
$SmTi_{0.67}Ta_{0.33}O_{3.67}$	pyrochlore	10.29, 90	1090	16	68.1	[223]
$PrTi_{0.67}Ta_{0.33}O_{3.67}$	$n = 3$	3.87, 5.51, 20.30, 90	432.0	6	72.0	

Table 62. Structure type and atomic packing density V/Z of some compounds ABO_x whose tendency to crystallize in an $A_nB_nO_{3n+2}$ or a pyrochlore structure is close to each other. Presented are the lattice parameters a, b, c, β, V and the number of formula units Z per unit cell. The pyrochlore structure is cubic and n refers to a orthorhombic or monoclinic $A_nB_nO_{3n+2}$ structure. See also Table 61. [1]Prepared by hydrothermal synthesis.

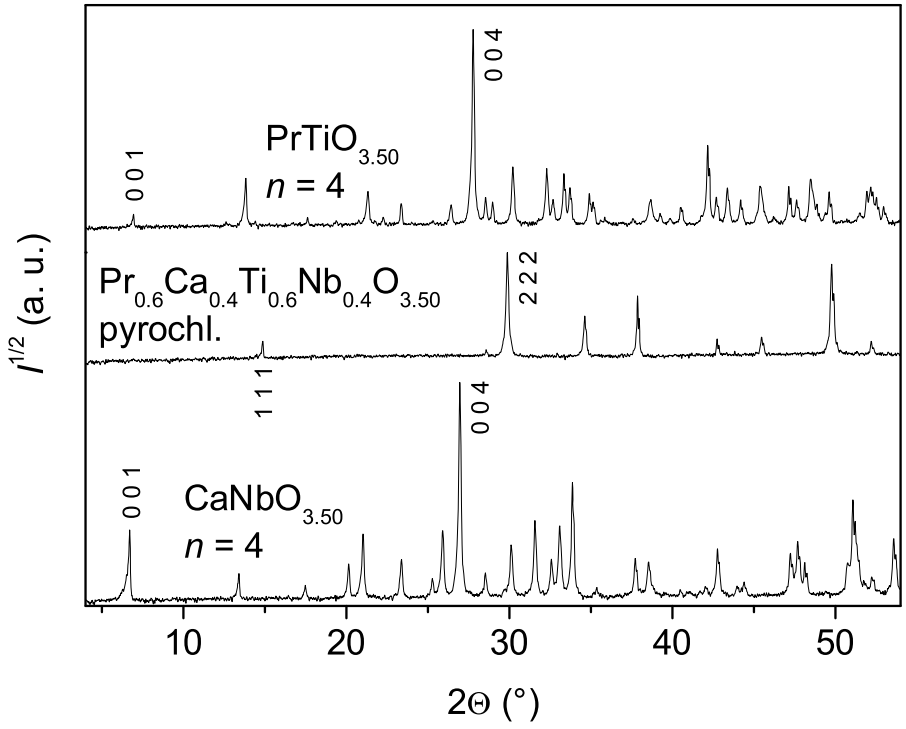

Fig. 40. Powder XRD pattern of $Pr_{1-y}Ca_yTi_{1-y}Nb_yO_{3.50}$ ($0 \leq y \leq 1$) for $y = 0$, 0.4 and 1. The end members $PrTiO_{3.50}$ ($y = 0$) and $CaNbO_{3.50}$ ($y = 1$) display an $n = 4$ structure, whereas a certain range of intermediate compositions crystallize in the pyrochlore structure, e.g. for $y = 0.4$. See also Table 62. For both $n = 4$ phases and the pyrochlore compound all observed peaks fit to a monoclinic $n = 4$ and a cubic pyrochlore structure, respectively. For clarity only a few peaks are indexed. Note that the structure of the related $y = 0.4$ composition $La_{0.6}Ca_{0.4}Ti_{0.6}Nb_{0.4}O_{3.50}$ is of the type $n = 4$, see Figure 42.

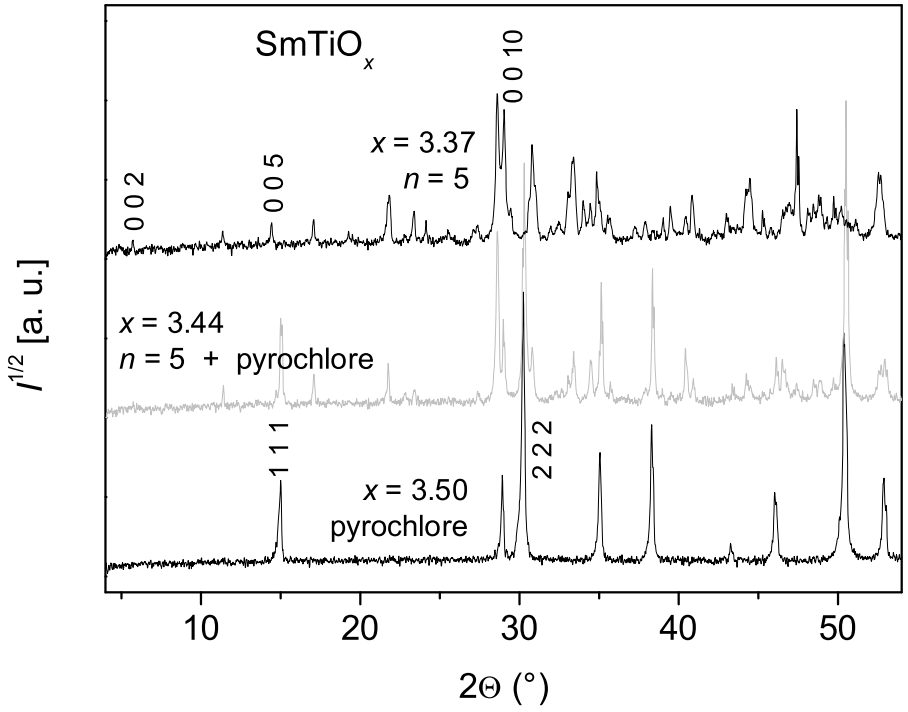

Fig. 41. Powder XRD pattern of $SmTiO_x$. For $x = 3.50$ and $x = 3.37$ all observed peaks fit to a cubic pyrochlore and a monoclinic $n = 5$ structure, respectively. For $x = 3.44$ (light grey pattern) the material consists of two phases, pyrochlore and $n = 5$, and there are no indications for the presence of an $n = 4.5$ type phase. For clarity only a few peaks are indexed.

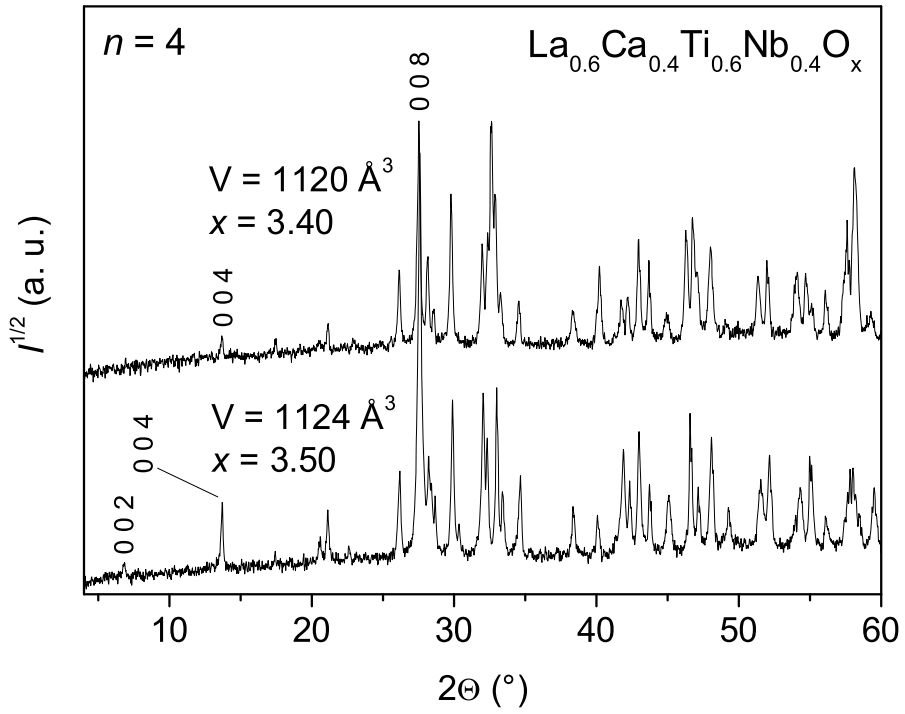

Fig. 42. Powder XRD pattern of monoclinic $La_{0.6}Ca_{0.4}Ti_{0.6}Nb_{0.4}O_x$. Also for $x = 3.40$, which is usually of the type $n = 5$, an $n = 4$ structure is observed. All observed peaks fit to a monoclinic $n = 4$ type structure. For clarity only a few peaks are indexed. Note that structure type of the related compound $Pr_{0.6}Ca_{0.4}Ti_{0.6}Nb_{0.4}O_{3.50}$ is not $n = 4$ but pyrochlore, see Figure 40.

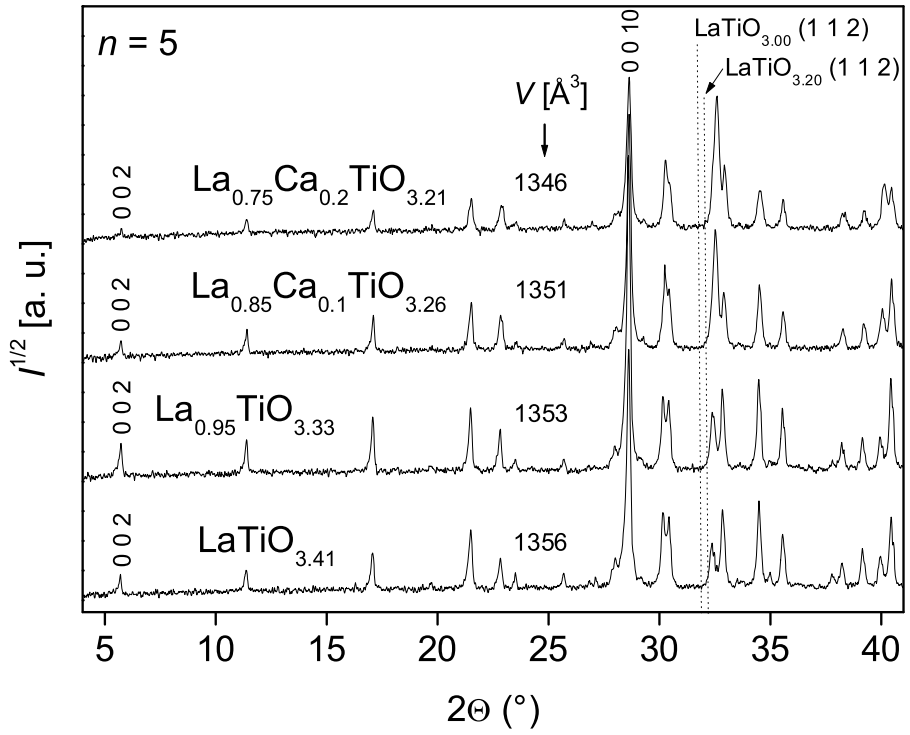

Fig. 43. Powder XRD pattern of monoclinic $n = 5$ titanates, three significantly non-stoichiometric compounds $A_{0.95}TiO_{3.40-y}$ $(0 < y \leq 0.19)$ and nearly stoichiometric $LaTiO_{3.41}$. The ideal $n = 5$ composition is $ATiO_{3.40}$. All observed peaks fit to a monoclinic $n = 5$ structure. For clarity only a few peaks are indexed. The unit cell volume V is also provided. The dotted lines at $2\Theta = 31.9°$ and $32.2°$ display the position of the highest intensity peak of the orthorhombic perovskite $LaTiO_{3.00}$ $(n = \infty)$ and $LaTiO_{3.20} = La_{0.94}Ti_{0.94}O_{3.00}$ $(n = \infty)$, respectively [117,124,126,127]. There are no peaks detected at these both positions.

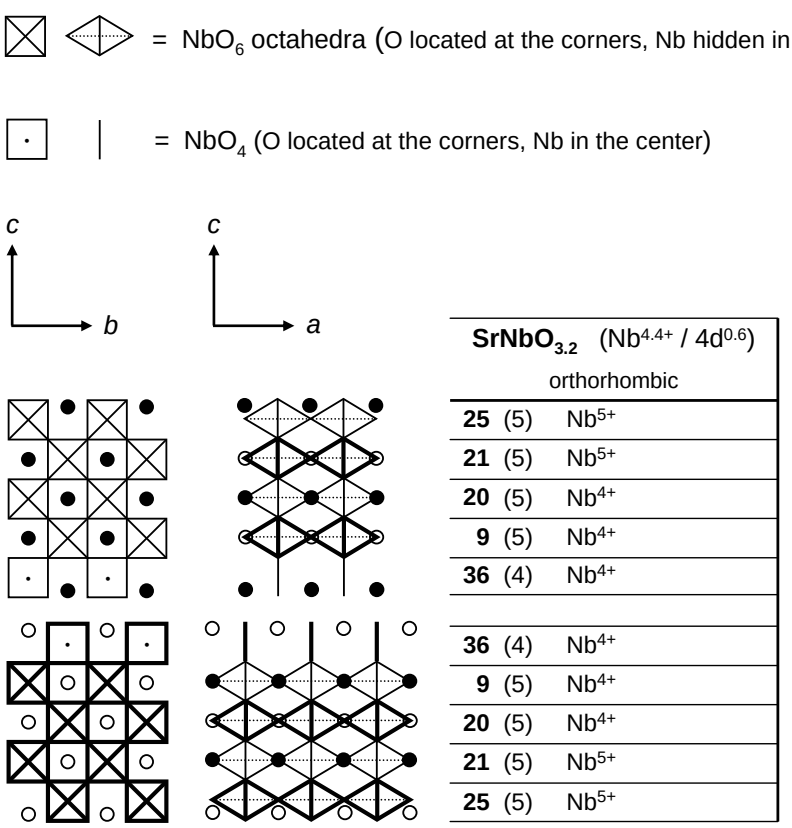

Fig. 44. Sketch of the idealized crystal structure of $SrNbO_{3.2} = Sr_5Nb_5O_{16}$ and some features of its Nb−O polyhedra. The way of drawing is analogous to that of Fig. 6 and 15. Along the *c*-axis the layers are five NbO_6 polyhedra thick, namely four NbO_6 octahedra and one NbO_4 polyhedron. The circles represent the Sr ions. Shown are the percentage values of the Nb−O polyhedra distortions in bold numbers after Eq. (1), the number of different Nb−O bond lengths per polyhedron in parenthesis, and the distribution of Nb^{5+} and Nb^{4+} according to a computed Coulomb contribution of the lattice energy. The data were calculated or taken from the results of a crystallographic study on $SrNbO_{3.2}$ by Schückel and Müller-Buschbaum [193]. $SrNbO_{3.2} = Sr_5Nb_5O_{16}$ can be considered as an oxygen-deficient $n = 5$ structure of $A_nB_nO_{3n+2} = ABO_x$, i.e. $Sr_5Nb_5O_{17-\Delta} = SrNbO_{3.4-\delta}$ with $\Delta = 1$ and $\delta = 0.2$, whereby the oxygen vacancies are fully ordered and located in one of the both boundary regions of the layers.

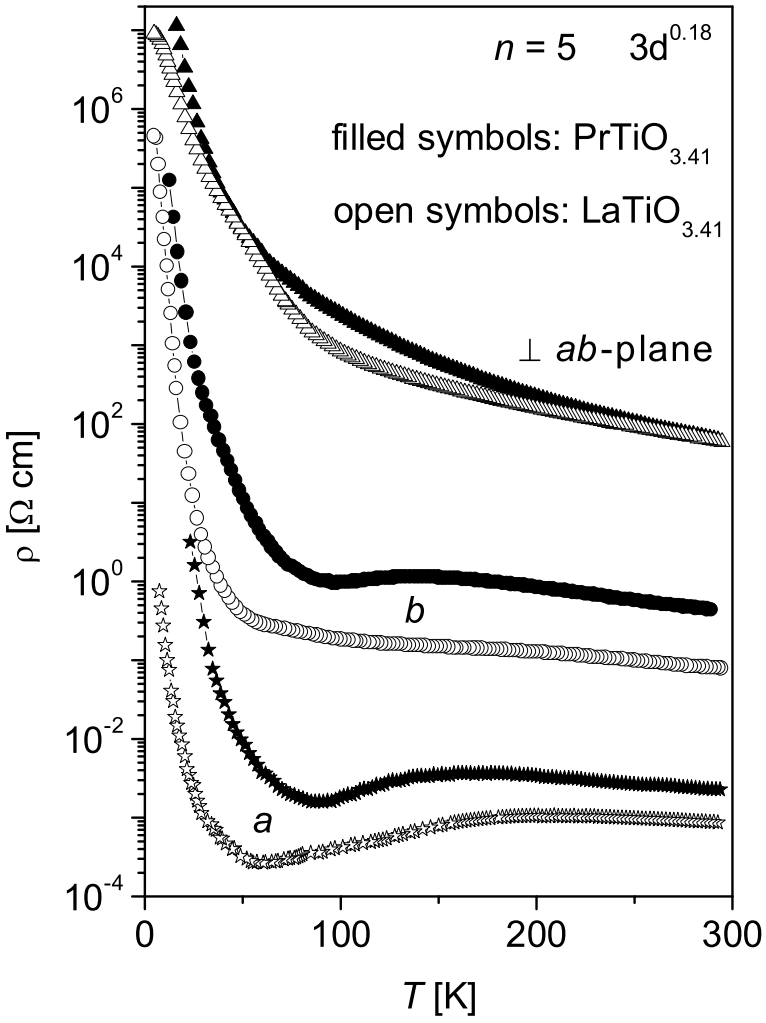

Fig. 45. Log-linear plot of the resistivity $\rho(T)$ of the monoclinic $n = 5$ titanates $PrTiO_{3.41}$ and $LaTiO_{3.41}$ along the a- and b-axis and perpendicular to the ab-plane. The data of $LaTiO_{3.41}$ are from Ref. [127].

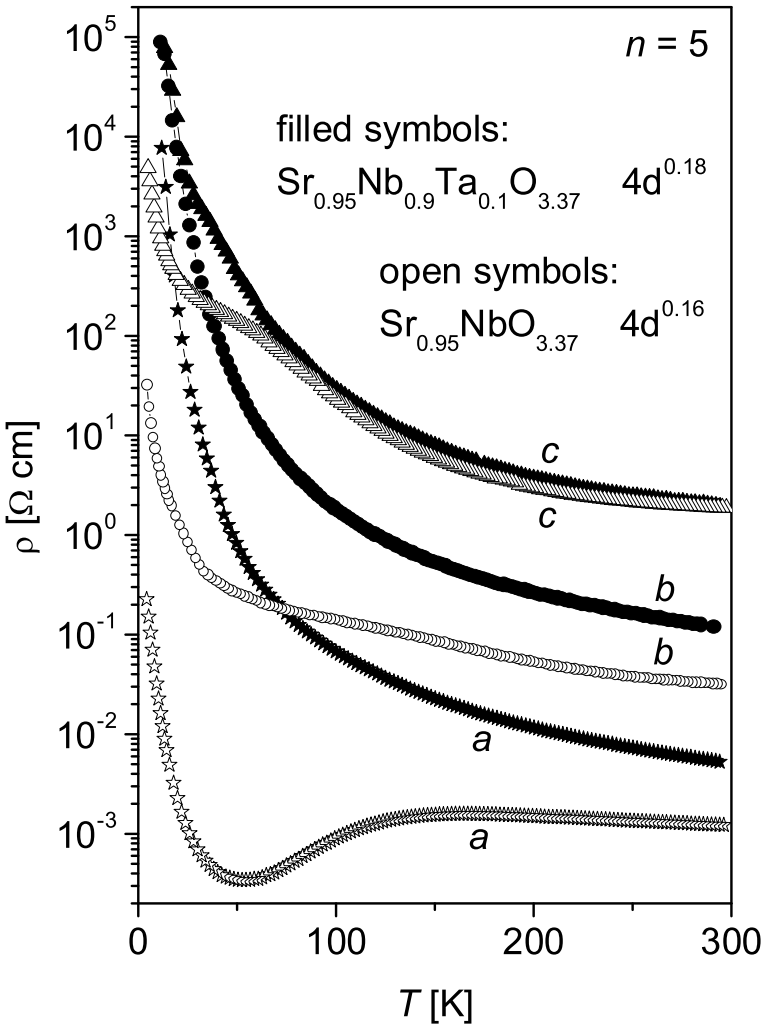

Fig. 46. Log-linear plot of the resistivity $\rho(T)$ along the a-, b- and c-axis of two significantly non-stoichiometric orthorhombic $n = 5$ compounds $Sr_{0.95}BO_{3.37}$ with B = Nb and $B = Nb_{0.9}Ta_{0.1}$. The data for $Sr_{0.95}NbO_{3.37}$ are from Ref. [127].

Ion	Nb^{4+} V^{4+} Ti^{3+}	V^{3+}	Mn^{4+} V^{2+}	Mn^{3+}	Fe^{3+}	Ta^{5+} Nb^{5+} Ti^{4+}
Electronic configuration	$4d^1$ $3d^1$ $3d^1$	$3d^2$	$3d^3$	$3d^4$	$3d^5$	$5d^0$ $4d^0$ $3d^0$
Multiplet ground state $^{2S+1}L_J$	$^2D_{3/2}$	$^3F_2$	$^4F_{3/2}$	$^5D_0$	$^6S_{5/2}$	$^1S_0$
g	2 [1]	2 [1]	2 [1]	2 [1]	2	–
q_{th} [μ_B] [1]	1.73 [1]	2.83 [1]	3.87 [1]	4.90	5.90	0

Table 63. Magnetic properties of some transition metal ions after Ref. [104]. Recall that L = S, P, D, F, G, H, I stands for L = 0, 1, 2, 3, 4, 5, 6, respectively. g is the free-ion Lande factor after Eq. (19). q_{th} is the theoretical free-ion value of the effective magnetic moment in units of the Bohr magneton μ_B after Eq. (18). [1]Spin-only value, i.e. $L = 0$ and thus $J = S$, because in solids the orbital angular momentum L of the d elements is usually quenched by the crystal field.

Ion	Ce^{4+} La^{3+}	Ce^{3+}	Pr^{3+}	Nd^{3+}	Sm^{3+}	Eu^{3+}	Eu^{2+} Gd^{3+}	Yb^{3+}
Electronic configuration	$4f^0$	$4f^1$	$4f^2$	$4f^3$	$4f^5$	$4f^6$	$4f^7$	$4f^{13}$
Multiplet ground state $^{2S+1}L_J$	$^1S_0$	$^2F_{5/2}$	$^3H_4$	$^4I_{9/2}$	$^6H_{5/2}$	$^7F_0$	$^8S_{7/2}$	$^2F_{7/2}$
g	–	6/7	4/5	8/11	2/7	–	2	8/7
q_{th} [μ_B]	0	2.54	3.58	3.62	0.84	0	7.94	4.54
Δ [K]		3150	3100	2750	1450	500	– [2]	14800
χ_V [10^{-6} emu G^{-1} mol^{-1}]		45	97	174	739	6000	–	8
ξ [10^{-6} K^{-1}] in $\chi_V/\chi_C = \xi T$		56	61	106	8276	∞ [1]	–	3

Table 64. Magnetic properties of some rare earth ions after Ref. [89,104]. Recall that L = S, P, D, F, G, H, I stands for L = 0, 1, 2, 3, 4, 5, 6, respectively. g is the free-ion Lande factor after Eq. (19). q_{th} is the theoretical free-ion value of the effective magnetic moment in units of the Bohr magneton μ_B after Eq. (18). Δ is the energy difference between the first excited state $^{2S+1}L_{J+1}$ and the ground state $^{2S+1}L_J$ of the multiplet. χ_V is the molar Van Vleck paramagnetic susceptibility after Eq. (14). The parameter $\xi = 2S(L+1)/[g^2J(J+1)^2\Delta]$, when multiplied with the temperature T, represents the ratio of the temperature-independent Van Vleck susceptibility χ_V to the Curie susceptibility $\chi_C = C/T$. [1]Here $\xi = \infty$ indicates symbolically the exclusive presence of the Van Vleck paramagnetism because the Curie susceptibility is absent owing to $J = 0$. [2]Due to $L = 0$ there is no spin-orbit interaction and therefore Δ does not exist because the different levels of a multiplet arise from the spin-orbit coupling.

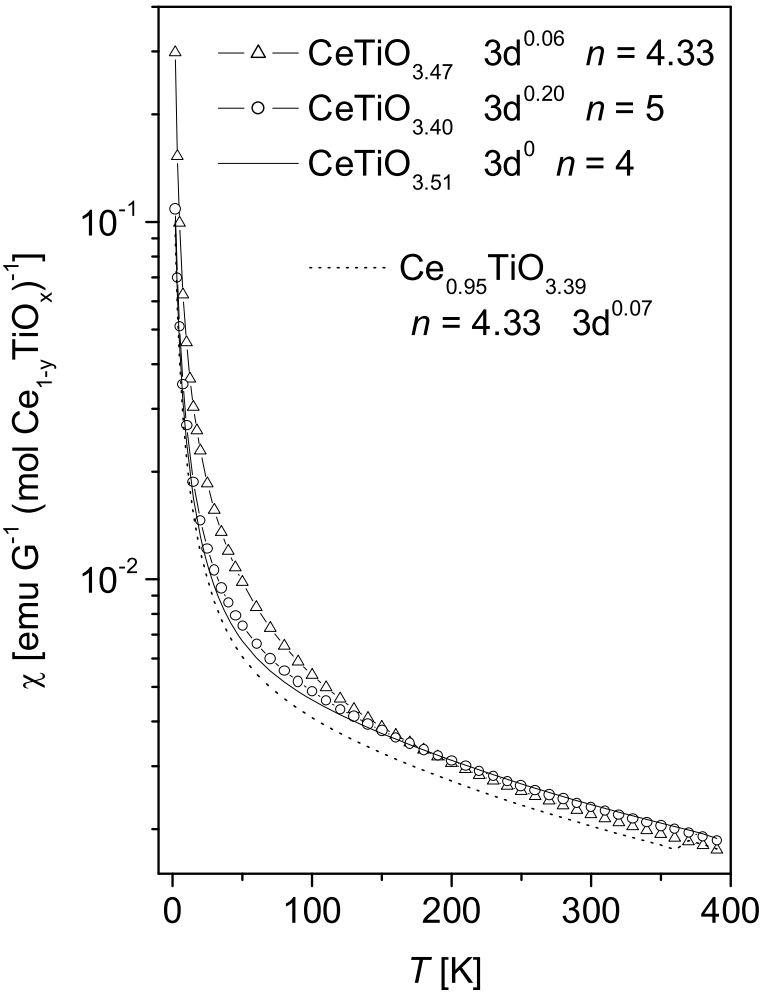

Fig. 47. Log-linear plot of the molar magnetic susceptibility $\chi(T)$ in a field of $H = 500$ G of titanates $Ce_{1-y}TiO_x$ with $y = 0$ or $y = 0.05$. For $T \geq 100$ K the susceptibility fits well to the Curie-Weiss function $C/(T - \theta)$, see Fig. 52 and Table 65.

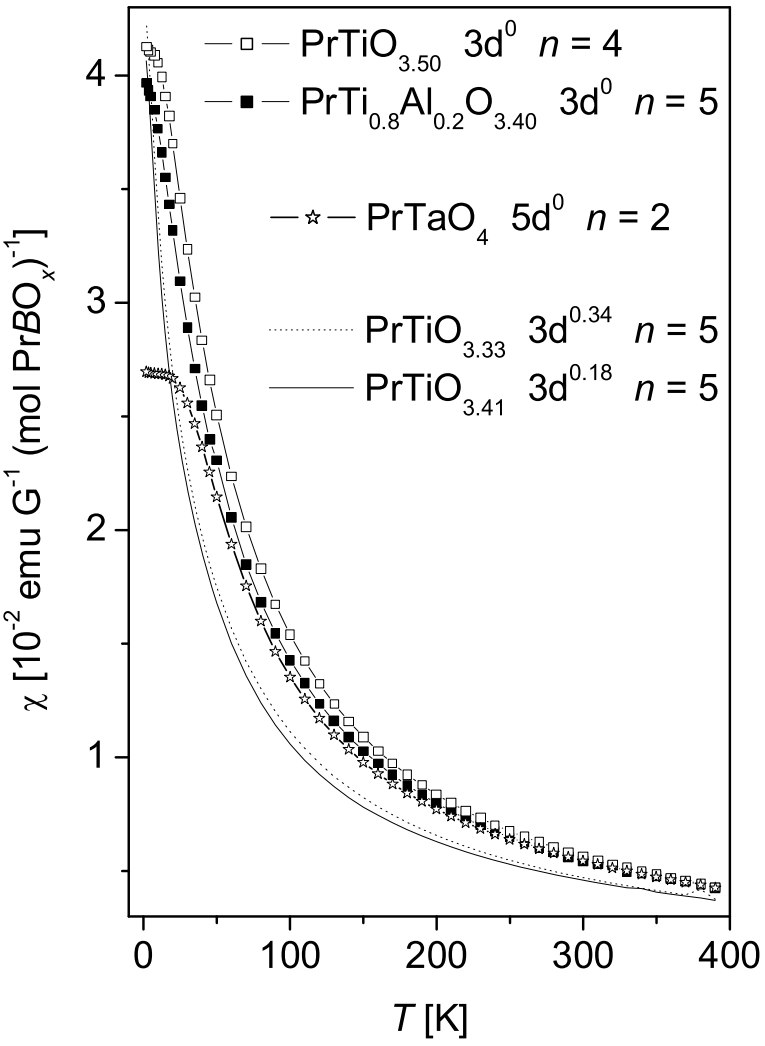

Fig. 48. Molar magnetic susceptibility $\chi(T)$ in a field of $H = 500$ G of some compounds $PrBO_x$. For $T \geq 100$ K the susceptibility fits well to the Curie-Weiss function $C/(T-\theta)$, see Fig. 59 as well as Table 66 and 69. The resistivity $\rho(T)$ of $PrTiO_{3.41}$ is shown in Figure 45.

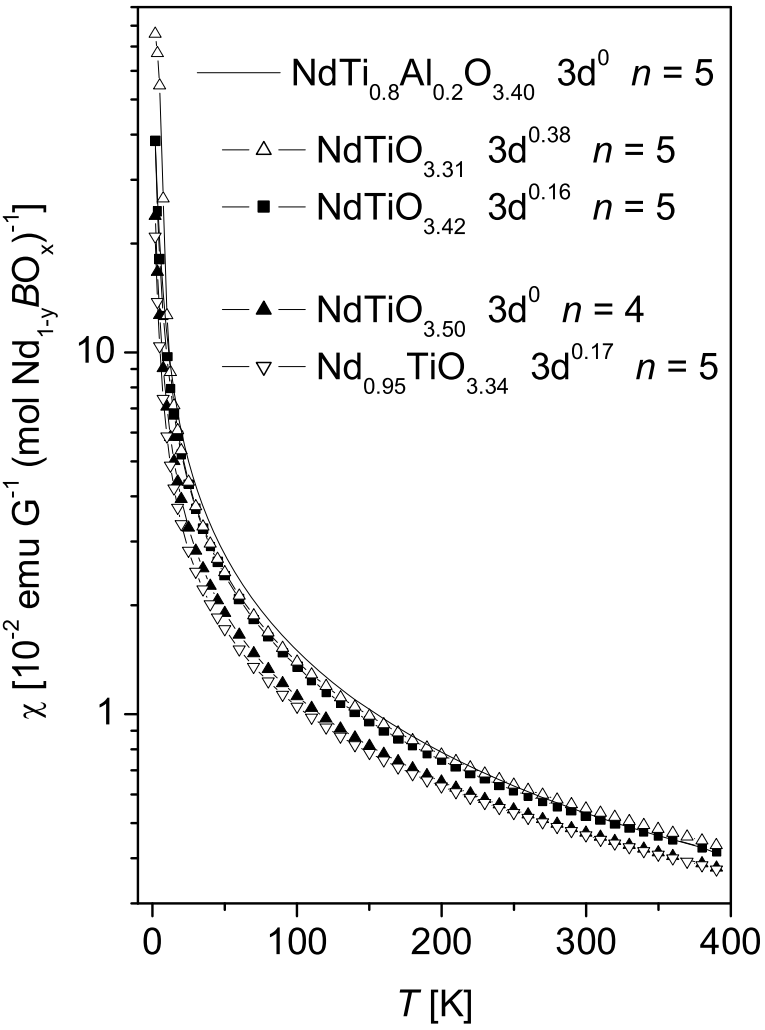

Fig. 49. Log-linear plot of the molar magnetic susceptibility $\chi(T)$ in a field of $H = 500$ G of titanates $Nd_{1-y}BO_x$ with $y = 0$ or $y = 0.05$. For $T \geq 100$ K the susceptibility fits well to the Curie-Weiss function $C/(T - \theta)$, see Fig. 50 and Table 67.

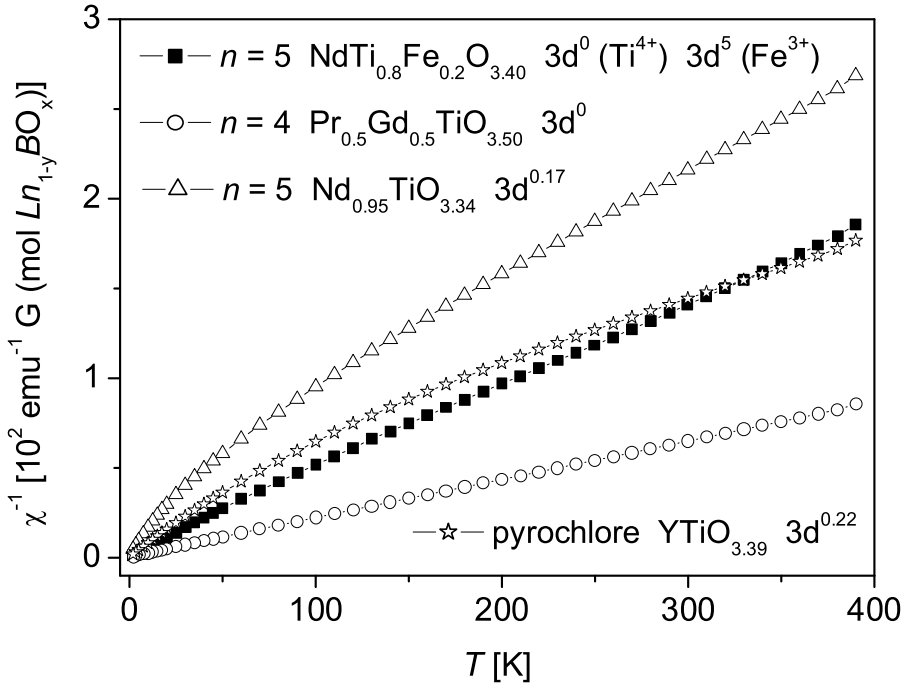

Fig. 50. Inverse molar magnetic susceptibility $\chi(T)^{-1}$ in a field of $H = 500$ G of some $A_nB_nO_{3n+2}$ or pyrochlore compounds $Ln_{1-y}BO_x$ with $y = 0$ or $y = 0.05$. For $T \geq 100$ K the susceptibility $\chi(T)$ fits well to the Curie-Weiss function $C/(T - \theta)$, see Table 67 and 68.

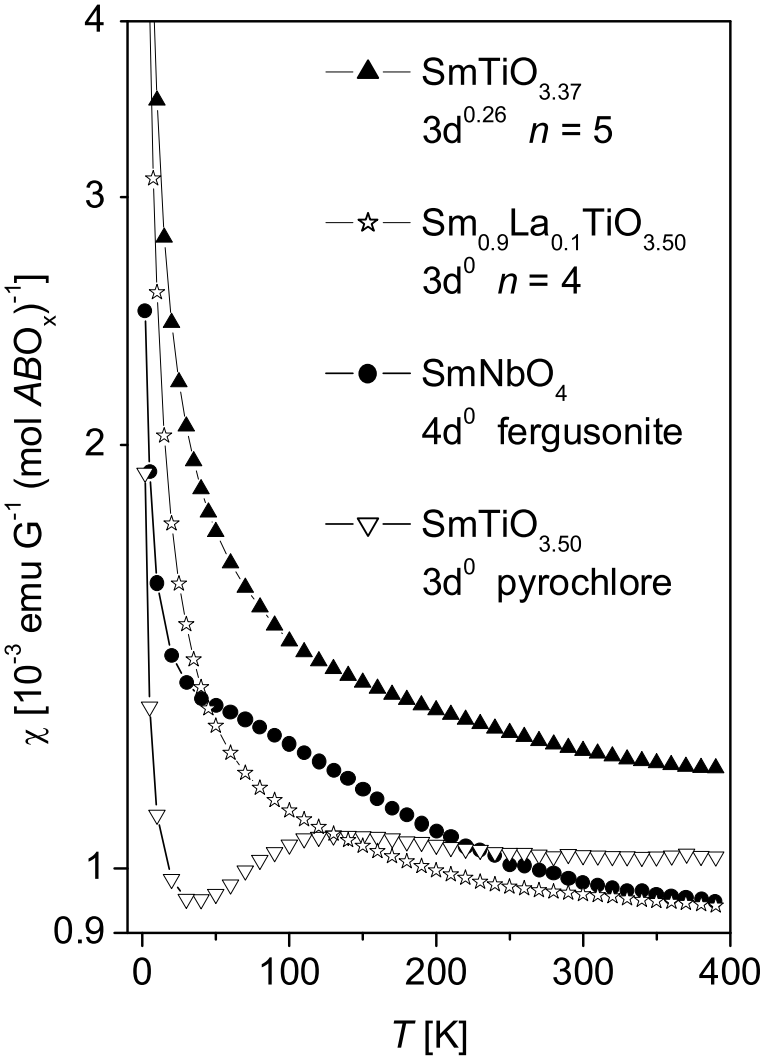

Fig. 51. Log-linear plot of the molar magnetic susceptibility $\chi(T)$ in low fields $H \leq 500\,\mathrm{G}$ of some compounds ABO_x with $A_nB_nO_{3n+2}$, pyrochlore or fergusonite structure and Sm at the A site. Some curves of $\chi(T)^{-1}$ are shown in Figure 52.

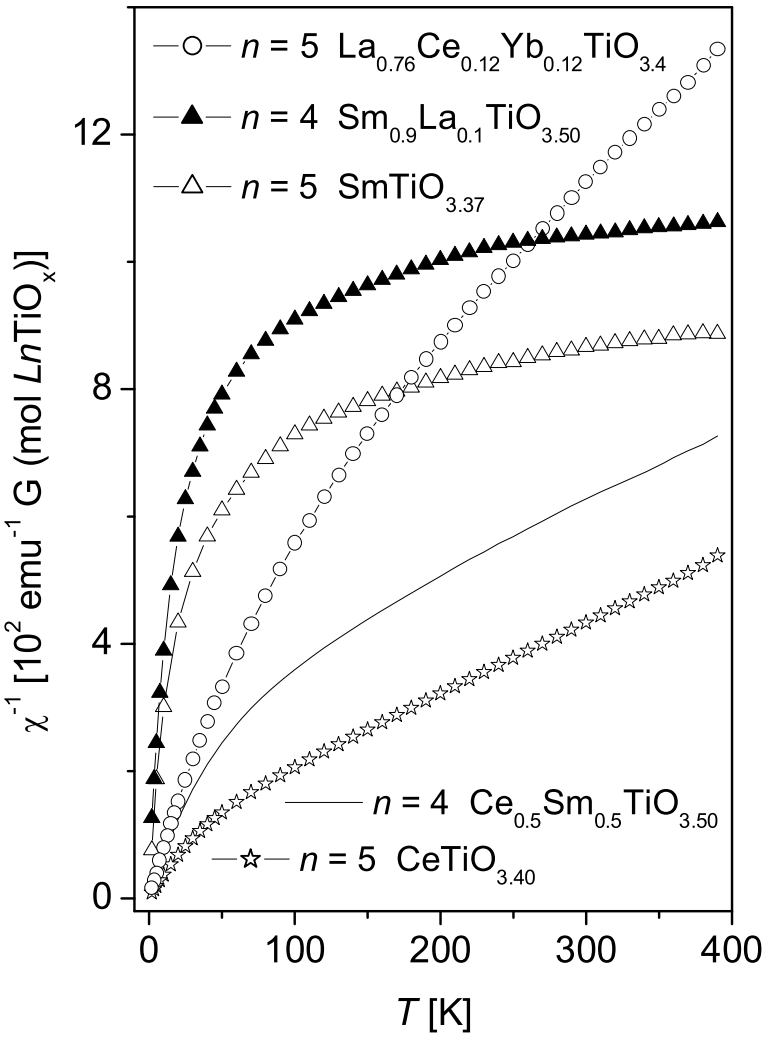

Fig. 52. Inverse molar magnetic susceptibility $\chi(T)^{-1}$ in a field of $H = 500$ G of some titanates $Ln\mathrm{TiO}_x$ with Ln = La, Ce, Sm and/or Yb. For $T \geq 100$ K and ≥ 200 K the susceptibility of $\mathrm{CeTiO}_{3.40}$ and $\mathrm{La}_{0.76}\mathrm{Ce}_{0.12}\mathrm{Yb}_{0.12}\mathrm{TiO}_{3.4}$, respectively, fits well to the Curie-Weiss function $C/(T - \theta)$, see Table 65. There is no Curie-Weiss behavior for $\mathrm{SmTiO}_{3.37}$ and $\mathrm{Sm}_{0.9}\mathrm{La}_{0.1}\mathrm{TiO}_{3.50}$. For $\mathrm{Ce}_{0.5}\mathrm{Sm}_{0.5}\mathrm{TiO}_{3.50}$ see also Figure 53.

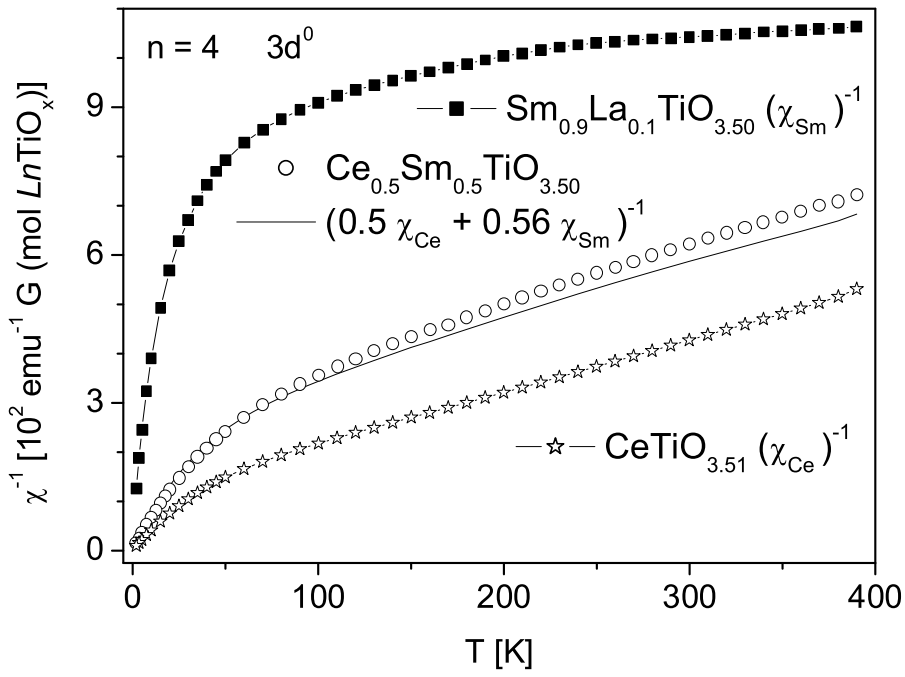

Fig. 53. Inverse molar magnetic susceptibility $\chi(T)^{-1}$ in a field of $H = 500$ G of the $n = 4$ insulators $Ce_{0.5}Sm_{0.5}TiO_{3.50}$, $CeTiO_{3.51}$ and $Sm_{0.9}La_{0.1}TiO_{3.50}$. The linear temperature dependence of $\chi(T)^{-1}$ of $Ce_{0.5}Sm_{0.5}TiO_{3.50}$ at high T suggests the presence of a Curie-Weiss behavior. However, to a good approximation $\chi(T)^{-1}$ of $Ce_{0.5}Sm_{0.5}TiO_{3.50}$ results from the inverse of the molar weighted sum of $\chi(T)$ of $CeTiO_{3.51}$ and $Sm_{0.9}La_{0.1}TiO_{3.50}$ ($0.56 \times 0.9 = 0.5$).

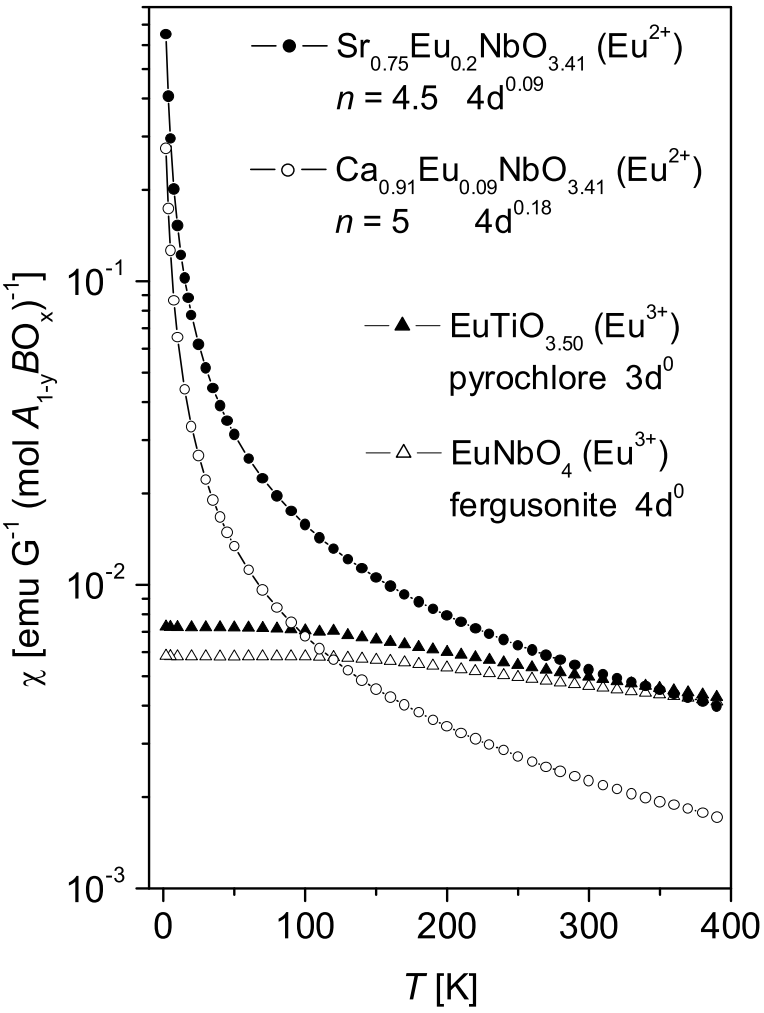

Fig. 54. Log-linear plot of the molar magnetic susceptibility $\chi(T)$ in low fields $H \leq$ 500 G of $A_{1-y}BO_x$ ($y = 0$ or $y = 0.05$) with fergusonite, pyrochlore or $A_nB_nO_{3n+2}$ structure and Eu at the A site. The susceptibility of the $n = 4.5$ and $n = 5$ niobates fits well to the Curie-Weiss function $C/(T - \theta)$ and indicates that Eu is in the valence state Eu^{2+}, see Fig. 55 and Table 68. In spite of $J = 0$ for Eu^{3+} (see Table 64) the susceptibility of the Eu^{3+} compounds is paramagnetic and temperature-independent at low T. This reflects the presence of the Van Vleck paramagnetism.

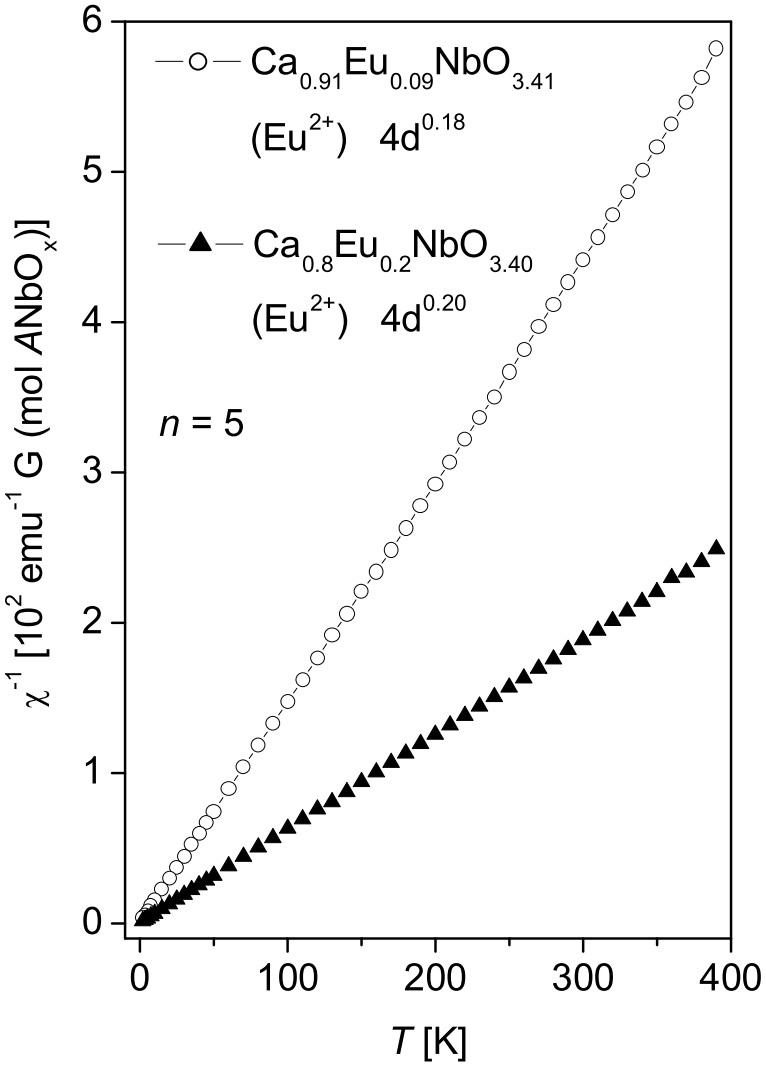

Fig. 55. Inverse molar magnetic susceptibility $\chi(T)^{-1}$ in a field of $H = 500\,\mathrm{G}$ of $n = 5$ niobates $Ca_{1-y}Eu_yNbO_x$. In the whole temperature range the susceptibility fits well to the Curie-Weiss function $C/(T - \theta)$ and indicates that Eu is in the valence state Eu^{2+}, see Table 68.

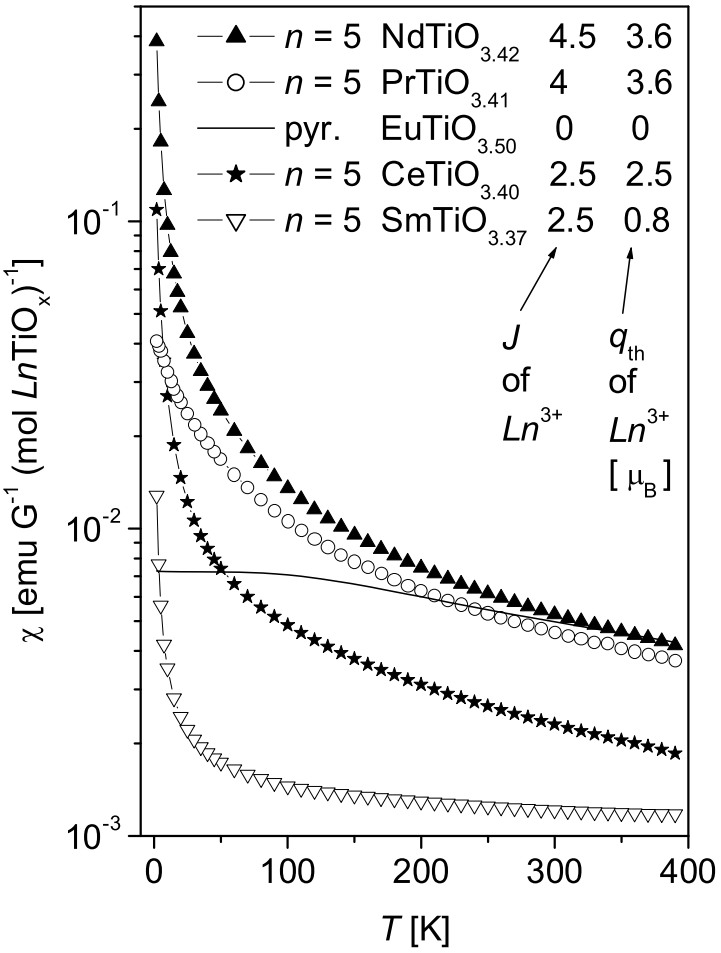

Fig. 56. Log-linear plot of the molar magnetic susceptibility $\chi(T)$ in fields of $H \leq 500$ G of some titanates $Ln\mathrm{TiO}_x$: The $n = 5$ electrical conductors $\mathrm{CeTiO}_{3.40}$ ($3d^{0.20}$), $\mathrm{PrTiO}_{3.41}$ ($3d^{0.18}$), $\mathrm{NdTiO}_{3.42}$ ($3d^{0.16}$), $\mathrm{SmTiO}_{3.37}$ ($3d^{0.26}$), and the insulator $\mathrm{EuTiO}_{3.50}$ ($3d^0$) with pyrochlore structure. The susceptibility results predominantly from the paramagnetic moments of the rare earth ions Ln^{3+}. Therefore this plot represents a comparison of the magnitude and the temperature dependence of $\chi(T)$ resulting from Ce^{3+}, Pr^{3+}, Nd^{3+}, Sm^{3+} and Eu^{3+}. J is the quantum number of the total angular momentum of Ln^{3+} and q_{th} the associated theoretical free-ion value of the effective magnetic moment, see Table 64. The susceptibility of the Ce^{3+}, Pr^{3+} and Nd^{3+} titanates displays a Curie-Weiss behavior, see Fig. 52, 59 and Table 65, 67 and 69. The susceptibility of $\mathrm{SmTiO}_{3.37}$ is markedly influenced by the Van Vleck type paramagnetism, see Table 64 and also Fig. 51 and 52. The paramagnetic susceptibility of $\mathrm{EuTiO}_{3.50}$ results exclusively from the Van Vleck type paramagnetism, see Table 64 and also Fig. 54.

Compound structure type , N	C [emu G^{-1} K (mol $Ln_{1-y}TiO_x)^{-1}$]	θ [K]	R^2	p_{exp} [μ_B]	p_{th} [μ_B] of Ln^{3+}
$\mathbf{Ce_{0.5}Pr_{0.5}TiO_{3.4}}$ [2] $n = 5$, $3d^{0.2}$	1.154	− 45	0.9999	3.04	3.10
$\mathbf{Ce_{0.5}Pr_{0.5}TiO_{3.50}}$ $n = 4$, $3d^{0}$	1.201	− 36	0.9999	3.10	
$\mathbf{CeTiO_{3.40}}$ $n = 5$, $3d^{0.20}$	0.877	− 82	0.9998	2.65	2.54
$\mathbf{CeTiO_{3.47}}$ [1] $n = 4.33$, $3d^{0.06}$	0.749	− 43	0.9987	2.45	
$\mathbf{Ce_{0.95}TiO_{3.39}}$ $n = 4.33$, $3d^{0.07}$	0.809	− 98	0.9999	2.54	2.48
$\mathbf{CeTiO_{3.51}}$ $n = 4$, $3d^{0}$	0.957	− 108	0.9998	2.77	2.54
$\mathbf{La_{0.5}Ce_{0.5}TiO_{3.4}}$ [1 2] $n = 5$, $3d^{0.2}$	0.470	− 85	0.9997	1.94	1.80
$\mathbf{La_{0.67}Ce_{0.33}TiO_{3.50}}$ [1] $n = 4$, $3d^{0}$	0.279	− 89	0.9999	1.49	1.46
$\mathbf{La_{0.76}Ce_{0.12}Yb_{0.12}TiO_{3.4}}$ [2] $n = 5$, $3d^{0.2}$	0.415	− 164	0.9992	1.82	1.80

Table 65. Results of fitting the molar magnetic susceptibility $\chi(T)$ of $Ln_{1-y}TiO_x$ with $y = 0$ or $y = 0.05$ to the Curie-Weiss function $C/(T - \theta)$. The fit was performed in the range $T \geq 100\,K$ ($\geq 200\,K$ for $La_{0.76}Ce_{0.12}Yb_{0.12}TiO_{3.4}$). Some curves of $\chi(T)$ or $\chi(T)^{-1}$ are shown in Fig. 47, 52 and 56. R^2 describes the goodness of the fit. p_{exp} is the experimentally determined effective magnetic moment after Eq. (15) and (16). p_{th} is the corresponding theoretical value resulting from Ln^{3+} after Eq. (17) and Table 64. [1]Compound reported in Ref. [127]. [2]Because a thermogravimetric determination of x was not possible, as discussed in Ref. [127] for $La_{0.5}Ce_{0.5}TiO_{3.4}$, the ideal $n = 5$ value $x = 3.4$ was assigned.

Compound structure type , N	C [emu G^{-1} K (mol $ABO_x)^{-1}$]	θ [K]	R^2	p_{exp} [μ_B]	p_{th} [μ_B] of Pr^{3+}
$\mathbf{Pr_{0.6}Ca_{0.4}Ti_{0.6}Nb_{0.4}O_{3.50}}$ pyrochlore , $3d^0$, $4d^0$	0.900	− 52	0.9996	2.68	2.77
$\mathbf{PrTaO_4}$ $n = 2$, $3d^0$	1.820	− 35	0.9999	3.81	3.58
$\mathbf{PrTiO_{3.50}}$ $n = 4$, $3d^0$	1.784	− 15	0.9996	3.78	
$\mathbf{PrTiO_{3.33}}$ $n = 5$, $3d^{0.34}$	1.634	− 47	0.9998	3.61	
$\mathbf{PrO_{1.50}}$ C-rare earth (bixbyite) , −		− 73		3.59	

Table 66. Results of fitting the molar magnetic susceptibility $\chi(T)$ of some ABO_x materials with Pr at the A site to the Curie-Weiss function $C/(T - \theta)$. The fit was performed in the range $T \geq 100$ K (≥ 200 K for the pyrochlore compound). Some curves of $\chi(T)$ are shown in Figure 48. R^2 describes the goodness of the fit. p_{exp} is the experimentally determined effective magnetic moment after Eq. (15) and (16). p_{th} is the corresponding theoretical value resulting from Pr^{3+} after Eq. (17) and Table 64. For the sake of comparison the values of $Pr_2O_3 = PrO_{1.50}$ are also presented, after Ref. [99]. For data of further Pr compounds see Table 69.

Compound structure type , N	C [emu G^{-1} K (mol $Nd_{1-y}BO_x)^{-1}$]	θ [K]	R^2	p_{exp} [μ_B]	p_{th} [μ_B] of Nd^{3+}	p_{th} [μ_B] of Nd^{3+} and Ti^{3+} (or Fe^{3+})
NdTiO$_{3.31}$ $n = 5$, $3d^{0.38}$	1.794	− 30	0.9992	3.79	3.62	3.77 [1]
Nd$_{0.95}$**TiO**$_{3.34}$ $n = 5$, $3d^{0.17}$	1.657	− 60	0.9992	3.64	3.53	3.60 [1]
NdTiO$_{3.42}$ $n = 5$, $3d^{0.16}$	1.713	− 28	0.9993	3.70	3.62	3.69 [1]
NdTi$_{0.8}$**Al**$_{0.2}$**O**$_{3.40}$ $n = 5$, $3d^0$	1.652	− 10	0.9999	3.63	3.62	
NdTi$_{0.8}$**Fe**$_{0.2}$**O**$_{3.40}$ $n = 5$, $3d^0$	2.233	− 16	0.9998	4.23	3.62	4.41
NdTiO$_{3.50}$ $n = 4$, $3d^0$	1.619	− 47	0.9992	3.60	3.62	

Table 67. Results of fitting the molar magnetic susceptibility $\chi(T)$ of $Nd_{1-y}BO_x$ with $y = 0$ or $y = 0.05$ to the Curie-Weiss function $C/(T - \theta)$. The fit was performed in the range $T \geq 100\,K$ ($100\,K \leq T \leq 350\,K$ for $NdTi_{0.8}Fe_{0.2}O_{3.40}$). Some curves of $\chi(T)$ or $\chi(T)^{-1}$ are shown in Fig. 49, 50 and 56. R^2 describes the goodness of the fit. p_{exp} is the experimentally determined effective magnetic moment after Eq. (15) and (16). p_{th} is the corresponding theoretical value resulting from Nd^{3+} as well as from Nd^{3+} and Ti^{3+} (or Fe^{3+}) after Eq. (17) and Table 63 and 64. [1]In this case G_1 in Eq. (17) corresponds to the amount of Ti^{3+} per Ti resulting from charge neutrality which is equal to the nominal number of 3d electrons per Ti.

Compound structure type , N	C [emu G^{-1} K (mol $A_{1-y}BO_x)^{-1}$]	θ [K]	R^2	p_{exp} [μ_B]	p_{th} [μ_B] of Ln^{3+} or Eu^{2+}	p_{th} [μ_B] of Ln^{3+} and Ti^{3+}
$\mathbf{YbTiO_{3.39}}$ pyrochlore , $3d^{0.22}$	2.778	− 102	0.9995	4.71	4.54	4.61 [1]
$\mathbf{Gd_{0.5}Pr_{0.5}TiO_{3.50}}$ $n = 4$, $3d^0$	4.622	− 3	0.9998	6.08	6.16	
$\mathbf{Sr_{0.75}Eu_{0.2}NbO_{3.41}}$ $n = 4.5$, $4d^{0.09}$	1.584	− 0.4	0.9999	3.56	3.55	
$\mathbf{Ca_{0.8}Eu_{0.2}NbO_{3.40}}$ $n = 5$, $4d^{0.20}$	1.594	− 0.5	0.9998	3.57	3.55	
$\mathbf{Ca_{0.91}Eu_{0.09}NbO_{3.41}}$ $n = 5$, $4d^{0.18}$	0.686	− 1.4	0.9999	2.34	2.38	

Table 68. Results of fitting the molar magnetic susceptibility $\chi(T)$ of $A_{1-y}BO_x$ ($y = 0$ or $y = 0.05$) with some of the heavier Ln ions at the A site to the Curie-Weiss function $C/(T - \theta)$. The fit was performed in the range $T \geq 100$ K (≥ 200 K for the pyrochlore compound). Some curves of $\chi(T)$ or $\chi(T)^{-1}$ are shown in Fig. 50, 54, 55 and 56. R^2 describes the goodness of the fit. p_{exp} is the experimentally determined effective magnetic moment after Eq. (15) and (16). p_{th} is the corresponding theoretical value resulting from Ln^{3+} or Eu^{2+} as well as from Ln^{3+} and Ti^{3+} after Eq. (17) and Table 63 and 64. [1]In this case G_1 in Eq. (17) corresponds to the amount of Ti^{3+} per Ti resulting from charge neutrality which is equal to the nominal number of 3d electrons per Ti.

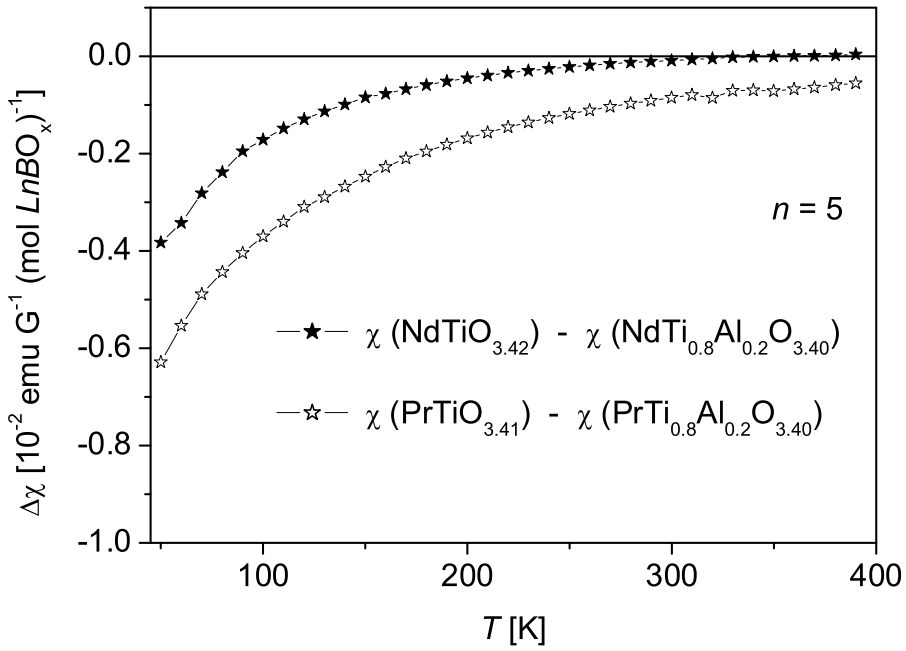

Fig. 57. Difference of the molar magnetic susceptibility, $\Delta\chi(T)$, between the $n = 5$ electrical conductor $Ln\mathrm{TiO}_{3.4}$ ($\approx 3\mathrm{d}^{0.2}$) and the corresponding $n = 5$ insulator $Ln\mathrm{Ti}_{0.8}\mathrm{Al}_{0.2}\mathrm{O}_{3.40}$ ($3\mathrm{d}^0$) for Ln = Pr and Nd. See also Fig. 48, 49 and 58.

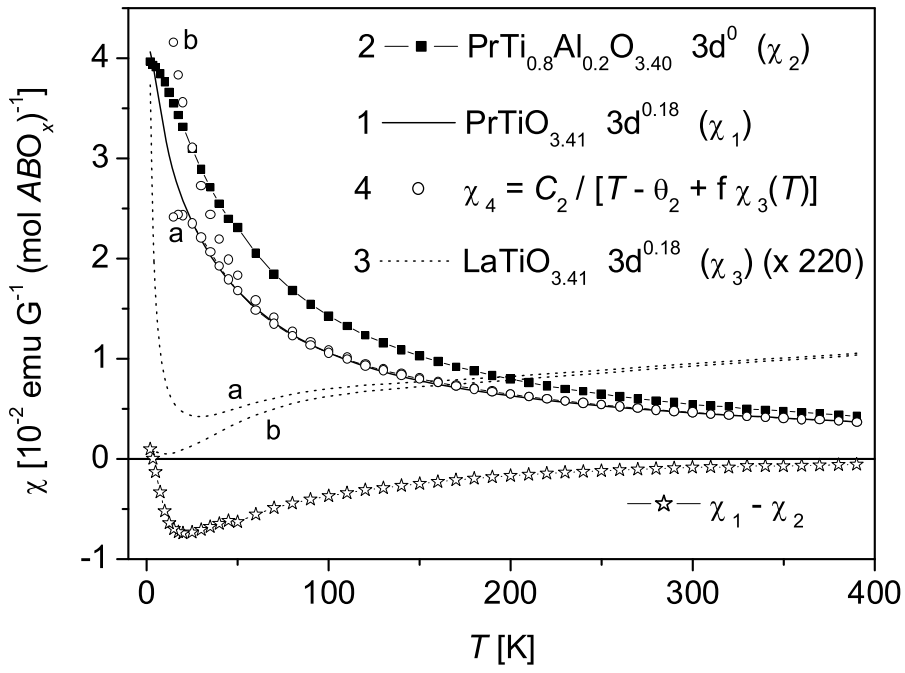

Fig. 58. Molar magnetic susceptibility $\chi(T)$ in a field of $H = 500$ G of $n = 5$ titanates: The insulator $PrTi_{0.8}Al_{0.2}O_{3.40}$ (χ_2), the quasi-1D metal $PrTiO_{3.41}$ (χ_1), their difference $\chi_1 - \chi_2$, and the 220-fold of the quasi-1D metal $LaTiO_{3.41}$ (χ_3). Also shown is the artificially constructed function $\chi_4(T)$. For $LaTiO_{3.41}$ the curve (a) displays the as-measured susceptibility and (b) that obtained by subtracting from (a) the Curie contribution from paramagnetic impurities which dominate the low T behavior, see Table 69. For $T \geq 100$K the curves $\chi_1(T)$, $\chi_2(T)$ and $\chi_4(T)$ fit well to the Curie-Weiss function $C/(T-\theta)$, see Fig. 59 and Table 69. The function $\chi_4(T)$ (a,b) represents an attempt to describe the behavior of $PrTiO_{3.41}$ by that of $LaTiO_{3.41}$ (a,b) and $PrTi_{0.8}Al_{0.2}O_{3.40}$. See also Fig. 59, Table 69 and text. The parameter f in $\chi_4(T)$ was determined to $f =$ [1.3836 (a) or 1.4089 (b)] $\times 10^6$ K emu^{-1} G mol, simply by the requirement $\chi_4(T) = \chi_1(T)$ at $T = 390$ K.

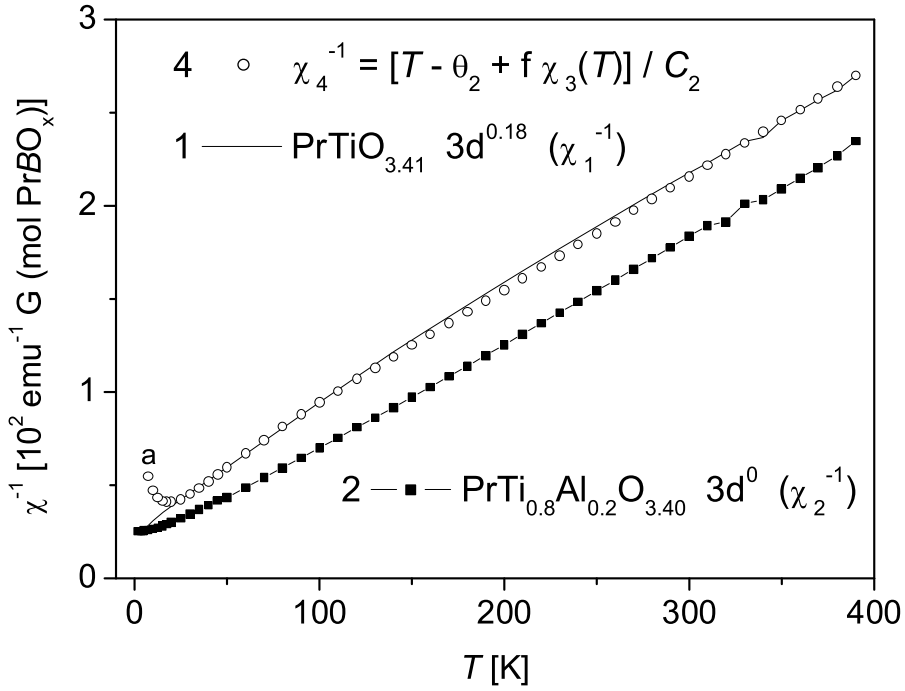

Fig. 59. Inverse molar magnetic susceptibility $\chi(T)^{-1}$ of $n = 5$ titanates: The insulator $PrTi_{0.8}Al_{0.2}O_{3.40}$ (χ_2^{-1}) and the quasi-1D metal $PrTiO_{3.41}$ (χ_1^{-1}). Also shown is the version (a) of the artificially constructed function $\chi_4(T)^{-1}$. For $T \geq 100$ K the curves fit well to the inverse Curie-Weiss function $\chi^{-1} = (T - \theta)/C$. The function $\chi_4(T)$ represents an attempt to describe the behavior of $PrTiO_{3.41}$ by that of $LaTiO_{3.41}$ and $PrTi_{0.8}Al_{0.2}O_{3.40}$. See Fig. 58, Table 69 and text.

No. i	**Compound** structure type , N	Fit range T [K]	D_i [emu G^{-1} mol^{-1}]	C_i [K emu G^{-1} mol^{-1}]	θ_i [K]	R^2	p_{exp} [μ_B]	p_{th} [μ_B] of Pr^{3+}
2	**$PrTi_{0.8}Al_{0.2}O_{3.40}$** $n = 5$, $3d^0$	≥ 100	0	1.779	-24	0.9998	3.77	
1	**$PrTiO_{3.41}$** $n = 5$, $3d^{0.18}$	≥ 100	0	1.627	-56	0.9988	3.61	3.58
4	$\chi_4(T) =$ $C_2/[T - \theta_2 + f\,\chi_3(T)]$	≥ 100	0	1.650 [a] 1.622 [b]	-56 [a] -50 [b]	0.9999 [a] 0.9999 [b]	3.63 [a] 3.60 [b]	
	$f\,\chi_3(390\text{ K}) = 66$ K [a b] $f\,\chi_3(100\text{ K}) = 44$ K [a] $f\,\chi_3(100\text{ K}) = 41$ K [b]							
3	**$LaTiO_{3.41}$** $n = 5$, $3d^{0.18}$	≤ 20	3.03 $\times 10^{-6}$	3.37 $\times 10^{-4}$	0	0.9998		

Table 69. Results of fitting the molar magnetic susceptibility $\chi(T)$ of $PrBO_x$, $LaTiO_{3.41}$ and $\chi_4(T)$ to the function $D_i + C_i/(T - \theta_i)$. See also Fig. 48, 58 and 59. R^2 describes the goodness of the fit. p_{exp} is the experimentally determined effective magnetic moment after Eq. (15) and (16). $p_{th} = q_{th}$ is the corresponding theoretical value resulting from Pr^{3+} after Table 64. The artificially constructed function $\chi_4(T)$ represents an attempt to describe the behavior of the quasi-1D metal $PrTiO_{3.41}$ by that of the quasi-1D metal $LaTiO_{3.41}$ and the insulator $PrTi_{0.8}Al_{0.2}O_{3.40}$, see Fig. 58 and 59. The different results (a) and (b) for $\chi_4(T)$ refer to different $\chi_3(T)$ curves of $LaTiO_{3.41}$, namely (a) the as-measured and (b) that obtained by subtracting from (a) the Curie contribution C_3/T from impurities which dominate the low T behavior, see Fig. 58. The parameter f in $\chi_4(T)$ was determined to f = [1.384 (a) or 1.409 (b)] $\times$ 10^6 K emu^{-1} G mol, simply by the requirement $\chi_4(T) = \chi_1(T)$ at $T = 390$ K. For data of further Pr compounds see Table 66.

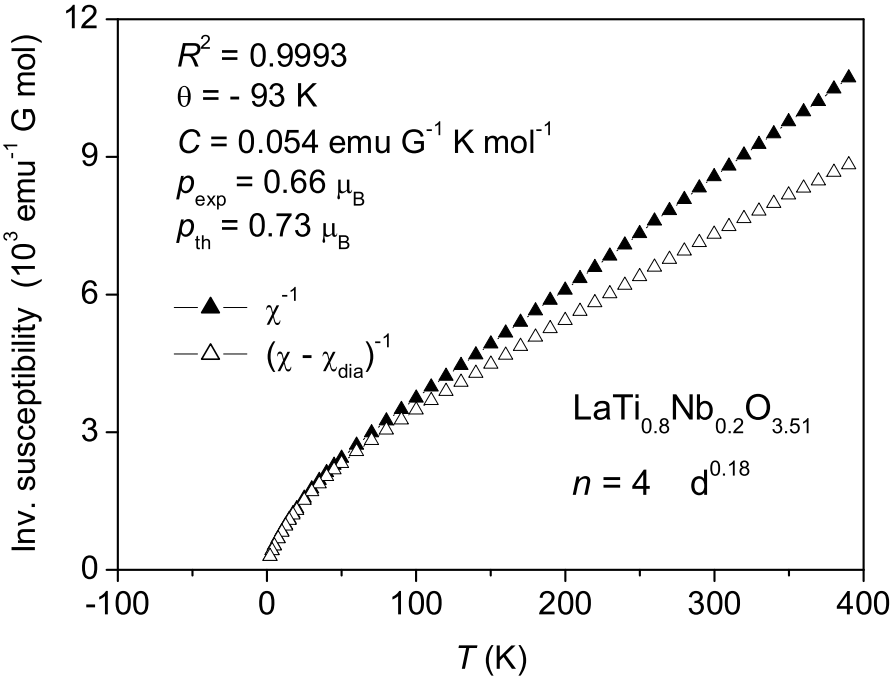

Fig. 60. Inverse molar magnetic susceptibility in a field of $H = 500$ G of the $n = 4$ type $LaTi_{0.8}Nb_{0.2}O_{3.51}$, a compound reported in Ref. [127]. $\chi(T)^{-1}$ represents the as-measured curve. The temperature-independent diamagnetism from closed electron shells was taken into account by using $\chi_{dia} = -2 \times 10^{-5}$ emu G^{-1} mol^{-1} which is the approximate experimental susceptibility of the diamagnetic insulator $LaTiO_{3.50}$ [127]. The Curie-Weiss behavior at high temperatures indicates the presence of localized paramagnetic moments from Ti^{3+} and/or Nb^{4+}. For $T \geq 150$ K the corrected curve, $\chi(T) - \chi_{dia}$, was fitted to $C/(T - \theta)$. R^2 describes the goodness of the fit. p_{exp} is the experimentally determined effective magnetic moment after Eq. (15) and (16). p_{th} is the corresponding theoretical free-ion value resulting from Ti^{3+} and/or Nb^{4+} after Eq. (17) with $N_{TM} = 1$ and Table 63. In Eq. (17) G_1 corresponds to the amount of Ti^{3+} and/or Nb^{4+} per $Ti_{0.8}Nb_{0.2}$ resulting from charge neutrality which is equal to the number of d electrons per $Ti_{0.8}Nb_{0.2}$ and thus $G_1 = 0.18$.

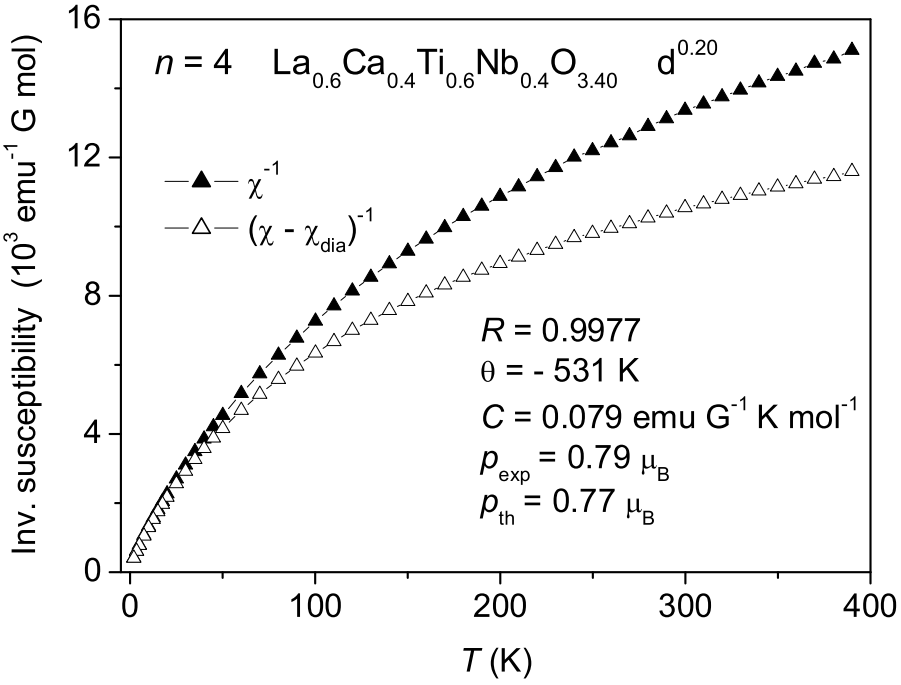

Fig. 61. Inverse molar magnetic susceptibility in a field of $H = 500$ G of the significantly oxygen-deficient $n = 4$ compound $La_{0.6}Ca_{0.4}Ti_{0.6}Nb_{0.4}O_{3.40}$, see also Figure 42. $\chi(T)^{-1}$ represents the as-measured curve. The temperature-independent diamagnetism from closed electron shells was taken into account by using $\chi_{dia} = -2 \times 10^{-5}$ emu G^{-1} mol^{-1} which is the approximate experimental susceptibility of the diamagnetic insulators $LaTiO_{3.50}$ and $CaNbO_{3.50}$ [127]. The Curie-Weiss behavior at high temperatures indicates the presence of localized paramagnetic moments from Ti^{3+} and/or Nb^{4+}. For $T \geq 250$ K the inverse corrected curve, $(\chi(T) - \chi_{dia})^{-1}$, was fitted linearly to the inverse Curie-Weiss function $(T - \theta)/C$. R describes the goodness of the fit. p_{exp} is the experimentally determined effective magnetic moment after Eq. (15) and (16). p_{th} is the corresponding theoretical free-ion value resulting from Ti^{3+} and/or Nb^{4+} after Eq. (17) with $N_{TM} = 1$ and Table 63. In Eq. (17) G_1 corresponds to the amount of Ti^{3+} and/or Nb^{4+} per $Ti_{0.6}Nb_{0.4}$ resulting from charge neutrality which is equal to the number of d electrons per $Ti_{0.6}Nb_{0.4}$ and thus $G_1 = 0.20$.

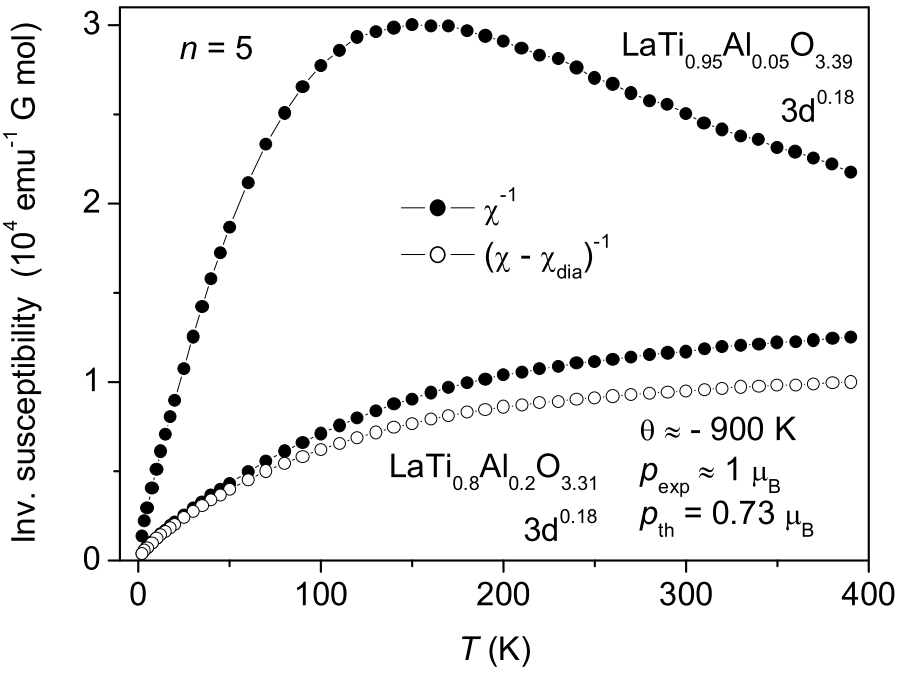

Fig. 62. Inverse molar magnetic susceptibility in a field of $H = 500$ G of the $n = 5$ titanates $LaTi_{0.95}Al_{0.05}O_{3.39}$ and $LaTi_{0.8}Al_{0.2}O_{3.31}$. $\chi(T)^{-1}$ represents the as-measured curve. For $LaTi_{0.8}Al_{0.2}O_{3.31}$ the temperature-independent diamagnetism from closed electron shells was taken into account by using $\chi_{dia} = -2\times10^{-5}$ emu G^{-1} mol^{-1} which is the approximate experimental susceptibility of the diamagnetic insulator $LaTiO_{3.50}$ [127]. At high temperatures the behavior of $LaTi_{0.8}Al_{0.2}O_{3.31}$ is approximately linear which suggests the presence of localized paramagnetic moments from Ti^{3+}. Above 200 K the corrected curve, $(\chi(T) - \chi_{dia})^{-1}$, was fitted linearly to the inverse Curie-Weiss function $(T - \theta)/C$. The resulting values are $R \approx 0.996$, $C \approx 0.13$ emu G^{-1} K mol^{-1} and $\theta \approx -900$ K whereby R describes the goodness of the fit. p_{exp} is the experimentally determined effective magnetic moment after Eq. (15) and (16). p_{th} is the corresponding theoretical free-ion value resulting from Ti^{3+} after Eq. (17) and Table 63. In Eq. (17) G_1 corresponds to the amount of Ti^{3+} resulting from charge neutrality which is equal to the number of 3d electrons per $Ti_{0.8}Al_{0.2}$ and thus $G_1 = 0.18$.

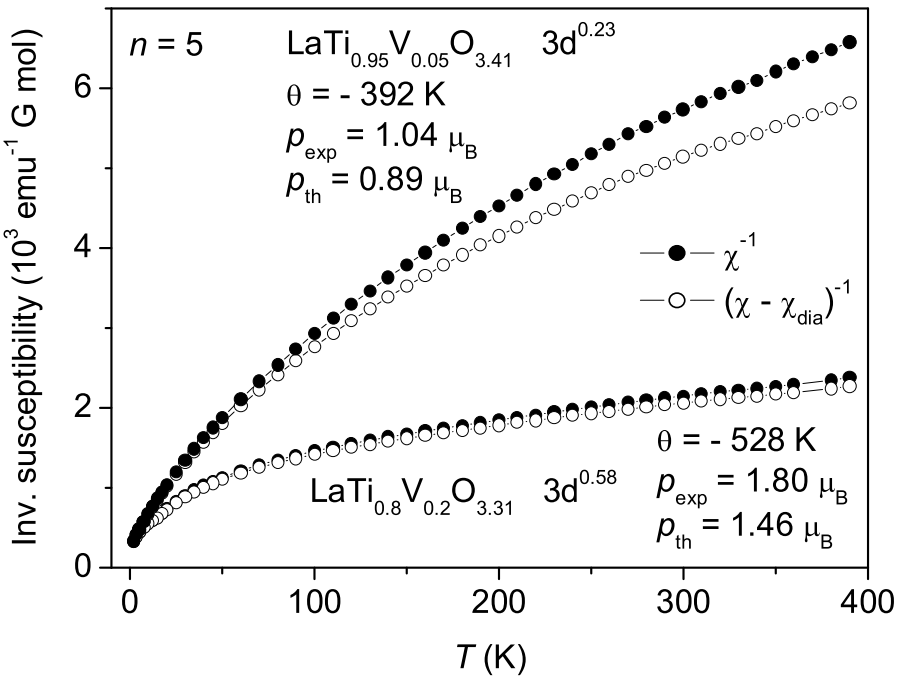

Fig. 63. Inverse molar magnetic susceptibility in a field of $H = 500$ G of the $n = 5$ compounds $LaTi_{0.95}V_{0.05}O_{3.41}$ and $LaTi_{0.8}V_{0.2}O_{3.31}$. $\chi(T)^{-1}$ represents the as-measured curve. The temperature-independent diamagnetism from closed electron shells was taken into account by using $\chi_{dia} = -2 \times 10^{-5}$ emu G^{-1} mol^{-1} which is the approximate experimental susceptibility of the diamagnetic insulator $LaTiO_{3.50}$ [127]. The Curie-Weiss behavior at high temperatures indicates the presence of localized paramagnetic moments, probably from V^{3+} and Ti^{3+}. For $T \geq 290$ K and $T \geq 210$ K, respectively, the corrected curve, $(\chi(T) - \chi_{dia})^{-1}$, was fitted linearly to the inverse Curie-Weiss function $(T - \theta)/C$. The resulting values are $R = 0.9997$ and 0.9984, $C =$ (0.13 and 0.40) emu G^{-1} K mol^{-1}, $\theta = -392$ K and -528 K, respectively, whereby R describes the goodness of the fit. p_{exp} is the experimentally determined effective magnetic moment after Eq. (15) and (16). For the estimation of the corresponding theoretical free-ion value p_{th} see Eq. (22) – (25) and text.

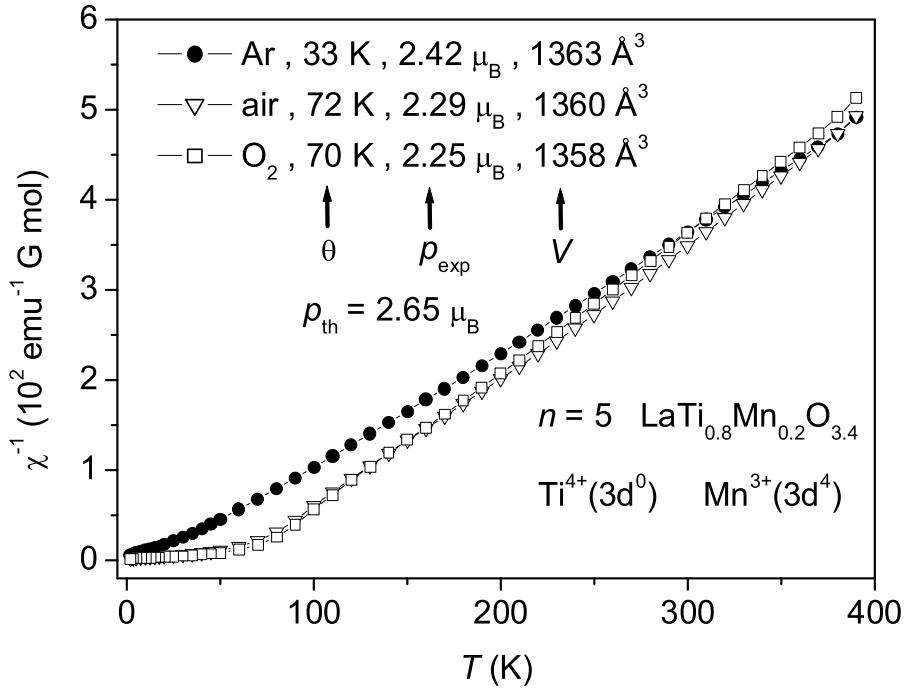

Fig. 64. Inverse molar magnetic susceptibility $\chi(T)^{-1}$ in a field of $H = 500$ G of the $n = 5$ insulator $LaTi_{0.8}Mn_{0.2}O_{3.4}$ prepared by floating zone melting in Ar, air and O_2 , respectively. The $\chi(T)^{-1}$ curves were fitted linearly to the inverse Curie-Weiss function $(T - \theta)/C$ in the range 220 K $\leq T \leq$ 380 K where all curves are strictly linear. This resulted in the θ values shown in the Figure, $C =$ (0.73, 0.65 and 0.63) emu G^{-1} K mol^{-1}, respectively, and $R = 0.9999$ for all fits. R describes the goodness of the fit. p_{exp} is the experimentally determined effective magnetic moment after Eq. (15) and (16). p_{th} is the corresponding theoretical free-ion value resulting from Mn^{3+} after Eq. (17) and Table 63. Also presented is the unit cell volume V from Table 37. Compared to the samples synthesized in Ar, the samples grown in air and O_2 display a smaller value of V and p_{exp}. This suggests the presence of a small amount of Mn^{4+}.

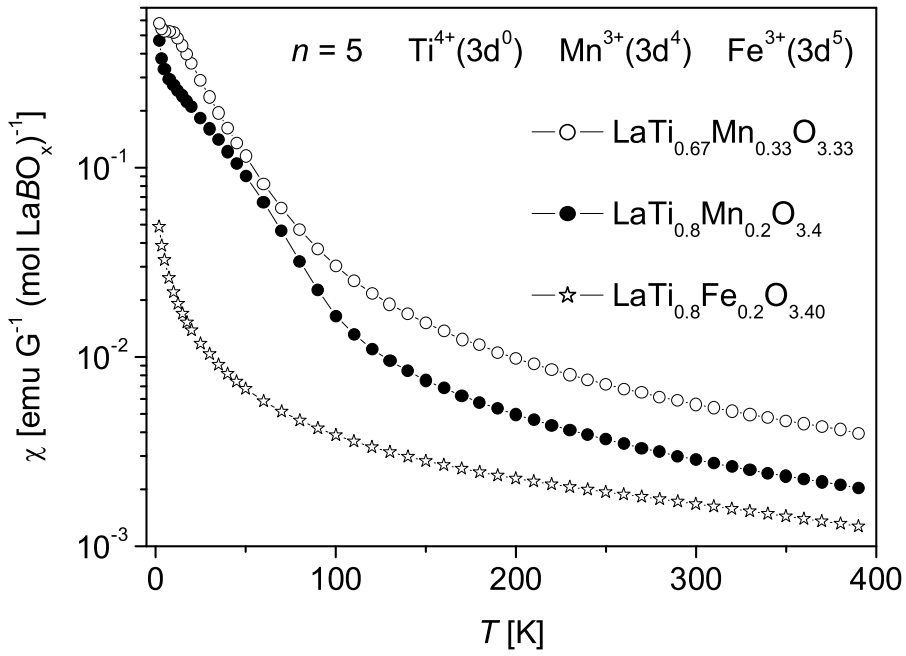

Fig. 65. Log-linear plot of the molar magnetic susceptibility $\chi(T)$ in a field of $H = 500$ G of the $n = 5$ insulators $LaTi_{0.8}Mn_{0.2}O_{3.4}$, $LaTi_{0.67}Mn_{0.33}O_{3.33}$ and, for the sake of comparison, $LaTi_{0.8}Fe_{0.2}O_{3.40}$. All samples were prepared by floating zone melting in air. Note that the composition $LaTi_{0.67}Mn_{0.33}O_{3.33}$ did not result in an $n = 6$ structure but emerged as an oxygen-deficient $n = 5$ type. The inverse molar magnetic susceptibility $\chi(T)^{-1}$ of $LaTi_{0.8}Mn_{0.2}O_{3.4}$ is shown in Fig 64 and 66. For $LaTi_{0.8}Fe_{0.2}O_{3.40}$ see also Fig. 67 – 69.

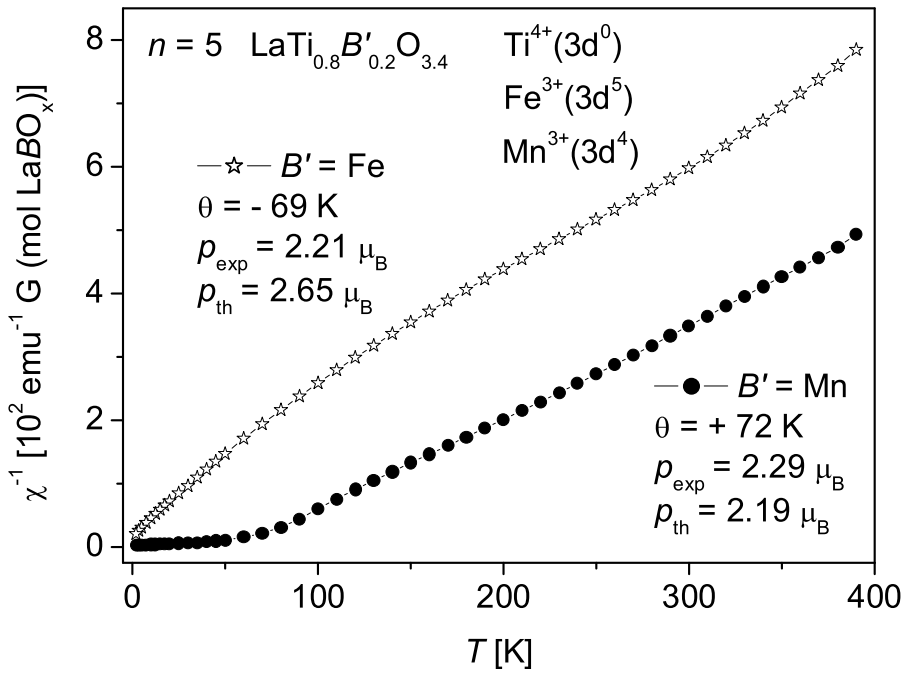

Fig. 66. Inverse molar magnetic susceptibility $\chi(T)^{-1}$ in a field of $H = 500$ G of the $n = 5$ insulators $LaTi_{0.8}Mn_{0.2}O_{3.4}$ and $LaTi_{0.8}Fe_{0.2}O_{3.4}$. Both samples were prepared by floating zone melting in air. For $LaTi_{0.8}Mn_{0.2}O_{3.4}$ the $\chi(T)^{-1}$ curve was fitted linearly to the inverse Curie-Weiss function $(T-\theta)/C$ in the range 220 K $\leq T \leq$ 380 K. This resulted in $C = 0.65$ emu G^{-1} K mol^{-1}, $\theta = +72$ K and $R = 0.9999$ whereby R describes the goodness of the fit. p_{exp} is the experimentally determined effective magnetic moment after Eq. (15) and (16). p_{th} is the corresponding theoretical free-ion value resulting from Mn^{3+} after Eq. (17) and Table 63. For $LaTi_{0.8}Fe_{0.2}O_{3.4}$ the values presented in the Figure are those obtained from a fit for temperatures below 300 K, see Figure 69.

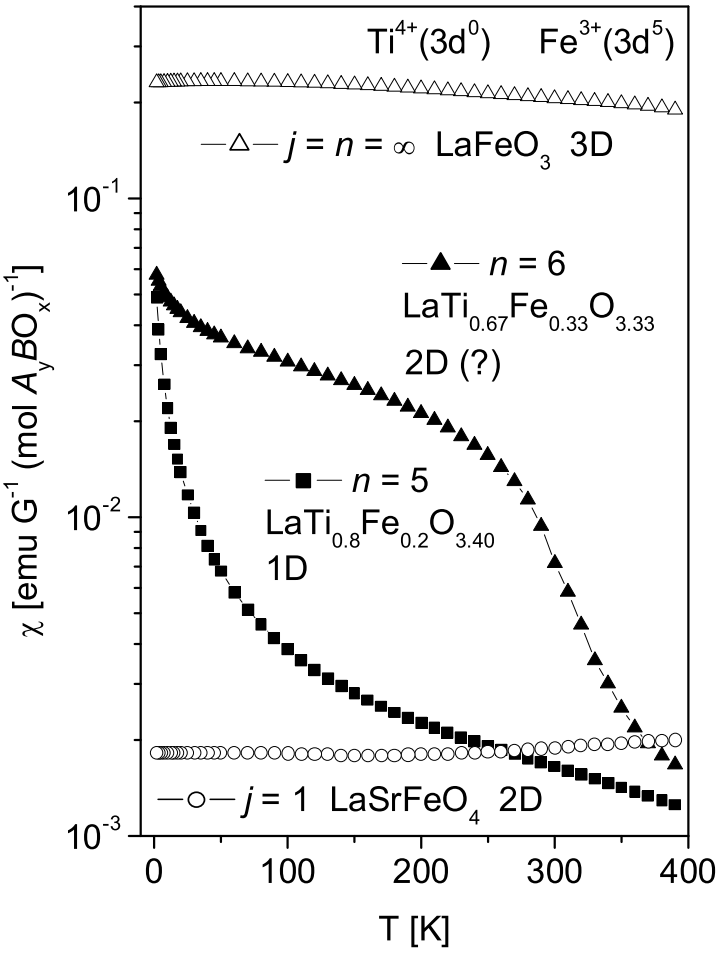

Fig. 67. Log-linear plot of the molar magnetic susceptibility $\chi(T)$ in a field of $H = 500$ G of the $j = 1$, $n = 5$, $n = 6$ and $j = n = \infty$ insulators $LaSrFeO_4$, $LaTi_{0.8}Fe_{0.2}O_{3.40}$, $LaTi_{0.67}Fe_{0.33}O_{3.33}$ and $LaFeO_3$, respectively. All samples were prepared by floating zone melting in air. The inverse molar susceptibility $\chi(T)^{-1}$ of the $n = 5$ and $n = 5$ compound is shown in Fig. 68 and 69. $LaFeO_3$ is as a canted antiferromagnet, i.e. a weak ferromagnet, with a Neel temperature of $T_N = 740$ K [176] and $LaSrFeO_4$ an antiferromagnet with $T_N = 350$ K [95]. The specification of the dimensionality such as 1D or 2D refers to the $Fe - O$ network constituted by corner-shared FeO_6 octahedra, see text and Fig. 1, 5 and 16. It is reported by Titov et al. [227,228] that the Fe^{3+} ions in the $n = 5$ compound are exclusively located in the central octahedra.

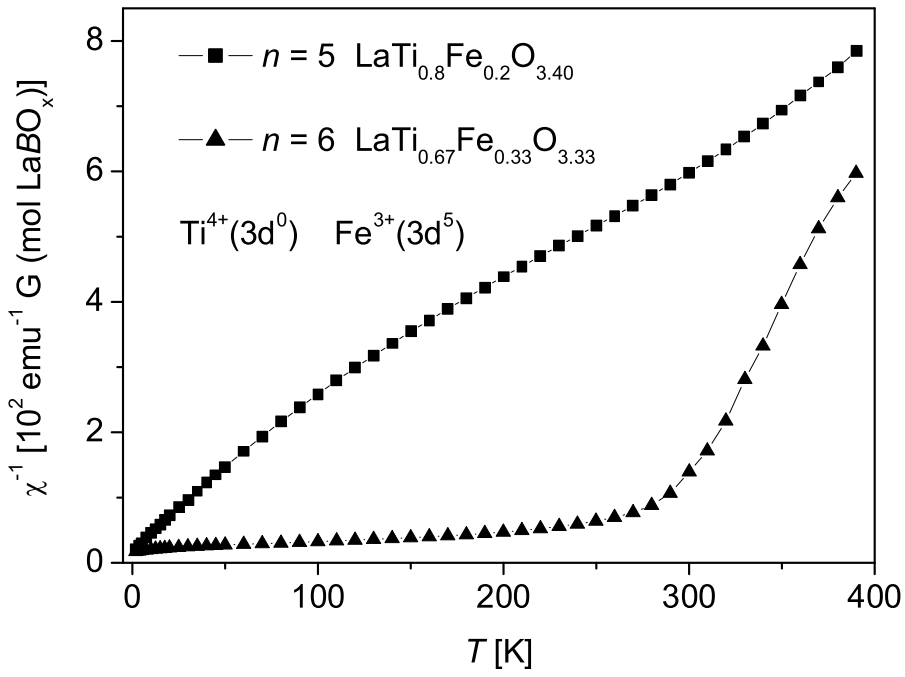

Fig. 68. Inverse molar magnetic susceptibility $\chi(T)^{-1}$ in a field $H = 500$ G of the $n = 5$ and $n = 6$ insulators $LaTi_{0.8}Fe_{0.2}O_{3.40}$ and $LaTi_{0.67}Fe_{0.33}O_{3.33}$, respectively.

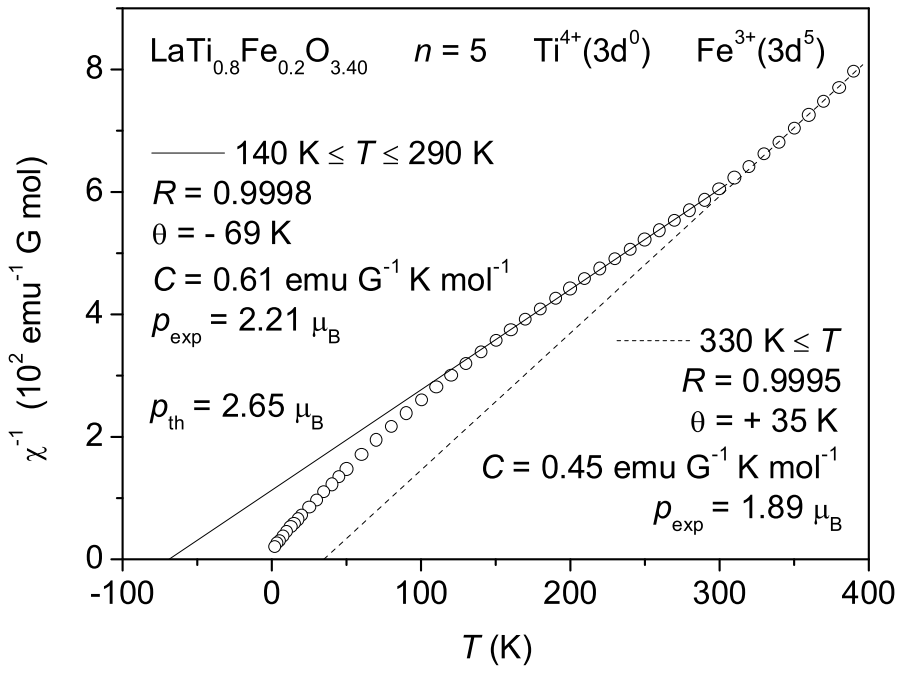

Fig. 69. Inverse molar magnetic susceptibility in a field $H = 500$ G of the $n = 5$ insulator $LaTi_{0.8}Fe_{0.2}O_{3.40}$. The open circles represents the as-measured curve $\chi(T)^{-1}$. The solid and the dotted line was obtained by a linear fit in two different temperature ranges of $\chi(T)^{-1}$ to the inverse Curie-Weiss function $(T - \theta)/C$ and its extrapolation to $\chi^{-1} = 0$. R describes the goodness of the fit. p_{exp} is the experimentally determined effective magnetic moment after Eq. (15) and (16). p_{th} is the corresponding theoretical free-ion value resulting from Fe^{3+} after Eq. (17) and Table 63. The curve $\chi(T)^{-1}$ displays a change of the slope at $T \approx 300$ K. This and the result from the linear fit in the lower and higher temperature range suggests a crossover from an antiferromagnetic ($\theta = -69$ K) to a ferromagnetic interaction ($\theta = +35$ K) between the magnetic moments of Fe^{3+}.

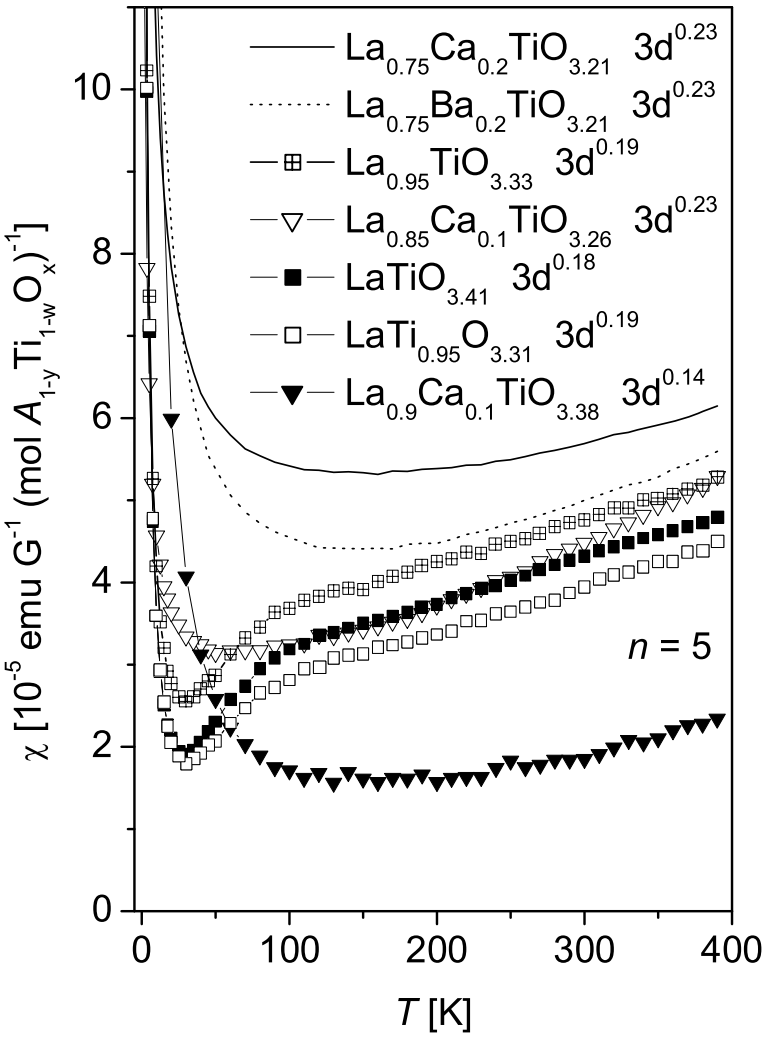

Fig. 70. Molar magnetic susceptibility $\chi(T)$ in low fields $H \leq 1000$ G of monoclinic $n = 5$ titanates: five significantly non-stoichiometric compounds $A_{1-y}Ti_{1-w}O_x$ with $0 \leq y \leq 0.05$, $w = 0$ or 0.05 and $3.21 \leq x \leq 3.33$ as well as two nearly stoichiometric materials $LaTiO_{3.41}$ and $La_{0.9}Ca_{0.1}TiO_{3.38}$. The two latter were investigated by resistivity and/or optical measurements and are reported as quasi-1D metals, see Table 35. The ideal $n = 5$ composition is $ATiO_{3.40}$.

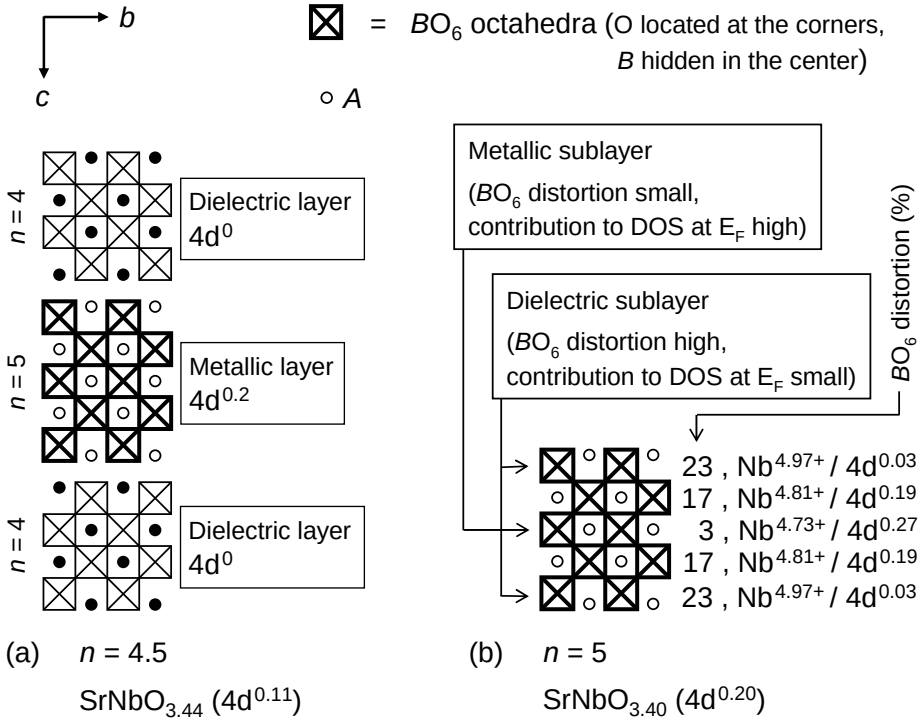

Fig. 71. Illustration how quasi-1D metals of the type $n = 4.5$ and $n = 5$ of $A_nB_nO_{3n+2} = ABO_x$ can be viewed from the perspective of the hypothetical excitonic type of superconductivity. This view refers to the original proposal by Ginzburg to realize excitonic superconductivity in quasi-2D systems, namely a metallic layer which is surrounded by two dielectric sheets [58]. Sketched in the same way as in Fig. 4 − 6 is the idealized structure of the layers. The $n = 4.5$ member represents the ordered stacking sequence $n = 4, 5, 4, 5, ...$ Ideal compositional examples are taken from $SrNbO_x$. (a) Viewing the $n = 4.5$ type as a heterostructure of dielectric and metallic layers. The specified allocation of the nominal 0.11 4d electrons per Nb in $4d^0$ for the $n = 4$ layers and in an average of $4d^{0.2}$ for the $n = 5$ layers corresponds to the extreme case where all 4d electrons are located in the metallic $n = 5$ layers. This picture or its approximate realization is supported by the experimental finding that the metallic character in conducting (Sr,La)NbO_x is relatively weak for $n = 4$ whereas it is relatively high for $n = 4.5$ and $n = 5$ [113]. (b) Even a single $n = 5$ layer or an $n = 5$ material can approximately be considered as a metallic sublayer surrounded by two dielectric sublayers. This picture is supported by results from band structure calculations on $SrNbO_{3.41}$: The major contribution to the electronic density of states (DOS) at the Fermi energy E_F comes from those Nb atoms which are located in the central octahedra of the layers [110,244]. The displayed representative values of octahedra distortion are from $SrNbO_{3.41}$ (Fig. 15). The view resulting from the band structure calculations is qualitatively in accordance with the distribution of the Nb valence / 4d electron count. Their specified values are from $CaNbO_{3.41}$ (Fig. 15) and should be considered as an approximate scenario.

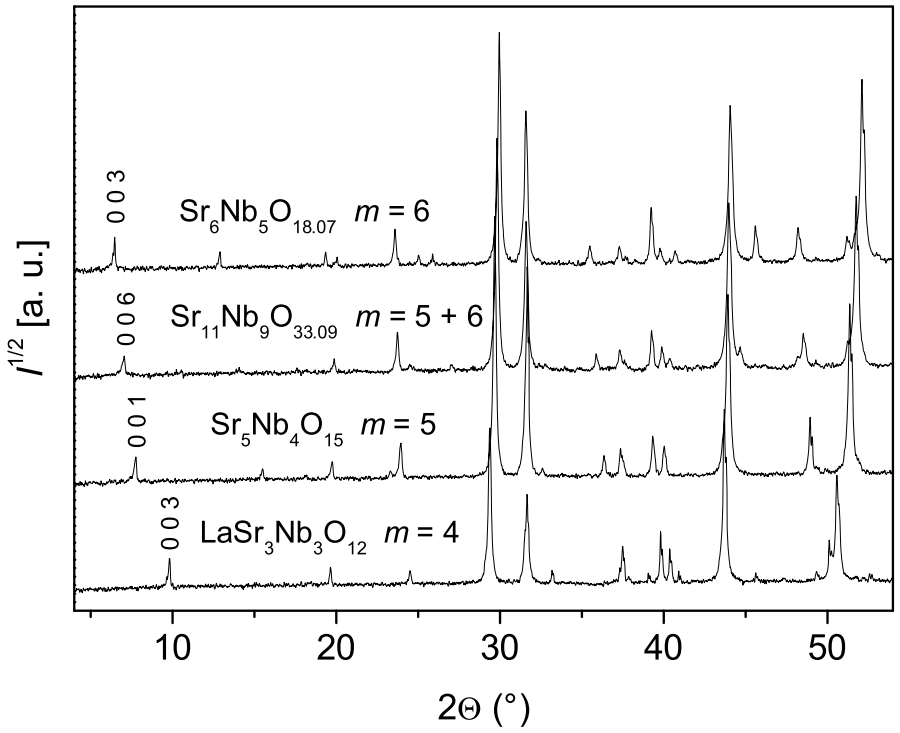

Fig. 72. Powder XRD pattern of hexagonal $LaSr_3Nb_3O_{12}$ ($m = 4$), $Sr_5Nb_4O_{15}$ ($m = 5$), $Sr_{11}Nb_9O_{33.09}$ ($m = 5 + 6$) and $Sr_6Nb_5O_{18.07}$ ($m = 6$). All observed peaks fit to a hexagonal $A_mB_{m-1}O_{3m}$ structure, in the case of $m = 5 + 6$ to a hexagonal $A_5B_4O_{15} + A_6B_5O_{18} = A_{11}B_9O_{33}$ type. For clarity only the low-angle peak, which indicates the structure type m, is indexed.

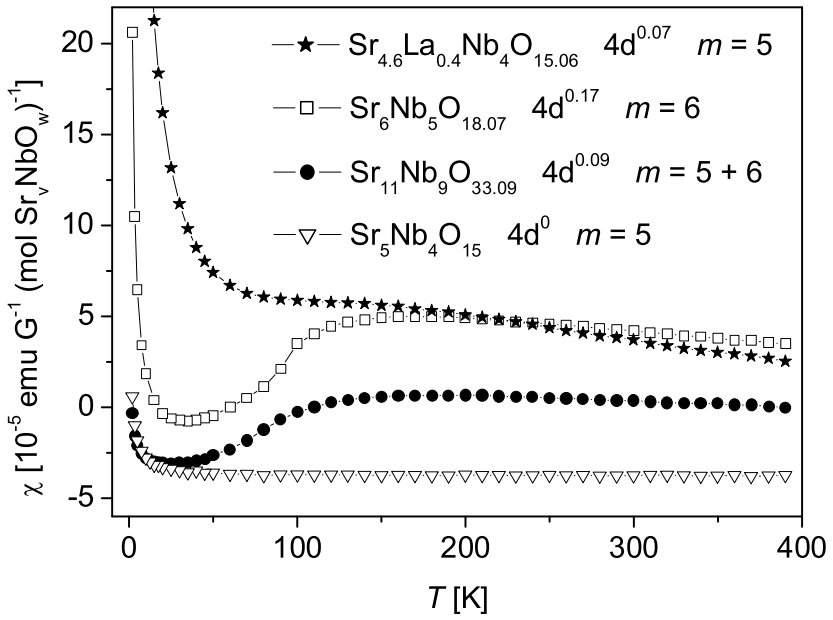

Fig. 73. Molar magnetic susceptibility $\chi(T)$ in low fields $H \leq 1000$ G of several $A_mB_{m-1}O_{3m}$ niobates. The increase at low temperatures is most probably due to paramagnetic impurities. $\chi(T)$ fits well to $D + C/T$ in the full temperature range for the diamagnetic insulator $Sr_5Nb_4O_{15}$ ($m = 5$) and in the range $T \leq 25$ K for the electrical conductors $Sr_{11}Nb_9O_{33.09}$ ($m = 5 + 6$) and $Sr_6Nb_5O_{18.07}$ ($m = 6$), see Table 70. To facilitate a comparison, the molar susceptibility is normalized to 1 mol Nb, i.e. to the formula Sr_vNbO_w.

Compound structure type , N	Fit range T [K]	D [10^{-5} emu G^{-1} (mol Sr$_v$NbO$_w$)$^{-1}$]	C [10^{-5} emu G^{-1} K (mol Sr$_v$NbO$_w$)$^{-1}$]	R^2
Sr$_5$Nb$_5$O$_{17.04}$ $n = 5$, 4d$^{0.18}$	≤ 30	-1.92	2.09	0.9992
Sr$_9$Nb$_9$O$_{31.05}$ $n = 4.5$, 4d$^{0.10}$	≤ 20	-2.29	6.18	0.9989
Sr$_6$Nb$_5$O$_{18.07}$ $m = 6$, 4d$^{0.17}$	≤ 25	-2.69	46.5	0.9997
Sr$_{11}$Nb$_9$O$_{33.09}$ $m = 5 + 6$, 4d$^{0.09}$	≤ 20	-3.39	6.21	0.9990
Sr$_5$Nb$_4$O$_{15}$ $m = 5$, 4d^0	≤ 390	-3.78	9.17	0.9950

Table 70. Results of fitting the molar magnetic susceptibility $\chi(T)$ of some niobates, see Fig. 73, 74, 76 and 78, to the function $D + C/T$. The as-measured $\chi(T)$ of the $n = 4.5$ and $n = 5$ niobates is shown in Fig. 26 in Ref. [127]. D represents a temperature-independent diamagnetic contribution and C/T the Curie term from paramagnetic impurities. R^2 describes the goodness of the fit. To facilitate a comparison, the molar susceptibility is normalized to 1 mol Nb, i.e. to the formula Sr$_v$NbO$_w$.

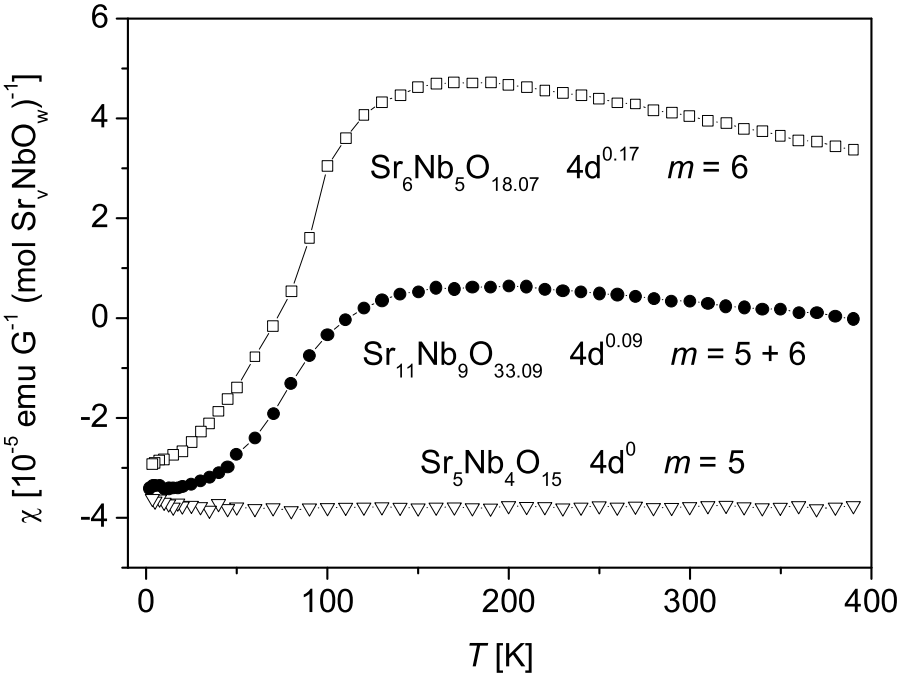

Fig. 74. Molar magnetic susceptibility $\chi(T)$ in low fields $H \leq 1000$ G of $Sr_5Nb_4O_{15}$ ($m = 5$), $Sr_{11}Nb_9O_{33.09}$ and ($m = 5 + 6$) and $Sr_6Nb_5O_{18.07}$ ($m = 6$) without the Curie contribution C/T from paramagnetic impurities which dominate the low temperature behavior, see Fig. 73 and Table 70. To facilitate a comparison, the molar susceptibility is normalized to 1 mol Nb, i.e. to the formula Sr_vNbO_w.

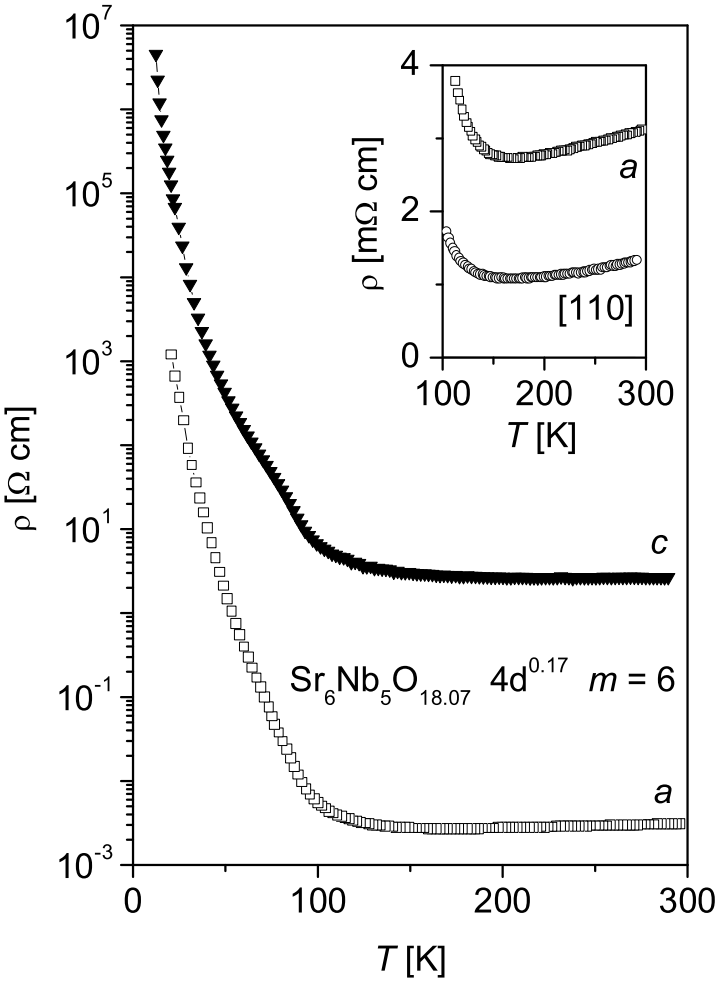

Fig. 75. Log-linear plot of the resistivity $\rho(T)$ of hexagonal $Sr_6Nb_5O_{18.07}$ ($m = 6$) along the a- and c-axis. The linear-linear type inset displays the presence of metallic behavior along the a-axis more clearly. Also shown in the inset is a part of $\rho(T)$ along the [110] direction obtained from another crystal of the same batch.

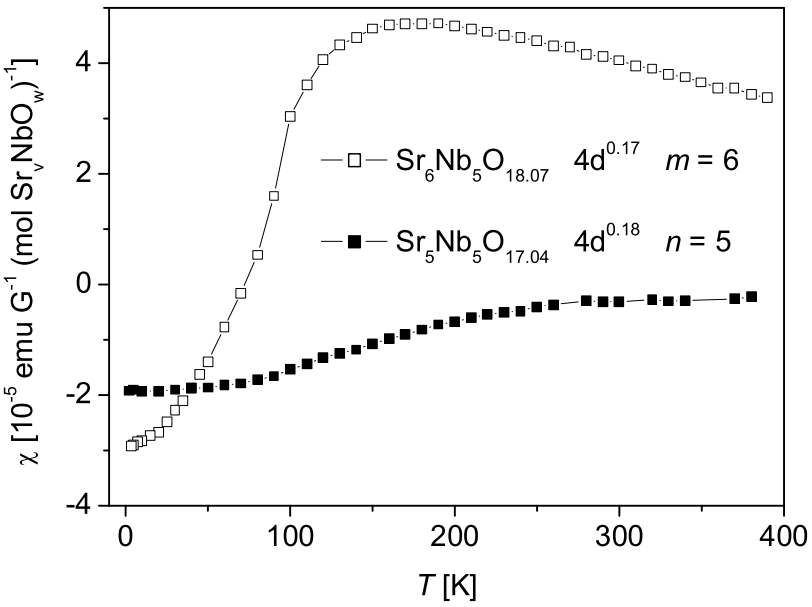

Fig. 76. Molar magnetic susceptibility $\chi(T)$ in low fields $H \leq 1000$ G of the quasi-2D metal $Sr_6Nb_5O_{18.07}$ ($m = 6$ of $A_mB_{m-1}O_{3m}$) and the quasi-1D metal $Sr_5Nb_5O_{17.04} = SrNbO_{3.41}$ ($n = 5$ of $A_nB_nO_{3n+2}$) without the Curie contribution C/T from paramagnetic impurities which dominate the low temperature behavior. The as-measured $\chi(T)$ of the $m = 6$ niobate is shown in Fig. 73 in this work and that of the $n = 5$ niobate in Fig. 26 in Ref. [127], see also Table 70 in this work. To facilitate a comparison, the molar susceptibility is normalized to 1 mol Nb, i.e. to the formula Sr_vNbO_w.

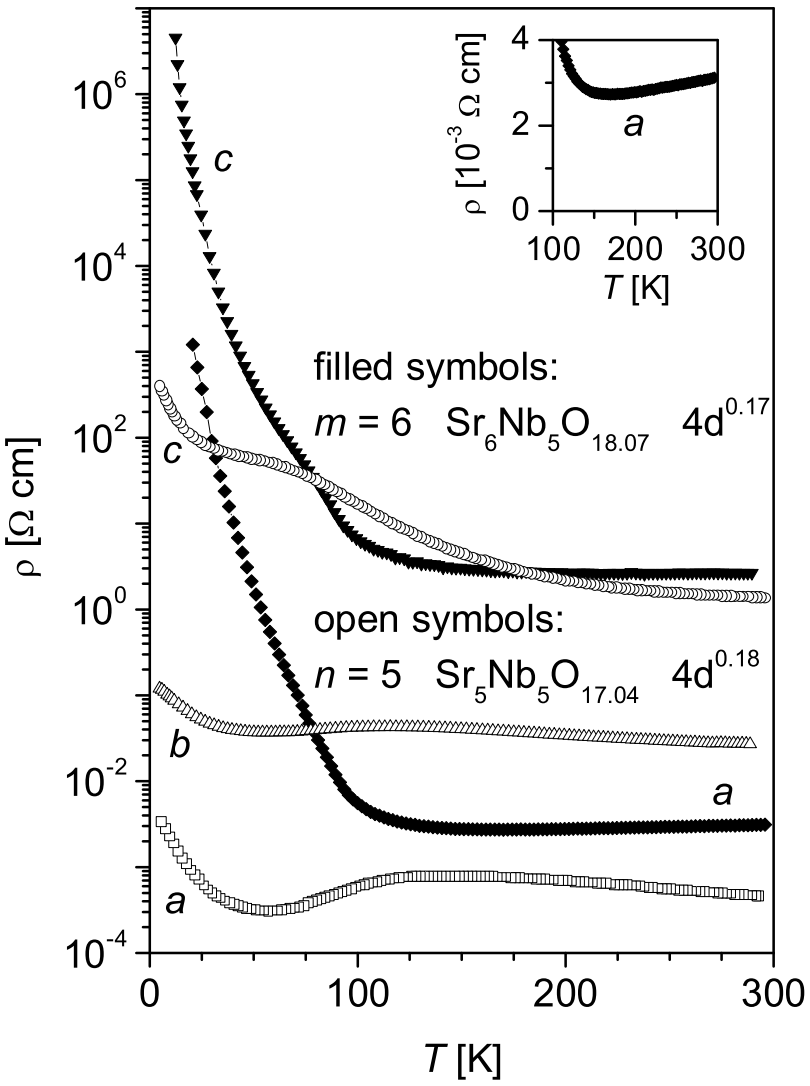

Fig. 77. Log-linear plot of the resistivity $\rho(T)$ of hexagonal $Sr_6Nb_5O_{18.07}$ ($m = 6$ of $A_mB_{m-1}O_{3m}$) along the a- and c-axis and orthorhombic $SrNbO_{3.41} = Sr_5Nb_5O_{17.04}$ ($n = 5$ of $A_nB_nO_{3n+2}$) along the a-, b- and c-axis. The linear-linear type inset displays the presence of metallic behavior along the a-axis of the $m = 6$ niobate more clearly. The data of the $n = 5$ niobate $SrNbO_{3.41} = Sr_5Nb_5O_{17.04}$ are from Ref. [127].

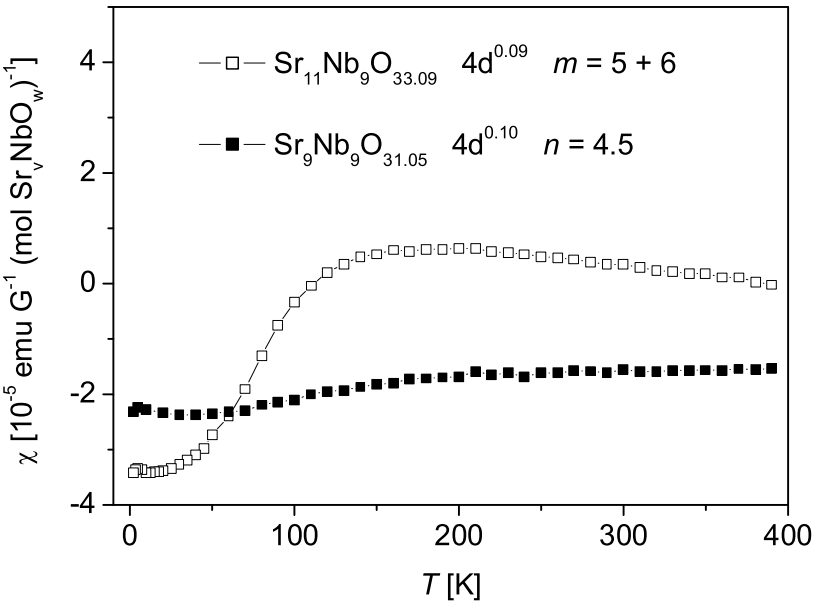

Fig. 78. Molar magnetic susceptibility $\chi(T)$ in low fields $H \leq 1000$ G of $Sr_{11}Nb_9O_{33.09}$ ($m = 5 + 6$ of $A_mB_{m-1}O_{3m}$) and the quasi-1D metal $Sr_9Nb_9O_{31.05} = SrNbO_{3.45}$ ($n = 4.5$ of $A_nB_nO_{3n+2}$) without the Curie contribution C/T from paramagnetic impurities which dominate the low temperature behavior. The as-measured $\chi(T)$ of the $m = 5 + 6$ niobate is shown in Fig. 73 in this work and that of the $n = 4.5$ niobate in Fig. 26 in Ref. [127], see also Table 70 in this work. To facilitate a comparison, the molar susceptibility is normalized to 1 mol Nb, i.e. to the formula Sr_vNbO_w.

References

1. Abakumov A M, Shpanchenko R V, Antipov E V, Lebedev O I, van Tendeloo G, Amelinckx S. J Solid State Chem 1998;141:492.
2. Abrahams S C, Schmalle H W, Williams T, Reller A, Lichtenberg F, Widmer D, Bednorz J G, Spreiter R, Bossard C, Günter P. Acta Cryst B 1998;54:399.
3. Akishige Y, Kobayashi M, Ohi K, Sawaguchi E. J Phys Soc Jpn 1986;55:2270.
4. Akishige Y, Kamata M, Fukano K. J Korean Phys Soc 2003;42:S1187.
5. Allender D, Bray J, Bardeen J. Phys Rev B 1973;7:1020.
6. Antonov V A, Arsen'ev P A, Bagdasarov Kh S, Evdokimov A A, Kopylova E K, Tadzhi-Aglaev Kh G. Inorg Mater 1986;22:401.
7. Antonov V A, Arsen'ev P A, Kopylova E K. Soviet Physics / Crystallography 1990;35:368.
8. Arkhipova E V, Zuev M G, Zolotukhina L V. J Alloys Comp 2000;305:58.
9. Batista C D. Phys Rev Lett 2002;89:166403.
10. Batista C D, Gubernatis J E, Bonca J, Lin H Q. Phys Rev Lett 2004;92:187601.

11. Becker O S. Dissertation, University of Augsburg 2000 (in German). ISBN 3-89825-269-8. Can be purchased online via the website http://www.dissertation.de
12. Bednorz J G, Müller K A. Z Phys B 1986;64:189.
13. Bednorz J G, Takashige M, Müller K A. Europhys Lett 1987;3:379.
14. Bednorz J G, Müller K A. Angew Chem 1988;100:757.
15. Bernier J C, Lejus A M, Collongues R. Solid State Comm 1975;16:349.
16. Birman J L, Weger M. Phys Rev B 2001;64:174503.
17. Bobnar V, Lunkenheimer P, Hemberger J, Loidl A, Lichtenberg F, Mannhart J. Phys Rev B 2002;65:155115.
18. Bondarenko T N, Uvarov V N, Borisenko S V, Teterin Yu A, Dzeganovski V P, Sych A M, Titov Yu A. J Korean Phys Soc 1998;32:S65.
19. Bontchev R, Darriet B, Darriet J, Weill F. Eur J Solid State Inorg Chem 1993;30:521.
20. Boullay P, Teneze N, Trolliard G, Mercurio D, Perez-Mato J M. J Solid State Chem 2003;174:209.
21. Boullay P, Mercurio D, Bencan A, Meden A, Drazic G, Kosec M. J Solid State Chem 2003;170:294.
22. Bowden M E, Jefferson D A, Brown I W M. J Solid State Chem 1995;117:88.
23. Buckel W, Kleiner R. Supraleitung, 6. vollständig überarbeitete und erweiterte Auflage, 2004, p. 75 - 104 (in German), ISBN 3-527-40348-5.
24. Buixaderas E, Kamba S, Petzelt J. J Phys: Condens Mattter 2001;13:2823.
25. Calvo C, Ng H N, Chamberland B L. Inorg Chem 1978;17:699.
26. Canales-Vazquez J, Irvine J T S, Zhou W. J Solid State Chem 2004;177:2039.
27. Canales-Vazquez J, Smith M J, Irvine J T S, Zhou W. Adv Funct Mater 2005;15:1000.
28. J R Carruthers, Grasso M. In: Phase Diagrams for Ceramists, Vol. III, 1975, published by the American Ceramic Soceity, Fig. 4362.
29. Cava R J, Roth R S. In: Modulated Structures (AIP Conference Proceedings No. 53), New York, John M Cowley, ISSN 0094-243X; 1979. p. 361.
30. Cava R J, Roth R S. J Solid State Chem 1981;36:139.
31. Chamberland B L, Hubbard F C. J Solid State Chem 1978;26:79.
32. Connoly E, Sloan J, Tilley R J D. Eur J Solid State Inorg Chem 1996;33:371.
33. Daniels P, Tamazyan R, Kuntscher C A, Dressel M, Lichtenberg F, van Smaalen S. Acta Cryst B 2002;58:970.
34. Daniels P, Lichtenberg F, van Smaalen S. Acta Cryst C 2003;59:i15.
35. de Jongh L J. Physica C 1988;152:171.
36. Dion M, Ganne M, Tournoux M. Mat Res Bull 1981;16:1429. (in French, abstract in English)
37. Dion M, Ganne M, Tournoux M, Ravez J. Revue De Chimie Minrale 1984;21:92. (in French, abstract also in English)
38. Dion M, Ganne M, Tournoux M. Revue De Chimie Minrale 1986;23:61. (in French, abstract also in English)
39. Drews A R, Wong-Ng W, Roth R S, Vanderah T A. Mat Res Bull 1996;31:153.
40. Drews A R, Wong-Ng W, Vanderah T A, Roth R S. J Alloys Comp 1997;255:243.
41. van Duivenboden H C, Zandbergen H W, Ijdo D J W. Acta Cryst C 1986;42:266.
42. D'yachenko O, Antipov E. International Centre for Diffraction Data (ICDD). Database / PDF No. 48-0419. ICDD Grant-in-Aid 1997.
43. Ebbinghaus S G, Lichtenberg F. Unpublished.
44. Ebbinghaus S G. Acta Cryst C 2005;61:i96.
45. Elcoro L, Perez-Mato J M, Withers R. Z Kristallogr. 200;215:727.

46. Elcoro L, Perez-Mato J M, Withers R L. Acta Cryst B 2001;57:471.
47. Elcoro L, Zuniga F J, Perez-Mato J M. Acta Cryst B 2004;60:21.
48. Eyert V, Ebbinghaus S G, Kopp T. Phys Rev Lett 2006;96:256401.
49. Fang L, Zhang H, Wu B. International Centre for Diffraction Data (ICDD). Database / PDF No. 51-1876. ICDD Grant-in-Aid 2000.
50. Fedorov N F, Mel'nikova O V, Saltykova, Chistyakova M V. Russ J Inorg Chem 1979;24:649.
51. Frank S, Kuntscher C A, Loa I, Syassen K, Lichtenberg F. Phys Rev B 2006;74:054105. ; Kuntscher C A, Frank S, Loa I, Syassen K, Lichtenberg F, Yamauchi T, Ueda Y. Infrared Phys Tech 2006;49:88.
52. Fukuoka H, Isami T, Yamanaka S. Chem Lett 1997;26:703.
53. Fukuoka H, Isami T, Yamanaka S. J Solid State Chem 2000;151:40.
54. German M, Kovba L M. Russ J Inorg Chem 1983;28:1349.
55. German M, Kovba L M, Shturm K. Russ J Inorg Chem 1984;29:1257.
56. German M. International Centre for Diffraction Data (ICDD). Database / PDF No. 49-0335. 1984. Further reference: German M, Kovba L. Russ J Inorg Chem 1985;30:317.
57. German M. International Centre for Diffraction Data (ICDD). Database / PDF No. 49-0334. 1984. Further reference: German M, Kovba L. Russ J Inorg Chem 1985;30:317.
58. Ginzburg V L. Soviet Physics Uspekhi 1970;13:335.
59. Gopalakrishnan J, Bhat V, Raveau B. Mat Res Bull 1987;22:413.
60. Grebille D, Berar J F, Queyroux F, Nanot M, Gilles J C, Bronsema K D, van Smaalen S. Mat Res Bull 1987;22:253.
61. Greenblatt M. In: Schlenker C, Dumas J, Greenblatt M, van Smaalen S, editors. Physics and chemistry of low-dimensional inorganic conductors, Plenum Press, New York, 1996, ISBN 0-306-45304-5. Chapter 2.
62. Guevarra J, van Smaalen S, Daniels P, Rotiroti N, Lichtenberg F. Z Kristallogr 220;19:2005.
63. Guevarra J, van Smaalen S, Rotiroti N, Paulmann C, Lichtenberg F. J Solid State Chem 2005;178:2934.
64. Guevarra J. Dissertation, University of Bayreuth (Germany); 2006.
65. Guevarra J, Schönleber A, van Smaalen S, Lichtenberg F. Acta Crys. B 2007;63:183.
66. Guha J. J Am Ceram Soc 1991;74:878.
67. Gweon G H, Allen J W, Clack J A, Zhang Y X, Poirier D M, Benning P J, Olson C G, Marcus J, Schlenker C. Phys Rev B 1997;55:R13353.
68. Hamada D, Machida M, Sugahara Y, Kuroda K. J Mater Chem 1996;6:69.
69. Hamada D, Sugimoto W, Sugahara Y, Kuroda K. J Ceram Soc Japan Int Ed 1997;105:305.
70. Harre N, Mercurio D, Trolliard G, Frit B. Mat Res Bull 1998;33:1537.
71. Harre N, Mercurio D, Trolliard G, Frit B. Eur J Solid State Inorg Chem 1998;35:77.
72. Hase I, Nishihara Y. Phys Rev B 1998;58:R1707.
73. Hervieu M, Suder F, Raveau B. J Solid State Chem 1977;22:273.
74. Hirose T, Furukawa K. Phys Stat Sol 2006;203:608.
75. Hong Y S, Kim S J. Bull Korean Chem Soc 1996;17:730.
76. Hong Y S, Kim S J, Kim S J, Choy J H. J Mater Chem 2000;10;1209.
77. Hwang D W, Lee J S, Li W, Oh S H. J Phys Chem B 2003;107:4963.
78. Ishizawa N, Marumo F, Kawamura T, Kimura M. Acta Cryst B 1975;31:1912.
79. Ishizawa N, Marumo F, Kawamura T, Kimura M. Acta Cryst B 1976;32:2564.

80. Ishizawa N, Marumo F, Iwai S, Kimura M, Kawamura T. Acta Cryst B 1980;36:763.
81. Ishizawa N, Marumo F, Iwai S. Acta Cryst B 1981;37:26.
82. Ishzawa N, Marumo F, Iwai S, Kimura M, Kawamura T. Acta Cryst B 1982;38:368.
83. Isupov V A, Smirnova E P, Isupova E N, Zaitseva N V, Pikush L G, Smolenskii G A. Sov Phys Solid State 1976;18:835.
84. Isupov V A, Smirnova E P, Isupova E N, Zaitseva N V, Shemenev L A, Pavlova N G, Chikanova M K, Smolenskii G A. Sov Phys Solid State 1977:19:544.
85. Isupov V A. Ferroelectrics 1999;220:79.
86. Jacobsen H, Lissner F, Manek E, Meyer G Z Kristallogr 1996;211:547.
87. Jacobson A J, Johnson J W, Lewandowski J T. Inorg Chem 1985;24:3727.
88. Jacobson A J, Lewandowski J T, Johnson J W. J Less-Common Metals 1986;116:137.
89. Jensen J, Mackintosh A R. Rare Earth magnetism: Structures and Excitations, Oxford Science Publications, 1991, ISBN 0-19-852027-1. Chapter 1.2.
90. Jing X, West A. International Centre for Diffraction Data (ICDD). Database / PDF No. 43-0253. ICDD Grant-in-Aid 1992.
91. Jing X, West A. International Centre for Diffraction Data (ICDD). Database / PDF No. 43-0254. ICDD Grant-in-Aid 1992.
92. Jing X, West A. International Centre for Diffraction Data (ICDD). Database / PDF No. 43-0255. ICDD Grant-in-Aid 1992.
93. Jing X, West A. International Centre for Diffraction Data (ICDD). Database / PDF No. 43-0252. ICDD Grant-in-Aid 1992.
94. Jing X, West A. International Centre for Diffraction Data (ICDD). Database / PDF No. 43-0460. ICDD Grant-in-Aid 1992.
95. Jung M H, Alsmadi A M, Chang S, Fitzsimmons M R, Zhao Y, Lacerda A H, Kawanaka H, El-Khatib S, Nakotte H. J Appl Phys 2005;97:10A926.
96. Kagoshima S, Nagasawa H, Sambongi T. One-Dimensional Conductors, Springer Series in Solid State Sciences 72, 1988, ISBN 3-540-18154-7, Chapter 3.2 and 3.3.
97. Kemmler-Sack S. Z anorg allg Chem 1980;461:151.
98. Kemmler-Sack S, Treiber U. Z anorg allg Chem 1980;462:166.
99. Kern S. J Chem Phys 1964;40:208.
100. Khalifah P, Osborn R, Huang Q, Zandbergen H W, Jin R, Liu Y, Mandrus D, Cava R J. Science 2002;297:2237.
101. Kim J, Hwang D W, Kim H G, Bae S W, Lee J S, Li W, Oh S H. Topics in Catalysis 2005;35:295.
102. Kimura M, Nanamatsu S, Kawamura T, Matsushita S. Jpn J Appl Phys 1974;13:1473.
103. Kinase W, Nishimata, T, Kuwata S. Ferroelectrics 1989;96:37.
104. Kittel C. Introduction to Solid State Physics, Seventh Edition, 1996, John Wiley, New York, ISBN 0-471-11181-3. Chapter 14.
105. Kittel C. Introduction to Solid State Physics, Seventh Edition, 1996, John Wiley, New York, ISBN 0-471-11181-3. Chapter 13.
106. Kolar D, Gaberscek S, Volavsek B, Parker H S, Roth R S. J Solid State Chem 1981;38:158.
107. Koz'min P A, Zakharov N A, Surazhskaya M D. Inorg Mat 1997;33:850.
108. Krivolapov Y, Mann A, Birman J L. Phys Rev B 2007;75:092503.
109. Kuang X, Liao F, Tian S, Jing X. Mat Res Bull 2002;37:1755.
110. Kuntscher C A, Gerhold S, Nücker N, Cummins T R, Lu D H, Schuppler S, Gopinath C S, Lichtenberg F, Mannhart J, Bohnen K P. Phys Rev B 2000;61:1876.
111. Kuntscher C A, Schuppler S, Haas P, Gorshunov B, Dressel M, Grioni M, Lichtenberg F, Herrnberger A, Mayr F, Mannhart J. Phys Rev Lett 2002;89:236403.

112. Kuntscher C A, van der Marel D, Dressel M, Lichtenberg F, Mannhart J. Phys Rev B 2003;67:035105.
113. Kuntscher C A, Schuppler S, Haas P, Gorshunov B, Dressel M, Grioni M, Lichtenberg F. Phys Rev B 2004;70:245123.
114. Kurova T A, Aleksandrov V B. Dokl Akad Nauk SSSR 1971;201:1095.
115. Landoldt-Börnstein, New Series, Group II, Vol. 8, Part 1, Springer-Verlag, Berlin, 1976, ISBN 3-540-07441-4, p. 27.
116. Landoldt-Börnstein, New Series, Group II, Vol. 8, Part 1, Springer-Verlag, Berlin, 1976, ISBN 3-540-07441-4, p. 4 and 5.
117. International Centre for Diffraction Data (ICDD). Database / PDF No. 84-1089, 73-0069 or 49-0426.
118. Le Berre F, Crosnier-Lopez M P, Fourquet J L. Solid State Science 2004;6:53.
119. Leshchenko P P, Shevchenko A V, Lykova L N, Kovba L M, Ippolitova E A. In: Phase Equilibra Diagrams (Phase Diagrams for Ceramists), Annual 92, 1992, The American Ceramic Soceity, ISBN 0-944904-51-3, Fig. 92-006.
120. Levin I, Bendersky L A, Vanderah T A, Roth R S, Stafsudd O M. Mat Res Bull 1998;33;501.
121. Levin I, Bendersky L A. Acta Cryst B 1999;55:853.
122. Levin I, Bendersky L A, Vanderah T A. Phil Mag A 2000;80;411.
123. Lewandowski J T, Pickering I J, Jacobson A J. Mat Res Bull 1992;27:981.
124. Lichtenberg F. Dissertation, University of Zurich, 1991.
125. Lichtenberg F, Williams T, Reller A, Widmer D, Bednorz J G. Z Phys. B 1991;84:369.
126. Lichtenberg F, Widmer D, Bednorz J G, Williams T, Reller A. Z Phys. B 1991;82:211.
127. Lichtenberg F, Herrnberger A, Wiedenmann K, Mannhart J. Prog Solid State Chem 2001;29:1.
128. Lichtenberg F. Prog Solid State Chem 2002;30:103.
129. Little W A. Phys Rev 1964;134:A1416.
130. Little W A. Int J Quantum Chem: Quantum Chem Symp 1981;15:545.
131. Little W A. Journal de Physique (Colloque C3, supplement au n 6) 1983;C3:819. (in English, abstract also in French)
132. Little W A. In: Stuart A W, Kresin V Z, editors. Novel Superconductivity (Proceedings of the International Workshop on Novel Mechanisms of Superconductivity), Plenum Press, New York, 1987, ISBN 0-306-42691-9. p. 341.
133. Liu D, Yao X, Smyth D M. Mat Res Bull 1992;27:387.
134. Loa I, Syassen K, Wang X, Lichtenberg F, Hanfland M, Kuntscher C A. Phys Rev B 2004;69:224105.
135. Long X, Han X. J Crystal Growth 2004;275:492.
136. Lu D H, Gopinath C S, Schmidt M, Cummins T R, Nüecker N, Schuppler S, Lichtenberg F. Physica C 1997;282-287:995.
137. Lunkenheimer P, Bobnar V, Pronin A V, Ritus A I, Volkov A A, Loidl A. Phys Rev B 2002;66:052105.
138. Mackenzie A P, Maeno M. Rev Mod Phys 2003;75:657.
139. Maeno Y, Hashimoto H, Yoshida K, Nishizaki S, Fujita T, Bednorz J G, Lichtenberg F. Nature (London) 1994;372:532.
140. Mansikka K, Mikkola S. J Phys C: Solid State Phys 1974;7:3737.
141. Mourachkine A. Room-Temperature Superconductivity. Cambridge Int. Science Publishing; 2004 [ISBN 1-904602-27-4].
142. Mourachkine A. Room-Temperature Superconductivity. Cambridge Int. Science Publishing; 2004 [ISBN 1-904602-27-4]. p. 292 and 293.

143. Mitchell R H. Perovskites - Modern and Ancient. Almaz Press; 2002 [ISBN 0-9689411-0-9]. p. 117.
144. Mitchell R H. Perovskites - Modern and Ancient. Almaz Press; 2002 [ISBN 0-9689411-0-9]. p. 196 - 198.
145. Mössner B, Kemmler-Sack S. J Less-Common Metals 1985;105:165.
146. Mössner B, Kemmler-Sack S. J Less-Common Metals 1986;120:287.
147. Moini A, Subramanian A, Clearfield A, DiSalvo F J, McCarroll W H. J Solid State Chem 1987;66:136.
148. Nakamura A. Jpn J Appl Phys 1994;33:L583.
149. Nanamatsu S, Kimura M. J Phys Soc Jpn 1974;36:1495.
150. Nanamatsu S, Kimura M, Doi K, Matsushita S, Yamada N. Ferroelectrics 1974;8:511.
151. Nanamatsu S, Kimura M, Kawamura T. J Phys Soc Jpn 1975;38:817.
152. Nanot M, Queyroux F, Gilles J C, Carpy A, Galy J. J Solid State Chem 1974:11:272. (in French)
153. Nanot M, Queyroux F, Gilles J C, Chevalier R. Acta Cryst B 1976;32:1115. (in French, abstract in English)
154. Nanot M, Queyroux F, Gilles J C. J Solid State Chem 1979;28:137. (in French, abstract in English)
155. Nanot M, Queyroux F, Gilles J C, Portier R. J Solid State Chem 1981;38:74.
156. Nanot M, Queyroux F, Gilles J C. In: Metselaar R, Heijligers H J M, Schonman J, editors. Studies in Inorganic Chemistry, Vol 3. Amsterdam, Elsevier, 1983, p. 623.
157. Nanot M, Queyroux F, Gilles J C, Capponi J J. J Solid State Chem 1986;61:315.
158. Nolting W. Quantentheorie des Magnetismus, Teil 1. Stuttgart, Teubner, 1986 [ISBN 3-519-03084-5], p. 271 - 279. (in German)
159. Nolting W. Quantentheorie des Magnetismus, Teil 1. Stuttgart, Teubner, 1986 [ISBN 3-519-03084-5], p. 259 - 270. (in German)
160. Nolting W. Quantentheorie des Magnetismus, Teil 1. Stuttgart, Teubner, 1986 [ISBN 3-519-03084-5], p. 216 - 222. (in German)
161. Nolting W. Quantentheorie des Magnetismus, Teil 1. Stuttgart, Teubner, 1986 [ISBN 3-519-03084-5], p. 200 - 215. (in German)
162. Ohi K, Kojima S. Jpn J Appl Phys (Suppl 24-2) 1985;24:817.
163. Ohi K, Ishii S, Omura H. Ferroelectrics 1992;137:133.
164. Ohi K, Ito K, Sugata T, Ohkoba M. J Korean Phys Soc 1998;32:S59.
165. Ohtomo A, Muller D A, Grazul J L, Hwang H Y. Appl Phys Lett 2002;80:3922.
166. Olsen A, Roth R S. J Solid Sate Chem 1985;60:347.
167. Ostorero J, Nanot M, Queyroux F, Gilles J C, Makram H. J Crystal Growth 1983;65:576.
168. Pagola S, Massa N E, Polla G, Leyva G, Carbonio R E. Physica C 1994;235-240:755.
169. Pagola S, Polla G, Leyva G, Casais M T, Alonso J A, Rasines I, Carbonio R E. Materials Science Forum 1996;228-231:819.
170. Pasero D, Tilley R J D. J Solid State Chem 1998;135:260.
171. Petricek V, Elcoro L, Perez-Mato J M, Darriet J, Teneze N, Mercurio D. Ferroelectrics 2001;250:31.
172. Podkrytov A L, Animitsa I E, Shindel'man N K, Zhukovskii V M, Lozhkina E B, Perelyaeva L A. Inorg Mat 1988;24:1742.
173. Portengen T, Östreich Th, Sham L J. Phys Rev B 1996;54:17452.
174. Range K J, Haase H. Acta Cryst 1990;C46:317.

175. Ratheesh R, Sreemoolanadhan H, Sebastian M T. J Solid State Chem 1997;131:2.
176. Rearick T M, Catchen G L, Adams J M. Phys Rev B 1993;48:224.
177. Reich S, Tsabba Y. Eur Phys J B 1999;9:1.
178. Reich S, Leitus G, Tsabba Y, Levi Y, Sharoni A, Millo O. J Superconductivity 2000;13:855.
179. Roth R S. J Res Natl Bur Std 1956;56:17.
180. Roth R S, Negas T, Parker H S, Minor D B, Jones C. Mat Res Bull 1977;12:1173.
181. Rother H J, Kemmler-Sack S, Treiber U, Cyris W R. Z anorg allg Chem 1980;466:131.
182. Sato M, Abo J, Jin T, Ohta M. Solid State Ionics 1992;51:85.
183. Sato K, Adachi G Y, Shiokawa J. J Solid State Chem 1978;24:169.
184. Sato M, Abo J, Jin T. Solid State Ionics 1992;57:285.
185. Sato M, Kono Y, Jin T. J Ceram Soc Japan (Int Ed) 1993;101:954.
186. Sayagues M, Titmuss K, Meyer R, Kirkland A, Sloan J, Hutchison J, Tilley R. Acta Cryst B 2003;59:449.
187. Scheunemann K, Müller-Buschbaum Hk. J Inorg Nucl Chem 1974;36:1965.
188. Scheunemann K, Müller-Buschbaum Hk. J Inorg Nucl Chem 1975;37:1879.
189. Scheunemann K, Müller-Buschbaum Hk. J Inorg Nucl Chem 1975;37:2261.
190. Schlittenhelm H J, Kemmler-Sack S. Z anorg allg Chem 1980;465:183.
191. Schmalle H W, Williams T, Reller A, Linden A, Bednorz J G. Acta Cryst B 1993;49:235.
192. Schmehl A, Lichtenberg F, Bielefeldt, Mannhart J, Schlom D G. Appl Phys Lett 2003;82:3077
193. Schückel K, Müller-Buschbaum Hk. Z Anorg Allg Chem 1985;528:91. (in German, abstract also in English)
194. Schückel K, Müller-Buschbaum Hk. Z anorg allg Chem 1985;523:69. (in German, abstract also in English)
195. Seo J W, Fompeyrine J, Locquet J P. Proceedings of SPIE 1998;3481:326.
196. Seo J W, Fompeyrine J, Siegwart H, Locquet J P. Phys Rev B 2001;63:205401.
197. Seraji S, Wu Y, Limmer S, Chou T, Nguyen C, Forbess M, Cao G Z. Mat Sci Eng B 2002;88:73.
198. Shanks H R. Solid State Comm 1974;15:753.
199. Shannon J, Katz L. Acta Cryst B 1970;26:102.
200. Shengelaya A, Reich S, Tsabba Y, Müller K A. Eur Phys J B 1999;12:13.
201. Shoup S, Bamberger C, Haverlock T. International Centre for Diffraction Data (ICDD). Database / PDF No. 47-0667. Private Communication 1996.
202. Shoyama M, Tsuzuki A, Kato K, Murayama N. Appl Phys Lett 1999;75:561.
203. Sirotinkin V P, Averkova O E, Starikov A M, Evdokimov A A. Russ J Inorg Chem 1987;32:150.
204. Sloan J, Tilley R J D. Eur J Solid State Inorg Chem 1994;31:673.
205. Sugimoto W, Ohkawa H, Naito M, Sugahara Y, Kuroda K. J Solid State Chem 1999;148:508.
206. Sun G F, Wong K W, Xu B R, Xin Y, Lu D F. Phys Lett A 1994;192:122.
207. Suzuki I S, Morillo J, Burr C R, Suzuki M. Phys Rev B 1994;50:216.
208. Sych A M, Titov Yu A. Russ J Inorg Chem 1981;26:1077.
209. Sych A M, Titov Yu A. Russ J Inorg Chem 1981;26:469.
210. Sych A M, Stefanovich S Yu, Titov Yu A, Bondarenko T N, Mel'nik V M. Inorg Mater 1991;27:2229.
211. Tanaka M, Sekii H, Ohi K. Jpn J Appl Phys (Suppl 24-2) 1985;24:814.
212. van Tendeloo G, Amelinckx S, Darriet B, Bontchev R, Darriet J, Weill F. J Solid State Chem 1994;108:314.

213. Teneze N, Mercurio D, Trolliard G, Champarnaud-Mesjard J C. Z Kristallogr NCS 2000;215:12.
214. Takano Y, Taketomi H, Tsurumi H, Yamadaya T, Mori N. Physica B 1997;237-238:68.
215. Takano Y, Takayanagi S, Ogawa S, Yamadaya T, Mori N. Solid State Comm 1997;103:215.
216. Takano Y, Kimishima Y, Yamadaya T, Ogawa S, Mori N. Rev High Pressure Sci Technol 1998;7:589.
217. Teneze N, Boullay P, Trolliard G, Mercurio D. Solid State Sci 2002;4:1119.
218. Thirunavukkuarasu K, Lichtenberg F, Kuntscher C A. J Phys: Condensed Matter 2006;18:9173.
219. Titov Yu A, Sych A M, Mel'nik V M, Bondarenko TN. Russ J Inorg Chem 1987;32:1.
220. Titov Yu A, Sych A M, Kapshuk A A. Inorg Mat 1998;34:496.
221. Titov Yu A, Sych A M, Sokolov A N, Kapshuk A A, Markiv V Ya, Belyavina N M. J Alloys Comp 2000;311:252.
222. Titov Yu A, Sych A M, Markiv V Ya, Belyavina N M, Kapshuk A A, Yaschuk V P. J Alloys Comp 2001;316:309.
223. Titov Yu A, Sych A M, Kapshuk A A, Yashchuk V P. Inorg Mater 2001;37:363.
224. Titov Yu A, Sych A M, Markiv V Ya, Belyavina N M, Kapshuk A A, Yaschuk V P, Slobodyanik M S. J Alloys Comp 2002;337:89.
225. Titov Y A, Sych A M, Markiv V Ya, Belyavina N M, Kapshuk A A, Slobodyanik M S. Rep Natl Sci Ukraine 2002;4:162. (in Ukrainian)
226. Titov Yu A, Belyavina N M, Markiv V Ya, Slobodyanik M S, Chumak V V. J Alloys Comp 2005;387:82.
227. Titov Y A, Belyavina N M, Markiv V Ya, Slobodyanik M S, Chumak V V, Yaschuk V P. Rep Natl Sci Ukraine 2005;12:149. (in Ukrainian)
228. Titov Y A, Belyavina N M, Markiv V Ya, Slobodyanik M S, Chumak V V, Yaschuk V P. J Alloys Comp 2007;430:81.
229. Titov Y A, Belyavina N M, Markiv V Ya, Slobodyanik M S, Chumak V V. Rep Natl Sci Ukraine 2006;8:181. (in Ukrainian)
230. Toda K, Kameo Y, Fujimoto M, Sato M. J Ceram Soc Japan (Int Ed) 1994;102:735.
231. Toda K, Teranishi T, Sato M. J Europ Ceram Soc 1999;19:1525.
232. Trolliard G, Teneze N, Boullay Ph, Manier M, Mercurio D. J Solid State Chem 2003;173:91.
233. Trolliard G, Teneze N, Boullay Ph, Mercurio D. J Solid State Chem 2004;177:1188.
234. Tsuda N, Nasu K, Yanase A, Siratori K. Electronic Conduction in Oxides, 1990, Springer Series in Solid State Sciences, ISBN 3-540-52637-4. p. 24, 25, 102 and 103.
235. Tsunetsugu H, Sigrist M, Ueda K. Rev Mod Phys 1997;69:809.
236. Uma S, Gopalakrishnan J. J Solid State Chem 1993;102:332.
237. Uma S, Gopalakrishnan J. Chem Mater 1994;6:907.
238. Uno M, Kosuga A, Okui M, Horisaka K, Yamanaka S. J Alloys Comp 2005;400:270.
239. Vanderah T A, Collins T R, Wong-Ng W, Roth R S, Farber L. J Alloys Comp 2002;116:346.
240. Vanderah T A, Miller V L, Levin I, Bell S M, Negas T. J Solid State Chem 2004;177:2023.
241. Vineis C, Davies P K, Negas T, Bell S. Mat Res Bull 1996;31:431.
242. Weber J E, Kegler C, Büttgen N, Krug von Nidda H A, Loidl A, Lichtenberg F. Phys Rev B 2001;64:235414.

243. Williams T, Lichtenberg F, Widmer D, Bednorz J G, Reller A. J Solid State Chem 1993;103:375.
244. Winter H, Schuppler S, Kuntscher C A. J Phys Cond Matter 2000;12:1735.
245. Xiong R, Xiao Q, Shi J, Liu H, Tang W, Tian D, Tian M. Mod Phys Lett B 2000;14:345.
246. Yamamoto N. Acta Cryst A 1982;38:780.
247. Yuan Q. Eur Phys J B 2002;25:281.
248. Zakharov N A, Stefanovich S Yu, Kustov E F, Venevtsev Yu N. Kristall und Technik 1980;15:29.
249. Zakharov N A, Orlovsky V P, Klyuev V A. Bull Russ Acad Sci (Physics) 1996;60:1567.
250. Zubkov V. International Centre for Diffraction Data (ICDD). Database / PDF No. 47-0283. ICDD Grant-in-Aid 1995.
251. Zubkov V, Tyutyunnik A. International Centre for Diffraction Data (ICDD). Database / PDF No. 51-0412. ICDD Grant-in-Aid 1999.
252. Zuniga F J, Darriet J. Acta Cryst C 2003;59:i18.

10 Appendix: Tables of powder XRD data of some compounds

In this appendix we provide the powder XRD data of the following compounds:

- $BaCa_{0.6}La_{0.4}Nb_2O_{7.00}$ $(k = 2$ of $A'A_{k-1}B_kO_{3k+1})$
- $BaCa_2Nb_3O_{10.07}$ $(k = 3$ of $A'A_{k-1}B_kO_{3k+1})$
- $Ce_5Ti_5O_{17.00} = CeTiO_{3.40}$ $(n = 5$ of $A_nB_nO_{3n+2} = ABO_x)$
- $Pr_5Ti_5O_{17.06} = PrTiO_{3.41}$ $(n = 5$ of $A_nB_nO_{3n+2} = ABO_x)$
- $Sm_5Ti_5O_{16.85} = SmTiO_{3.37}$ $(n = 5$ of $A_nB_nO_{3n+2} = ABO_x)$
- $La_5Ti_4MnO_{17} = LaTi_{0.8}Mn_{0.2}O_{3.4}$ $(n = 5$ of $A_nB_nO_{3n+2} = ABO_x)$
- $La_6Ti_4Fe_2O_{20} = LaTi_{0.67}Fe_{0.33}O_{3.33}$ $(n = 6$ of $A_nB_nO_{3n+2} = ABO_x)$
- $Sr_6Nb_5O_{18.07}$ $(m = 6$ of $A_mB_{m-1}O_{3m})$
- $Sr_{11}Nb_9O_{33.09}$ $(m = 5 + 6$ of $A_mB_{m-1}O_{3m})$

The following tables present the observed (obs) and calculated (calc) peak positions as 2Θ and d-values, their difference (diff), and the observed (obs) Intensities I. The calculated values were obtained by lattice parameter refinement. Also provided are the refined lattice parameters.

				2Θ (°)			*d* (Å)			*I*
No.	**h**	**k**	**l**	calc	obs	diff	calc	obs	diff	obs
1	0	0	2	8.854	8.913	-0.059	9.9793	9.9136	0.0657	58
2	0	1	3	17.506	17.534	-0.027	5.0618	5.0540	0.0078	17
3	0	0	4	17.762	17.795	-0.033	4.9896	4.9804	0.0092	25
4	1	0	1	22.676	22.724	-0.048	3.9181	3.9099	0.0082	23
5	0	2	2	24.486	24.523	-0.037	3.6325	3.6271	0.0054	60
6	0	1	5	25.039	25.061	-0.022	3.5534	3.5504	0.0031	35
7	1	0	3	25.991	26.017	-0.027	3.4255	3.4221	0.0035	73
8	0	0	6	26.779	26.785	-0.006	3.3264	3.3257	0.0007	1000
9	0	2	4	29.036	29.046	-0.010	3.0728	3.0717	0.0010	547
10	1	1	4	30.851	30.859	-0.008	2.8961	2.8953	0.0007	53
11	1	0	5	31.658	31.682	-0.025	2.8240	2.8219	0.0021	216
12	1	2	1	32.362	32.400	-0.038	2.7641	2.7610	0.0032	107
13	0	1	7	33.434	33.438	-0.004	2.6779	2.6776	0.0003	142
14	0	2	6	35.439	35.422	0.017	2.5309	2.5321	-0.0012	72
15	0	0	8	35.969	35.964	0.005	2.4948	2.4952	-0.0004	966
16	1	1	6	36.973	37.008	-0.035	2.4294	2.4271	0.0022	57
17	1	0	7	38.767	38.788	-0.021	2.3210	2.3197	0.0012	24
18	1	2	5	39.360	39.411	-0.052	2.2874	2.2845	0.0029	7
19	0	3	5	41.411	41.425	-0.014	2.1786	2.1780	0.0007	25
20	1	3	2	42.420	42.404	0.016	2.1291	2.1299	-0.0008	98
21	0	2	8	43.003	42.979	0.025	2.1016	2.1028	-0.0012	110
22	1	1	8	44.315	44.332	-0.017	2.0424	2.0417	0.0007	139
23	0	0	10	45.405	45.395	0.010	1.9959	1.9963	-0.0004	760
24	0	4	0	46.534	46.504	0.030	1.9500	1.9513	-0.0012	175
25	0	3	7	47.275	47.331	-0.056	1.9212	1.9190	0.0022	15
26	1	3	6	49.993	50.024	-0.031	1.8229	1.8219	0.0011	24
27	0	2	10	51.386	51.392	-0.005	1.7767	1.7766	0.0002	279
28	1	2	9	52.674	52.669	0.005	1.7363	1.7364	-0.0002	460
29	2	0	6	53.454	53.454	0.000	1.7128	1.7128	0.0000	45
30	1	4	3	54.070	54.070	0.000	1.6947	1.6947	0.0000	36
31	2	2	4	54.758	54.729	0.029	1.6750	1.6758	-0.0008	148
32	0	0	12	55.180	55.156	0.024	1.6632	1.6639	-0.0007	258
33	1	0	11	55.584	55.575	0.009	1.6521	1.6523	-0.0002	107
34	1	4	5	57.376	57.349	0.027	1.6047	1.6054	-0.0007	93
35	2	0	8	59.200	59.191	0.009	1.5595	1.5597	-0.0002	115

Table 71. $BaCa_{0.6}La_{0.4}Nb_2O_{7.00}$ ($k = 2$ of $A'A_{k-1}B_kO_{3k+1}$, Dion-Jacobson type without any alkali metal). The calculated values refer to a primitive orthorhombic cell with $a = 4.00$ Å, $b = 7.80$ Å and $c = 19.96$ Å.

				2Θ (°)			d (Å)			I
No.	**h**	**k**	**l**	calc	obs	diff	calc	obs	diff	obs
1	0	0	2	6.284	6.315	-0.031	14.0535	13.9851	0.0684	12
2	0	0	4	12.587	12.576	0.012	7.0267	7.0332	-0.0064	16
3	0	0	6	18.929	18.958	-0.029	4.6845	4.6774	0.0071	101
4	0	2	0	22.877	22.847	0.030	3.8842	3.8892	-0.0050	62
5	0	2	2	23.747	23.743	0.004	3.7439	3.7444	-0.0006	14
6	0	0	8	25.330	25.344	-0.014	3.5134	3.5114	0.0019	1000
7	1	2	0	25.686	25.723	-0.037	3.4654	3.4606	0.0049	730
8	0	2	4	26.194	26.209	-0.015	3.3994	3.3975	0.0020	31
9	2	1	3	27.604	27.692	-0.089	3.2289	3.2188	0.0101	33
10	0	2	6	29.858	29.821	0.037	2.9901	2.9937	-0.0036	134
11	2	0	6	30.085	30.001	0.084	2.9680	2.9761	-0.0082	78
12	1	2	5	30.274	30.348	-0.074	2.9499	2.9429	0.0071	104
13	0	0	10	31.812	31.833	-0.021	2.8107	2.8089	0.0018	524
14	2	1	6	32.262	32.278	-0.016	2.7725	2.7712	0.0013	197
15	1	0	10	33.940	33.993	-0.053	2.6392	2.6352	0.0040	53
16	0	2	8	34.391	34.374	0.017	2.6056	2.6069	-0.0013	76
17	0	1	11	37.006	37.012	-0.006	2.4273	2.4269	0.0004	11
18	3	0	4	37.390	37.458	-0.068	2.4032	2.3990	0.0042	11
19	0	0	12	38.401	38.403	-0.002	2.3423	2.3421	0.0001	632
20	2	1	9	38.921	38.983	-0.063	2.3122	2.3086	0.0036	100
21	2	0	11	42.473	42.485	-0.012	2.1266	2.1261	0.0006	47
22	3	1	7	43.507	43.487	0.020	2.0784	2.0794	-0.0009	90
23	2	1	11	44.116	44.145	-0.028	2.0512	2.0499	0.0013	58
24	1	1	13	45.065	45.080	-0.015	2.0102	2.0095	0.0006	397
25	0	2	12	45.168	45.171	-0.003	2.0058	2.0057	0.0001	500
26	3	0	9	45.823	45.770	0.052	1.9786	1.9808	-0.0021	215
27	3	2	6	46.700	46.700	0.000	1.9435	1.9435	0.0000	51
28	2	3	7	48.028	47.958	0.070	1.8928	1.8954	-0.0026	38
29	1	4	1	48.417	48.456	-0.039	1.8785	1.8771	0.0014	31
30	0	1	15	50.033	50.018	0.015	1.8216	1.8221	-0.0005	26
31	0	2	14	51.177	51.182	-0.005	1.7835	1.7833	0.0002	107
32	3	2	9	51.813	51.783	0.030	1.7631	1.7640	-0.0010	145
33	0	0	16	52.016	52.049	-0.033	1.7567	1.7557	0.0010	175
34	3	3	5	52.841	52.827	0.014	1.7312	1.7316	-0.0004	31
35	2	4	3	53.757	53.762	-0.005	1.7038	1.7037	0.0001	141

Table 72. $BaCa_2Nb_3O_{10.07}$ ($k = 3$ of $A'A_{k-1}B_kO_{3k+1}$, Dion-Jacobson type without any alkali metal). The calculated values refer to a primitive orthorhombic cell with $a = 7.77$ Å, $b = 7.67$ Å and $c = 28.11$ Å. Continuation in Table 73.

				2Θ (°)			d (Å)			I
No.	**h**	**k**	**l**	calc	obs	diff	calc	obs	diff	obs
36	4	2	3	54.179	54.183	-0.005	1.6916	1.6914	0.0001	238
37	1	1	16	54.857	54.828	0.029	1.6722	1.6731	-0.0008	54
38	2	3	11	55.902	55.893	0.009	1.6434	1.6437	-0.0002	108
39	4	1	9	57.582	57.594	-0.012	1.5994	1.5991	0.0003	68
40	0	0	18	59.116	59.102	0.014	1.5615	1.5618	-0.0003	189

Table 73. Continuation from Table 72.

				2Θ (°)			d (Å)			I
No.	**h**	**k**	**l**	calc	obs	diff	calc	obs	diff	obs
1	0	0	2	5.696	5.716	-0.020	15.5039	15.4501	0.0538	9
2	0	0	4	11.406	11.384	0.021	7.7520	7.7664	-0.0145	6
3	1	0	4	17.069	17.088	-0.019	5.1906	5.1847	0.0059	18
4	0	1	4	19.722	19.723	-0.001	4.4978	4.4976	0.0002	10
5	0	1	5	21.529	21.546	-0.017	4.1242	4.1211	0.0032	55
6	2	0	0	22.806	22.806	0.000	3.8961	3.8961	0.0000	15
7	0	0	8	22.926	22.983	-0.057	3.8760	3.8665	0.0094	21
8	1	1	-5	23.562	23.571	-0.009	3.7728	3.7714	0.0015	10
9	0	1	-7	25.762	25.708	0.054	3.4554	3.4625	-0.0071	11
10	1	1	-7	27.204	27.221	-0.017	3.2754	3.2734	0.0020	9
11	2	1	-2	28.027	28.037	-0.010	3.1811	3.1799	0.0012	23
12	2	0	-7	28.600	28.608	-0.008	3.1187	3.1178	0.0008	1000
13	2	0	6	30.331	30.298	0.032	2.9445	2.9476	-0.0031	127
14	2	0	-8	30.475	30.456	0.020	2.9309	2.9327	-0.0018	145
15	2	0	-9	32.516	32.503	0.012	2.7515	2.7525	-0.0010	124
16	2	1	-7	32.958	32.978	-0.020	2.7156	2.7139	0.0016	187
17	2	1	6	34.492	34.490	0.002	2.5982	2.5984	-0.0001	119
18	3	0	1	34.985	35.000	-0.015	2.5627	2.5616	0.0011	19
19	0	2	-5	35.562	35.587	-0.026	2.5225	2.5207	0.0018	40
20	1	1	-11	36.363	36.381	-0.017	2.4687	2.4675	0.0011	5

Table 74. $Ce_5Ti_5O_{17.00} = CeTiO_{3.40}$ ($n = 5$ of $A_nB_nO_{3n+2} = ABO_x$). The calculated values refer to a primitive monoclinic cell with $a = 7.85$ Å, $b = 5.52$ Å, $c = 31.24$ Å and $\beta = 97.0°$. Continuation in Table 75.

				2Θ (°)			d (Å)			I
No.	**h**	**k**	**l**	calc	obs	diff	calc	obs	diff	obs
21	3	0	4	37.806	37.831	-0.025	2.3777	2.3762	0.0015	12
22	3	1	0	38.262	38.261	0.001	2.3504	2.3505	-0.0001	22
23	2	0	10	39.229	39.253	-0.023	2.2947	2.2933	0.0013	33
24	3	1	3	40.237	40.164	0.073	2.2395	2.2434	-0.0039	47
25	2	1	9	40.400	40.445	-0.045	2.2308	2.2284	0.0024	151
26	2	0	11	41.727	41.768	-0.041	2.1629	2.1609	0.0020	22
27	1	2	-9	42.648	42.676	-0.027	2.1183	2.1170	0.0013	17
28	0	2	-10	43.869	43.830	0.039	2.0621	2.0639	-0.0018	128
29	1	1	-14	44.253	44.271	-0.018	2.0451	2.0443	0.0008	62
30	2	1	11	44.975	44.978	-0.003	2.0139	2.0138	0.0001	58
31	1	2	-11	46.486	46.518	-0.032	1.9520	1.9507	0.0013	328
32	1	0	15	46.771	46.785	-0.015	1.9407	1.9402	0.0006	47
33	3	2	-3	48.084	48.096	-0.012	1.8907	1.8903	0.0005	112
34	4	1	0	49.581	49.598	-0.017	1.8371	1.8365	0.0006	28
35	1	0	-17	49.912	49.911	0.001	1.8257	1.8257	-0.0001	98
36	0	3	5	51.762	51.791	-0.028	1.7647	1.7638	0.0009	86
37	4	1	4	52.439	52.415	0.024	1.7435	1.7443	-0.0008	54
38	0	3	-7	53.893	53.887	0.006	1.6999	1.7000	-0.0002	20
39	0	3	8	55.195	55.187	0.008	1.6628	1.6630	-0.0002	153
40	1	2	14	55.511	55.502	0.010	1.6541	1.6543	-0.0003	160
41	0	3	9	56.646	56.616	0.031	1.6236	1.6244	-0.0008	97
42	4	2	0	57.884	57.882	0.002	1.5918	1.5918	-0.0001	122
43	2	1	-18	58.278	58.267	0.011	1.5820	1.5822	-0.0003	103
44	1	1	18	58.651	58.623	0.029	1.5728	1.5735	-0.0007	104
45	2	3	6	59.143	59.148	-0.005	1.5609	1.5608	0.0001	41
46	4	1	-13	59.894	59.893	0.001	1.5431	1.5431	0.0000	26

Table 75. Continuation from Table 74.

				2Θ (°)			d (Å)			I
No.	**h**	**k**	**l**	calc	obs	diff	calc	obs	diff	obs
1	0	0	2	5.729	5.708	0.021	15.4145	15.4705	-0.0560	7
2	1	0	-1	11.372	11.404	-0.033	7.7750	7.7529	0.0222	15
3	1	0	4	17.056	17.075	-0.019	5.1944	5.1886	0.0058	33
4	0	1	5	21.586	21.591	-0.005	4.1135	4.1125	0.0010	87
5	2	0	0	22.784	22.815	-0.031	3.8999	3.8946	0.0053	9
6	0	0	8	23.061	23.127	-0.066	3.8536	3.8428	0.0109	15
7	0	1	6	23.633	23.607	0.026	3.7616	3.7658	-0.0042	4
8	0	1	7	25.855	25.828	0.027	3.4432	3.4467	-0.0036	6
9	1	0	-9	27.193	27.249	-0.057	3.2768	3.2701	0.0067	14
10	0	1	8	28.216	28.190	0.026	3.1602	3.1631	-0.0029	97
11	2	1	-3	28.530	28.609	-0.078	3.1261	3.1177	0.0084	1000
12	2	1	-4	29.300	29.372	-0.072	3.0457	3.0384	0.0073	18
13	2	1	-5	30.335	30.456	-0.120	2.9441	2.9327	0.0114	150
14	2	1	4	31.342	31.324	0.018	2.8518	2.8534	-0.0016	17
15	1	0	-11	32.671	32.669	0.003	2.7387	2.7389	-0.0002	72
16	2	1	-7	33.111	33.094	0.017	2.7033	2.7047	-0.0013	199
17	1	1	9	33.869	33.798	0.071	2.6446	2.6499	-0.0054	9
18	0	2	4	34.477	34.485	-0.007	2.5993	2.5987	0.0006	83
19	1	2	1	34.669	34.682	-0.013	2.5853	2.5844	0.0009	59
20	2	0	-10	34.955	35.007	-0.052	2.5648	2.5611	0.0037	34
21	3	0	2	35.640	35.632	0.008	2.5171	2.5176	-0.0005	39
22	0	0	13	37.909	37.860	0.049	2.3715	2.3744	-0.0030	13
23	2	1	8	38.265	38.287	-0.022	2.3502	2.3489	0.0013	13
24	3	1	2	39.306	39.324	-0.018	2.2904	2.2894	0.0010	27
25	3	1	-6	40.464	40.464	0.001	2.2274	2.2275	0.0000	124

Table 76. $Pr_5Ti_5O_{17.06} = PrTiO_{3.41}$ ($n = 5$ of $A_nB_nO_{3n+2} = ABO_x$). The calculated values refer to a primitive monoclinic cell with $a = 7.85$ Å, $b = 5.52$ Å, $c = 31.03$ Å and $\beta = 96.5°$. Continuation in Table 77.

				2Θ (°)			d (Å)			I
No.	**h**	**k**	**l**	calc	obs	diff	calc	obs	diff	obs
26	3	1	4	41.232	41.233	-0.001	2.1877	2.1876	0.0001	26
27	1	1	-13	41.826	41.870	-0.044	2.1580	2.1559	0.0022	24
28	1	2	-9	42.794	42.776	0.018	2.1114	2.1123	-0.0008	17
29	1	0	14	43.944	43.936	0.008	2.0588	2.0591	-0.0003	100
30	2	0	12	44.342	44.327	0.014	2.0412	2.0419	-0.0006	27
31	2	1	11	44.990	45.081	-0.092	2.0133	2.0094	0.0039	55
32	2	1	-13	45.471	45.418	0.052	1.9931	1.9953	-0.0022	13
33	4	0	0	46.537	46.540	-0.003	1.9499	1.9498	0.0001	126
34	1	2	-11	46.677	46.674	0.003	1.9444	1.9445	-0.0001	99
35	3	0	-12	46.755	46.778	-0.023	1.9413	1.9404	0.0009	116
36	3	0	10	48.253	48.224	0.029	1.8845	1.8856	-0.0011	105
37	0	3	1	49.572	49.594	-0.022	1.8374	1.8367	0.0008	32
38	2	1	13	49.999	50.000	-0.001	1.8227	1.8227	0.0000	44
39	1	2	12	50.837	50.815	0.022	1.7946	1.7953	-0.0007	27
40	1	3	-4	52.066	52.047	0.020	1.7551	1.7557	-0.0006	32
41	4	0	-10	52.555	52.492	0.063	1.7399	1.7419	-0.0019	87
42	4	0	-11	54.106	54.065	0.041	1.6936	1.6948	-0.0012	19
43	0	3	8	55.262	55.258	0.004	1.6609	1.6611	-0.0001	94
44	2	3	-3	55.443	55.435	0.008	1.6559	1.6562	-0.0002	92
45	0	2	15	55.709	55.707	0.002	1.6487	1.6487	-0.0001	163
46	4	1	-11	56.814	56.843	-0.029	1.6192	1.6184	0.0008	34
47	1	2	15	58.196	58.201	-0.005	1.5840	1.5839	0.0001	82
48	3	0	-17	58.605	58.628	-0.023	1.5739	1.5733	0.0006	92
49	1	1	-19	59.190	59.191	-0.001	1.5597	1.5597	0.0000	28

Table 77. Continuation from Table 76.

				2Θ (°)			d (Å)			I
No.	**h**	**k**	**l**	calc	obs	diff	calc	obs	diff	obs
1	0	0	2	5.743	5.728	0.015	15.3767	15.4176	-0.0409	11
2	1	0	0	11.402	11.365	0.036	7.7547	7.7792	-0.0246	21
3	0	0	5	14.389	14.445	-0.056	6.1507	6.1271	0.0235	45
4	0	1	2	17.067	17.094	-0.027	5.1913	5.1831	0.0081	26
5	1	0	5	19.330	19.334	-0.004	4.5883	4.5872	0.0010	24
6	1	0	6	21.756	21.697	0.059	4.0818	4.0928	-0.0109	54
7	2	0	1	23.408	23.416	-0.008	3.7973	3.7960	0.0013	77
8	2	0	2	24.241	24.134	0.107	3.6687	3.6847	-0.0160	35
9	1	1	-6	25.525	25.541	-0.016	3.4869	3.4847	0.0022	35
10	1	0	-9	27.363	27.348	0.016	3.2567	3.2585	-0.0018	32
11	2	1	1	28.516	28.591	-0.075	3.1276	3.1196	0.0081	1000
12	2	0	-7	29.035	29.037	-0.002	3.0729	3.0727	0.0002	746
13	2	1	-4	29.495	29.475	0.020	3.0260	3.0280	-0.0020	85
14	0	1	9	30.757	30.778	-0.021	2.9047	2.9028	0.0019	407
15	0	0	11	31.987	31.946	0.040	2.7958	2.7992	-0.0034	40
16	0	2	0	32.442	32.469	-0.027	2.7575	2.7553	0.0023	88
17	2	0	-9	33.030	33.046	-0.016	2.7098	2.7085	0.0013	125
18	2	1	-7	33.352	33.362	-0.011	2.6844	2.6835	0.0008	486
19	1	1	9	33.888	33.990	-0.102	2.6431	2.6354	0.0077	75
20	3	0	-1	34.483	34.463	0.020	2.5989	2.6003	-0.0014	110
21	3	0	-3	34.857	34.840	0.017	2.5718	2.5730	-0.0012	197
22	3	0	-4	35.417	35.509	-0.092	2.5324	2.5261	0.0063	66
23	1	0	-12	35.687	35.685	0.002	2.5139	2.5140	-0.0001	44
24	3	0	-6	37.233	37.255	-0.022	2.4130	2.4116	0.0014	44
25	3	0	4	37.845	37.905	-0.060	2.3754	2.3717	0.0036	48
26	3	1	0	38.429	38.371	0.059	2.3406	2.3440	-0.0035	21
27	2	1	-10	38.955	39.009	-0.054	2.3102	2.3071	0.0031	56
28	3	1	2	39.463	39.470	-0.007	2.2816	2.2812	0.0004	94
29	2	1	9	40.408	40.422	-0.014	2.2304	2.2297	0.0008	84
30	3	1	-6	40.785	40.799	-0.014	2.2106	2.2099	0.0007	100

Table 78. $Sm_5Ti_5O_{16.85} = SmTiO_{3.37}$ ($n = 5$ of $A_nB_nO_{3n+2} = ABO_x$). The calculated values refer to a primitive monoclinic cell with $a = 7.80$ Å, $b = 5.52$ Å, $c = 30.93$ Å and $\beta = 96.1°$. Continuation in Table 79.

				2Θ (°)			d (Å)			I
No.	**h**	**k**	**l**	calc	obs	diff	calc	obs	diff	obs
31	3	1	4	41.353	41.303	0.049	2.1816	2.1841	-0.0025	15
32	0	2	9	42.072	42.139	-0.067	2.1459	2.1427	0.0033	18
33	1	2	-9	42.942	42.967	-0.025	2.1045	2.1033	0.0012	89
34	3	0	8	44.209	44.190	0.019	2.0471	2.0479	-0.0008	148
35	1	2	9	44.514	44.496	0.017	2.0338	2.0345	-0.0008	249
36	2	0	-14	45.201	45.260	-0.059	2.0044	2.0019	0.0025	85
37	2	1	-13	45.783	45.794	-0.011	1.9803	1.9798	0.0005	34
38	1	2	10	46.513	46.495	0.018	1.9509	1.9516	-0.0007	75
39	2	2	-9	46.975	46.978	-0.003	1.9328	1.9327	0.0001	108
40	2	1	12	47.462	47.417	0.045	1.9141	1.9158	-0.0017	855
41	2	2	8	48.100	48.094	0.005	1.8902	1.8904	-0.0002	82
42	0	2	-12	48.452	48.444	0.008	1.8772	1.8775	-0.0003	104
43	3	2	-4	48.785	48.784	0.001	1.8652	1.8653	0.0000	147
44	4	0	-7	49.288	49.313	-0.025	1.8473	1.8465	0.0009	68
45	4	1	-3	49.716	49.730	-0.014	1.8324	1.8320	0.0005	120
46	3	2	-6	50.200	50.204	-0.004	1.8159	1.8158	0.0001	151
47	0	3	-4	51.040	51.085	-0.045	1.7880	1.7865	0.0015	36
48	4	1	4	52.533	52.548	-0.015	1.7406	1.7402	0.0005	191
49	2	1	14	52.655	52.697	-0.043	1.7369	1.7356	0.0013	222
50	3	2	-10	55.079	55.013	0.066	1.6660	1.6679	-0.0018	46
51	2	3	1	55.490	55.455	0.035	1.6547	1.6556	-0.0010	272
52	3	1	12	55.614	55.625	-0.011	1.6513	1.6510	0.0003	208
53	2	1	-17	56.273	56.234	0.039	1.6335	1.6345	-0.0011	138
54	3	0	-16	56.514	56.516	-0.001	1.6271	1.6270	0.0000	60
55	3	2	9	57.571	57.586	-0.014	1.5997	1.5993	0.0004	112
56	1	2	-16	58.679	58.639	0.040	1.5721	1.5731	-0.0010	99
57	1	1	18	58.953	58.951	0.001	1.5654	1.5655	0.0000	256
58	5	0	-3	59.260	59.235	0.025	1.5581	1.5587	-0.0006	159
59	3	2	10	59.386	59.373	0.014	1.5551	1.5554	-0.0003	87

Table 79. Continuation from Table 78.

				2Θ (°)			d (Å)			I
No.	**h**	**k**	**l**	calc	obs	diff	calc	obs	diff	obs
1	0	0	2	5.647	5.697	-0.050	15.6367	15.4994	0.1374	17
2	1	0	0	11.353	11.384	-0.031	7.7878	7.7665	0.0213	11
3	0	0	6	16.997	17.027	-0.030	5.2123	5.2033	0.0090	42
4	1	1	0	19.656	19.710	-0.054	4.5128	4.5007	0.0121	28
5	0	1	5	21.415	21.473	-0.058	4.1460	4.1348	0.0111	109
6	2	0	-1	22.623	22.595	0.028	3.9273	3.9320	-0.0047	24
7	2	0	0	22.819	22.921	-0.102	3.8939	3.8768	0.0171	55
8	1	1	4	23.475	23.478	-0.004	3.7866	3.7861	0.0006	21
9	0	0	9	25.615	25.679	-0.064	3.4748	3.4663	0.0085	29
10	2	0	4	26.854	26.884	-0.030	3.3173	3.3137	0.0036	18
11	0	1	8	27.916	27.885	0.030	3.1935	3.1970	-0.0034	78
12	2	0	5	28.514	28.513	0.001	3.1279	3.1279	-0.0001	1000
13	1	0	-10	29.333	29.262	0.071	3.0424	3.0496	-0.0072	31
14	2	0	-8	30.187	30.198	-0.011	2.9582	2.9571	0.0011	641
15	1	0	-11	32.051	32.097	-0.046	2.7903	2.7864	0.0039	198
16	0	2	0	32.309	32.330	-0.021	2.7686	2.7668	0.0018	269
17	0	1	10	32.864	32.871	-0.007	2.7231	2.7225	0.0005	598
18	3	0	-3	34.472	34.456	0.016	2.5997	2.6008	-0.0011	200
19	0	2	-5	35.428	35.438	-0.010	2.5317	2.5310	0.0007	190
20	0	1	-12	38.134	38.163	-0.029	2.3580	2.3563	0.0017	47
21	3	0	-8	39.040	39.078	-0.038	2.3054	2.3032	0.0022	69
22	2	2	0	39.923	39.979	-0.057	2.2564	2.2533	0.0031	165
23	3	1	3	40.284	40.282	0.002	2.2370	2.2371	-0.0001	137
24	2	2	3	41.550	41.573	-0.022	2.1717	2.1706	0.0011	32

Table 80. $La_5Ti_4MnO_{17} = LaTi_{0.8}Mn_{0.2}O_{3.4}$ ($n = 5$ of $A_nB_nO_{3n+2} = ABO_x$). The calculated values refer to a primitive monoclinic cell with $a = 7.86$ Å, $b = 5.54$ Å, $c = 31.54$ Å and $\beta = 97.5°$. Continuation in Table 81.

				2Θ (°)			d (Å)			I
No.	**h**	**k**	**l**	calc	obs	diff	calc	obs	diff	obs
25	2	2	4	42.495	42.509	-0.014	2.1256	2.1249	0.0007	52
26	1	0	14	43.545	43.544	0.001	2.0767	2.0768	0.0000	194
27	2	2	5	43.624	43.624	0.000	2.0731	2.0731	0.0000	246
28	1	2	-10	44.195	44.132	0.063	2.0477	2.0504	-0.0028	69
29	2	2	-8	44.800	44.767	0.033	2.0214	2.0228	-0.0014	78
30	3	0	-12	45.983	45.987	-0.004	1.9721	1.9720	0.0002	110
31	4	0	-3	46.271	46.277	-0.006	1.9605	1.9603	0.0002	310
32	0	0	16	46.419	46.424	-0.005	1.9546	1.9544	0.0002	236
33	2	2	-10	47.858	47.867	-0.009	1.8991	1.8988	0.0003	169
34	3	2	-3	47.965	47.978	-0.012	1.8952	1.8947	0.0005	171
35	0	3	2	49.699	49.700	-0.001	1.8330	1.8330	0.0000	156
36	3	2	-8	51.546	51.558	-0.012	1.7716	1.7712	0.0004	189
37	1	3	-5	52.548	52.550	-0.003	1.7402	1.7401	0.0001	81
38	4	1	5	53.665	53.589	0.076	1.7065	1.7088	-0.0023	45
39	2	3	-1	54.921	54.930	-0.009	1.6705	1.6702	0.0003	324
40	1	2	14	55.249	55.256	-0.007	1.6613	1.6611	0.0002	191
41	2	3	3	56.300	56.299	0.001	1.6328	1.6328	0.0000	152
42	4	0	9	57.116	57.142	-0.026	1.6114	1.6107	0.0007	204
43	2	1	-18	57.616	57.607	0.009	1.5986	1.5988	-0.0002	412
44	2	3	-7	57.879	57.895	-0.015	1.5919	1.5915	0.0004	240
45	1	3	-10	58.436	58.394	0.042	1.5780	1.5791	-0.0010	107
46	4	2	2	58.862	58.850	0.012	1.5676	1.5679	-0.0003	79
47	4	2	3	59.605	59.609	-0.004	1.5499	1.5498	0.0001	80

Table 81. Continuation from Table 80.

				2Θ (°)			d (Å)			I
No.	**h**	**k**	**l**	calc	obs	diff	calc	obs	diff	obs
1	0	0	2	4.788	4.869	-0.081	18.4414	18.1345	0.3069	23
2	0	0	6	14.397	14.436	-0.039	6.1471	6.1308	0.0163	47
3	0	1	2	16.680	16.650	0.029	5.3108	5.3201	-0.0093	13
4	0	0	8	19.236	19.216	0.020	4.6104	4.6150	-0.0047	13
5	0	0	9	21.668	21.650	0.018	4.0981	4.1015	-0.0034	138
6	2	0	1	22.901	22.902	-0.001	3.8802	3.8801	0.0001	61
7	0	0	10	24.110	24.165	-0.055	3.6883	3.6800	0.0083	34
8	0	1	8	25.098	25.107	-0.009	3.5453	3.5441	0.0012	16
9	1	0	10	26.712	26.755	-0.043	3.3346	3.3293	0.0053	21
10	2	1	1	28.043	28.003	0.041	3.1793	3.1838	-0.0045	34
11	2	0	7	28.442	28.416	0.026	3.1357	3.1384	-0.0028	52
12	0	1	10	29.052	29.073	-0.020	3.0711	3.0690	0.0021	1000
13	2	1	5	30.497	30.475	0.022	2.9288	2.9309	-0.0021	533
14	2	0	9	31.637	31.651	-0.014	2.8258	2.8246	0.0013	111
15	0	2	1	32.351	32.331	0.020	2.7651	2.7667	-0.0017	752
16	2	1	7	32.784	32.764	0.020	2.7296	2.7311	-0.0016	491
17	0	1	12	33.302	33.329	-0.028	2.6883	2.6861	0.0022	63
18	0	0	14	34.002	34.042	-0.040	2.6345	2.6315	0.0030	267
19	2	0	11	35.265	35.259	0.006	2.5430	2.5434	-0.0004	53
20	2	0	12	37.210	37.181	0.029	2.4144	2.4162	-0.0018	12
21	0	1	14	37.774	37.770	0.004	2.3796	2.3799	-0.0002	42
22	0	0	16	39.043	39.062	-0.019	2.3052	2.3041	0.0011	57
23	2	0	13	39.229	39.226	0.003	2.2947	2.2948	-0.0002	131
24	2	2	1	39.930	39.922	0.008	2.2560	2.2564	-0.0004	184

Table 82. $La_6Ti_4Fe_2O_{20}$ = $LaTi_{0.67}Fe_{0.33}O_{3.33}$ (n = 6 of $A_nB_nO_{3n+2}$ = ABO_x). The calculated values refer to a primitive orthorhombic cell with $a = 7.80$ Å, $b = 5.55$ Å and $c = 36.88$ Å. Continuation in Table 83.

				2Θ (°)			*d* (Å)			*I*
No.	**h**	**k**	**l**	calc	obs	diff	calc	obs	diff	obs
25	0	2	10	40.675	40.671	0.004	2.2164	2.2166	-0.0002	35
26	1	1	15	41.786	41.781	0.004	2.1600	2.1602	-0.0002	20
27	2	2	6	42.583	42.568	0.014	2.1214	2.1221	-0.0007	51
28	2	2	7	43.535	43.537	-0.002	2.0772	2.0771	0.0001	154
29	0	2	12	43.943	43.942	0.001	2.0588	2.0589	0.0000	187
30	2	2	9	45.810	45.829	-0.019	1.9792	1.9784	0.0008	50
31	1	1	17	46.385	46.387	-0.002	1.9560	1.9559	0.0001	457
32	1	2	13	47.255	47.281	-0.026	1.9220	1.9210	0.0010	101
33	0	2	14	47.571	47.572	-0.001	1.9099	1.9099	0.0000	190
34	2	2	11	48.536	48.548	-0.012	1.8742	1.8738	0.0004	64
35	4	1	0	49.488	49.477	0.010	1.8404	1.8407	-0.0004	37
36	2	2	12	50.053	49.993	0.059	1.8209	1.8229	-0.0020	24
37	1	0	20	50.834	50.833	0.001	1.7947	1.7948	0.0000	70
38	2	2	13	51.664	51.680	-0.016	1.7678	1.7673	0.0005	121
39	1	3	5	52.307	52.300	0.007	1.7476	1.7478	-0.0002	108
40	4	1	7	52.637	52.653	-0.016	1.7374	1.7369	0.0005	85
41	1	0	21	53.431	53.450	-0.019	1.7135	1.7129	0.0006	27
42	2	1	19	55.352	55.331	0.020	1.6585	1.6590	-0.0006	216
43	3	2	11	55.618	55.641	-0.023	1.6512	1.6505	0.0006	132
44	2	3	5	56.429	56.378	0.052	1.6293	1.6307	-0.0014	81
45	2	1	20	57.689	57.643	0.046	1.5967	1.5979	-0.0012	264
46	4	2	1	57.793	57.812	-0.020	1.5941	1.5936	0.0005	338
47	2	3	8	58.739	58.795	-0.056	1.5706	1.5693	0.0014	39

Table 83. Continuation from Table 82.

				2Θ (°)			*d* (Å)			*I*
No.	**h**	**k**	**l**	calc	obs	diff	calc	obs	diff	obs
1	0	0	3	6.412	6.470	-0.057	13.7728	13.6507	0.1221	12
2	0	0	6	12.845	12.912	-0.067	6.8864	6.8509	0.0356	4
3	0	0	9	19.318	19.357	-0.038	4.5909	4.5819	0.0090	8
4	1	0	4	20.021	20.056	-0.035	4.4314	4.4237	0.0077	2
5	1	0	7	23.562	23.588	-0.026	3.7728	3.7687	0.0041	22
6	1	0	8	25.014	25.053	-0.039	3.5570	3.5515	0.0055	4
7	0	0	12	25.855	25.886	-0.031	3.4432	3.4391	0.0041	4
8	1	0	11	29.936	29.959	-0.023	2.9824	2.9802	0.0022	1000
9	1	1	0	31.563	31.581	-0.018	2.8323	2.8308	0.0016	464
10	1	0	14	35.467	35.477	-0.009	2.5289	2.5283	0.0006	17
11	1	1	9	37.272	37.266	0.006	2.4105	2.4109	-0.0004	8
12	2	0	4	37.661	37.713	-0.051	2.3865	2.3834	0.0031	8
13	0	0	18	39.215	39.231	-0.016	2.2955	2.2946	0.0009	80
14	2	0	7	39.763	39.763	0.000	2.2651	2.2651	0.0000	9
15	2	0	8	40.688	40.682	0.006	2.2157	2.2160	-0.0003	9
16	2	0	11	44.057	44.056	0.001	2.0538	2.0538	-0.0001	587
17	1	0	19	45.593	45.597	-0.004	1.9881	1.9879	0.0002	35
18	2	0	14	48.201	48.205	-0.004	1.8864	1.8863	0.0001	34
19	1	1	18	51.182	51.189	-0.007	1.7833	1.7831	0.0002	24
20	1	0	22	52.102	52.110	-0.007	1.7540	1.7537	0.0002	940
21	1	1	19	53.049	53.088	-0.039	1.7249	1.7237	0.0012	7
22	2	1	11	55.200	55.174	0.026	1.6627	1.6634	-0.0007	287
23	3	0	0	56.206	56.194	0.012	1.6353	1.6356	-0.0003	164
24	1	0	25	58.920	58.922	-0.002	1.5662	1.5662	0.0001	51
25	0	0	27	60.445	60.429	0.016	1.5303	1.5307	-0.0004	3
26	1	0	26	61.263	61.248	0.015	1.5118	1.5122	-0.0003	11
27	2	0	22	62.204	62.193	0.012	1.4912	1.4915	-0.0003	187
28	1	1	24	63.149	63.143	0.006	1.4712	1.4713	-0.0001	5

Table 84. $Sr_6Nb_5O_{18.07}$ ($m = 6$ of $A_mB_{m-1}O_{3m}$). The calculated values refer to a primitive hexagonal cell with $a = 5.67$ Å and $c = 41.32$ Å.

				2Θ (°)			d (Å)			I
No.	**h**	**k**	**l**	calc	obs	diff	calc	obs	diff	obs
1	0	0	6	7.003	7.050	-0.047	12.6119	12.5283	0.0836	4
2	0	0	9	10.513	10.574	-0.061	8.4079	8.3597	0.0483	1
3	0	0	12	14.033	14.059	-0.026	6.3059	6.2941	0.0118	3
4	1	0	7	19.863	19.877	-0.014	4.4664	4.4633	0.0031	4
5	1	0	13	23.703	23.735	-0.032	3.7507	3.7456	0.0050	22
6	1	0	14	24.488	24.488	0.000	3.6321	3.6322	-0.0001	3
7	1	0	17	27.030	27.024	0.006	3.2961	3.2968	-0.0007	2
8	1	0	20	29.800	29.817	-0.017	2.9957	2.9940	0.0017	1000
9	1	1	1	31.593	31.594	-0.001	2.8297	2.8296	0.0001	432
10	1	0	23	32.751	32.800	-0.049	2.7322	2.7283	0.0040	3
11	1	0	26	35.849	35.871	-0.022	2.5029	2.5014	0.0015	7
12	2	0	6	37.326	37.293	0.033	2.4072	2.4092	-0.0020	8
13	0	0	33	39.258	39.255	0.003	2.2931	2.2932	-0.0002	29
14	2	0	13	39.858	39.878	-0.020	2.2599	2.2588	0.0011	12
15	2	0	14	40.356	40.357	-0.001	2.2332	2.2331	0.0001	7
16	1	1	23	42.067	42.083	-0.016	2.1462	2.1454	0.0008	2
17	2	0	20	43.965	43.973	-0.008	2.0578	2.0575	0.0004	623
18	1	0	34	44.677	44.671	0.005	2.0267	2.0269	-0.0002	14
19	1	0	37	48.168	48.163	0.006	1.8876	1.8878	-0.0002	6
20	2	0	26	48.504	48.526	-0.021	1.8753	1.8746	0.0008	38
21	0	0	41	49.336	49.314	0.023	1.8456	1.8464	-0.0008	5
22	1	1	33	51.222	51.227	-0.004	1.7820	1.7819	0.0001	28
23	1	0	40	51.752	51.758	-0.006	1.7650	1.7648	0.0002	564
24	2	1	20	55.127	55.143	-0.016	1.6647	1.6642	0.0005	435
25	3	0	1	56.236	56.236	0.000	1.6345	1.6345	0.0000	155
26	1	0	46	59.194	59.197	-0.003	1.5596	1.5596	0.0001	16
27	2	1	28	60.516	60.474	0.042	1.5287	1.5296	-0.0010	3
28	2	0	40	61.896	61.895	0.001	1.4979	1.4979	0.0000	213

Table 85. $Sr_{11}Nb_9O_{33.09}$ ($m = 5 + 6$ of $A_mB_{m-1}O_{3m}$). The calculated values refer to a primitive hexagonal cell with $a = 5.66$ Å and $c = 75.67$ Å.